Dynamic Phasor Modeling of Type 3 Wind Farm including Multi-mass and LVRT Effects

A Thesis Submitted to

The College of Graduate Studies and Research

In Partial Fulfillment of the Requirements

For the Degree of Master of Science

In the Department of Electrical and Computer Engineering

University of Saskatchewan

by

Binay Kumar Thakur

Saskatoon, Saskatchewan, Canada

Permission to Use

In presenting this thesis in partial fulfillment of the requirements for a Postgraduate degree from the University of Saskatchewan, it is agreed that the Libraries of this University may make it freely available for inspection. Permission for copying of this thesis in any manner, in whole or in part, for scholarly purposes may be granted by the professors who supervised this thesis work or, in their absence, by the Head of the Department of Electrical and Computer Engineering or the Dean of the College of Graduate Studies and Research at the University of Saskatchewan. Any copying, publication, or use of this thesis, or parts thereof, for financial gain without the written permission of the author is strictly prohibited. Proper recognition shall be given to the author and to the University of Saskatchewan in any scholarly use which may be made of any material in this thesis.

Request for permission to copy or to make any other use of material in this thesis in whole or in part should be addressed to:

Head of the Department of Electrical and Computer Engineering
57 Campus Drive
University of Saskatchewan
Saskatoon, Saskatchewan, Canada
S7N 5A9

Abstract

The proportion of power attributable to wind generation has grown significantly in the last two decades. System impact studies such as load flow studies and short circuit studies, are important for planning before integration of any new wind generation into the existing power grid. Short circuit modelling is central in these planning studies to determine protective relay settings, protection coordination, and equipment ratings.

Numerous factors, such as low voltage situations, power electronic switching, control actions, sub-synchronous oscillations, etc., influence the response of wind farms to short circuit conditions, and that makes short circuit modelling of wind farms an interesting, complex, and challenging task. Power electronics-based converters are very common in wind power plants, enabling the plant to operate at a wide range of wind speeds and provide reactive power support without disconnection from the grid during low voltage scenarios. This has led to the growth of Type 3 (with rotor side converter) and Type 4 (with stator side full converter) wind generators, in which power electronics-based converters and controls are an integral part. The power electronics in these generators are proprietary in nature, which makes it difficult to obtain the necessary information from the manufacturer to model them accurately in planning studies for conditions such as those found during faults or low voltage ride through (LVRT) periods. The use of power electronic controllers also has led to phenomena such as sub-synchronous control interactions in series compensated Type 3 wind farms, which are characterized by non-fundamental frequency oscillations.

The above factors have led to the need to develop generic models for wind farms that can be used in studies by planners and protection engineers. The current practice for short circuit modelling of wind farms in the power industry is to utilize transient stability programs based on either simplified electromechanical fundamental frequency models or detailed electromagnetic time domain models. The fundamental frequency models are incapable of representing the majority of critical wind generator fault characteristics, such as during power electronic switching conditions and sub-synchronous interactions. The detailed time domain models, though accurate, demand high levels of computation and modelling expertise. A simple yet

accurate modelling methodology for wind generators that does not require resorting to fundamental frequency based simplifications or time domain type simulations is the basis for this research work.

This research work develops an average value model and a dynamic phasor model of a Type 3 DFIG wind farm. The average value model replaces the switches and associated phenomena by equivalent current and voltage sources. The dynamic phasor model is based on generalized averaging theory, where the system variables are represented as time varying Fourier coefficients known as dynamic phasors. The two types models provide a generic type model and achieve a middle ground between conventional electromechanical models and the cumbersome electromagnetic time domain models. The dynamic phasor model enables the user to consider each harmonic component individually; this selective view of the components of the system response is not achievable in conventional electromagnetic transient simulations. Only the appropriate dynamic phasors are selected for the required fault behaviour to be represented, providing greater computational efficiency than detailed time domain simulations. A detailed electromagnetic transient (EMT) simulation model is also developed in this thesis using a real-time digital simulator (RTDS). The results obtained with the average value model and the dynamic phasor model are validated with an accurate electromagnetic simulation model and some state-of-the-art industrial schemes: a voltage behind transient reactance model, an analytical expression model, and a voltage dependent current source model.

The proposed RTDS models include the effect of change of flux during faulted conditions in the wind generator during abnormal system conditions instead of incorrectly assuming it is a constant. This was not investigated in previous studies carried out in the real-time simulations laboratory at the University of Saskatchewan or in various publications reported in the literature. The most commonly used LVRT topologies, such as rotor side crowbar circuit, DC-link protection scheme, and series dynamic braking resistance (SDBR) in rotor and stator circuits, are investigated in the short circuit studies. The RTDS model developed uses a multi-mass (three-mass) model of the mechanical drive train instead of a simple single-mass model to represent torsional dynamics. The single mass model considers the

blade inertia, the turbine hub, and the generator as a single lumped mass and so cannot reproduce the torsional behaviour.

The root cause of sub-synchronous frequencies in Type 3 wind generators is not well-understood by system planners and protection engineers. Some literature reports it is self excitation while others report it is due to sub-synchronous control inter-actions. One publication in the stability literature reports on a small signal analysis study aimed at finding the root cause of the problem, and a similar type of analysis was performed in this thesis. A linearized model was developed, which includes the generator model, a three mass drive train, rotor side converter, and the grid side converter represented as a constant voltage source. The linear model analysis showed that the sub-synchronous oscillations are due to control interactions between the rotor side controller of the Type 3 wind power plant and the series capacitor in the transmission line. The rotor side controls were tuned to obtain a stable response at higher levels of compensation.

A real-time simulation model of a 450 MW Type 3 wind farm consisting of 150 units transmitting power via 345 kV transmission line was developed on the RTDS. The dynamic phasor method is shown to be accurate for representing faults at the point of interconnection of the wind farm to the grid for balanced and unbalanced faults as well as for different sub-synchronous oscillation frequencies.

Acknowledgments

First and foremost, I wish to acknowledge and extend my heartfelt gratitude to my advisor, Prof. Ramakrishna Gokaraju for his patient and thoughtful guidance and support that motivated and inspired me to successfully complete my research work and thesis. I would like to thank Prof. Ramakrishna Gokaraju for entrusting me and giving me this opportunity to pursue the M.Sc program in power research group. I also thank him for providing financial support through NSERC Grants.

I would like to thank the faculty of the Department of Electrical and Computer Engineering at the University of Saskatchewan for providing the foundation for my research work through courses and financial support through the Graduate Research Fellowship (GRF) and the Departmental scholarship. I would also like to thank Mr. Sriram Chandrasekar and Mr. Gopiram Maddela (Former Graduate Students of University of Saskatchewan), Mr. Jason Pannell (Graduate Student), Dr. Ali B. Dehkordi from RTDS Technologies Inc., Dr. Aryan Saadat Mehr from University of Saskatchewan, Dr. D.H.R. Suriyaarachchi from TransGrid Solutions, for their inputs during the course of my research work. The inputs of Prof. M. Ramamoorty (Retired Director General of Central Power Research Institute, Bangalore, India) with regards to modelling of flux decrement effects are appreciated. I would like to thank Mr. Dean Miller, Chair of the Working Group C17.0 of the IEEE Power Systems Relaying Committee for providing the final report of "Fault Current Contributions from Wind Plants". I would also like to thank Prof. Kai Strunz from Technical University of Berlin for providing his slides on "Multi-Scale Modeling and Simulation of Power Systems".

Many thanks go to the students from the Power Systems Simulation Laboratory for a pleasant working atmosphere and the continuous support they gave me. I also thank my family and friends, without whom this would not have been possible. I especially thank my father and my wife, Sonam for their endless encouragement and support.

−Binay Kumar Thakur

Dedicated

to my

late mother

Table of Contents

Permission to Use i

Abstract ii

Acknowledgments v

Dedication vi

Table of Contents vii

List of Tables xiii

List of Figures xiv

List of Symbols and Abbreviations xxi

1 Introduction 1

1.1 Background 1

1.2 Wind Power 2

1.2.1 Growth of Wind Power Generation 2

1.2.2 Short Circuit modelling of Wind Generators and Challenges 5

1.3 Literature Review 7

1.3.1 Type 1 and Type 2 Generators 7

1.3.1.1 Type 1 Wind Generator 7

1.3.1.2 Type 2 Wind Generator 8

1.3.2 Type 3 Wind Generators 9

1.3.2.1 modelling Issues . . . 9
1.3.2.2 modelling Methods . . . 14
1.3.3 Type 4 Wind Generators . . . 21
1.4 Objective of the Thesis . . . 21
1.5 Organization of the Thesis . . . 22
List of Symbols and Abbreviations 1
2 Various Types of Wind Turbine Generators and Short Circuit modelling 24
2.1 Introduction . . . 24
2.2 Types of Wind Turbine Generators . . . 25
2.2.1 Type 1 Squirrel Cage Induction Generator . . . 25
2.2.2 Type 2 Wound Rotor Induction Generator . . . 26
2.2.3 Type 3 Doubly Fed Induction Generator (DFIG) . . . 27
2.2.3.1 Basic Operation of DFIG . . . 29
2.2.4 Type 4 Full Converter Wind Turbine Generator . . . 30
2.3 Commonly Used Short Circuit modelling Methods for Wind Turbine Generators 31
2.3.1 Voltage behind Transient Reactance Representation . . . 32
2.3.1.1 Type 1 Wind Generator . . . 32
2.3.1.2 Type 2 Wind Generator . . . 36
2.3.1.3 Type 3 Wind Generator . . . 38
2.3.1.4 Key Findings . . . 40
2.3.2 Analytical Expression Representation . . . 40

2.3.2.1 Type 1 Wind Generator 41
2.3.2.2 Type 2 Wind Generator 43
2.3.2.3 Type 3 Wind Generator 44
2.3.2.4 Key Findings 45
2.3.3 Voltage Dependent Current Source Modelling 45
2.3.3.1 Introduction 45
2.3.3.2 Type 3 Wind Generator Modelling 46
2.3.3.3 Key Findings 48
2.3.4 WECC Type 3 WTG Generic Model 48
2.4 Summary 52
3 Modelling of DFIG Wind Power Plant including LVRT and Flux Decrement Effects 54
3.1 Introduction 54
3.2 Real Time Digital Simulator (RTDS) 55
3.3 Development of DFIG Wind Power Plant in RTDS 56
3.3.1 Wind Turbine Model 58
3.3.2 Mechanical Drive Train Model 61
3.3.3 Induction Generator Part 62
3.3.4 Back to Back Conveter 66
3.3.4.1 Back to Back Converter Modulation Scheme 66
3.3.4.2 Grid Side Converter (GSC) Control 67
3.3.4.3 Rotor Side Converter (RSC) Control 70

3.4 LVRT based Protection Scheme 72
3.4.1 Conventional Crowbar Protection Scheme 73
3.4.2 DC Link Voltage Protection Scheme 75
3.4.3 Series Dynamic Braking Resistor (SDBR) in Rotor Circuit 76
3.4.4 Series Dynamic Braking Resistor (SDBR) in Stator Circuit 78
3.5 Flux Decrement in Generator 80
3.6 DFIG model validation results 83
3.7 Summary 89
4 Small Signal Analysis of DFIG Wind Power Plant 90
4.1 Introduction 90
4.2 Sub-synchronous Oscillations in Wind Plants 90
4.3 Test System Simulation and Analysis 92
4.3.1 Application of Symmetrical Fault 93
4.3.2 Application of Unsymmetrical Fault 98
4.4 Frequency Scanning 99
4.5 Small Signal Analysis 100
4.5.1 Stability of Linearized Systems 101
4.5.1.1 Eigenvalue 101
4.5.1.2 Modes 102
4.5.1.3 Right Eigenvectors 103
4.5.1.4 Left Eigenvectors 104

4.5.1.5 Participation factor 104
4.5.2 Wind Turbine Model 105
4.5.3 Mechanical Drive Train Model 105
4.5.4 Induction Generator Model 106
4.5.5 Grid Side Converter (GSC) 107
4.5.6 Rotor Side Converter (RSC) 108
4.5.7 DC Link Capacitor Model 110
4.5.8 Series Compensated Transmission Line 111
4.5.9 Complete system 111
4.5.10 Results 112
4.6 Summary 114
5 Dynamic Phasor Model and Average Value Model of DFIG 116
5.1 Introduction 116
5.2 Dynamic Phasor Approach 117
5.2.1 Shift Frequency Concept 119
5.3 Dynamic Phasor Modelling of DFIG 125
5.3.1 Fault behaviour without Series Compensated Transmission Line . . . 131
5.3.1.1 Symmetrical Fault behaviour 131
5.3.1.2 Unsymmetrical Fault behaviour 134
5.3.2 Fault behaviour with a Series Compensated Transmission Line 137
5.3.2.1 Symmetrical Fault behaviour 137

5.3.2.2 Unsymmetrical Fault behaviour 143
5.4 Average Value Model 147
5.4.1 Average Value modelling of DFIG 148
5.4.2 Simulation Results 151
5.5 Summary 153
6 Summary, Conclusions, Contributions and Future Work 155
6.1 Summary 155
6.2 Conclusions 156
6.3 Contributions of the Thesis 157
6.4 Future Work 159
References 160
Appendix A 173
A.1 Type 1 Wind Generator Test System Parameters 173
A.2 Type 2 Wind Generator Test System Parameters 173
A.3 Type 3 Wind Generator Test System Parameters 174
A.4 Mechanical Drive Train parameters 174
Appendix B 175
B.1 Relationship between $\alpha\beta$ and dq reference frames 175
B.2 Relationship between two reference frames in dq domain 176
Appendix C 177
Appendix D 180

List of Tables

2.1 Comparison of results for Type 1 wind generator - ungrounded system 35

2.2 Comparison of results for Type 1 wind generator - grounded system 36

2.3 Comparison of results for Type 2 wind generator 38

2.4 Accuracy of voltage behind transient reactance modelling for Type 3 wind generator 39

4.1 Prony analysis of phase A symmetrical fault current with 50% compensation 97

4.2 Prony analysis of phase A symmetrical fault current with 70% compensation 98

5.1 Selection of appropriate dynamic phasors 126

A.1 Type 1 wind generator test system data 173

A.2 Type 2 wind generator test system data 173

A.3 Type 3 wind generator test system data 174

A.4 Mechanical Drive Train parameters 174

List of Figures

1.1 Renewable energy contribution to global power production, 2013 2

1.2 Growth of wind power installed capacity from 2000 to 2015(GW) 3

1.3 Growth of wind power installed capacity in 2015(GW) 4

1.4 Canada's wind power installed capacity from 2000 to 2015(MW) 4

1.5 Trend in market penetration of different types of wind generators 5

2.1 Types of wind turbine generators 24

2.2 Type 1 wind turbine generator 26

2.3 Type 2 wind turbine generator 27

2.4 Type 3 wind turbine generator 28

2.5 Type 4 wind turbine generator 31

2.6 Upper and lower envelopes of the fault current waveform 32

2.7 Type 1 wind generator test system 33

2.8 Equivalent circuit of the Type 1 wind generator test system 33

2.9 Voltage behind transient reactance model (positive sequence network) of Type 1 wind generator test system for symmetrical fault 35

2.10 Type 2 wind generator test system 36

2.11 Positive sequence network of Type 2 wind generator test system 37

2.12 Voltage behind transient reactance model (positive sequence network) of Type 3 wind generator test system for a symmetrical fault 39

2.13 AC Component of Phase A fault current 41

2.14 DC Component of Phase A fault current 42

2.15 Three phase fault - Phase A stator currents - Type 1 wind generator - EMT model versus analytical expression 42

2.16 Phase A Stator Currents - Type 2 wind generator - EMT model versus analytical expression 43

2.17 Phase B stator currents - Type 3 wind generator - EMT model versus analytical expression 44

2.18 Short circuit currents for different percentages of 3-phase voltage sags for a Type 3 generator 46

2.19 Maximum and minimum short circuit current envelopes as a function of the applied voltage sag 47

2.20 Voltage dependent current source model of Type 3 wind generator 48

2.21 Structure of a first generation Type 3 WTG 49

2.22 Structure of a second generation Type 3 WTG 50

2.23 Real and Reactive power for a balanced 3 phase voltage dip of 20% 51

2.24 Real and Reactive power for a balanced 3 phase voltage dip of 75% 52

3.1 DFIG system 57

3.2 Interface Transformer 57

3.3 C_p-λ characteristics 59

3.4 Wind turbine characteristics with β=0 60

3.5 Wind turbine pitch angle controller 61

3.6 Three mass drive train model 62

3.7 Schematic winding diagram of the stator and rotor side of the induction generator 63

3.8 Back to Back Converter 66

3.9 SPWM Scheme 67

3.10 Schematic diagram to demonstrate GSC control 68

3.11 Control scheme implemented for GSC 69

3.12 Outer capacitive voltage regulator loop implemented in RTDS 70

3.13 Control scheme implemented for RSC 71

3.14 LVRT characteristics used in the test system 73

3.15 DFIG unit breaker protection based on LVRT Scheme, converter blocking and crowbar triggering 74

3.16 Converters with DC link shunt resistor 75

3.17 Crowbar control scheme 76

3.18 Crowbar switching action during an external fault 76

3.19 SDBR in Rotor Circuit with DC-Link Voltage Protection Scheme 77

3.20 (a) Stator currents (b) Rotor currents with SDBR in rotor circuit 78

3.21 SDBR in Stator Circuit with DC-Link Voltage Protection Scheme 79

3.22 (a)Stator currents (b) Rotor currents with SDBR in stator circuit 80

3.23 Comparison of A Phase current with constant and variable flux 81

3.24 Comparison of B Phase current with constant and variable flux 82

3.25 Comparison of C Phase current with constant and variable flux 82

3.26 Steady state Real and Reactive Power 83

3.27 Steady state Stator currents 84

3.28 Response of Active Power and Pitch Angle to change in wind speed 85

3.29 Active Power variation for symmetrical fault 86

3.30 DFIG stator current variation for symmetrical fault 87

3.31 Active power variation for unsymmetrical fault 88

3.32 DFIG stator current variation for unsymmetrical fault 88

4.1 DFIG wind generator test system with series compensation 92

4.2 Type 3 wind farm symmetrical fault current with sub-synchronous frequency components (50% compensation) 94

4.3 Comparison of stator fault current without and with compensation for a three phase fault 95

4.4 FFT analysis of phase A symmetrical fault current with 50% compensation . 96

4.5 FFT analysis of phase A symmetrical fault current with 70% compensation . 96

4.6 Prony analysis of phase A symmetrical fault current with 50% compensation 97

4.7 Comparison of phase A stator fault current without and with series compensation for a phase A to ground fault 98

4.8 Frequency Scanning - magnitude and phase angle plot of network driving point impedance 100

4.9 PI controllers for GSC 108

4.10 PI controllers for RSC 109

4.11 DC Link 110

4.12 Series Compensated Line 111

4.13 Participation factors of sub-synchronous mode with 50% compensation . . . 112

4.14 Sensitivity of damping to RSC q-axis controller 113

4.15 Sensitivity of damping to RSC d-axis controller 114

5.1 Window of time-period T sliding over time varying signal 118

5.2 Frequency spectrum of real signal 119

5.3 Frequency spectrum of analytical signal 119

5.4 Frequency spectrum of shifted signal 120

5.5 Frequency spectrum of baseband signal with higher harmonics 121

5.6 Frequency spectrum of Dynamic phasors 122

5.7 Fault current for Type 3 wind farm symmetrical fault application - EMT model131

5.8 Relative magnitude of positive and negative sequence dynamic phasors for a symmetrical fault 132

5.9 Comparison of EMT and dynamic phasor modelling for symmetrical fault . . 133

5.10 Rotor speed for symmetrical fault 134

5.11 Fault current for Type 3 wind farm unsymmetrical fault application - EMT model 135

5.12 Relative magnitude of positive and negative sequence dynamic phasors for an unsymmetrical fault 136

5.13 Comparison of EMT and dynamic phasor modelling for Type 3 wind farm unsymmetrical fault application 136

5.14 Rotor speed for unsymmetrical fault 137

5.15 Type 3 wind farm phase A fault current for symmetrical fault with 50% compensation - EMT model 138

5.16 Relative magnitude of positive and sub-synchronous component dynamic phasors for a symmetrical fault in a 50% compensated Type 3 wind farm 139

5.17 Comparison of EMT and dynamic phasor modelling for 50% compensated Type 3 wind farm symmetrical fault application 139

5.18 Rotor speed for 50% compensation under symmetrical fault 140

5.19 Type 3 wind farm phase A fault current for symmetrical fault with 70 % series compensation - EMT model 141

5.20 Relative magnitude of positive and sub-synchronous component dynamic phasors for a symmetrical fault in 70% compensated Type 3 wind farm 141

5.21 Comparison of EMT and dynamic phasor modelling for 70 % compensated Type 3 wind farm symmetrical fault application 142

5.22 Rotor speed for 70% compensation under symmetrical fault 142

5.23 Type 3 wind farm phase A fault current for unsymmetrical fault with 50 % series compensation - EMT model 143

5.24 Relative magnitude of positive sequence, negative sequence and sub-synchronous component dynamic phasors for an unsymmetrical fault in a 50% compensated Type 3 wind farm 144

5.25 Comparison of EMT and dynamic phasor modelling for 50 % compensated Type 3 wind farm unsymmetrical fault application 144

5.26 Rotor speed for 50% compensation under unsymmetrical fault 145

5.27 Type 3 wind farm phase A fault current for unsymmetrical fault with 70 % series compensation - EMT model 145

5.28 Relative magnitude of positive sequence, negative sequence and sub-synchronous component dynamic phasors for an unsymmetrical fault in a 70 % compensated Type 3 wind farm 146

5.29 Comparison of EMT and dynamic phasor modelling for 70 % compensated Type 3 wind farm unsymmetrical fault application 146

5.30 Rotor speed for 70% compensation under unsymmetrical fault 147

5.31 PWM scheme and Average value output 148

5.32 Average value model for back to back converters 150

5.33 Phase A stator current for symmetrical fault 151

5.34 Phase A stator current for unsymmetrical fault 152

5.35 Rotor speed for symmetrical fault 153

B.1 $\alpha\beta$ to dq transformation 175

B.2 Two reference frames in dq domain 176

C.1 Sub-systems Interconnections 177

D.1 Inductance 180

D.2 Trapezoidal rule of Integration 181

D.3 Equivalent circuit for inductor 182

D.4 Capacitance 182

D.5 Equivalent circuit for capacitance 183

D.6 Equivalent circuit for all power systems 183

List of Symbols and Abbreviations

AVM	Average value model
C_{dc}	Capacitance of the DC link capacitor
C_p	Performance coefficient
$DFIG$	Doubly fed induction generator
EMT	Electromagnetic transient
$FACTS$	Flexible AC transmission systems
FFT	Fast Fourier transform
GSC	Grid side converter
H	Inertia constant (sec)
$I_{dg}*, I_{qg}*$	Reference d and q components of grid side converter current
I_{dr}, I_{qr}	d and q components of rotor current
$I_{dr}*, I_{qr}*$	Reference d and q components of rotor side converter current
I_{ds}, I_{qs}	d and q components of stator current
$IGBT$	Insulated gate bipolar transistor
I_L	Lower value of fault current at inception of fault
I_{sc}	Short circuit current
I_U	Upper value of fault current at inception of fault
$K_{p,Idg}, K_{i,Idg}$	Proportional and Integral gain of the GSC d axis current controller
$K_{p,Idr}, K_{i,Idr}$	Proportional and Integral gain of the RSC d axis current controller
$K_{p,Iqg}, K_{i,Iqg}$	Proportional and Integral gain of the GSC q axis current controller
$K_{p,Iqr}, K_{i,Iqr}$	Proportional and Integral gain of the RSC q axis current controller

$K_{p,Qs}, K_{i,Qs}$	Proportional and Integral gain of the stator reactive power controller
$K_{p,Vdc}, K_{p,Vdc}$	Proportional and Integral gain of the dc voltage controller
$K_{p,\omega_r}, K_{i,\omega_r}$	Proportional and Integral gain of the generator speed controller
L_{ls}, L_{lr}	Stator winding and Rotor winding leakage inductance
L_m	Magnetizing inductance
$LVRT$	Low voltage ride through
PCC	Point of common coupling
P_r, P_g	Real power flow at rotor side and grid side converters
P_s, Q_s	Stator real and reactive power
P_t	Power extracted by wind turbine
P_{wind}	Available wind power
Q_s*	Reference stator reactive power
R, L, C	Line resistance, inductance and capacitance
$R_{crowbar}$	Rotor crowbar resistance
$R_{IGBT-OFF}$	IGBT OFF resistance
$R_{IGBT-ON}$	IGBT ON resistance
rms	Root Mean Square
R_{rext}	Rotor external resistance
r_s, r_r	Stator winding and Rotor winding resistance
RSC	Rotor side converter
$SCGI$	Squirrel cage induction generator
$SPWM$	Sinusoidal pulse-width modulation
$SSCI$	Sub-synchronous control interaction

SSR	Sub-synchronous resonance
TSR	Tip speed ratio
T_e	Electrical torque
T_m	Mechanical torque
VBR	Voltage behind transient reactance
VSC	Voltage source converter
V_∞	Infinite bus voltage
V_{dc}	DC link voltage
$V_{dc}*$	Reference DC link capacitor voltage
V_{di}, V_{qi}	d and q components of infinite bus voltage
V_{dr}, V_{qr}	d and q components of rotor voltage
V_{ds}, V_{qs}	d and q components of stator voltage
V_{wind}	Wind speed $[m/sec]$
$WRIG$	Wound rotor induction generator
X_k	k_{th} Fourier coefficient
$\langle x \rangle_k(t)$	k^{th} dynamic phasor
ρ	Air density $[kg/m^3]$
ψ_{dr}, ψ_{qr}	d and q components of rotor flux linkage
ψ_{ds}, ψ_{qs}	d and q components of stator flux linkage
ω_0	Angular base speed (377 rad/sec)
ω_r	Rotor angular speed
ω_r*	Reference rotor angular speed
ω_s	Synchronous speed

Chapter 1

Introduction

1.1 Background

The proportion of installed renewable energy sources in the electric power system has increased significantly in the past decade. The most popular renewable energy technologies are wind power, photovoltaics, hydro power, and biomass. As of 2013, fossil fuels provided just over 78% of the world's energy and renewable energy about 19% (Figure 1.1). From 2010-2015, generation from wind power and solar photovoltaics grew at annual average rates of 17 and 42%, respectively, which are very high compared to growth rates for fossil fuel power generation for the same period [1].

Fiscal incentives to customers from governments have also contributed to the significant increase of renewable power. For instance, a new energy agreement was reached in Denmark in March 2012 that contains initiatives to bring Denmark closer to a target of 100 percent renewable energy in the energy and transport sector by 2050. Ontario's Green Energy and Green Economy Act of 2009 established a feed-in-tariff program that offers payments for renewable energy power generation above market prices [2]. The South Australian government has granted final approval to build the Port Augusta Renewable Energy Park with 375 MW capacity [3].

Large integration of renewable sources into the grid also results in a number of operating challenges, such as increased fault current levels, subsynchronous oscillations, voltage stability issues, power quality issues, etc. Hence, accurate models for the renewables are necessary to assess system impact and make the necessary updates or changes in the system.

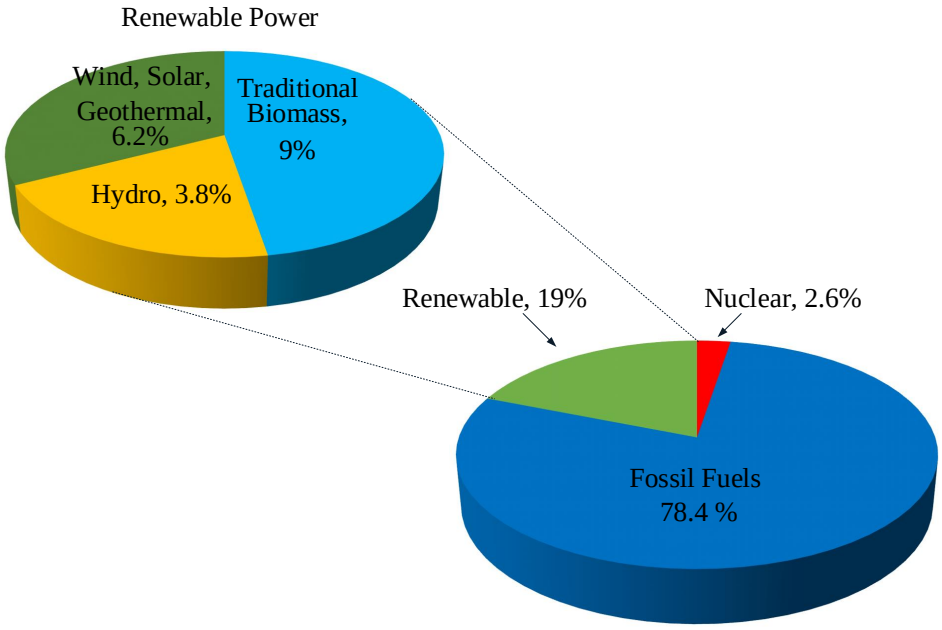

Figure 1.1: Renewable energy contribution to global power production, 2013

1.2 Wind Power

1.2.1 Growth of Wind Power Generation

Last decade has seen a tremendous growth in Wind Power Plants (WPP) in Canada and rest of the world. Figure 1.2 shows the growth from 2000 to 2015 [1]. Global wind power capacity 2015 ending was approximately 433 GW, with the largest capacity addition of approximately 64 GW happening in 2015. Figure 1.3 shows the installed wind power numbers in different regions of the world up by the end of 2014 and in 2015. This growth trend will continue with many countries setting targets to increase the wind energy contribution to 20% by 2020.

Figure 1.4 shows the Canada's wind power capacity from 2000 to 2015. Canada's wind power capacity by 2015 was 11,205 MW with addition of 1,506 MW in 2015. Today, wind energy supplies approximately 5 % of Canada's electricity demand. The wind energy industry in Canada is growing with an average annual growth rate of 23 % [4].

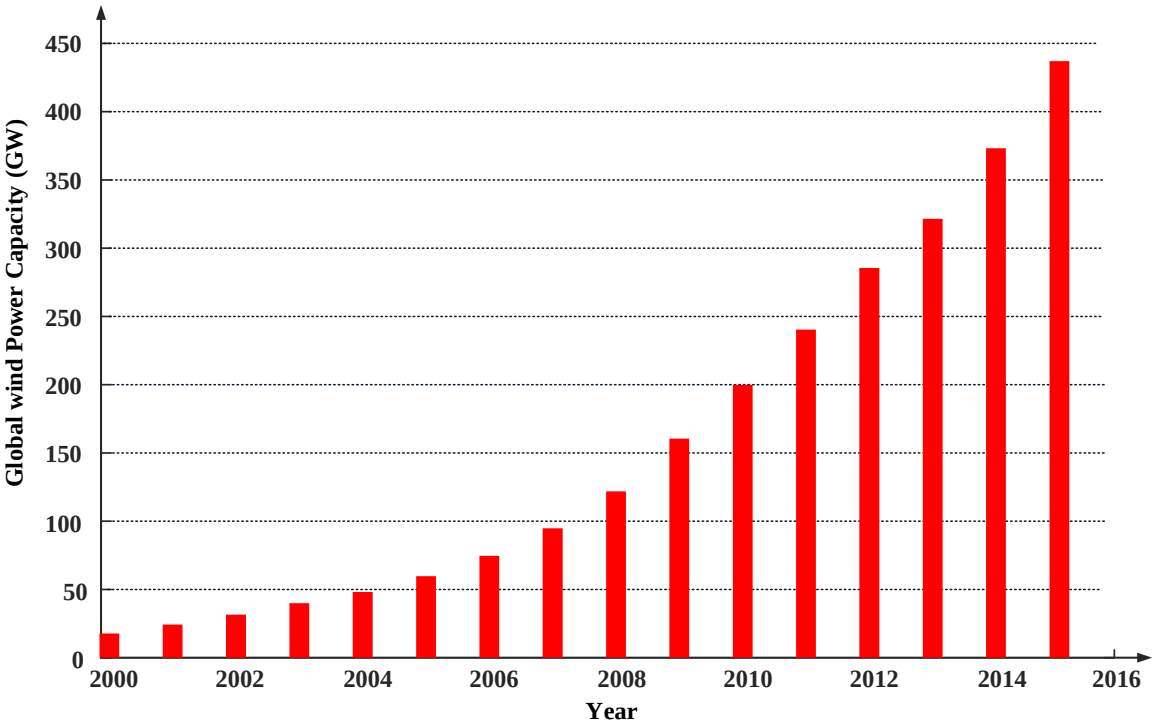

Figure 1.2: Growth of wind power installed capacity from 2000 to 2015(GW)

Wind is an intermittent source of power with a low capacity factor (the amount of output a power plant produces divided by the amount it would have produced, had it been in operation 24 hours/day, 365 days/year) of 20 to 40% [5]. It is clear that the wind market will keep increasing steadily and thus keep propelling the wind power generation technology to more advanced levels. Wind turbine generators are classified into four types based on the control strategies that are used to deal with wind variability, namely Type 1 (Squirrel cage induction generator), Type 2 (Wound rotor induction generator), Type 3 (Doubly fed induction generator), and Type 4 (Full converter based wind generator).

Type 3 wind turbine generators have gained the highest popularity among the different types with respect to market penetration [6]. Figure 1.5 shows the global trend in market penetration of the four types of wind generators [7]. Type 3 wind generator technology has been and continues to be the most installed type among the four wind generator types. This factor, along with the need to model the complex behaviour of the Type 3 wind generator

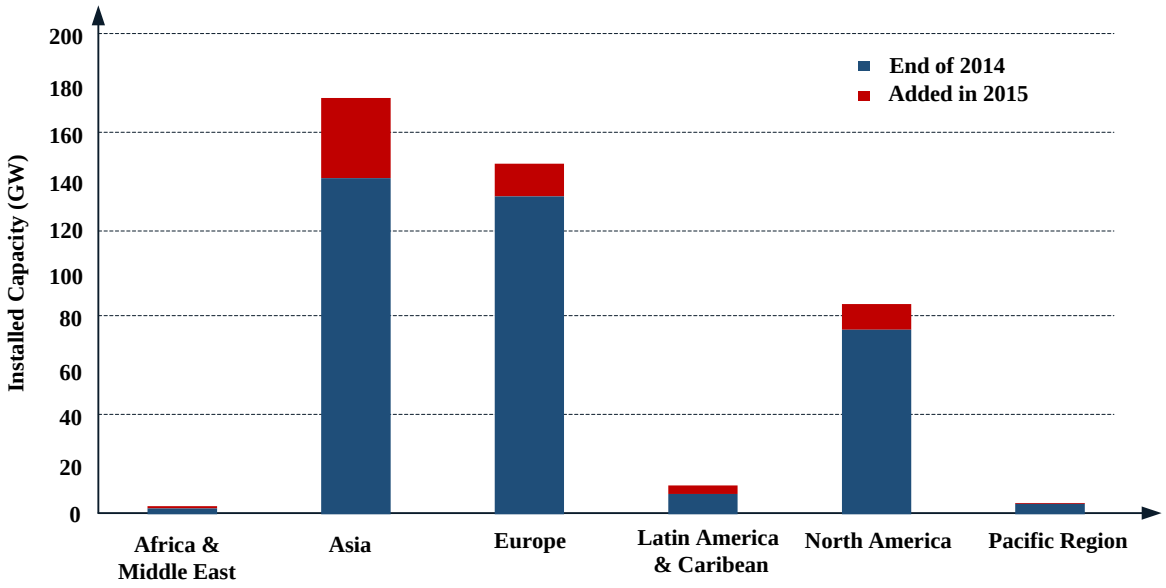

Figure 1.3: Growth of wind power installed capacity in 2015(GW)

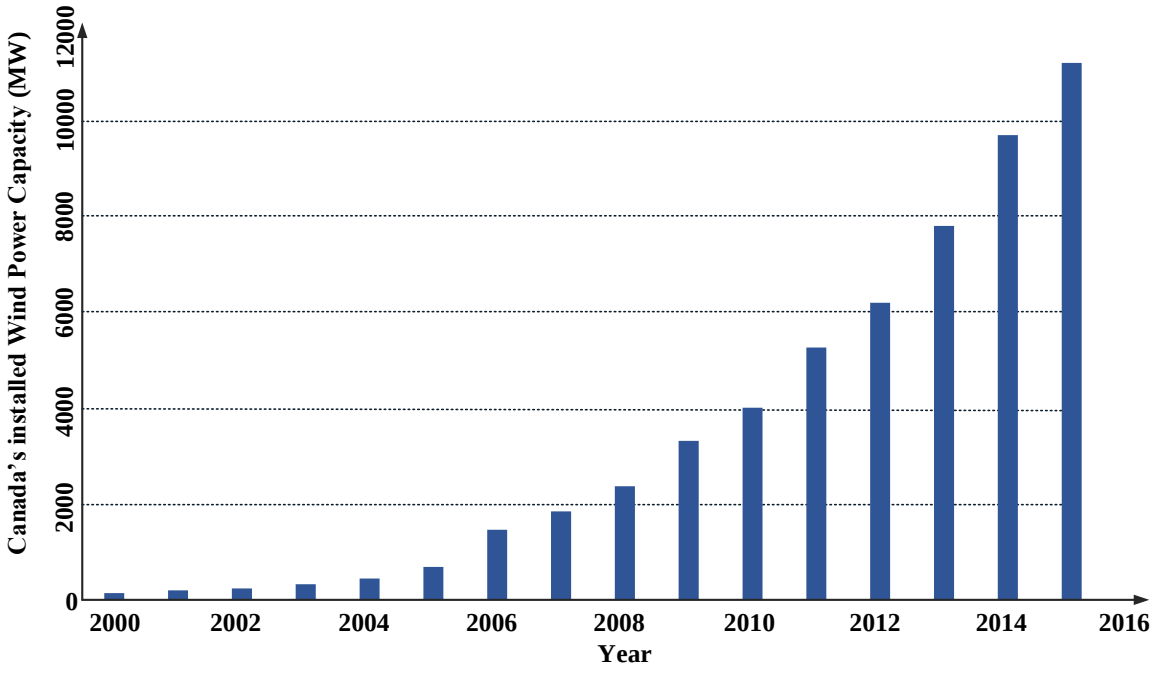

Figure 1.4: Canada's wind power installed capacity from 2000 to 2015(MW)

and its controls, make it an ideal candidate for performing modelling studies.

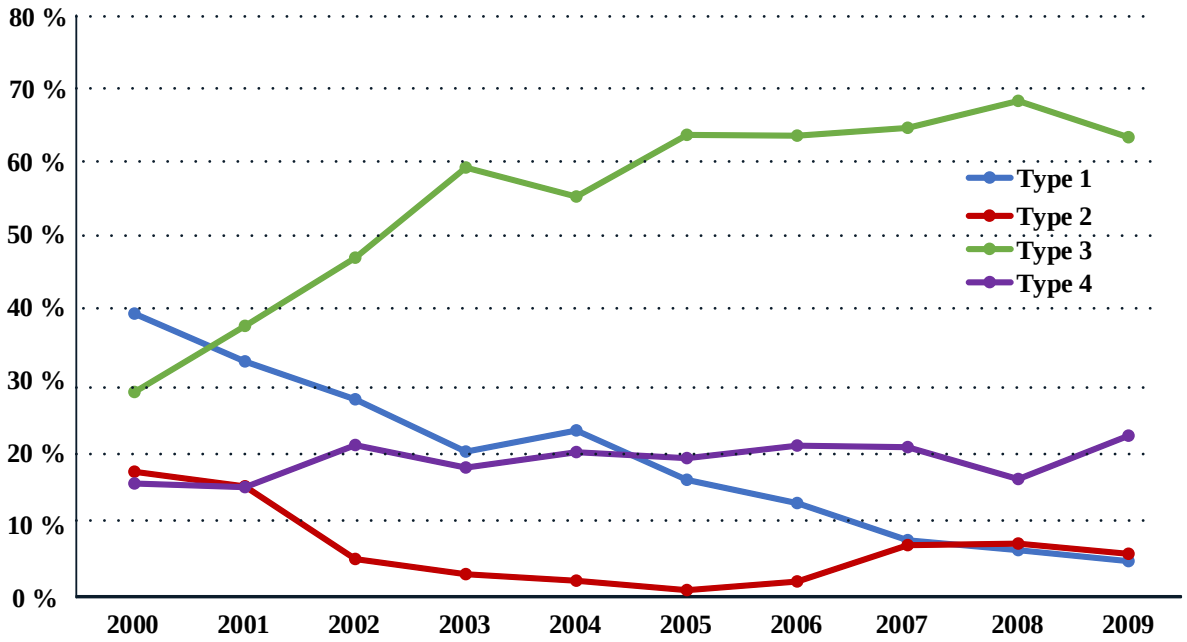

Figure 1.5: Trend in market penetration of different types of wind generators

1.2.2 Short Circuit modelling of Wind Generators and Challenges

As mentioned earlier, interconnection of wind power plants to the power grid results in protection issues. It is important to understand the short-circuit behaviour in order to develop adequate protection systems that will make the system safer and easy to operate. Short-circuit studies allow protection engineers to selectively determine which circuit breaker ratings, relay settings, and protection methods to adopt for a particular section of the power system. The reliability of relay settings depends on the accuracy of the short circuit models. Hence proper models for wind generators are very important.

The short-circuit behaviour of Type 1 (Squirrel cage induction generator) and Type 2 (Wound rotor induction generator) depends upon the physical characteristics(transient and subtransient impedances) of the WTGs and is therefore well understood [8]. On the other hand, Type 3 WTGs have much more complex fault current behaviours and pose difficulties in modelling due to various types of converter controls used in these generators. The short

circuit behaviour of a Type 3 wind generator is more complex than even the Type 4 wind generators (full-converter types), as the full power converter in the latter means that the fault current is limited by the rating of the converter [9].

Various types of Low voltage ride through (LVRT) configurations and control schemes used for the converters, contribute to the increased complexity of modelling Type 3 wind generators. Series compensation of transmission lines to deliver more power from remote high wind locations to load centers has also led to resonance/control interactions that affect the short circuit behaviour of wind farms, particularly the Type 3 wind farm [10]. The proprietary nature of information for these generators also makes it quite difficult to obtain this information from manufacturers.

The focus of this thesis is to develop a simplified short circuit model of wind generators (especially Type 3 wind generator) using purely the name plate details of the converters and standard type of dq controls. The model does not need depend on the exact internals of the wind generator systems. The model could be used by protection engineers to design protection and control settings for wind farms without the need to model the wind farm in detail. Various short circuit modelling techniques have been developed and utilized to model the short circuit behaviour of the different types of wind generators. The choice of the appropriate modelling technique for a particular wind generator depends on the extent to which that technique can accurately represent the complexities unique to that wind generator.

Common practice is to model wind generators with fundamental frequency synchronous generator equivalents. This is a simplified method of modelling the wind farm's behaviour and does not ensure a high level of accuracy. Due to power electronic converters employed in the energy conversion systems of wind generators, it is very difficult to accurately represent short circuit behaviour with these fundamental frequency representations.

Electromagnetic transient (EMT) modelling, which uses small time-step time domain $dq0$ differential equations, is used as a benchmark model to validate the modelling techniques discussed in this thesis. With electromagnetic transient modelling all the associated frequency components could be captured. EMT modelling is highly accurate and detailed,

but is cumbersome for modelling large and complex systems, such as a Type 3 wind farm consisting of multiple wind generators, and is computationally demanding.

Developing a model that includes different frequency behaviours, is fast and is not cumbersome as the detailed EMT model is crucial for the studies. Simplifying the modelling of power systems yet retaining the essential system characteristics based on the purpose of the study in hand [11–13] is needed. This calls for developing a middle ground between the detailed EMT and fundamental frequency models; which is the main focus of the modelling technique proposed in this research work.

1.3 Literature Review

1.3.1 Type 1 and Type 2 Generators

The standard techniques proposed in the literature to model the short circuit behaviour of Type 1 and Type 2 wind generators are summarized here:

1.3.1.1 Type 1 Wind Generator

The first generation of wind turbine generators was Type 1 wind generators based on a squirrel cage induction generator [14]. It used blade pitch angle control for the control mechanism. Type 1 has the advantage of mechanical simplicity, high efficiency, and low maintenance requirements [7].

Induction machines result in significant fault current contributions and the fault current contribution due to induction machines can be characterized by performing a series of tests [15]. The typical fault behaviour of an induction machine can be described in terms of the symmetrical and DC components present in the stator fault current. The DC component also is a significant part of the fault current and needs to be accounted for in modelling [15].

The instantaneous peak fault current after the fault is the most important quantity to be obtained, as this determines the rating of the protective relaying [16]. An expression for the

short circuit current as a function of rotor and stator time constants is derived and compared with the results from tests on real induction machines, indicating that the model provides adequate representation. A similar approach is described in [17] where the short circuit contribution is derived in the form of an analytical expression for an induction machine. In [18] and [19], the analytical expression modelling is used for short circuit modelling of Type 1 wind generators. These works show that the short circuit current of a Type 1 wind generator can be accurately obtained from the analytical expression of the stator fault current.

A technique based on voltage behind transient reactance (VBR) representation is presented in [20] to model the short circuit behaviour for symmetrical and unsymmetrical fault conditions. The modelling is based on developing a VBR representation by using sequence component networks and solving for the fault current at the inception of the fault. The results are verified against an EMT simulation model of the test system and show a high level of accuracy for the Type 1 wind generator.

1.3.1.2 Type 2 Wind Generator

The Type 2 wind generator utilizes a wound rotor induction generator (WRIG) with a variable resistance in the rotor [21]. Though in Type 2 wind generator power is dissipated as losses in the external resistance, it provides an improved operating speed range compared to the Type 1 wind generator configuration.

In [22] and [23], the short circuit behaviour of a Type 2 wind generator and important issue of equivalencing of the wind farm collector system are discussed. The external rotor resistance value affects the damping of the short circuit current, with higher rotor resistance contributing to more damping. Further, a Type 2 wind farm model is developed both with and without inclusion of the impedances of the cables connecting the individual wind generators to the main transformer at the substation and the fault behaviour observed. The cable impedances can be completely neglected for external short circuit studies on Type 2 wind farms for faults outside the wind farm. However, this is not true for faults within the

wind farm where cable impedances needs to be considered.

1.3.2 Type 3 Wind Generators

1.3.2.1 modelling Issues

Type 3 wind generators also consist of a wound rotor induction generator; however, the rotor winding is connected to the stator side with a bi-directional back-to-back voltage source converter (VSC). Various works have been reported in the recent literature discussing the modelling complexities of Type 3 wind generators with the objective to simplify their representation yet not compromise the accuracy of the model.

A wind farm typically consists of several wind turbine generators arranged in a manner to maximize wind capture and connected to the main substation through cables forming the collector system. The wind generators are mostly the same type within a wind farm; however, the length of the cables from each unit to the common point of coupling may vary. This is an important consideration not only for studying the transient behaviour of Type 3 wind farms but also for all other wind farms in general. The recent trend has been towards an aggregated model for assessing the transient behaviour of a wind farm as a whole for grid-side studies for the purpose of simplifcation and simulation speed as long as the internal wind farm characteristics are captured accurately.

References [24], [25] and [26] discuss the impact of aggregating all of the wind turbine generators in a Type 3 wind farm and representation of their collective behaviour by a single equivalent generator. It is assumed in these studies that all of the generators in the wind farm are of the same type and that all of the wind turbines see the same wind speed [27]. It is also assumed that all units in the wind farm trip for a fault outside it, whereas in reality not all of the units would trip.

Reference [28] discusses a dynamic equivalent model for large-scale wind power plants based on an aggregation technique. The authors tested the developed aggregated model against the original large-scale wind power plant and concluded that the aggregated model

has identical dynamic performance and the same effects on power system dynamics as a original wind power plant.

The above works conclude that, with the assumptions, the aggregated model still provides a good representation of the performance of the wind farm for faults outside the wind farm but is not as accurate for faults inside the wind farm. For the research discussed in this thesis, an aggregated model of the Type 3 wind farm is used for the purpose of grid-side fault studies to represent the collective behaviour [29].

Flux Decrement:

Reference [30] discusses flux decrement effect in the context of synchronous generators and the same context applies for induction generators. The flux linking the rotor is constant in steady state condition but when a fault occurs, the flux linking the rotor is no more constant, and starts decaying. For accurate modelling of the induction generator, this effect needs to be taken into consideration.

LVRT Requirements:

The low voltage ride-through (LVRT) requirement is another important consideration to avoid significant loss of wind power in the event of grid side faults. In the past, wind turbines were only required to disconnect from the grid when a grid fault was detected where the conventional generation units would provide the voltage support. However, with the increased capacity of wind power in the power system over the years, such a disconnection of wind turbines could generate problems in the control of frequency and voltage in the system, and in worst case would result in system voltage collapse. The increased penetration of wind energy into the power system over the last decade has therefore led to serious concerns about its influence on the dynamic behaviour of the power system. It has resulted in the power system operators revising the LVRT requirements in several countries [31].

LVRT requirements defined by utilities make it necessary for wind farms to stay connected to the grid and support the system for normally cleared disturbances [32], [24]. This is necessary to enable more integration of wind energy into the existing grid and for wind

generators to support the voltage and frequency of the grid during and immediately following grid failure due to faults. In [33], a comparative overview and analysis of the main requirements had been conducted, comprising several national and regional codes from many countries where high wind penetration levels have been achieved or expected in the future. The objectives of these requirements is to provide wind farms with the control and regulation capabilities encountered in conventional power plants and necessary for the safe, reliable and economic operation of the system.

Low voltages due to faults/disturbances cause a rise in the stator current of the wind generator and also lead to high rotor current through induction. If the wind generator must stay connected to the grid, a mechanism has to be provided to by-pass this high rotor current and prevent damage of the rotor side power electronic circuits. This is done via crowbar circuits, which give the wind generators the ability to stay connected to the grid during voltage dips [34]. Reference [34] describes a $dq0$ model for the Type 3 wind generator where the short circuit behaviour is discussed with and without the crowbar circuit in place. The crowbar activation could result in problems: when the rotor side converter (RSC) is disconnected it may lead to loss of controllability of DFIG during fault condition [35].

Reference [36] proposes a new converter protection method, primarily based on a series dynamic braking resistor (SDBR) that prevents the doubly-fed induction generator (DFIG) control being disabled by crowbar protection during fault conditions. The purpose of an SDBR is to avoid the frequent use of crowbar short circuit and is inserted in rotor circuit to maximize the operation time of the RSC. However, this configuration does not control the magnitude of stator current during fault condition.

The research work described in this thesis examines different topologies for enhancement of LVRT capability. The SDBR is placed in stator circuit and the result is compared with results from other schemes. Merits and drawbacks of different topologies are mentioned as well.

Multi-mass model of Drive Train system:

Since the wind turbine consists of number of masses, the mechanical system of a gen-

eration units has number of natural frequencies. A system disturbance excites the natural modes in both the electrical and mechanical systems. Thus the mechanical torque in the turbine-shaft system consists of its natural frequencies where as the electromagnetic torque produced by the armature currents consist of the sub-synchronous frequency components corresponding to the network resonances. If the frequency of the induced sub-synchronous electromagnetic torque is close to one of the natural frequencies of the turbine-generator shaft system, the electrical system oscillations will sustain or grow the mechanical system oscillations. This phenomena is known as torsional interaction. The single mass model are usually used in many studies and assume blade inertia-turbine hub-generator as a single lumped mass. Although simple, this single mass model is not capable of showing torsional oscillations of wind generator. The three mass model is used in this thesis to consider potential torsional interactions, if any.

Sub-synchronous Control Interactions:

Large-scale integration of wind farms in the transmission networks has led to several challenges. One of the challenges is the need for substantial upgrading of grid transmission infrastructures including the construction of new transmission lines to accommodate the increased power flow from the wind plants. It is well known that series compensation is an effective means of enhancing the power transfer capability of existing transmission lines. Hence, it is being increasingly considered for integrating large wind generation plants. The presence of series capacitors in the line may also potentially cause sub-synchronous resonance (SSR) in induction generator based wind turbine generators [37–39]. Reference [10] shows that undamped sub-synchronous oscillations, termed sub-synchronous control interactions (SSCI), could potentially occur in Type 3 wind turbine generators with power electronic converters and controls that operate near series compensated transmission lines. Sub-synchronous control interactions (SSCI) are mainly due to the interactions between DFIG wind turbine controllers and the series compensated transmission line, to which the wind farm is connected [40], [41].

Unlike other known sub-synchronous resonance (SSR) types [42–45], the SSCI does not have a well-defined frequency range due to the fact that the frequency of oscillations in

SSCI depends not only on the configuration of the series compensated transmission line and induction generator parameters, but also on the wind turbine controller configuration and parameters [6], [7]. Moreover, the oscillations caused by the SSCI may grow faster compared to other SSR types, since the undamped oscillation in SSCI completely depends on the electrical and controller interactions, which have a smaller time constant.

Reference [46] investigated the interactions in multi infeed highvoltage dc(HVDC) system. Multi-infeed HVDC interactions were analyzed by using the eigenvalues and eigenvectors obtained from the linearized state-space model. Small signal analysis technique was used to study the interactions. This paper shows the importance of conducting a small-signal interaction study for any system consisting of power electronic converters.

An analysis of sub-synchronous interactions in a series compensated Type 3 wind farm is explained in [47], [48] in order to identify the cause of the interactions. References [49], [50] and [51] describe various techniques to identify the frequency of the sub-synchronous interactions and also the elements in the system causing them. The analytical method of frequency scanning, where the driving point impedance over the frequency range of interest is calculated looking into the system from the generator terminals is utilized in this thesis.

Reference [52] uses eigenvalue analysis to detect unstable sub-synchronous mode and proposed an optimal controller for damping SSCI. In [47], it is shown that SSCI is very sensitive to the inner current controllers of the RSC and an observed state feedback controller for SSCI damping is proposed. Other works to mitigate Type 3 wind farm sub-synchronous control interaction issues are discussed in references [40], [53], [54], and [55].

The above works clearly show the attention SSCI phenomena has gained in the research community and the practical relevance to the industry. The research described in this thesis shows the sub-synchronous oscillations (due to SSCI) distort the fault current waveforms and severely impact the short circuit current levels of Type 3 wind farms. This thesis also using small-signal analysis identify the factors which cause SSCI.

1.3.2.2 modelling Methods

Voltage behind Transient Reactance (VBR):

This method is based on modelling the wind generator as a Voltage source behind the transient reactance circuit to represent its short circuit behaviour. In this method, the sequence component networks are used as the basis for calculating the parameters of the VBR representation from which the short circuit current value at the inception of the fault can be calculated. The basis for this representation is that the generator's rotor flux remains relatively unchanged for a short duration immediately after a fault occurs, which allows the fault current to be calculated using basic circuit theory with the stator windings short-circuited [20].

Analytical Expression Representation:

In this type of methods, the fault current contribution of a conventional induction machine is expressed in terms of an analytical expression for the short circuit current. An analytical expression based approach for a Type 3 wind generator with crowbar protection is explained in [17]. Even though this approach includes the crowbar resistance in calculating the short circuit contribution of the Type 3 wind generator, it does not include LVRT based protection. This leads to the assumption that the crowbar is activated throughout the fault duration. It also does not include non- fundamental frequencies as part of the modelling, which means the approach is limited to representing balanced faults.

Voltage Dependent Current Source:

This type of modelling method is a black-box type approach provided by some manufacturer's and are useful for system planners for fault studies. It is capable of generating short circuit current characteristics in the form of upper and lower envelopes of fault currents. A voltage dependent current source model is developed in [9] to represent Type 3 and Type 4 wind generator short circuit behaviours. The accuracy of this model depends on the level of accuracy of the model used to obtain the fault current envelopes. A detailed EMT model is used in this case to obtain the fault current values. Thus, this method is not a standalone

model, as it requires the short circuit current values to be obtained from detailed EMT models or from the wind generator manufacturer, and does not give insight into phenomena such as crowbar activation or sub-synchronous behaviour.

WECC Working Group Generic Models:

The WECC working group on "Dynamic Performance of Wind Power Generation" and the IEEE working group on "Dynamic Performance of Wind Power Generation" jointly published a report "Description and Technical Specifications for Generic WTG Models- A Status Report" [56] in 2011. These models were referred to at that time as "first generation generic" WTG models. Although these developments represented a significant improvement on modelling capabilities of WTGs, the conditions in which the first generation WTG models were created were far from ideal [57]. The four prototype generic WTG models were developed by simplifying a detailed transient stability model. The generic Type 3 WTG was developed using as basis a GE's WTG model. The model consisted of four components: generator/converter, converter control, wind turbine and pitch control. Type 3 generator/converter eliminated the flux dynamics and some other simplifications were made to the GE model, such as elimination of active power control block. The models described in the report were not suitable to study varying wind conditions and were not designed for use in simulation studies that involved severe frequency excursions. Also the report [56] concluded that as additional information becomes available, the first generation WTG models, especially Type 3 and Type 4 WTG need to be updated. After publication of [56], additional information from different manufacturers became available and the working group developed the second generation of Type 3 and Type 4 generic WTGs, which was reported in [58] in 2013.

The WECC Renewable Energy modelling Task Force again published "Generic Wind Turbine Generator Models for WECC- A Second Status Report" [57] in 2015. The "second generation" models for Type 3 and Type 4 WTG utilized a modular approach. The models consisted of small modules which allowed for the representation of different plant topologies and to facilitate updating individual model components easily as new methods/technologies are developed and/or new information becomes available. Second generation generic Type 3

WTG has essentially seven modules: Generator/Converter, Electrical Control, Aerodynamic Conversion, Pitch Controller, Drive-Train, Torque Controller and Plant level Controller. One notable thing was the inclusion of both active power and reactive power controls in second generation. Other than the modular structure of WTG in second generation models, there were no changes made in the multimass model of the generator and turbine. Both first and second generation of WTG generic models used either a single lumped mass or a two mass model. As discussed earlier in the thesis, to capture the torsional oscillation behaviour in wind energy system, the proposed research utilizes a three mass model. Researchers at University of Manitoba also used a three mass model for Type 3 WTG for stability studies [48].

Average Value Model (AVM):

The average value model replaces the switches and associated phenomenon by equivalent current and voltage sources. Reference [59] discusses Average value models (AVMs) for power electronics converter and its dynamic performance. Detailed modelling of IGBT valves in EMT type programs use small integration time-steps to accurately represent fast switching events. The computational burden introduced by such detailed models highlights the need to develop more efficient models that provide similar dynamic response. These simplified models, also known as average-value models, replicate the average response of switching devices, converters and controls by using controlled sources and switching or averaged functions. AVM can be utilized to model power converter used in wind generators.

Reference [60] utilizes AVM of Type 3 wind farms to analyze the response of conventional line protection scheme and the supervisory elements associated with the farms. Type 3 generator controllers try to regulate the phase currents which limits the unbalance current during fault leading to insignificant current contribution from generator. No sensitive analysis with respect to generator controller is carried out but authors conclude that the protection and supervision schemes may face sensitivity issues with controllers. It is also concluded that fault selection didn't perform very well.

Reference [61] describes the basic voltage and flux linkage equations of an induction

machine. It further transforms the equations to the dq0 reference frame and describes a model that can be used to represent balanced and unbalanced conditions. The transformation to the dq0 reference frame helps eliminate the time varying coefficients that appear in the voltage equations due to mutual inductances and vary as a function of rotor angle. These equations in the dq0 reference frame are used as a basis to develop the EMT model of the generator used in the test system in this thesis.

Though capable of representing balanced fault conditions fairly accurately, fundamental frequency simplifications are viewed as non-inclusive of other essential non-fundamental frequency components required to represent sub-synchronous interactions, such as in the case of Type 3 wind farms. Detailed EMT models based on dq0 equations of the machine are h capable of representing the short circuit behaviour of a Type 3 wind farm. However, they are computationally demanding as they include all of the frequency components and also provide little insight into control interactions. Also, developing a detailed EMT model would require manufacturer proprietary information, such as control algorithms, which are often difficult to figure out.

The performance of Average Value Model is generally poor during transient period.

Generalized Averaging Theory (or Dynamic Phasor modelling):

The Generalized Averaging Concept (or Dynamic Phasor Modelling) is a core part of the research work described in this thesis. The theory is described for DFIGs with the objectives listed below:

- It should be capable of representing fault current behaviour for balanced faults, unbalanced faults, and faults with sub-synchronous interactions for a Type 3 wind farm.
- This model should be more sophisticated than fundamental frequency type models and at the same time simpler than a EMT model. It should also facilitate designing both protection and controls for wind farms.
- In order for this model to be more computationally efficient and faster than an EMT model, it should have the capacity to selectively model only the required frequency

components to accurately represent the desired fault behaviour of a Type 3 wind farm.

- The manufacturer nameplate details of DFIG should be good enough for modelling. A power utility engineer should be able to use the model to design the protection and controls of a Type 3 without the need of exact modelling details.

The generalized averaging theory which is commonly referred to as dynamic phasor modelling, was originally developed by an MIT researcher in 1991 for modelling power converter circuits [62]. It is capable of accommodating arbitrary types of waveforms and is based on time varying Fourier series representation for a sliding time window of a given waveform. The main essence of this scheme is to model a periodically driven system, such as power converter circuits, and retain only particular Fourier coefficients based on the behaviour of interest of the system under study. Simplifying approximations are made by omitting insignificant terms from the series.

In [63], the authors refer to the "baseband quantities" as "dynamic phasors". In [64], the authors refer "frequency shifted quantities" as "dynamic phasors". However in the context of this work, the definition of dynamic phasor is different and will be discussed in detail in section 5.2.

Reference [65] discusses the application of generalized averaging model to large synchronous machines for symmetrical and unsymmetrical fault analysis. It shows that by the choice of appropriate harmonics (Fourier coefficients), the averaged model is capable of accurately capturing fault dynamics of a synchronous machine.

In [66], the author uses dynamic phasor model to solve power system equations. He uses an example to demonstrate the advantage of dynamic phasor model in terms of speed of simulations (simulation timestep). It is assumed that due to a contingency in power system, the system frequency may deviate by 2% (i.e., 58.8 Hz to 61.2 Hz variation in a 60 Hz system). Now assuming that 20 steps per cycle provides accurate results, one would need to use a simulation time step of 0.8 msec ($(1/60)/20 = 0.00083$ s) with a EMT and electromagnetic type simulation. The authors of the thesis shows that the same accuracy could be obtained with a dynamic phasor approach with a slower 8msec time step. Thus the

speed with which the computations could be performed increases 10 folds.

Reference [67] utilizes the generalized averaging scheme to model Type 1 wind generator and references [68, 69] utilizes the generalized averaging scheme to model Type 3 wind generators for short circuit modelling. These models dealt with fundamental frequency based modelling and were not sophisticated enough to represent sub-synchronous frequency control interactions. In [69], the detailed EMT model simulated a 50% balanced 3 phase voltage sag of 6 cycles in 42.68 sec; whereas, dynamic phasor model took 8.65 sec for the same simulation. Also, an unbalanced 50% voltage sag of 6 cycles is simulated by EMT model in 47.26 sec while 11.78 sec is the simulation time taken by dynamic phasor model for same scenario. Simulations showed that the dynamic phasor model was able to simulate the dynamic response to balanced and unbalanced voltage sags as accurately as the detailed EMT models while decreasing the required simulation time considerably.

References [70, 71] report research work carried at University of Saskatchewan. Authors discussed the development of a dynamic phasor model for a Type 3 wind farm including fundamental and nonfundamental subsynchronous frequencies effects. The developed model was tested for symmetrical and unsymmetrical fault behaviour. It was concluded that the dynamic phasor approach achieved a middle ground between conventional fundamental frequency based electromechanical models and detailed EMT models with the ability to also represent nonfundamental frequencies accurately.

Reference [72] uses dynamic phasor model approach for modelling modular multi-level converters. Reference [73] extends the application of the generalized averaging model to represent the dynamic behaviour of a thyristor-controlled series capacitor (TCSC) in a simple and accurate manner that is faster than detailed time domain simulation. The approach described shows that simply choosing the fundamental frequency harmonic for modelling is not accurate enough to represent TCSC behaviour when it is close to resonance, as there are other significant higher order harmonic components present as well. Other flexible AC transmission systems (FACTS) devices, such as the Dynamic Voltage Restorer (DVR) in [74], the unified power flow controller (UPFC) in [75], the static VAR compensator (SVC) in [53], and the synchronous static compensator (STATCOM) in [76], have been modeled using

dynamic phasors. In [77], author used dynamic phasors for modelling line-commutated converter HVDC transmission systems.

In reference [78], dynamic phasor model has been used to investigate unbalanced radial distribution systems consisting of a single-phase photovoltaic (PV), a three-phase induction machine load, a three-phase power factor correction capacitor (PFC) and a load. The simulation results of dynamic phasor model have been compared with the Matlab/SimPowerSystems model based simulation results. It is concluded that dynamic phasor based simulation is fast and accurate.

Reference [79] uses the dynamic phasor approach for modelling Multi-Generator variable frequency electrical power systems. A twin-generator electrical power system of more-electric aircraft (MEA) is simulated using dynamic phasor model and detailed EMT model. The two generators operate at two different frequency: 400 Hz and 405 Hz, respectively. The simulation time taken by detailed EMT model and Dynamic phasor model are recorded and compared to see how fast dynamic phasor model is. The simulation time to capture system response to step load change is 7983.0 sec for EMT and 42.97 sec for dynamic phasor model. In this case dynamic phasor model is approximately 185 times faster than EMT model. Also, a line to line fault is applied for 0.1 sec and the simulation time is compared. Dynamic phasor is 89.7 (approximate) times faster than detailed EMT model. It was concluded that dynamic phasor model allows larger simulation steps and hence accelerated simulations maintaining extremely high dynamic and steady state accuracy.

The above works in the literature show that there has been a good amount of work on dynamic phasor modelling of various components in power systems. This thesis extends the research work carried out in [70, 71]. This research includes multimass effect, flux decrement effect in dynamic phasor modelling of Type 3 wind power plant. The dynamic phasor model is compared with AVM Type 3 wind generator. The root cause of sub-synchronous oscillations in Type 3 wind farm connected to series compensated line is identified. Different topologies of LVRT are also discussed and compared.

1.3.3 Type 4 Wind Generators

The short-circuit behaviour of Type 4 wind generators is mainly determined by the way the grid side converter is controlled and it is therefore specific to each particular commercial wind turbine [8], [80] . Reference [9] shows that Type 4 wind generators can be represented by a current source with an upper and lower limit based on the power converter rating for short circuit analysis. Reference [81] goes further to show that Type 4 wind generator can simply be modeled as an ideal current source for fault analysis.

Short circuit modelling of Type 4 wind generators is quite well-understood and so this thesis does not analyse Type 4 behaviour further.

1.4 Objective of the Thesis

The following are the main objectives of this thesis :

1. Develop a detailed real-time EMT simulation model of a Type 3 wind generator in RTDS/RSCAD, including the effect of torsional oscillations and flux decrement effect. The detailed EMT model will be used to validate the proposed dynamic phasor model and other simplified models in this thesis.

2. Investigate and compare different RSC converter protection schemes (Rotor side crow-bar, DC-link Protection scheme, SDBR in rotor circuit, and SDBR in stator circuit) to enhance LVRT capability of a Type 3 wind farm.

3. Identify the root cause of sub-synchronous oscillations in a Type 3 wind farm connected to series compensated AC network. A linearized model of a Type 3 wind farm connected to series compensated AC network will be developed to analyze whether the root cause of the oscillations is sub-synchronous resonance or sub-synchronous control interacions.

4. Develop a simplified, fast, and accurate method of modelling the short circuit behaviour of Type 3 wind generators using dynamic phasor modelin and use nameplate details of

the generator and standard converter control methods to develop the equations. Test the developed model's capacity to represent the fault behaviour of the wind farm.

1.5 Organization of the Thesis

The thesis is organized into six chapters.

Chapter 1 gives the background with a discussion of the present scenario of wind power integration and its foreseeable growth for future energy needs. Following this, the significance of short circuit modelling of wind generators and the various issues associated with Type 3 wind generators are discussed. Various approaches to wind generator short circuit modelling in the literature are briefly discussed, along with their capabilities and limitations. This is followed by a discussion of the motivation behind the development of a dynamic phasor modelling technique that is capable of representing the previously discussed complexities, and which is the primary objective of the thesis.

Chapter 2 provides a review of the commonly used techniques (voltage behind transient reactance, analytical expression representation, voltage dependent current source) for modelling the short circuit behaviour of wind generators and discusses the results of application of these methods for different wind generator types. From the results obtained, the accuracy and applicability of these techniques along with their advantages and disadvantages for particular wind generator types are discussed. This chapter also discusses generic WTG models developed by the WECC working group.

Chapter 3 explains the detailed modelling of a Type 3 wind power plant. The wind power plant model includes the generator, mechanical drive train, rotor and grid side converter controllers, DC capacitor, and pitch controller models. The model includes the effect of change of flux in the wind generator during abnormal system conditions instead of assuming it is constant. The most commonly used low voltage ride through (LVRT) topologies, such as rotor side crowbar circuit, DC-link protection scheme, and series dynamic braking resistance (SDBR) in rotor and stator circuits are investigated in this chapter.

In Chapter 4, small signal analysis of a Type 3 wind power plant is discussed. A detailed linearized model of a Type 3 wind power plant is presented for small signal analysis. The reason for sub-synchronous interaction between a Type 3 wind power plant and a series compensated transmission line is identified.

In Chapter 5, the proposed dynamic phasor model of a Type 3 wind farm connected to a series compensated transmission line is discussed and developed. The accuracy of the proposed model to represent the short circuit behaviour is also illustrated. The average value model (AVM) of a Type 3 wind farm used in the literature is also developed and the transient response of the AVM compared with the EMT model.

Chapter 6 provides a summary, thesis contributions, and suggestions for future work.

Chapter 2

Various Types of Wind Turbine Generators and Short Circuit modelling

2.1 Introduction

The wind power generation systems have evolved significantly and make use of a variety of generators and power electronic configurations. The most commonly used generators in large wind energy conversion systems (WECS) [82, 83] are shown in Figure 2.1 below.

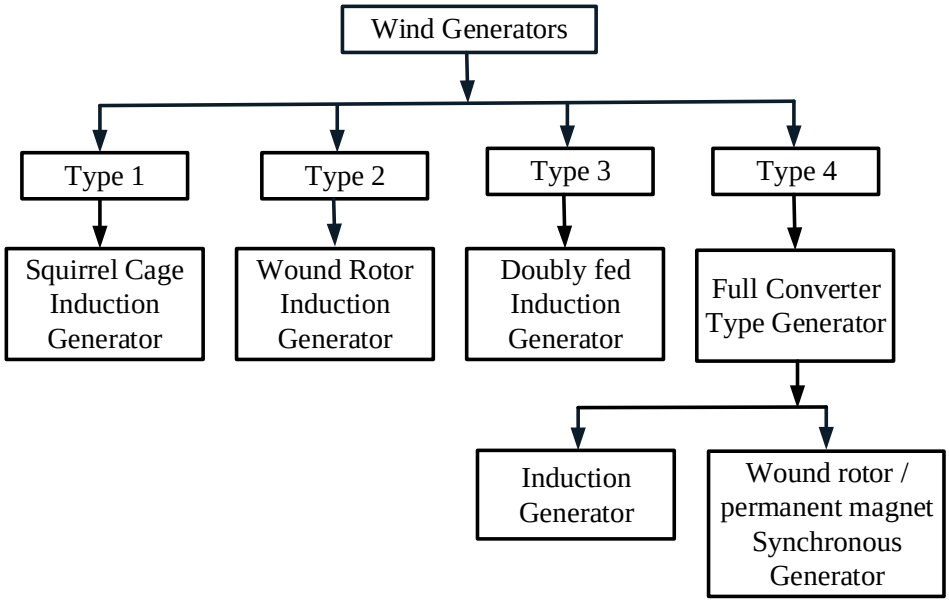

Figure 2.1: Types of wind turbine generators

Section 2.2 discusses the basic configurations of the various wind generator types. Since Type 3 DFIG are the main focus of this thesis work so only brief descriptions are provided

for Type 1 and Type 2 wind generators. Section 2.3 explains some of the state-of-the-art modelling approaches: Voltage behind Transient Reactance, Analytical Expression Representation, Voltage Dependent Current Source that have been used commonly for these types of generators. The Voltage behind Transient Reactance method developed in the course of the theses work of Mr. Sriram Chandrasekar [70] has been used in two of the laboratories of "Advanced Analysis of Electric Machines and Drive Systems", EE444 [84] course at the University of Saskatchewan.

Section 2.3 also discusses about WECC working group generic models reported in [56,57]. The WECC group developed first generation of generic WTG models in 2011 [56]. The four prototype generic WTG models were developed by simplifying a detailed transient stability model. The conditions under which the first generation WTG models were created were far from ideal, partuculary Type 3 and Type 4 WTG. The second generation of generic Type 3 and Type 4 WTG models were developed and reported in references [57, 58]. The second generation models were developed using modular approach. The seven modules used in generic Type 3 WTG are briefly discussed in this section.

2.2 Types of Wind Turbine Generators

2.2.1 Type 1 Squirrel Cage Induction Generator

Fixed speed wind turbines comprise of squirrel cage induction generator (SCIG) and is directly connected to the grid through a step-up transformer. A soft-starter is used to provide the smooth start-up, and a capacitor bank provides the reactive power compensation [85]. When these generators operate in a fixed speed mode of operation, any wind fluctuation would directly result in the fluctuation of the mechanical torque and the electrical power. While the mechanical torque fluctuations cause high mechanical stress, the electrical power fluctuations lead to voltage fluctuation and flicker effects in the case of weak grids. Pitch angle control is used to regulate the turbine shaft speed to nearly a constant speed.

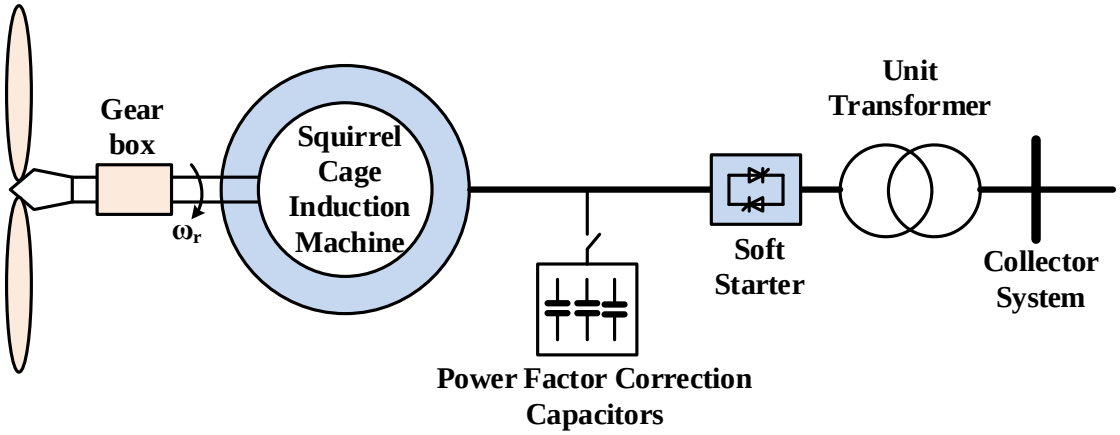

Figure 2.2: Type 1 wind turbine generator

2.2.2 Type 2 Wound Rotor Induction Generator

While fixed-speed wind turbines are simple and robust, they have a significant disadvantage: they cannot optimally extract power from the wind. It would be preferable to have the generator continue to output rated power at high wind speeds. In order to achieve this, Type 2 wind turbine generators consist of a wound rotor induction generator (WRIG), which makes connecting external resistances to the rotor winding possible. While largely relying on the same concepts as fixed-speed wind turbines at lower-than-rated wind speeds, they typically incorporate pitch control and output power control to optimize power extraction at higher-than-rated wind speeds. The Type-2 generator uses rotor resistance control to achieve output power control. This provides the ability to operate at a higher range of slip (10%) as compared to a Type 1 wind generator. This external resistance can be controlled by a high-frequency switch as shown in Figure 2.3, based on the speed of the wind. The shunt capacitor banks are used for power factor correction.

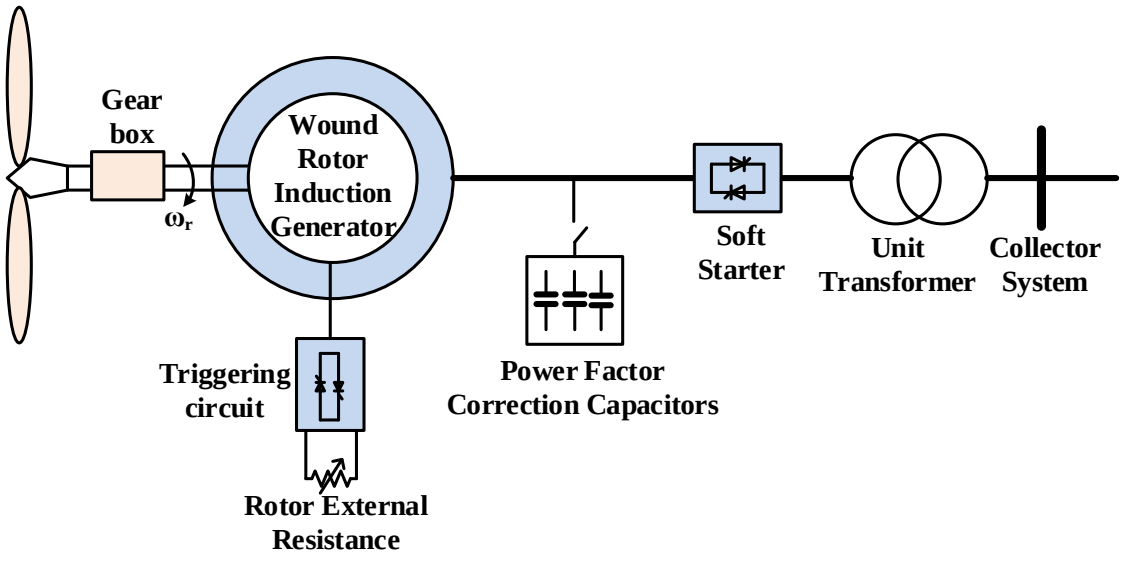

Figure 2.3: Type 2 wind turbine generator

2.2.3 Type 3 Doubly Fed Induction Generator (DFIG)

A schematic diagram of a Type 3 wind power plant is shown in Figure 2.4. The wind turbine-generator unit consists of a wind turbine connected to a doubly-fed induction generator (DFIG) via a shaft and a gear box. The induction generator is a wound-rotor induction machine. Slip-rings and brushes are usually used to access the rotor circuit. The three-phase stator winding is fed directly from the three-phase supply voltage. A back-to-back AC-DC-AC power electronic converter is used to rectify the supply voltage and convert it to three-phase AC at the desired frequency for rotor excitation [85]. Thus, unlike a singly-excited squirrel cage induction machine, stator and rotor windings of a DFIG are independently excited. The rotor speed is allowed to vary within a slip range of 30%. This implies that the power converter is rated for about 30% of the rated power [8].

The back-to-back converter is capable of extracting power from rotor as well as pushing power to rotor. The converter excites the rotor in such a manner that the resultant rotor magnetic field rotates at synchronous speed. The converter, whose ac side is connected to the rotor is commonly referred as the rotor side converter (RSC). The converter connected to the

external grid via the transformer is known as the grid side converter (GSC). The RSC controls the DFIG so that it extracts the maximum extractable wind energy while maintaining the system reactive power requirements. The function of the GSC is to maintain the dc link voltage. Although DFIG wind turbines are generally more complex and expensive than wind turbines employing uncontrolled squirrel-cage induction generators or rotor-resistance controlled wound rotor machines, they have certain advantages:

- Independent active real and reactive power control is possible.
- There is a wide generator shaft speed range of up to 30% above and below rated speed for which generation can take place with minimum slip losses.
- Maximized aerodynamic power extraction.
- Improved Low voltage ride-through performance.

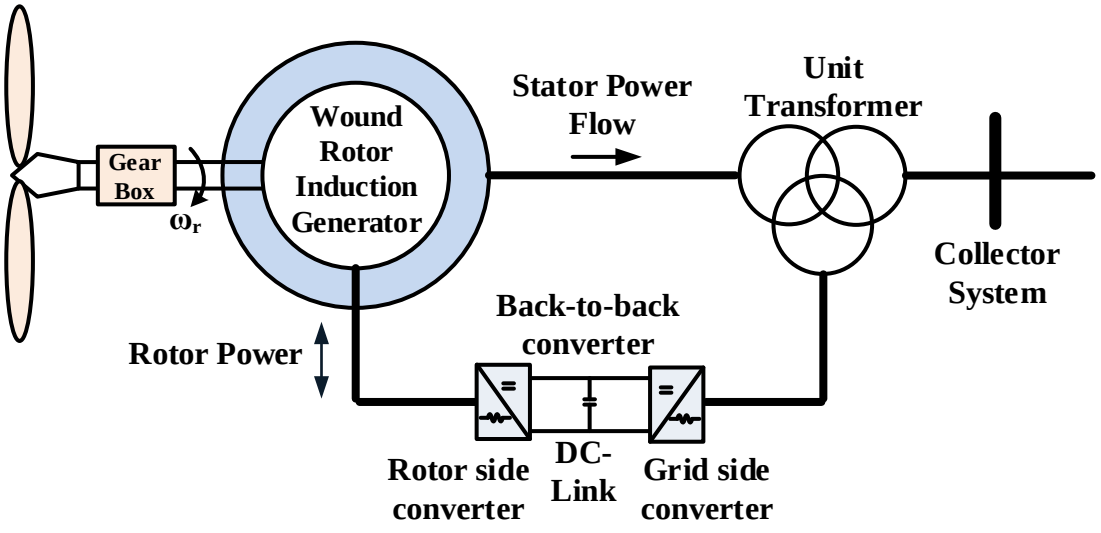

Figure 2.4: Type 3 wind turbine generator

2.2.3.1 Basic Operation of DFIG

Faraday's law of electromagnetic induction states that any change of flux in a moving coil will induce a voltage in the coil. This voltage is proportional to the rate of change of flux and the number of turns in the coil. Mathematically,

$$e = -N\frac{d\phi}{dt} \tag{2.1}$$

where e, N and ϕ are the electro-motive force (EMF) induced, number of turns in the coil and flux. Therefore, if a coil with N number of turns is rotated in a magnetic field , a voltage will be induced. Therefore, this machine can act as a generator. By the same principle, if current is applied in a region with variable magnetic field, force is induced. Therefore, the same machine can act as a motor. Induction machines are most widely used as motors. Due to their robust performance, they have nearly replaced DC drives, except for areas with critical speed/torque control requirements.

The electrical circuit consists of a three phase stationary winding (stator) and a cage/slip ring winding set, which is free to rotate within the stator. When the stator is fed by the power supply, it produces a sinusoidal magnetic field in all three phases. The resultant is a magnetic field rotating at system frequency which induces emf in the rotor.

Operation as a Motor: When the machine starts, the rotor is at rest. Hence, the rate of change of flux is maximum. Currents induced in the rotor are of the same frequency as the stator. These rotor currents are induced such that their magnetic field offsets the magnetic field of the stator. The interaction of these two fluxes induces a torque on the rotor. If the rotor is free to rotate, it will rotate in the direction of the stator flux vector to reduce the relative flux linkage. As the relative speed of stator field with respect to the rotor decreases, the rate of flux linkage also decreases. Therefore, rotor current and its frequency falls. If the machine is not loaded, the speed of the rotor will approach synchronous speed (speed of the stator flux vector). As the load increases, the rotor will decelerate, leading to increased flux linkage. This will lead to more emf on the rotor, and hence more current. This current will offset the stator field again, and the machine will gain torque and speed. After a few seconds, the speed will settle to a steady state subsynchronous speed. The ratio of this difference

between stator and rotor speed to the stator speed is called slip, s.

This implies that as the load of a machine increases, slip will increase. Therefore, the machine will draw in more current. Now, if the rotor is driven by an external force such that, the rotor is driven to rotate faster than the synchronous speed, the rotor field will continue trying to minimize flux linkage. However, it will now act in the same direction as stator flux vector since $\omega_r > \omega_s$. In other words, the rotor currents will reverse, and the machine will start acting as a generator. The key idea behind generated torque or current, therefore, is the flux linkage and its direction. So, to maintain generation, prime mover must ensure that rotor speed is near optimum.

The dynamic performance of the DFIG is dominated by the converters. To understand the control schemes of these converters to control real and reactive power, it is necessary to understand the detailed model of DFIG. Chapter 3 discusses detailed modelling and control of DFIG.

2.2.4 Type 4 Full Converter Wind Turbine Generator

Type 4 wind generators are not the main focus of this thesis work but are briefly described herein for completeness reason. For a Type 4 generator, the stator is connected to the grid through a back-to-back converter system with a common dc-link as shown in Figure 2.5. This converter is rated to the full power of the converter and hence it is also known as the full power converter type wind generator. It is common to design a power converter for a Type 4 wind turbine with an overload capability of 10% above rated. Type 4 wind turbine are expensive because of the high cost of converter. As the stator is directly connected to the converter pair, there is no need to incorporate slip ring connections to the rotor. Since the converter decouples the wind generator from the ac network, the machine can be operated at any speed, hence synchronous generators as well as induction generators can be used.

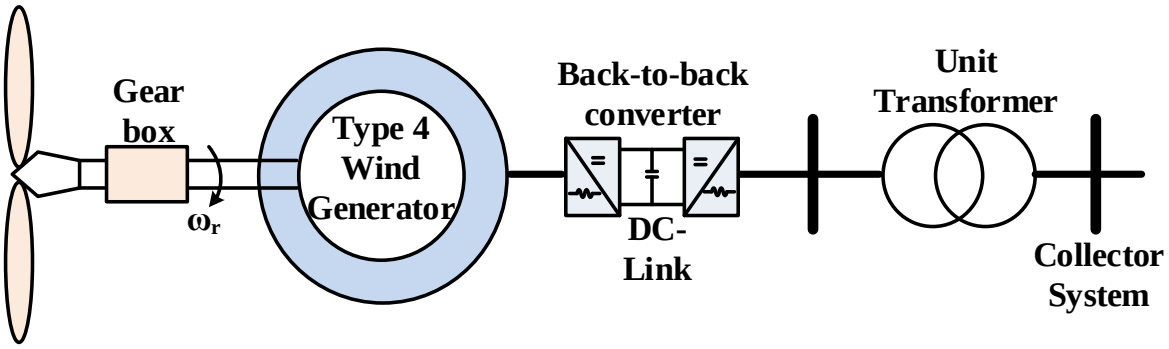

Figure 2.5: Type 4 wind turbine generator

2.3 Commonly Used Short Circuit modelling Methods for Wind Turbine Generators

This section provides a review of the commonly type of methods for modelling the short circuit behaviour of wind generators described in [18, 86]. The accuracy of these techniques is compared with the results obtained from a EMT model. The envelope of the fault current is obtained to find the fault current at the inception of the fault. For illustration, the phase A fault current obtained from the EMT simulation of a Type 1 generator for a three phase symmetrical fault at terminals is shown. The upper and lower envelopes of the waveform, as shown in Figure 2.6 below, are extrapolated to the instant of fault application [20]. MATLAB^{TM} [1] curve fitting toolbox is utilized to generate the fault current envelopes. Subtracting the value I_L from I_U gives the peak-peak fault current at fault inception from which the rms of fault current can be obtained. The rms fault current at fault inception obtained is $(11.123 - 0.06)kA/2\sqrt{2} = 3.91kA$.

As will be demonstrated later in Chapter 5, under subsynchronous conditions, the fault current waveform does not exhibit the typical behaviour of reaching the maximum value immediately after the fault happens. In these scenarios, the fault current magnitude after the first few cycles tends to be higher than the magnitude immediately after the fault application.

[1] MATLAB^{TM} is a registered trademark of The MathWorks, Inc.

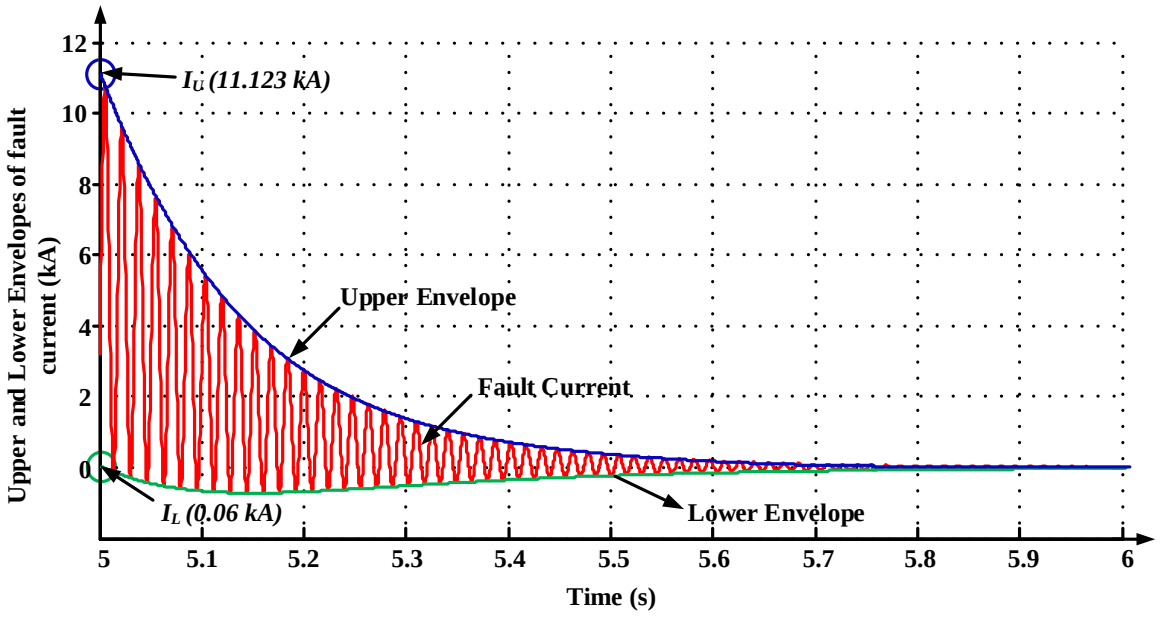

Figure 2.6: Upper and lower envelopes of the fault current waveform

2.3.1 Voltage behind Transient Reactance Representation

This method models the wind generator (induction generator) as a VBR circuit to represent its short circuit charcateristics. In this method, the sequence component networks are utilized for calculating the parameters of the VBR representation from which the current values at the inception of the fault can be obtained. The basis for this representation is that the rotor flux remains relatively unchanged for a small duration immediately after a fault occurs, which allows the current to be calculated using basic circuit theory with the stator short-circuited [20].

2.3.1.1 Type 1 Wind Generator

For a symmetrical three-phase-fault at the terminals of the generator, it is investigated whether the positive sequence network of the Type 1 generator (Figure 2.7) is sufficient to find the fault current at the fault inception.

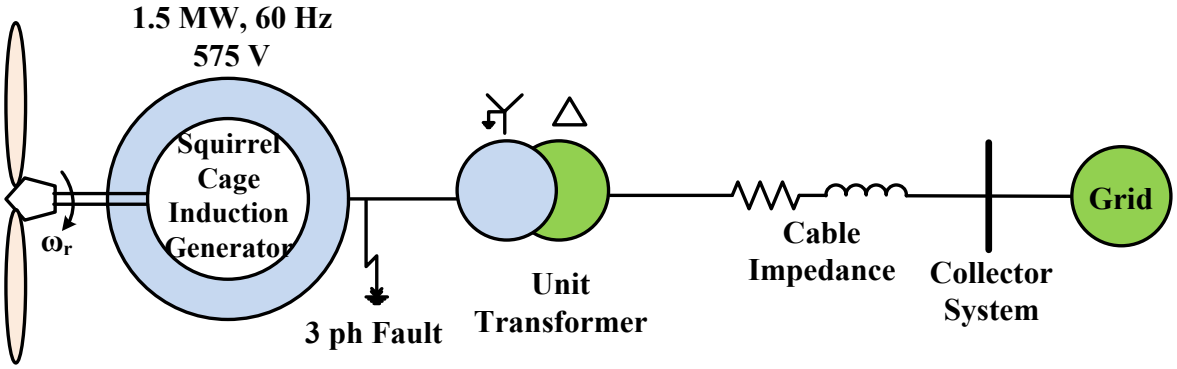

Figure 2.7: Type 1 wind generator test system

The equivalent circuit of the Type 1 generator is shown in Figure 2.8 below. It should be noted that, in all calculations, the rotor side quantities have been referred to the stator. The positive sequence network is obtained from this equivalent circuit.

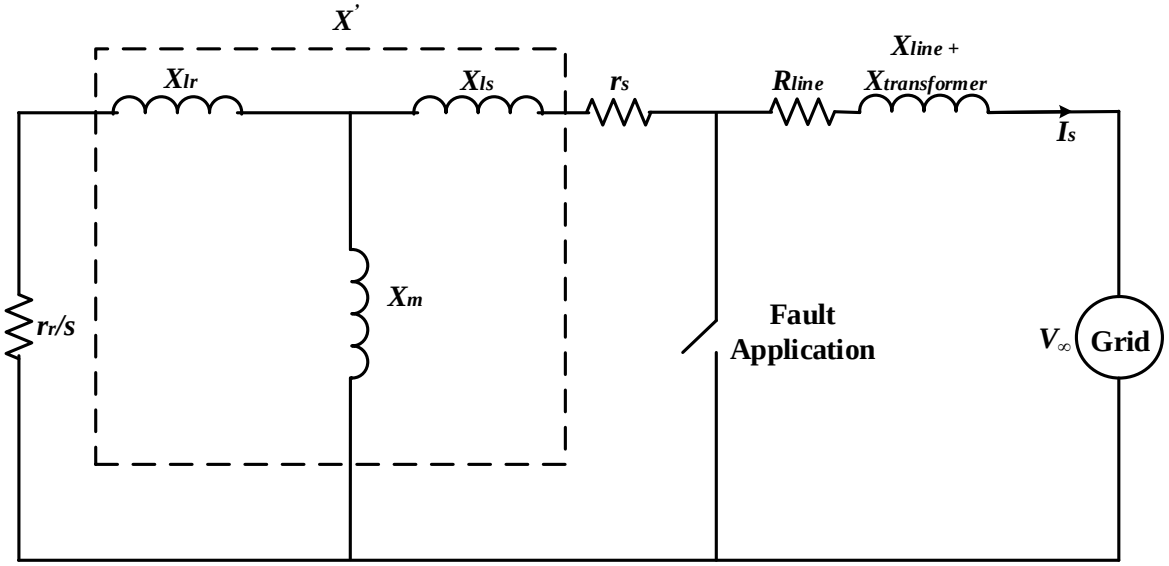

Figure 2.8: Equivalent circuit of the Type 1 wind generator test system

The transient reactance (X') and the voltage behind the transient reactance (V') can be

calculated from the equivalent circuit [20] and are given by the equations:

$$jX' = jX_{ls} + j(X_{lr} \| X_m) \tag{2.2}$$

and

$$V' = V_\infty + jI_s(X' + X_{line} + X_{transformer}), \tag{2.3}$$

where X_{ls}, X_{lr}, and X_m are the stator leakage, rotor leakage, and mutual reactances respectively, V_∞ is the voltage at the infinite bus (grid side), and I_s is the stator current. The winding resistances are not considered in the calculations as they are negligible values. However, this assumption is not valid for Type 2 and 3 generators as they have external rotor resistance and crowbar resistance effects, respectively.

From the X'and V' values, the short circuit current at the inception of the fault can be found from the equation

$$I_{sc} = \frac{V'}{X'}. \tag{2.4}$$

The positive sequence network used for the voltage behind transient reactance representation of a Type 1 generator for a symmetrical fault is shown in Figure 2.9 below. All of the resistances are neglected.

For an unsymmetrical Phase A-to-ground fault applied at the terminals of the generator, the methodology to find the fault current is very similar except that the sequence network would now also include the negative sequence component network. The negative sequence impedance is the same as the positive sequence impedance and all of the resistances are neglected. As the generator is wye-ungrounded and the unit transformer is delta on the secondary, there are no zero sequence components. Hence the zero sequence network is not included. The positive and negative sequence networks are connected in series for finding the fault current for a single-line-to-ground fault.

Table 2.1 shows the values of the Phase A RMS fault currents at the inception of the fault obtained from a EMT model found using the upper and lower envelopes described earlier and from the VBR model for both symmetrical and unsymmetrical faults. The voltage behind

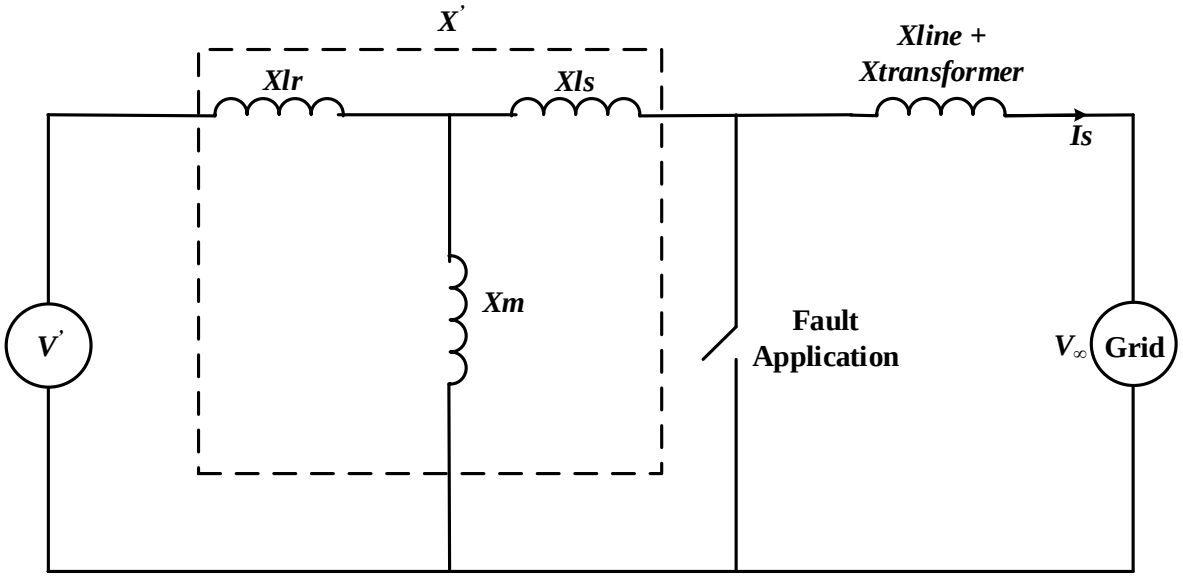

Figure 2.9: Voltage behind transient reactance model (positive sequence network) of Type 1 wind generator test system for symmetrical fault

transient reactance representation is fairly accurate with respect to representing the short circuit behaviour of a Type 1 generator, even by neglecting the winding resistances and considering only the winding reactances.

Table 2.1: Comparison of results for Type 1 wind generator - ungrounded system

modelling	**3 phase fault (kA)**	**A-G fault in ungrounded system (kA)**
EMT	3.91	2.51
VBR	3.944	2.696

A test scenario with a wye-grounded generator and wye-wye grounded unit transformer was modelled to assess the impact of the zero sequence component on the fault current magnitude and to find the accuracy of the VBR modelling. The zero sequence impedances for the generator, transformer, and transmission line respectively are half of, equal to, and 2.5 times of the positive sequence impedance. The results obtained and comparison with the EMT result are shown in Table 2.2.

Table 2.2: Comparison of results for Type 1 wind generator - grounded system

modelling	Phase A-G fault current for grounded system (kA)
EMT	5.424
VBR	5.106

2.3.1.2 Type 2 Wind Generator

This section discusses the modelling of a Type 2 generator test system (Figure 2.10) with the sequence networks for the symmetrical and unsymmetrical faults to find the current values. In case of a Type 1 generator, only the reactance values (neglecting the winding resistances) are used to calculate the transient reactance. However, the external rotor resistance value for a Type 2 wind generator plays an important role in finding the magnitude of the fault current.

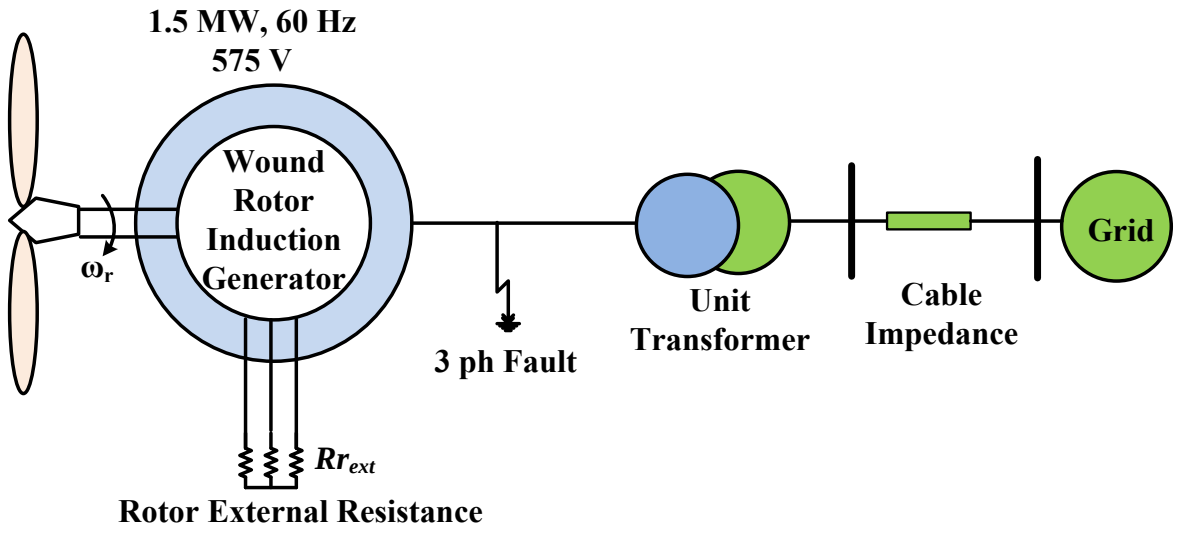

Figure 2.10: Type 2 wind generator test system

This means that the external rotor resistance $R_{r_{ext}}$ should be included in the calculation of the transient impedance Z' (transient reactance was used for Type 1 generator) which is shown in Equation 2.5 below. Figure 2.11 shows the voltage behind transient reactance

(positive sequence network) representation of the Type 2 generator for a symmetrical three phase fault where the winding resistances and the external rotor resistance have been included for the fault current calculation.

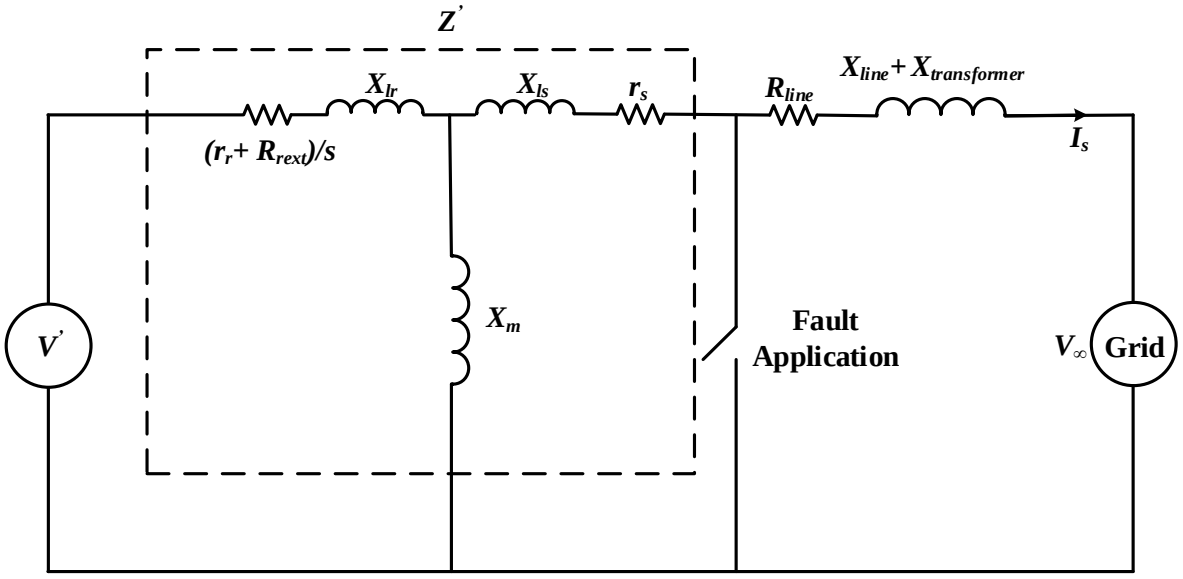

Figure 2.11: Positive sequence network of Type 2 wind generator test system

$$Z' = (r_s + jX_{ls}) + (((r_r + R_{r_{ext}})/s + jX_{lr}) \| jX_m) \tag{2.5}$$

Further, the voltage behind the transient impedance and the short circuit current are calculated from the following equations

$$V' = V_\infty + I_s(Z' + R_{line} + jX_{line} + jX_{transformer}) \tag{2.6}$$

and

$$I_{sc} = \frac{V'}{Z'}. \tag{2.7}$$

Similarly, for an unsymmetrical phase A-to-ground fault at the terminals of the Type 2 generator, the fault current at the inception of the fault is calculated from the positive and negative sequence symmetrical component circuits connected in series. However, the

negative sequence impedance is calculated as

$$Z'_{-} = (r_s + jX_{ls}) + (((r_r + R_{r_{ext}})/(2-s) + jX_{lr}) \| jX_m) \tag{2.8}$$

Table 2.3 shows the values of short circuit currents calculated for symmetrical and unsymmetrical fault conditions with and without considering the rotor external resistance. These are compared against the results from the EMT model. VBR1 represents the model results neglecting the effect of rotor external resistance and VBR2 represents the model results including the effect of rotor external resistance. Including the rotor external resistance value for the three-phase-fault current calculation reduces the error for both symmetrical and unsymmetrical faults.

Table 2.3: Comparison of results for Type 2 wind generator

modelling	**3 phase fault current (kA)**	**Phase A-G fault current (kA)**
EMT	3.025	1.944
$VBR1$	3.9602	2.759
$VBR2$	3.1668	2.074

The VBR method of modelling can be used to calculate fairly accurately, the symmetrical and unsymmetrical fault current contributions of Type 1 and Type 2 generators at the inception of the fault.

2.3.1.3 Type 3 Wind Generator

This section discusses the accuracy of the VBR model for a Type 3 generator. The short circuit behaviour of a Type 3 generator is much more complex compared to the Type 1 and Type 2 generators.

Figure 2.12 shows the positive sequence network of the Type 3 generator [18] where the rotor crowbar resistance is included in the circuit to protect the back-to-back converter in case of a fault. The fault current for a symmetrical-three-phase-fault applied at the

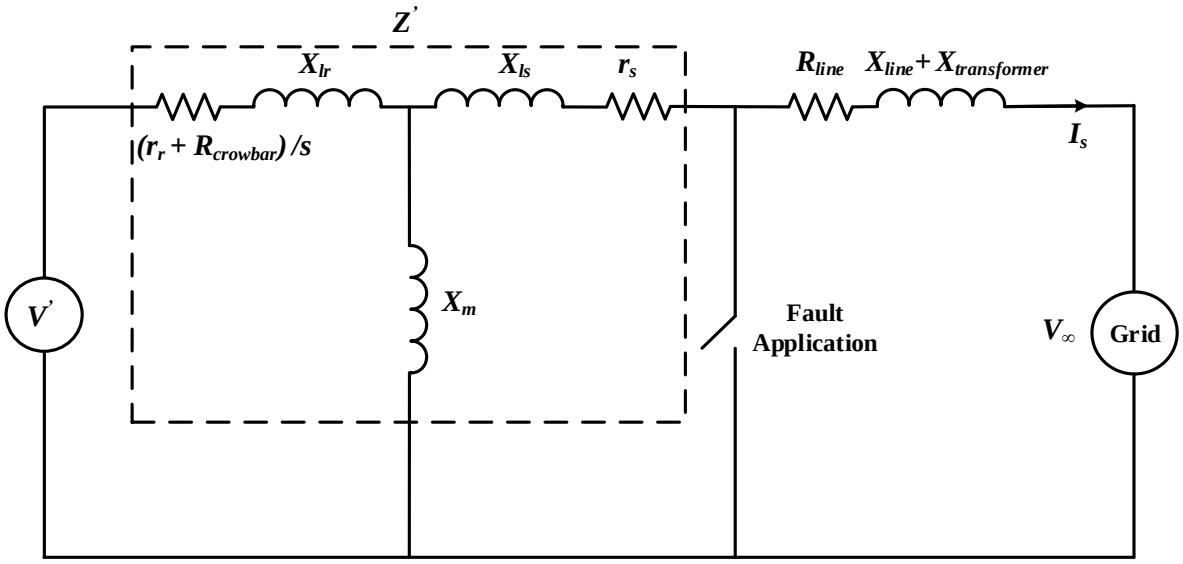

Figure 2.12: Voltage behind transient reactance model (positive sequence network) of Type 3 wind generator test system for a symmetrical fault

terminals is found using the positive sequence network where the net rotor resistance is found as $(r_r + R_{crowbar})/s$. All of the winding resistances and the rotor crowbar resistance are included in the short circuit current calculations. In the case of an unsymmetrical fault at the terminals of the generator, both the positive and negative sequence networks are included in the calculations. The net rotor resistance for the negative sequence network is calculated as $(r_r + R_{crowbar})/(2 - s)$. Table 2.4 below shows the accuracy of the VBR model for representing the Type 3 generator's symmetrical and unsymmetrical fault behaviour compared to the EMT model. It is not as accurate as demonstrated for the Type 1 and 2 generators.

Table 2.4: Accuracy of voltage behind transient reactance modelling for Type 3 wind generator

Modelling	**3 phase fault current (kA)**	**Phase A-G fault current (kA)**
EMT	6.31	4.80
VBR	6.618	3.8808

2.3.1.4 Key Findings

In the VBR modelling method, the positive sequence network equivalent was used for symmetrical three-phase-fault calculations. The sequence network consisting of the positive and negative sequence components was used for unsymmetrical phase A-to-ground fault calculations. This modelling technique was determined to be accurate enough for representing Type 1 and 2 generators. Including the external rotor resistance for short circuit calculations improved the accuracy for Type 2 generators. However this method is not as accurate for a Type 3 wind generator. This modelling technique yields the fault current at the moment the fault occurs but not during the entire period of fault.

2.3.2 Analytical Expression Representation

This method represents the short circuit current behaviour of wind generators by means of an analytical expression (induction motor modelling equations for transient studies). The equations representing the machine has been already discussed in Chapter 2.
As discussed in reference [17], the expression for the phase A stator fault current is

$$Is_a = \sqrt{2}\frac{V_s}{Z'}[e^{-t/T_s}\cos\alpha - (1-l)e^{j\omega_0 t}e^{-t/T_r}\cos(\omega_0 t + \alpha)]. \tag{2.9}$$

T_s and T_r are the damping time constants of the stator and rotor, respectively. They are computed using $T_s = L_{s-eqv}/r_s$ and $T_r = L_{r-eqv}/R_{r-eff}$. L_{s-eqv} is the equivalent inductance looking from the stator into the short circuited rotor given by $L_{ls} + (L_{lr} \| L_m)$ and L_{r-eqv} is the equivalent inductance looking from the rotor into the short circuited stator given by given by $L_{lr} + (L_{ls} \| L_m)$. R_{r-eff} is the effective rotor resistance and varies with the generator type. l is the leakage factor, which is calculated as $1 - (L_m^2/L_{ls}L_{lr})$. All of rotor parameters are referred to the stator side. Z' is the transient impedance and α is the voltage phase angle. The stator fault current for all wind generator types is obtained using Equation 2.9; however, the calculation of T_r, and Z' are dependent on the type of wind generator.

2.3.2.1 Type 1 Wind Generator

As discussed previously, the stator fault current of a Type 1 generator can be resolved into two components, namely an AC and a DC component [8] that are shown in Figures 2.13 and 2.14, respectively. The DC component shown in Figure 2.14 and in the first term of Equation 2.9 is a damped value with a time constant of T_s. Similarly the AC component shown in Figure 2.13 and in the second term of Equation 2.9 is a damped value with a time constant of T_r. This behaviour is expressed mathematically by the above Equation 2.9 where, for a Type 1 generator, it is sufficient to use the value of the transient reactance X' (Refer Equation 2.2) for Z' and L_{r-eqv}/r_r for T_r.

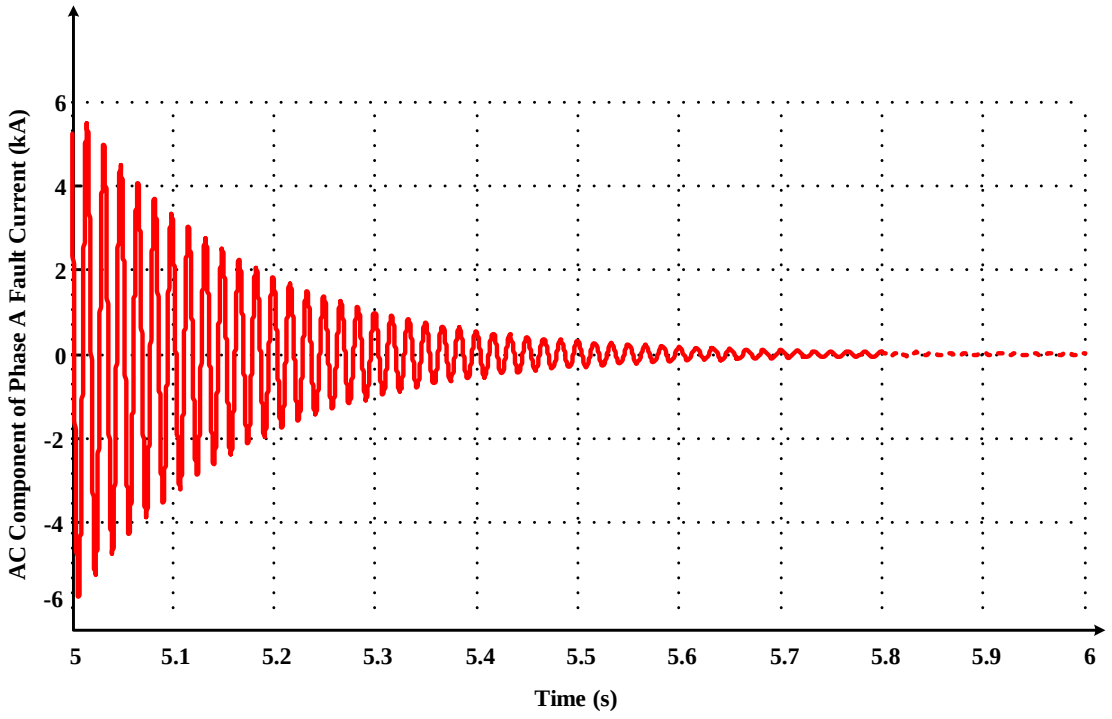

Figure 2.13: AC Component of Phase A fault current

The phase A stator fault current for a symmetrical three-phase-fault obtained from this analytical expression is compared against that obtained from the EMT simulations as shown in Figure 2.15. The analytical expression gives highly accurate results for a Type 1 generator.

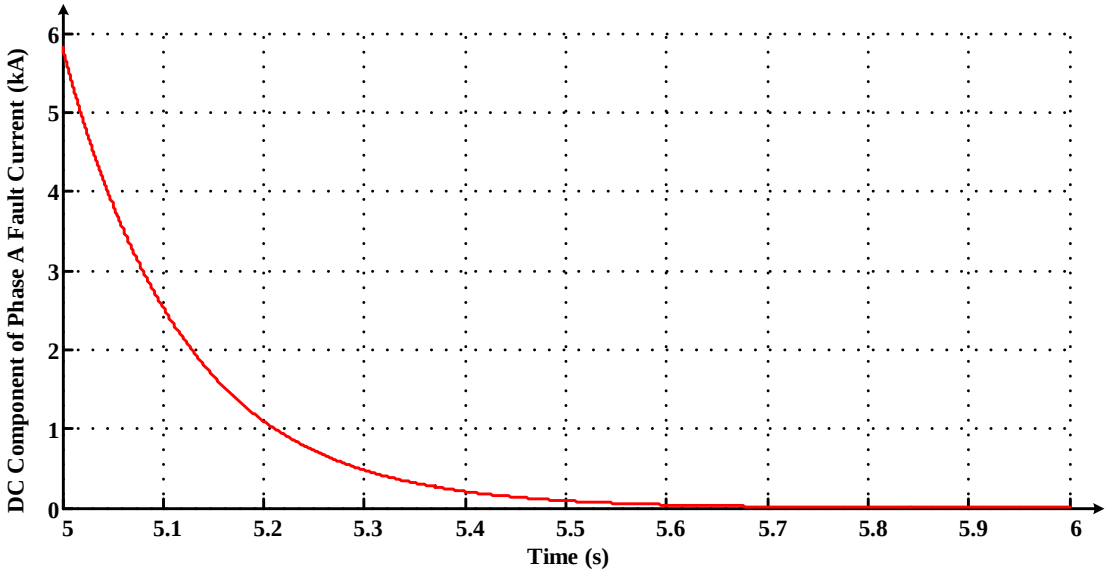

Figure 2.14: DC Component of Phase A fault current

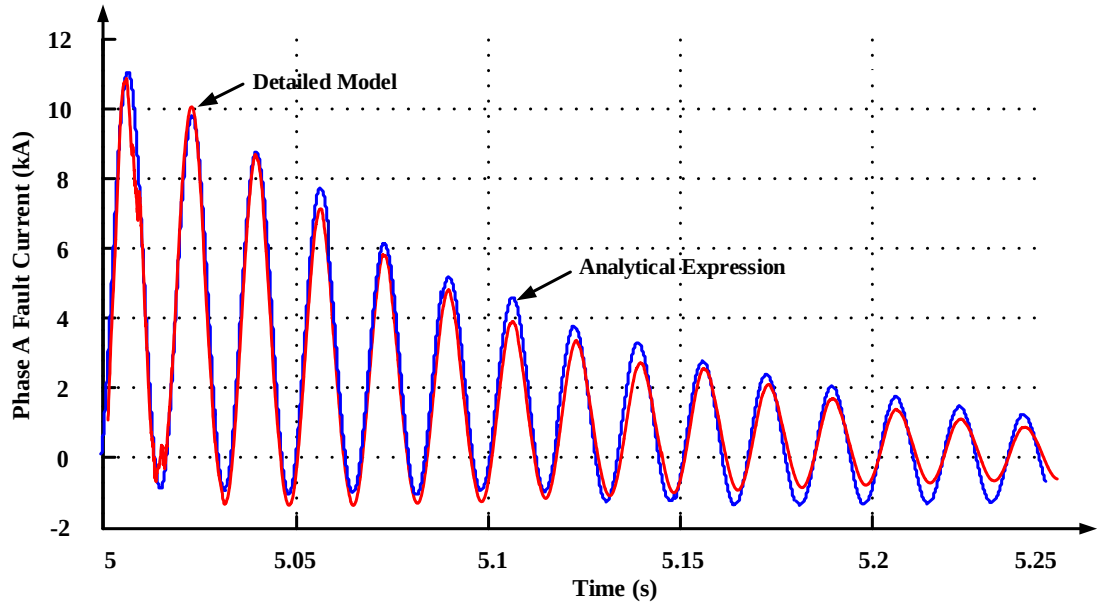

Figure 2.15: Three phase fault - Phase A stator currents - Type 1 wind generator - EMT model versus analytical expression

2.3.2.2 Type 2 Wind Generator

Similar to a Type 1 generator, the short circuit current of a Type 2 generator is found from the expression given in Equation 2.9. The effect of the external rotor resistance is found by using a value of $\sqrt{X'^2 + R_{r_{ext}}^2}$ for Z' in the denominator term ignoring the stator and rotor winding resistances [17]. The rotor decay time constant is calculated as $T_r = L_{r-eqv}/(r_r + R_{r_{ext}})$ for a Type 2 generator. Figure 2.16 shows the short circuit current waveforms obtained from the above expression with and without considering the external rotor resistance and compared with the EMT simulation results. The short circuit current obtained considering the external rotor resistance is more accurate and closer to the results from the EMT.

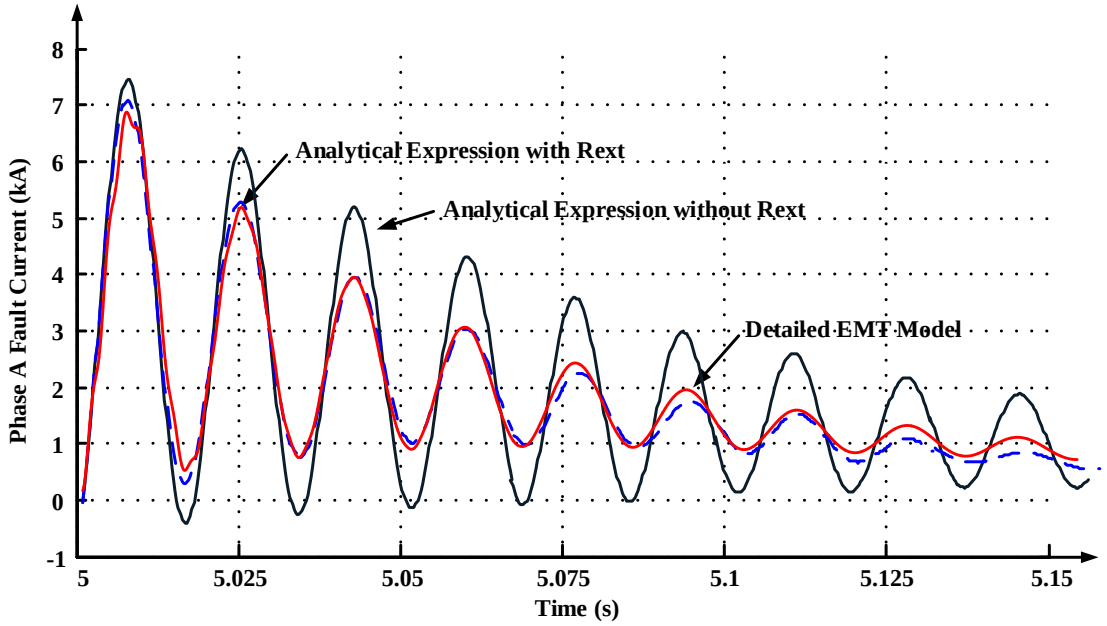

Figure 2.16: Phase A Stator Currents - Type 2 wind generator - EMT model versus analytical expression

2.3.2.3 Type 3 Wind Generator

Because different complexities influence how a Type 3 generator behaves for a short circuit, it is a challenging task to accurately represent it with simple modelling techniques. Some of these complexities, such as the unit breaker protection logic based on LVRT schemes, were discussed before.

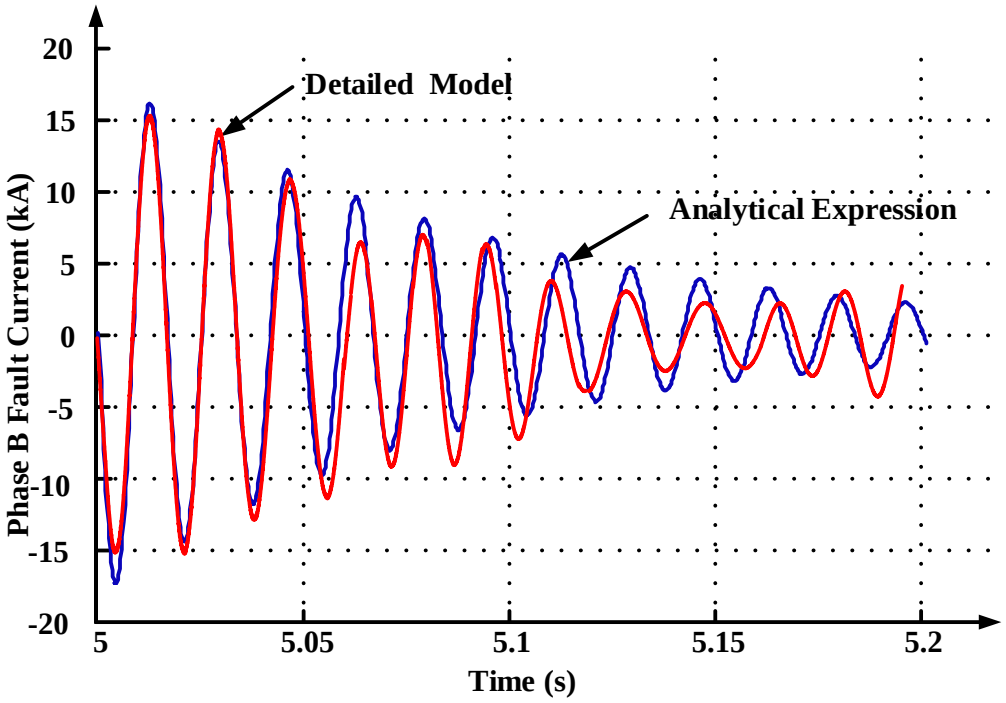

Figure 2.17: Phase B stator currents - Type 3 wind generator - EMT model versus analytical expression

In order to include the effect of the rotor crowbar resistance, the transient impedance calculated as $Z' = \sqrt{X'^2 + R_{crowbar}^2}$ ignoring the stator and rotor winding resistances and the rotor decay time constant calculated as $T_r = L_{r-eqv}/(r_r + R_{crowbar})$ are used in the Equation 2.9. The accuracy of this mathematical model as compared to the EMT model is shown in Figure 2.17. This model is not as accurate for Type 3 generators as for Type 1 and 2 generators. Though the effect of the crowbar resistance is taken into account, it is still not

accurate because it considers the crowbar resistance to be included in the rotor circuit for the entire fault duration. In reality, the duration of application of the crowbar resistance for a Type 3 generator is determined by the variation of the DC-link voltage during the fault, as explained in Section 3.4.

2.3.2.4 Key Findings

The mathematical method of short circuit modelling discussed in this section is capable of producing the current waveform as a function of time for the entire fault duration. This is not possible by using the previously discussed VBR representation, which only gives the fault current at the inception of the fault. This method is fairly accurate for short circuit representation of Type 1 and Type 2 generators. Though the effect of the crowbar resistance is taken into account for a Type 3 generator, the duration of application of the crowbar resistance is assumed for the entire fault duration. This leads to inaccuracy in representing the exact behaviour.

2.3.3 Voltage Dependent Current Source Modelling

2.3.3.1 Introduction

The short circuit behaviour of Type 1 and Type 2 generators can be sufficiently represented using the previously discussed simple techniques. Type 4 generators, with their fault current limited by their full power converter, can be accurately represented by a current source with upper and lower limits based on the converter rating for short circuit analysis [9]. Inaccuracies were still present in the modelling methods for Type 3 generators discussed so far. The voltage dependent current source modelling discussed in this section and the discussions in the forthcoming sections focus specifically on modelling short circuits in Type 3 generators.

2.3.3.2 Type 3 Wind Generator Modelling

The method of modelling discussed in this section is based on representing the short circuit behaviour of generators by voltage dependent current source models defined by look up tables. These look up tables contain data in the form of maximum and minimum short circuit current values as a function of the point of interconnection voltage.

The short circuit data that form the look up table can be obtained by measuring the maximum and minimum short circuit current of the generator when the point of interconnection voltage is varied by applying voltage sags in the range of 20% to 97.5% [9]. The short circuit behaviour in terms of the phase A stator current as observed for the different voltage sags are shown in Figure 2.18. A detailed EMT model of the Type 3 generator developed in RTDS was used in these cases to obtain the short circuit currents.

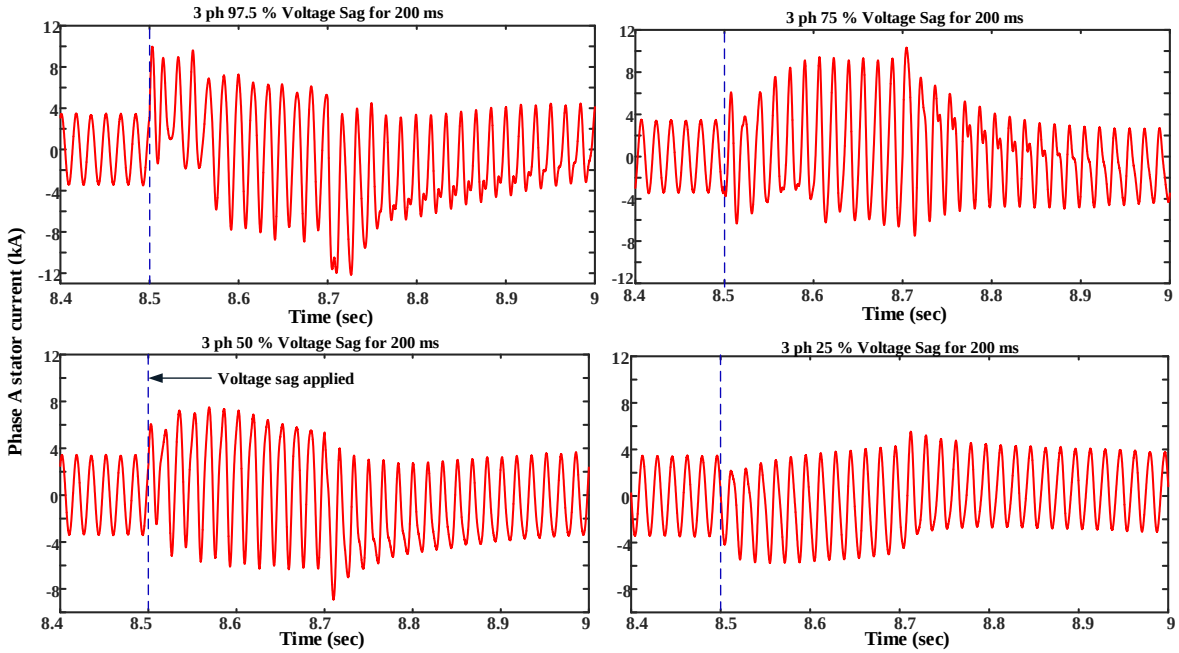

Figure 2.18: Short circuit currents for different percentages of 3-phase voltage sags for a Type 3 generator

In some cases in Figure 2.18, the stator current does not reach its maximum value immediately after application of the sag. Rather, it tends to be higher immediately after the

sag period when the voltage recovers. In such cases, using envelopes to find the fault current magnitude gives the fault current at the inception of the fault but not necessarily the maximum value, which is essential to determine relay settings.

The loci of the maximum and minimum fault currents obtained for different percentage sags form the upper and lower fault current envelopes, respectively, are shown in Figure 2.19. The data from these envelopes in the form of a look up table were used to model the voltage dependent current source model as shown in Figure 2.20 below.

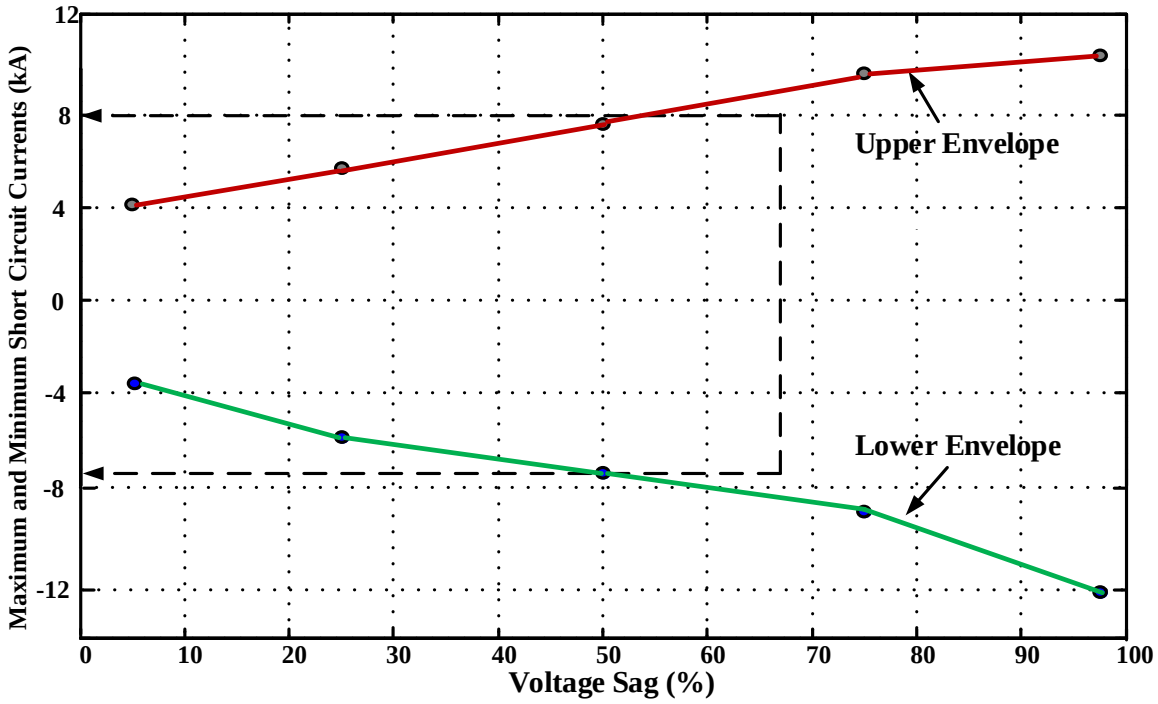

Figure 2.19: Maximum and minimum short circuit current envelopes as a function of the applied voltage sag

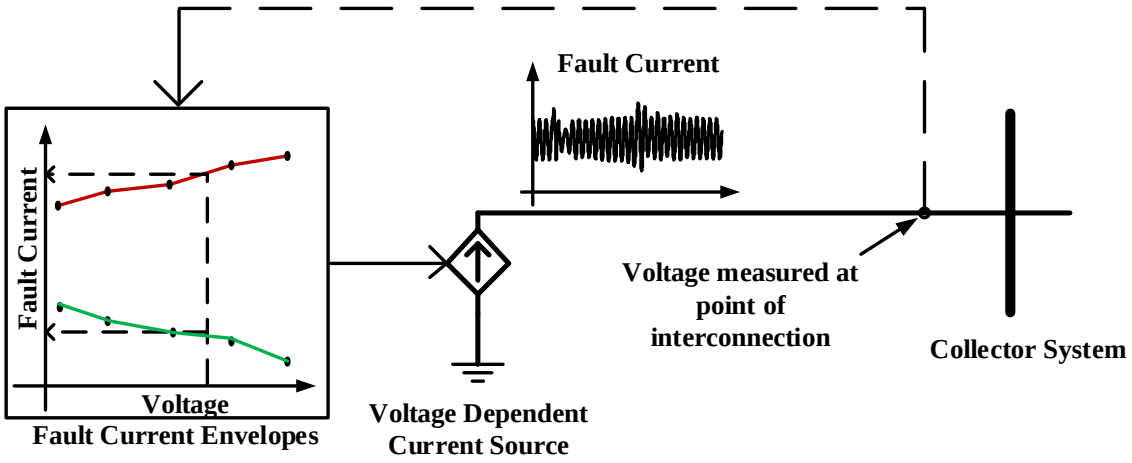

Figure 2.20: Voltage dependent current source model of Type 3 wind generator

2.3.3.3 Key Findings

The voltage dependent current source model is capable of generating the short circuit characteristics of the Type 3 generator using a black-box like approach. The accuracy of this model, i.e., the accuracy of the short circuit current envelopes, depends on the level of sophistication of the actual model used to obtain the maximum and minimum fault currents. In this case, a detailed EMT model was used for the purpose. It is clear that the voltage dependent current source model is not a stand-alone model, as it requires the short circuit current values to be obtained from the wind generator manufacturer or detailed EMT models.

2.3.4 WECC Type 3 WTG Generic Model

First Generation Generic Model:

Figure 2.22 shows structure of first generation Type 3 generic WTG developed by WECC working group. The first generation generic models were developed by simplifying detailed transient stability model. The Type 3 WTG model was developed on the basis of GE's model. It consisted of four components: generator/converter, converter control, wind turbine and

pitch control.

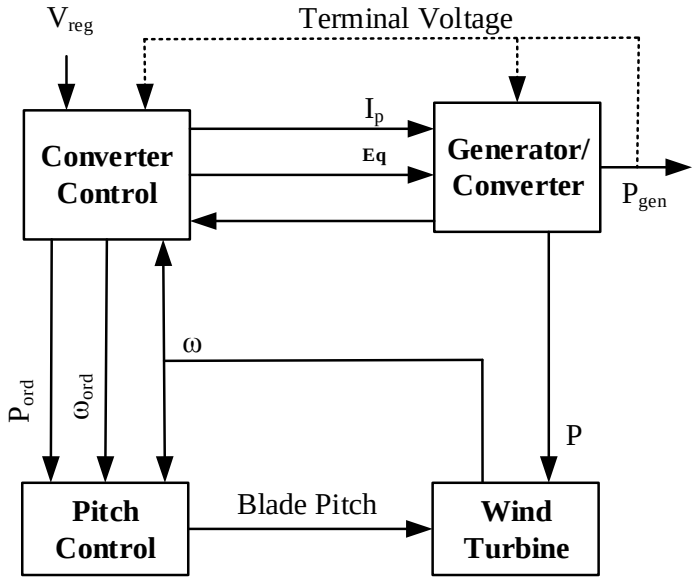

Figure 2.21: Structure of a first generation Type 3 WTG

The generator/converter model ignores the flux dynamics to reflect the rapid response of the converter to the higher level commands from electrical controls. The converter control regulates the active and reactive power to be delivered to system through I_p and E_q commands. The active power order is derived from the generator power and speed. The pitch controller module consists of two PI controllers that act on the speed and power errors. In this model, the blade position actuators are rate limited. A very simplified aerodynamic model is used. This model does not require the representation of the power coefficient curve and is based on the results of the investigation reported in [87]. There were lots of simplifications and assumptions made while developing first generation generic model such as elimination of active power control block. The models were not suitable for studying varying wind conditions and were not designed for use in simulation studies that involved severe frequency excursions. These limitations led to further updates for WTG models particulary for Type 3 and Type 4 WTG model.

Second Generation Generic Model:

The WECC working group for generic models reported second generation generic model in [57]. The model structure of second generation Type 3 WTG consists of seven modules as shown in Figure 2.22. The modules used in a generic wind power plant of Types 3 are: Generator/Converter, Electrical Control, Aerodynamic Conversion, Pitch Controller, Drive-Train, Torque Controller and Plant level Controller.

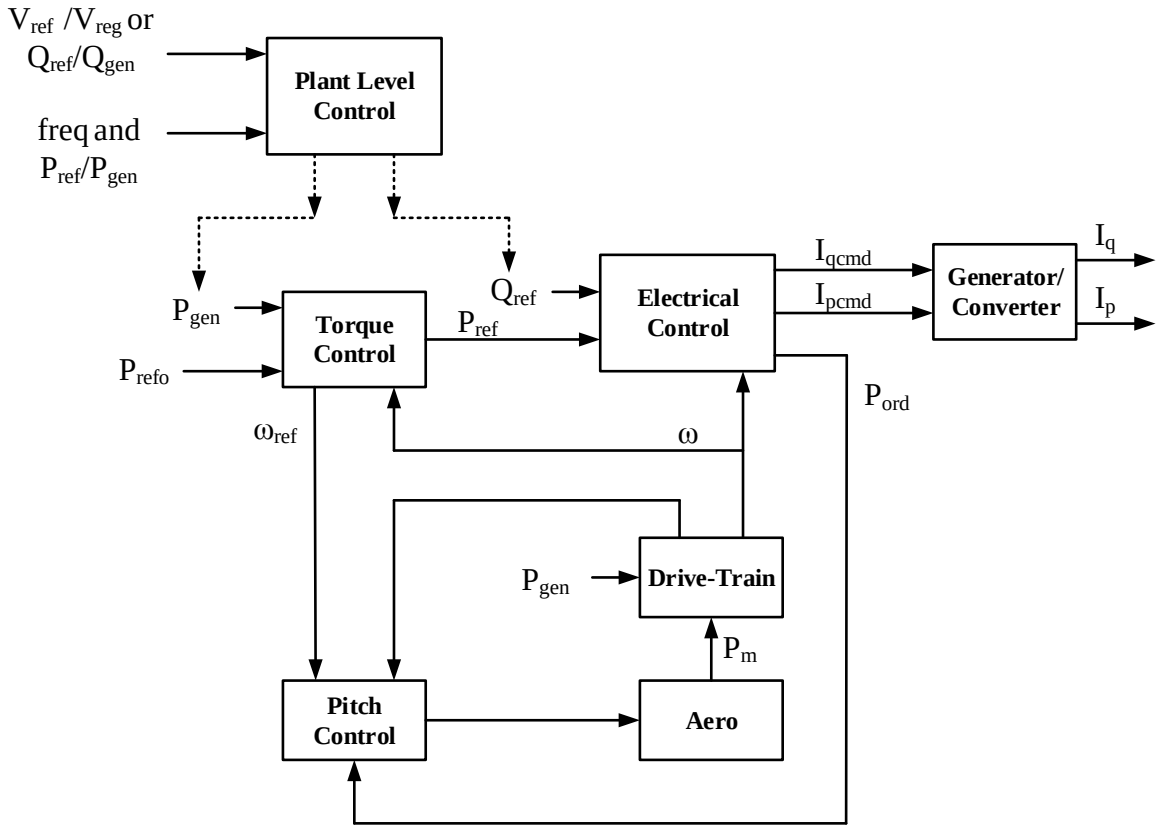

Figure 2.22: Structure of a second generation Type 3 WTG

The generator/converter module represents a high bandwidth current regulator that injects real and reactive components of inverter current into the external network during the network solution in response to real and reactive current commands. The electrical control module provides options for reactive power control, including constant power factor and voltage regulation.

The pitch controller module is very similar to pitch controller used in first generation

generic model except there is an additional speed error signal which is proportional to power deviation. The aerodynamic module used in the second generation generic WTG model is same as the aerodynamic module implemented in the first generation generic WTG models. The drive-train module allows for the use of single or two mass model for turbine-generator inertial representation. The torque controller is a PI controller designed to set the power reference for the electrical controller. It works for power command issued by either user defined power curve or plant level controller. The plant level controller is an optional module used when plant level control of active and/or reactive power is desired. The plant controller presently accommodates the ability to control one aggregated wind turbine generator.

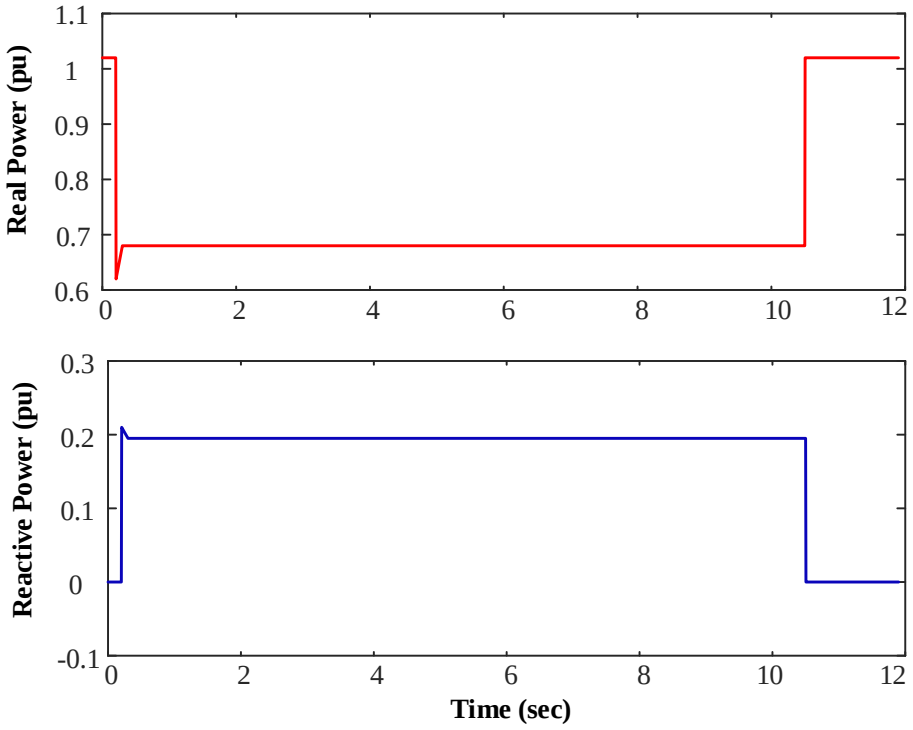

Figure 2.23: Real and Reactive power for a balanced 3 phase voltage dip of 20%

The real and reactive power response of Type 3 generic WTG to a 20% voltage dip at generator terminal is shown in Figure 2.23 as depicted in reference [88]. Figure 2.24 shows the response of real and reactive power to a voltage dip of 75% at generator terminal. Reference [88] claimed that these responses are very close to the responses obtained from

commercial Type 3 WTGs in the same scenario.

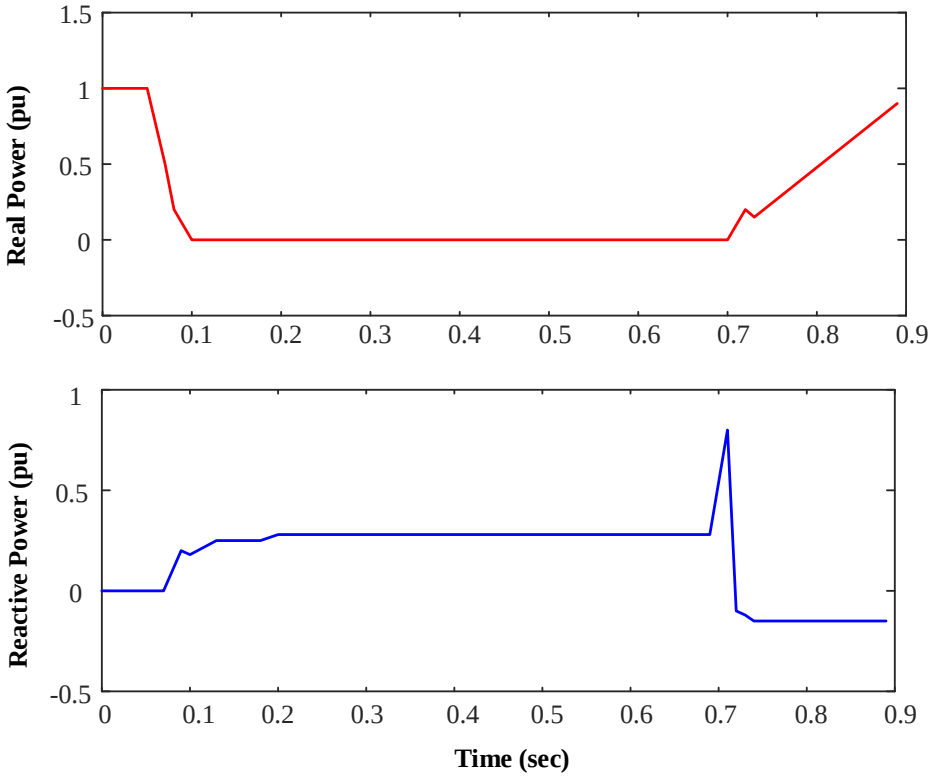

Figure 2.24: Real and Reactive power for a balanced 3 phase voltage dip of 75%

2.4 Summary

This chapter discussed different types of wind turbine generators and their operating principles. State-of-the-art modelling methods are also discussed in this chapter. Voltage behind transient reactance modelling is a fairly accurate method for Type 1 and 2 wind generators; however, it is not as accurate for Type 3 wind generators. The accuracy of this approach improves with the inclusion of the rotor external resistance and the crowbar resistance for modelling Type 2 and Type 3 wind generators, respectively.

Representation using the analytical expression is highly accurate for short circuit modelling of symmetrical fault behaviour in both Type 1 and Type 2 wind generators. The same

level of accuracy is not achieved for Type 3 wind generator representation as this model does not consider complexities such as crowbar activation.

The voltage dependent current source model is capable of representing the Type 3 wind generator short circuit behaviour through a black-box like approach, and its accuracy depends on the sophistication of the model that is actually used to obtain the fault current envelopes. A detailed EMT model developed in RTDS/RSCAD was used to generate lookup table applying voltage sag of 5% to 97.5%. The fault current envelopes was obtained using the lookup table. Thus, it is not a standalone model to represent the short circuit behaviour of a Type 3 wind generator.

The second generation generic model of Type 3 WTG developed by WECC working group was discussed in this chapter. It consisted of seven small modules each representing individual component of plant. The second generation of WTG generic model used either a single lumped mass or a two mass model. Eventhough the model is called generic model, the working group concluded that the future revisions of this model would be needed based on the feedback received from the users.

The next chapter describes detailed modelling of Type 3 DFIG wind farm including Multimass and Flux decrement effects. Different topologies of LVRT are also discussed in the next chapter.

Chapter 3

Modelling of DFIG Wind Power Plant including LVRT and Flux Decrement Effects

3.1 Introduction

An electromagnetic transient (EMT) model was used to validate the short circuit models developed in this thesis. EMT type programs facilitate modelling with precision and can reproduce the actual time-domain waveforms of variables due to their capabilitys to account for network non-linearities and unbalanced conditions [89]. These programs work for a wide range of frequency from 0 to 3 kHz.

This chapter describes the modelling of a Type 3 wind power plant in a real-time simulation environment. The modelling details of each components of DFIG wind power plant and their controls are discussed. The mechanical drive train system is simulated using a three mass model to capture potential torsional oscillations. DFIG utilizes back-to-back power electronic converters that consist of high frequency firing circuits. Smaller time-steps are needed to model the high frequency switching circuits. The power electronic converters are modeled in small time steps where typical time step is 1-4 μsec [90]. The most commonly used low voltage ride through (LVRT) topologies such as rotor side crowbar circuit, DC-link protection scheme, and series dynamic braking resistance (SDBR) in rotor and stator circuits, are investigated in Section 3.4. Section 3.5 discusses the flux decrement effect in induction generator.

3.2 Real Time Digital Simulator (RTDS)

The Real Time Digital Simulator (RTDS) is designed to study electromagnetic transient phenomena in real time environment [91]. RTDS is a fully digital simulator which utilizes advanced parallel processing techniques in order to achieve the computation speeds required to maintain continuous real time operation.

RTDS software includes accurate power system component models required to represent many of the complex elements which make up physical power systems. The overall network solution technique employed in the RTDS is based on nodal analysis. The underlying solution algorithms are those introduced by H. W. Dommel [92]. Dommel's solution algorithm is used in virtually all digital simulation programs designed for the study of electromagnetic transients. RTDS software also include a powerful and user friendly graphical user interface (GUI), referred to as RSCAD, through which the user is able to construct, run and analyze simulation cases [91]. The main hardware components of the RTDS are Workstation interface cards (GTWIF or WIF), PB5 Processor cards (PB5), GIGA Processor cards (GPC), analogue input/output cards (GTAI/GTAO, digital input/output cards (GTDI/GTDO) and network interface cards (GTNET).

RTDS computes the state of the power system model only at discrete instants in time. The time between these discrete instants is referred to as the simulation timestep (Δt). Many hundreds of thousands of calculations must be performed during each timestep in order to compute the state of the system at that instant. The temporary transients class of studies for which the RTDS is most often used requires Δt to be in the order of 50 to 60 μsec (frequency response accurate to approximately 3,000 Hz). By definition, in order to operate in realtime a 50 μsec timestep would require that all computations for the system solution be complete in less than 50 μsec of actual time. In order to realize and maintain the required computation rates for realtime operation, many high speed processors operating in parallel are utilized by the RTDS.

Small Time-Step Simulation

Power electronic converters are integral part of DFIG system. modelling those power elec-

tronic components like voltage source converter (VSC) in RTDS is challenging because firing circuit works at a high frequency. Multiple switching may occur within a typical simulation timestep of 50 μsec, also problems will arise when switching occurs at the end of the 50 μsec, because there will be little time left for solving the system. To tackle this problem, small time-step of 1-4 μsec is used to solve the power electronics and switchings separately and then connect them to main network which is simulated in 50 μsec time step [90]. An Interface Transformer model is used to interface the small time-step VSC network with the main-system network [91].

3.3 Development of DFIG Wind Power Plant in RTDS

In this section the modelling details of the components of DFIG wind power plant in RTDS are discussed. Figure 3.1 shows the schematic diagram of a DFIG wind power plant in RSCAD. The system consists of a 3 MW Type 3 wind generator connected to the collector system through a unit transformer and then to the grid through a feeder line. The generator, unit transformer and back-to-back converter are modeled in small time-step (each time step is about 1-4μs) and remaining systems are modeled in large time step in RSCAD. Figure 3.2 shows an interface transformer model in RSCAD which is used to interface between the small time step subnetwork and the grid simulated in the large time step.

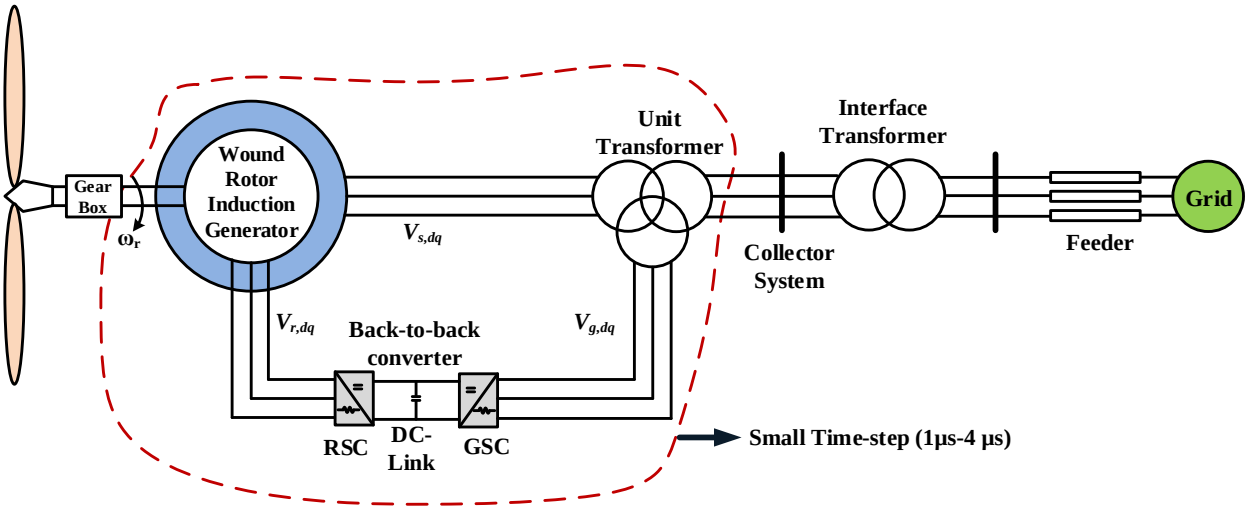

Figure 3.1: DFIG system

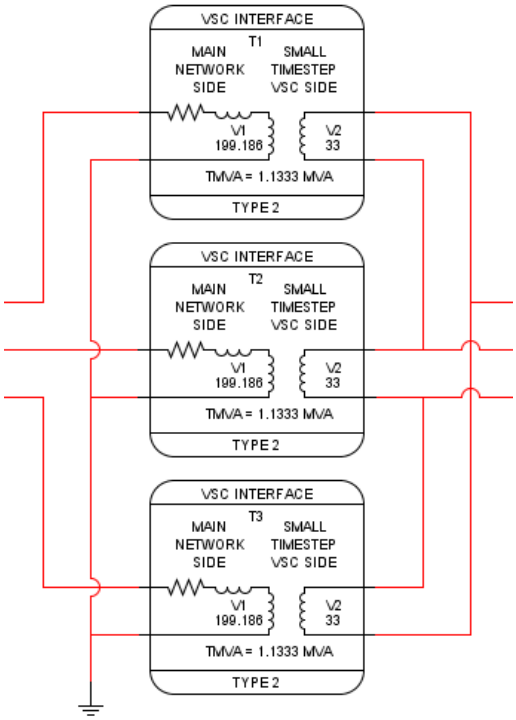

Figure 3.2: Interface Transformer

3.3.1 Wind Turbine Model

Wind turbine power generation depends on interaction between the wind turbine rotor and the wind. Power available in the wind is given by [7]:

$$P_{wind} = \frac{1}{2}\rho A V_{wind}^3 \tag{3.1}$$

where, ρ is the air density $[kg/m^3]$; A is the area swept by blades $[m^2]$ and V_{wind} is wind speed $[m/sec]$.

The power extracted from wind by a wind turbine is given by

$$P_t = \frac{1}{2}\rho\pi R^2 C_p(\lambda,\beta) V_{wind}^3 \tag{3.2}$$

where, R is the turbine blade length [m]; C_p is the performance coefficient. C_p is a function of tip speed ratio (TSR) and pitch angle β. The TSR denoted by λ, is the ratio of the blade tip linear speed to the wind speed. The TSR determines the fraction of available power extracted from the wind by the wind turbine rotor. In a fixed-speed wind turbine, the blade tip speed is held relatively constant since the rotor is connected directly to the induction generation via a gearbox, and the induction generator is directly connected to the grid. The TSR can be calculated as follows:

$$\lambda = \frac{\omega_t R}{V_{wind}} \tag{3.3}$$

where, ω_t is the angular velocity of the turbine.

In 1919, Betz proved that the maximum power extractable by an ideal turbine rotor with infinite blades from wind under ideal conditions is 16/27 (59.26%) of the power available in the wind. In practice, wind turbines are limited to two or three blades due to a combination of structural and economic considerations, and hence the amount of power they can extract is closer to about 50% (0.5 times) of the available power. However, commercial wind turbines typically have C_p in the range of 20% to 45% [93]. Various empirical formulae are given in the literature to represent the performance coefficient. In [94], the generic equation

$$C_p(\lambda,\beta) = c_1(\frac{c_2}{\alpha} - c_3\beta - c_4)exp(\frac{-c_5}{\alpha}) + c_6\lambda \tag{3.4}$$

$$with\ \frac{1}{\alpha} = \frac{1}{\lambda + 0.08\beta} - \frac{0.035}{\beta^3 + 1} \tag{3.5}$$

is used to model the coefficient. The coefficients c_1 to c_6 are: c_1= 0.5176, c_2= 116, c_3= 0.4, c_4= 5, c_5= 21, c_6= 0.0068. The variation of C_p versus the TSR for several pitch angles is shown in Figure 3.3.

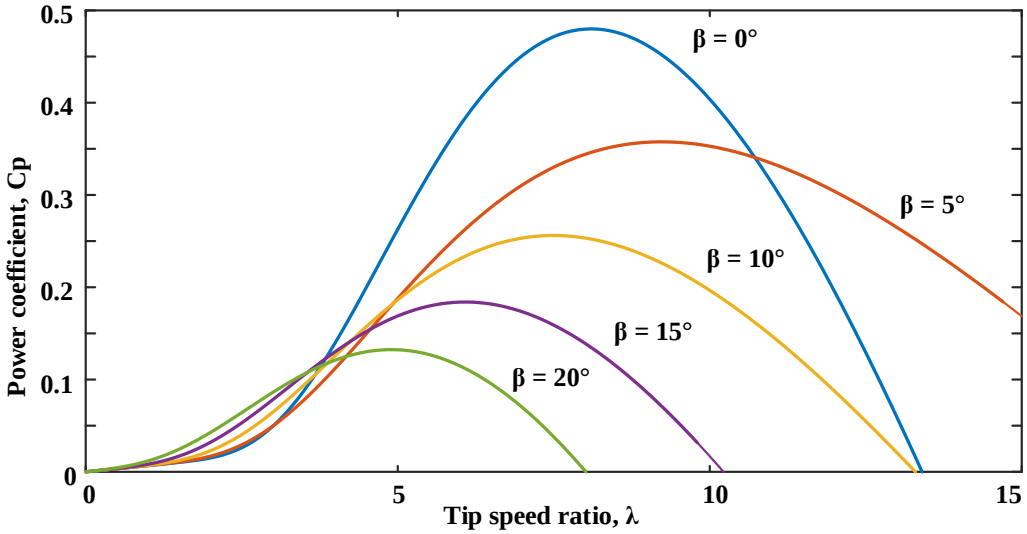

Figure 3.3: C_p-λ characteristics

As shown in the Figure 3.3, each pitch angle has an optimum value of λ where Cp is maximum. From Equation 3.2 it can be seen that if the wind turbine is operated at this optimum tip speed ratio, the power extracted from the wind is maximum for a given wind speed. Therefore, often wind turbines are operated at this optimum tip speed ratio. This operating mode is commonly referred to as maximum power tracking mode. A typical wind turbine characteristic is shown in Figure 3.4. As the wind speed changes, the generator speed (i.e. turbine rotation speed) is changed by the speed controller in order to keep the TSR at its optimum value.

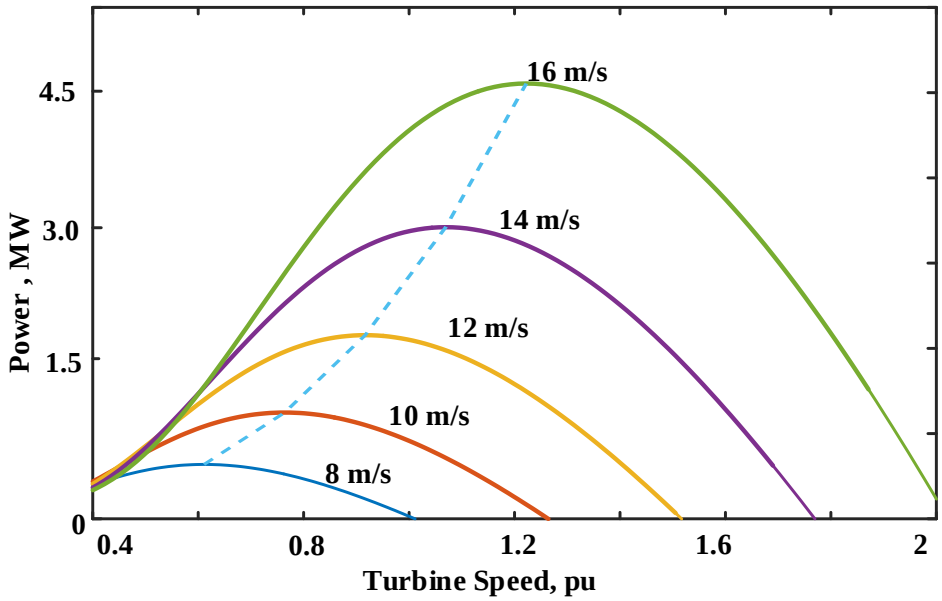

Figure 3.4: Wind turbine characteristics with β=0

If the turbine speed is ω_t, the mechanical torque T_m is given by, $T_m = P_t/\omega_t$. In per unit, $\omega_t = \omega_r$. Therefore, the mechanical torque input to the generator in per unit is given by,

$$T_m = P_t/\omega_r \tag{3.6}$$

From Equations 3.2 and 3.6 the generator mechanical torque in maximum power tracking mode can be written as,

$$T_m = \frac{1}{2}\frac{\rho\pi R^2 C_p(\lambda,\beta)V_{wind}^3}{\omega_r} \tag{3.7}$$

The wind speed at which the turbine extracts its rated power is called the rated wind speed. If the wind speed increases beyond the rated speed, the machine is forced out of the optimal TSR operation. In such a case the pitch controller changes the pitch angle of the turbine blades so that the power extracted by the wind turbine is limited to the rated power. When the wind speed is less than the rated speed, the pitch angle is adjusted to the minimum value to get the maximum mechanical power. In both cases, the pitch angle controller senses the speed change to regulate the output power. A typical structure of pitch angle controller

is shown in Figure 3.5. The actual rotor speed is compared with the reference value, and the error is sent to the PI controller to get the reference value of the pitch angle.

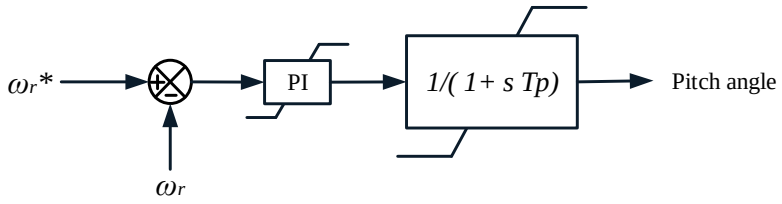

Figure 3.5: Wind turbine pitch angle controller

3.3.2 Mechanical Drive Train Model

The drive train model represents wind farms main mechanical dynamics. There are various models of varying degrees of complexity available in the literature for drive train modelling. The one-mass model assumes generator inertia, the turbine hub and blades as a single lumped mass. Although simple, this model is not capable of showing torsional oscillations in the wind power plant. In the two-mass model, the wind turbine and the generator are modeled as two masses connected via a flexible shaft. The torsional oscillation between the wind turbine and the generator is observable with this model. The three-mass model has been derived so that the blade oscillations can be observed in studies. In this model, the flexible portion of the blade is considered as one mass, the rigid part of the blades and turbine hub as another mass, and the generator as the third mass. These three masses are connected with each other via two flexible shafts as shown in Figure 3.6.

The fifth order model explained in [95] is used to model the three mass drive train. H_b, H_h, H_g are inertia constants (in seconds) of the masses representing the blades, hub, generator. K_1 is the stiffness coefficient (in pu torque/electrical radian) of the shaft connecting the blade and the hub, K_2 is the stiffness coefficient (in pu torque/electrical radian) of the shaft connecting the hub and the generator. ω_b, ω_h are the pu rotating speeds of blades and the hub. θ_{bh}, θ_{hg} are the angles between the blades and the hub and between the hub and the generator. The dynamic model of the three mass drive train model can be written

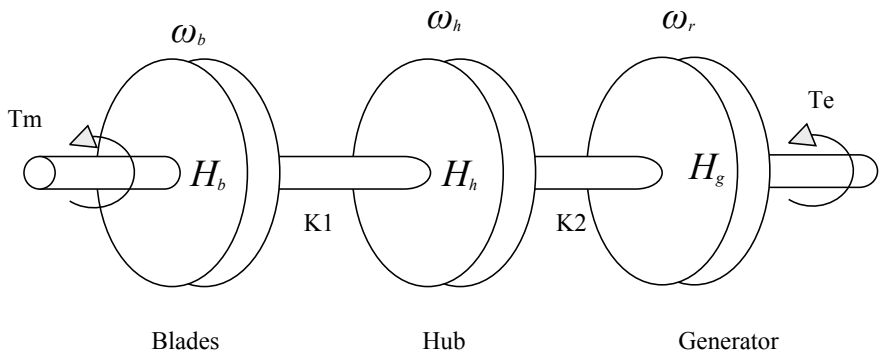

Figure 3.6: Three mass drive train model

as,

$$\dot{\omega_b} = \frac{1}{2H_b}(T_m - K_1\theta_{bh}) \tag{3.8}$$

$$\dot{\omega_h} = \frac{1}{2H_h}(K_1\theta_{bh} - K_2\theta_{hg}) \tag{3.9}$$

$$\dot{\omega_r} = \frac{1}{2H_g}(K_2\theta_{hg} - T_e) \tag{3.10}$$

$$\dot{\theta_{bh}} = \omega_0(\omega_b - \omega_h) \tag{3.11}$$

$$\dot{\theta_{hg}} = \omega_0(\omega_h - \omega_r) \tag{3.12}$$

In Equation (2.9), T_e represents the electromagnetic torque produced by the generator.

3.3.3 Induction Generator Part

The winding arrangement of a conventional 2-pole, 3-phase, wye-connected symmetrical induction generator is shown in Figure 3.7 for the purpose of explanation. The stator windings are identical with equivalent turns N_s and resistance r_s. The rotor windings can be approximated as identical windings with equivalent turns N_r and resistance r_r. The model assumes the air-gap is uniform and the windings are sinusoidally distributed.

In Figure 3.7, the winding of each phase is represented by an elementary coil. One side

of the coil is represented by a $\otimes$ indicating that the assumed positive direction of current is down the length of the stator (into the plane of the paper). The other side of the same coil is represented by a $\odot$ which indicates that the assumed positive direction of current is out of the plane of the paper. The axes a_s, b_s and c_s represent the positive directions of the magnetic fields produced due to the currents flowing in the stator windings of phase a, b and c, respectively. These directions are obtained using the right hand rule on the phase windings. Similarly axes a_r, b_r and c_r with respect to the rotor windings are shown. These rotor axes are fixed to the rotor and rotate with it at an angular velocity of ω_r. The angular displacement of the rotor with respect to the positive a_s axis is θ_r.

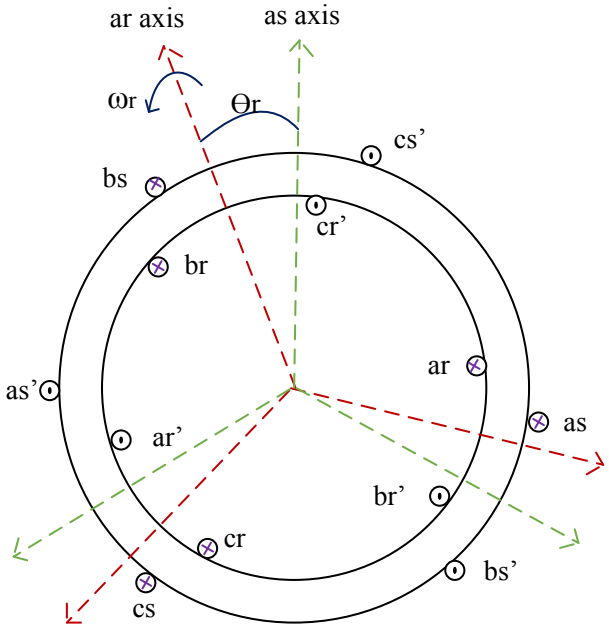

Figure 3.7: Schematic winding diagram of the stator and rotor side of the induction generator

Voltage equations for a three phase induction generator in pu are presented in the fol-

lowing equation.

$$\begin{bmatrix} V_{as} \\ V_{bs} \\ V_{cs} \\ V_{ar} \\ V_{br} \\ V_{cr} \end{bmatrix} = \begin{bmatrix} r_s & 0 & 0 & 0 & 0 & 0 \\ 0 & r_s & 0 & 0 & 0 & 0 \\ 0 & 0 & r_s & 0 & 0 & 0 \\ 0 & 0 & 0 & r_r & 0 & 0 \\ 0 & 0 & 0 & 0 & r_r & 0 \\ 0 & 0 & 0 & 0 & 0 & r_r \end{bmatrix} \begin{bmatrix} i_{as} \\ i_{bs} \\ i_{cs} \\ i_{ar} \\ i_{br} \\ i_{cr} \end{bmatrix} + \frac{d}{dt} \cdot \begin{bmatrix} \psi_{as} \\ \psi_{bs} \\ \psi_{cs} \\ \psi_{ar} \\ \psi_{br} \\ \psi_{cr} \end{bmatrix} \tag{3.13}$$

where, r_s and r_r are stator winding resistance and rotor winding resistance referred to stator in pu.

Equation 3.13 can be written as

$$\begin{bmatrix} V_{abcs} \\ V_{abcr} \end{bmatrix} = \begin{bmatrix} [r_s] & [0] \\ [0] & [r_r] \end{bmatrix} \begin{bmatrix} i_{abcs} \\ i_{abcr} \end{bmatrix} + \frac{d}{dt} \cdot \begin{bmatrix} \psi_{abcs} \\ \psi_{abcr} \end{bmatrix} \tag{3.14}$$

The flux linkage equation is

$$\begin{bmatrix} \psi_{abcs} \\ \psi_{abcr} \end{bmatrix} = \begin{bmatrix} [L_{ss}] & [L_{sr}] \\ [L_{sr}]^T & [L_{rr}] \end{bmatrix} \begin{bmatrix} i_{abcs} \\ i_{abcr} \end{bmatrix} \tag{3.15}$$

where $[L_{ss}]$ and $[L_{rr}]$ are the inductance matrices for stator and rotor windings, and $[L_{sr}]$ is the inductance matrix for the mutual inductances between the stator and rotor windings.

The voltages, currents and inductances in Equations 3.14 and 3.15 are derived in the stationary *abc* reference frame and are thus, time-variant. modelling and analysis for such a system is cumbersome. These time-variant quantities can be made time-invariant by transforming them into an appropriate rotating reference frame, in this case, the $dq0$ reference frame rotating at an angular speed determined by the synchronous angular speed of the system. Using Park's transform, Equation 3.14 become:

$$[V_{dq0s}] = [r_s].[I_{dq0s}] + \omega_e.[\psi_{dq0s}] + \frac{d}{dt}.[\psi_{dq0s}] \tag{3.16}$$

and

$$[V_{dq0r}] = [r_r].[I_{dq0r}] + (\omega_e - \omega_r)[\psi_{dq0r}] + \frac{d}{dt}.[\psi_{dq0r}] \tag{3.17}$$

where ω_e and ω_r are the angular speeds (rad/sec) of the $dq0$ reference frame and the rotor frame, respectively. Equations 3.16 and 3.17 can be written out explicitly, and the flux

linkage terms can be expanded as follows:

Stator Voltage Equations

$$V_{ds} = r_s.I_{ds} - \omega_e.\psi_{qs} + \frac{d}{dt}.\psi_{ds} \tag{3.18}$$

$$V_{qs} = r_s.I_{qs} + \omega_e.\psi_{ds} + \frac{d}{dt}.\psi_{qs} \tag{3.19}$$

$$V_{0s} = r_s.I_{0s} + \frac{d}{dt}.\psi_{0s} \tag{3.20}$$

Rotor Voltage equations referred to stator side

$$V_{dr} = r_r.I_{dr} - (\omega_e - \omega_r).\psi_{qr} + \frac{d}{dt}.\psi_{dr} \tag{3.21}$$

$$V_{qr} = r_r.I_{qr} + (\omega_e - \omega_r).\psi_{dr} + \frac{d}{dt}.\psi_{qr} \tag{3.22}$$

$$V_{0r} = r_r.I_{0r} + \frac{d}{dt}.\psi_{0r} \tag{3.23}$$

Stator Flux equations

$$\psi_{ds} = L_{ss}.I_{ds} + L_m.I_{dr} \tag{3.24}$$

$$\psi_{qs} = L_{ss}.I_{qs} + L_m.I_{qr} \tag{3.25}$$

$$\psi_{0s} = L_{ls}.I_{0s} \tag{3.26}$$

Rotor flux equations referred to stator side

$$\psi_{dr} = L_m.I_{ds} + L_{rr}.I_{dr} \tag{3.27}$$

$$\psi_{qr} = L_m.I_{qs} + L_{rr}.I_{qr} \tag{3.28}$$

$$\psi_{0r} = L_{lr}.I_{0r} \tag{3.29}$$

where, $L_{ss} = L_{ls} + L_m$ and $L_{rr} = L_{lr} + L_m$. L_m, L_{ls} and L_{lr} are magnetizing inductance, stator winding leakage inductance and rotor winding leakage inductance referred to stator, respectively.

The electromagnetic torque produced by the generator can be written as

$$T_e = \psi_{qr} I_{dr} - \psi_{dr} I_{qr} \tag{3.30}$$

Equation 3.30 shows that the torque can be expressed in terms of d-axis and q-axis currents and flux linkages, indicating that decoupled control of real and reactive power output of a DFIG may be feasible.

3.3.4 Back to Back Conveter

The back-to-back converter is a bidirectional power converter consisting of the Rotor side converter and the Grid side converter connected via a DC Link capacitor as shown in Figure 3.8. The two converters make use of insulated gate bipolar transistors (IGBT) provided with freewheeling diodes.

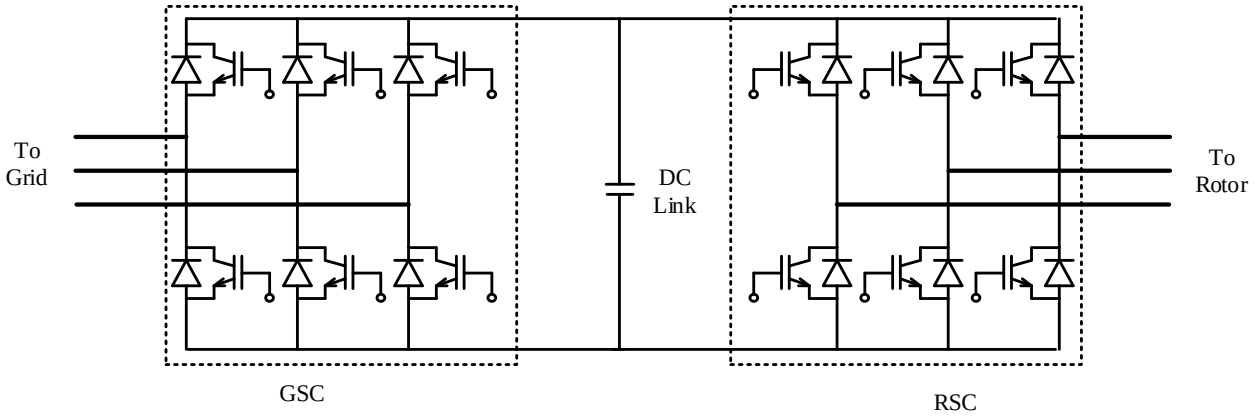

Figure 3.8: Back to Back Converter

3.3.4.1 Back to Back Converter Modulation Scheme

There are several modulation techniques for the inverter and rectifier sides of the back-to-back converter among which sinusoidal pulse-width modulation (SPWM) is used in this research.

In SPWM scheme, the firing pulses of the power electronic switches (i.e. IGBTs for the back-to-back SPWM converters) are generated in a way that the fundamental component of the output voltage has the desired magnitude and phase. In carrier-based SPWM, a sinusoidal reference signal is compared to a high frequency triangular signal in order to generate the firing pulses for the power electronic switches. The triangular signal should have a period much smaller than the smallest time constant of the system. The firing pulse is generated as follows:

$$\text{firing pulse} = \begin{cases} 1 & \text{if carrier} < \text{reference} \\ 0 & \text{if carrier} > \text{reference} \end{cases}$$

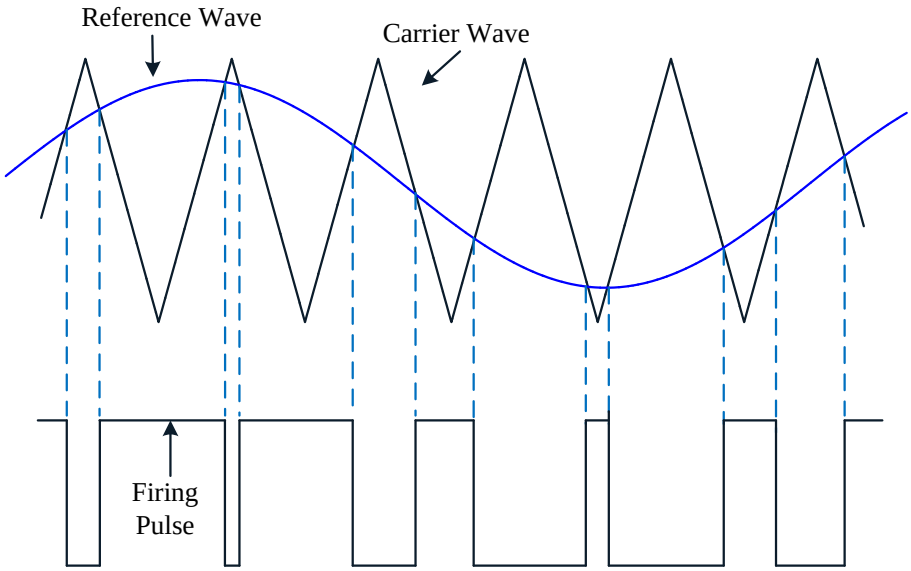

Figure 3.9: SPWM Scheme

In a three-phase SPWM controller, the reference signal corresponding to each leg of the converter is separately generated in a way that each is 120 degree apart from the other one. The output is a three-phase voltage, and the fundamental components of the three-phase output voltage are shifted by 120 degree.

3.3.4.2 Grid Side Converter (GSC) Control

The grid side converter (GSC) is a pulse width modulated voltage source conveter (VSC). The function of the GSC is to maintain constant capacitor voltage. The grid VSC is current regulated with the real component used to regulate the capacitor voltage and the quadrature component used to adjust terminal voltage. Regulation of current requires that it be transformed from 3 phase to 2 phase and then applied to a rotating reference frame, so that

the ac fundamental component is extracted. The resulting currents are called the direct and quadrature currents. All the controls convert engineering quantities into per unit on input. To develop the control strategy for the the grid VSC, it is first useful to write the voltage equations.

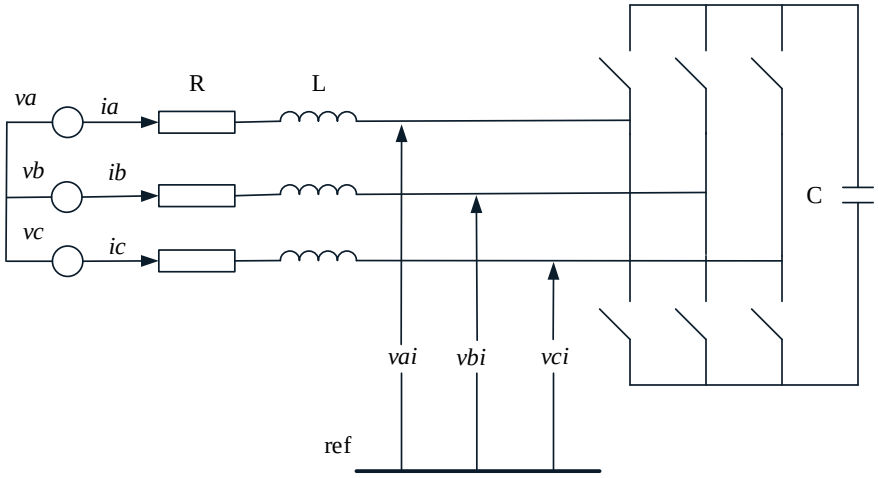

Figure 3.10: Schematic diagram to demonstrate GSC control

With reference to Figure 3.10, the voltage equations are,

$$\begin{bmatrix} v_a \\ v_b \\ v_c \end{bmatrix} = R. \begin{bmatrix} i_a \\ i_b \\ i_c \end{bmatrix} + L.\frac{d}{dt} \cdot \begin{bmatrix} i_a \\ i_b \\ i_c \end{bmatrix} + \begin{bmatrix} v_{ai} \\ v_{bi} \\ v_{ci} \end{bmatrix} \tag{3.31}$$

After converting the Equation 3.31 into a reference frame rotating at ω_e, the new sets of equations are,

$$v_d = Ri_d + L\frac{di_d}{dt} - \omega_e L i_q + v_{di} \tag{3.32}$$

$$v_q = Ri_q + L\frac{di_q}{dt} + \omega_e L i_d + v_{qi} \tag{3.33}$$

In these equations, the rotating reference frame is aligned with v_d. Therefore, v_q is zero and v_d is a constant. The control equations are [96],

$$v_{di}* = -v'_d + (\omega_e L i_q + v_d) \tag{3.34}$$

$$v_{qi}* = -v'_q - (\omega_e L i_d) \tag{3.35}$$

where the starred values are the computed references and the primed values are the outputs of the PI regulators as shown in Figure 3.11. The terms in brackets are the voltage compensation or cross coupling terms. The current references are derived from a slider for I_q and the outer capacitive voltage regulator loop as shown in Figure 3.12 for I_d. The PI gains were adjusted for satisfactory performance.

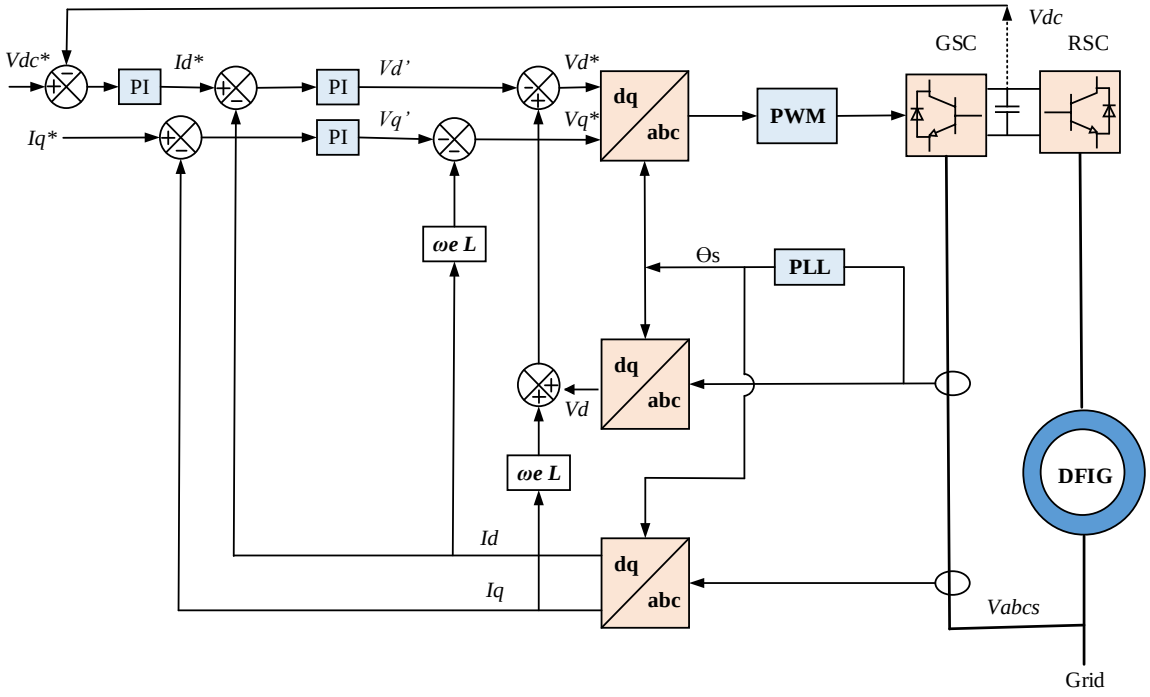

Figure 3.11: Control scheme implemented for GSC

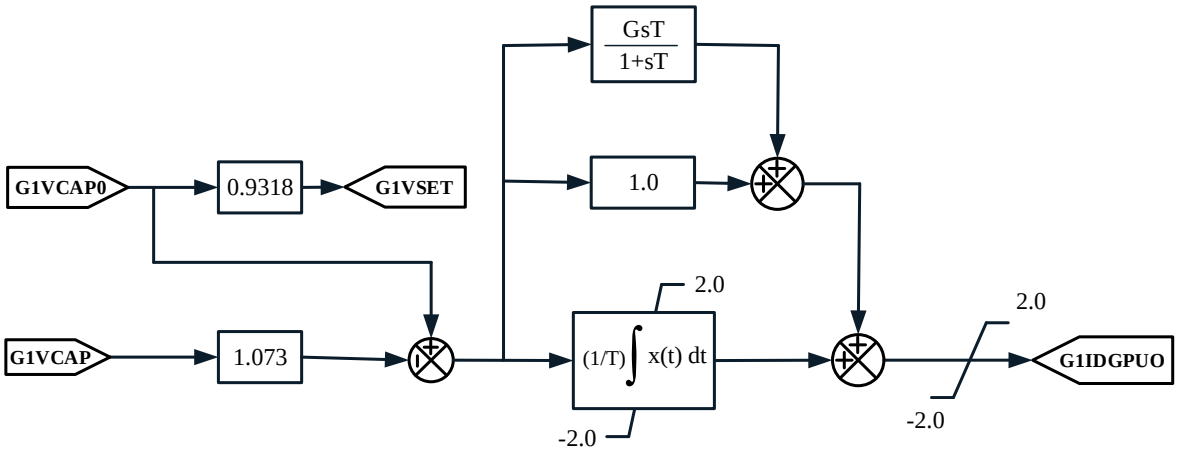

Figure 3.12: Outer capacitive voltage regulator loop implemented in RTDS

The per unit base for the capacitor voltage was chosen to be dc voltage of the bridge when blocked, or

$$v_{pu}* = \frac{3\sqrt{2}}{\pi} v_{l-l}$$

3.3.4.3 Rotor Side Converter (RSC) Control

The rotor side converter (RSC) is also a pulse width modulated voltage source conveter (VSC). The RSC regulates the flux in the DFIG. For super-synchronous speeds, it extracts the power from the rotor and supplies it to the grid via the DC link and the GSC. During sub-synchronous operation, it imports power from the grid to excite the rotor. This regulates the optimum flux to produce maximum torque for any given frequency. The RSC control is done using the stator flux vector orientation scheme where the dq axis are aligned with the stator flux allowing the simultaneous control of the electrical torque/real power and rotor excitation current/reactive power of the DFIG [96].

The d and q rotor voltage equations are [96],

$$v_{dr} = r_r i_{dr} + \sigma L_{rr} \frac{di_{dr}}{dt} - \omega_{slip}(\sigma L_{rr} i_{qr}) \tag{3.36}$$

$$v_{qr} = r_r i_{qr} + \sigma L_{rr} \frac{di_{qr}}{dt} + \omega_{slip}(L_{ms} i_{ms} + \sigma L_{rr} i_{qr}) \tag{3.37}$$

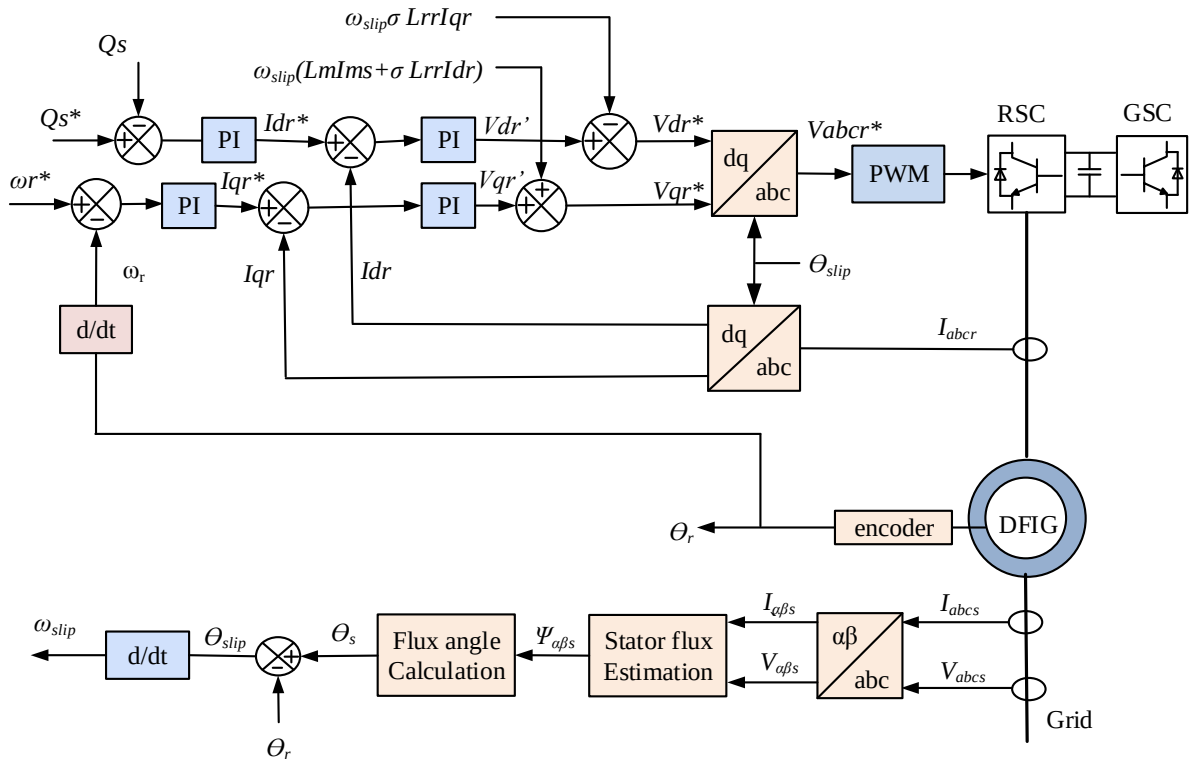

Figure 3.13: Control scheme implemented for RSC

where, $L_m = \frac{L_0^2}{L_{ss}}$ and $\sigma = 1 - \frac{L_0^2}{L_{ss}L_{rr}}$.

Figure 3.13 shows a schematic block diagram for the rotor-side converter control. The i_{dr} and i_{qr} error signals are processed by associated PI controllers to give v_{dr} and v_{qr}, respectively. From Equations 3.36 and 3.37 , define

$$v'_{dr} = r_r i_{dr} + \sigma L_{rr} \frac{di_{dr}}{dt} \tag{3.38}$$

$$v'_{qr} = r_r i_{qr} + \sigma L_{rr} \frac{di_{qr}}{dt} \tag{3.39}$$

To ensure good tracking of the rotor dq-axis currents, compensation terms are added to v'_{dr} and v'_{qr} to obtain the reference voltages $v_{dr}*$ and $v_{qr}*$ according to

$$v_{dr}* = v'_{dr} - \omega_{slip}(\sigma L_{rr} i_{qr}) \tag{3.40}$$

$$v_{qr}* = v'_{qr} + \omega_{slip}(L_{ms} i_{ms} + \sigma L_{rr} i_{qr}) \tag{3.41}$$

3.4 LVRT based Protection Scheme

DFIG is popular in wind generation application due to its variable speed capability and the reduced power rating of converters that are connected between the rotor and power grid. In DFIG-based wind generation system, the sudden dip of point of common coupling (PCC) bus voltage will result in an increase of both the stator and rotor current, because they are coupled with each other. The increase of rotor current may destroy the low power level converters which are connected to the rotor. The increase of stator current may affect power system stability. Another problem for wind power plants is the torque stress to gearbox under fault conditions. Limiting the overcurrent in rotor and stator is a significant issue for DFIG-based power generation system during transients.

As more and more wind power is integrated into the power grid, it is necessary to keep turbines connected to the grid during PCC voltage dip to maintain system stability. This helps both the frequency and voltage recovery after the fault has been cleared. The LVRT requirements make it necessary for wind farms to stay connected to the grid and provide reactive power support during and after voltage sags. This is required in order to maintain power availability and improve system voltage stability. These requirements are defined in grid codes issued by grid operators [33]. For the wind generator to achieve this, the use of a crowbar circuit is required to protect the back-to-back converter during such an operation. This introduces two factors that must be considered for determining the short circuit behaviour of the Type 3 wind generator, namely the crowbar resistance and the LVRT characteristics.

The protection philosophy utilizes the LVRT characteristics. It provides the capacity to stay connected to the grid during faults (based on LVRT curve) without tripping of the unit breaker. The high rotor side current during the fault is limited by crowbar activation and reactive power can be supplied to the grid side during voltage dips for voltage restoration.

The LVRT curve is a voltage vs time characteristic indicating the different voltage requirements after the occurrence of a voltage sag. The LVRT scheme incorporates grid codes that define that wind turbines must continue to operate if their voltage profile remains above

the LVRT curve. The LVRT characteristic utilized in the test system simulation is shown in Figure 3.14 [97].

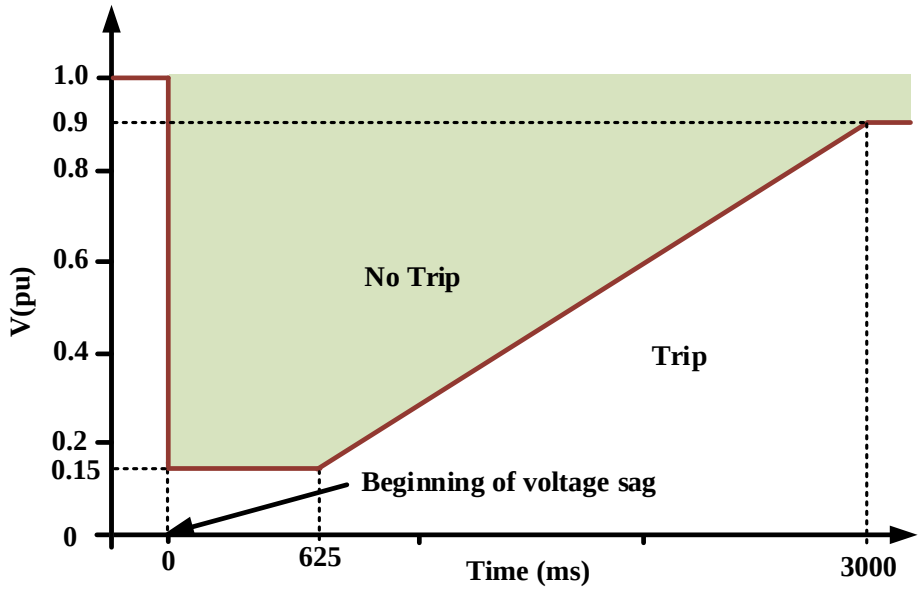

Figure 3.14: LVRT characteristics used in the test system

3.4.1 Conventional Crowbar Protection Scheme

Far away faults from the wind farm can lead to a voltage sag at the point of interconnection of the wind farm to the grid. Due to the occurrence of a fault or a voltage sag, the unit breaker trips if the voltage at the terminals of the generator becomes lower than the LVRT curve. During this period, the crowbar circuit is activated if the per-unit DC-link voltage becomes higher than the threshold value by providing the appropriate gating signals to the crowbar trigger circuit.

Meanwhile, the RSC is turned off to protect the back-to-back converter. The steps involved during the activation and deactivation of the crowbar system are: disconnection of the rotor windings from RSC, insertion of the three-phase resistance in series to the rotor windings, disconnection of the crowbar system from the rotor windings, and reconnection of

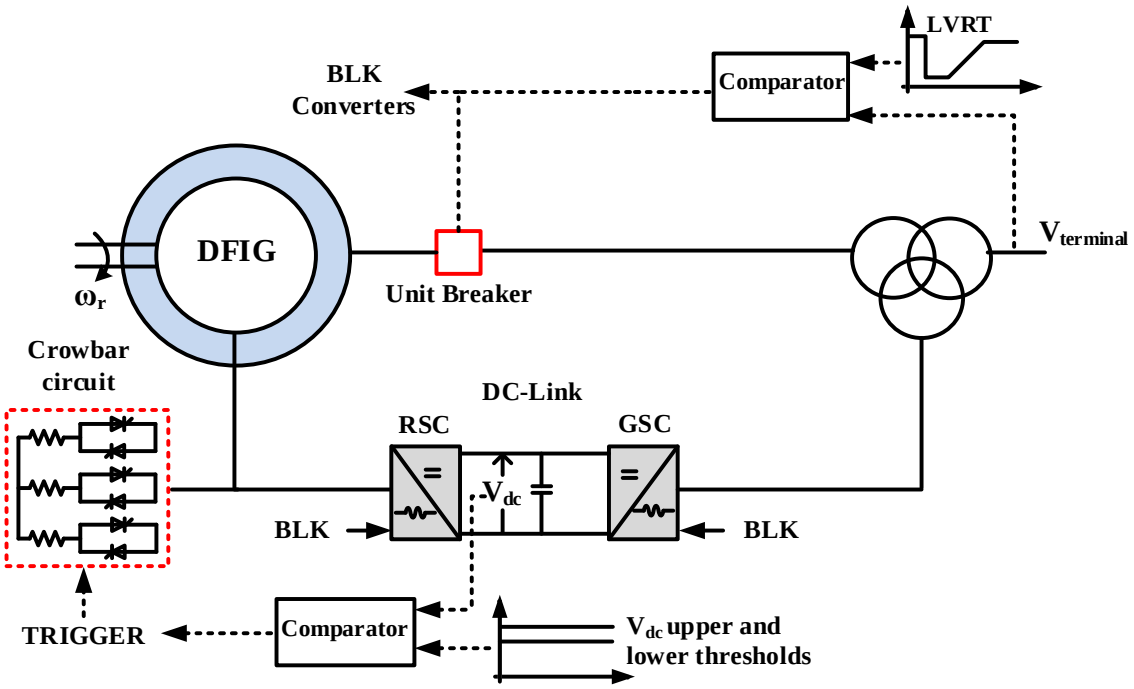

Figure 3.15: DFIG unit breaker protection based on LVRT Scheme, converter blocking and crowbar triggering

the RSC to the rotor windings. These actions will help to prevent the high rotor currents and excessive dc-link voltage. Amplitude of the resulting voltage in the rotor circuit is determined by the crowbar resistors. The crowbar resistor also acts as an active power sink, consuming active power to mitigate rotor over-speeding. During the time the crowbar is activated, the generator works as a conventional IG with high rotor resistance [98]. The value of the crowbar resistance affects the operation of the DFIG. High resistance values provide adequate damping to the fault transients when the crowbar is enabled but can create undesirable transients when the crowbar is turned off [99].

However, this method has nothing to do with the stator current which also has severe transients. The stator transients will cause fluctuation and affect the power system stability during fault situation.

3.4.2 DC Link Voltage Protection Scheme

The crowbar is a protective shunt resistor between the back to back RSC and GSC, in series with a switch as shown in Figure 3.16.

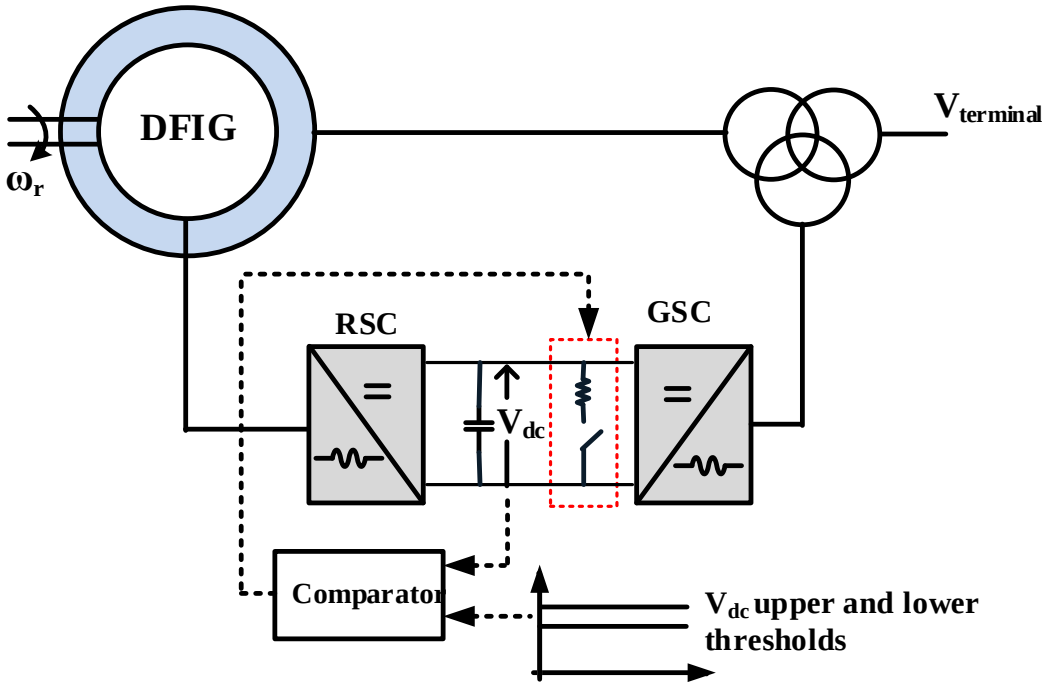

Figure 3.16: Converters with DC link shunt resistor

When the capacitor voltage rises beyond some threshold or the rotor currents exceed an upper limit, the switch is closed and the capacitor voltage is reduced. This excess current and voltage is usually due to external faults in the ac system.

The scheme for controlling the crowbar switch is shown in Figure 3.17. Capacitor voltage is compared to a trigger level, in this case 2.0 kV and latched in a flip flop when this is exceeded. When the voltage drops below 1.7 kV, the flip flop is reset and the crowbar is switched off as shown in Figure 3.18. This scheme is slightly superior than conventional crowbar scheme considering the issues of low component cost and better performance [100].

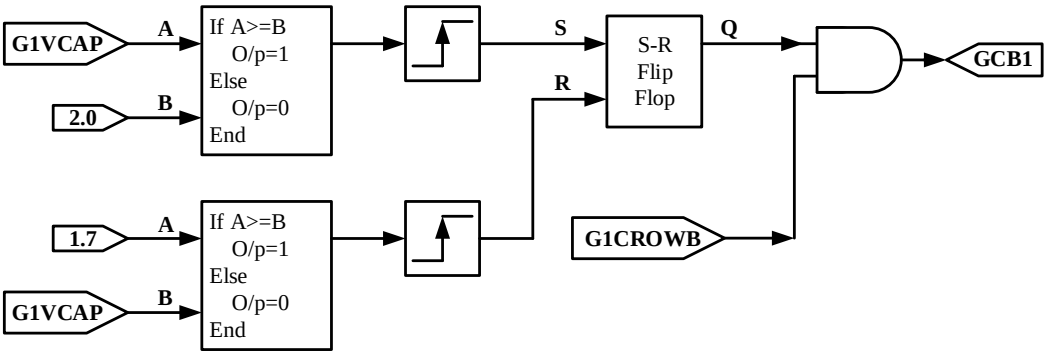

Figure 3.17: Crowbar control scheme

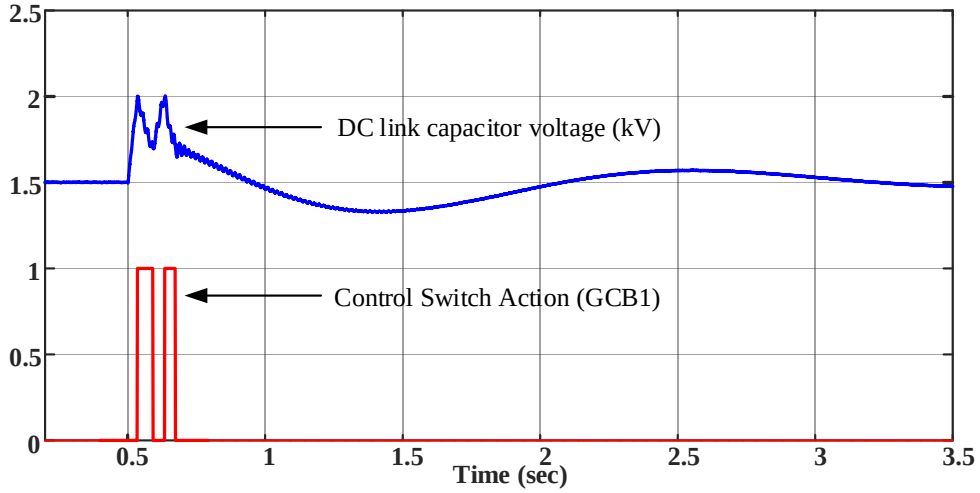

Figure 3.18: Crowbar switching action during an external fault

3.4.3 Series Dynamic Braking Resistor (SDBR) in Rotor Circuit

In this scheme, a series dynamic braking resistor (SDBR) is inserted in the rotor circuit as shown in Figure 3.19 [36]. The operation of the SDBR is incorporated with the dc-link protection scheme. In normal operation, the switch is ON and the resistor is bypassed, but the switch is OFF and the resistor is connected in series to the rotor circuit during fault condition.

The SDBR limits the rotor overcurrent. Moreover, with the SDBR, the high volt-

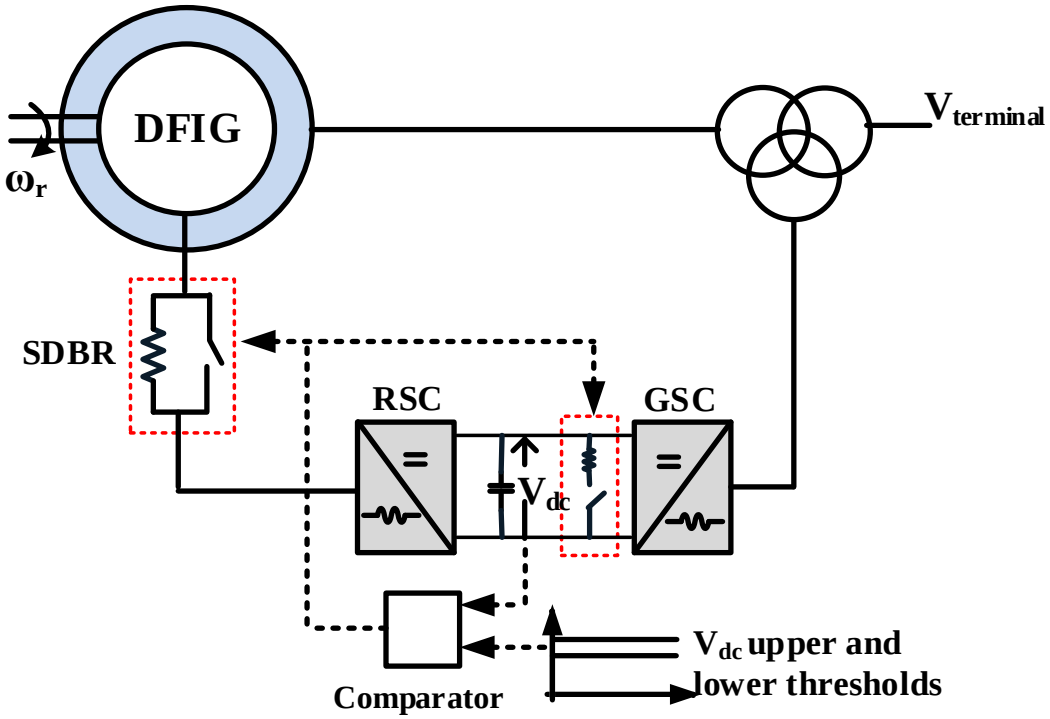

Figure 3.19: SDBR in Rotor Circuit with DC-Link Voltage Protection Scheme

age will be shared by the resistance because of the series topology; therefore, the induced overvoltage may not lead to the loss of converter control. Therefore, it not only controls the rotor overvoltage which could cause the RSC to lose control, but, more significantly, limits high rotor current.

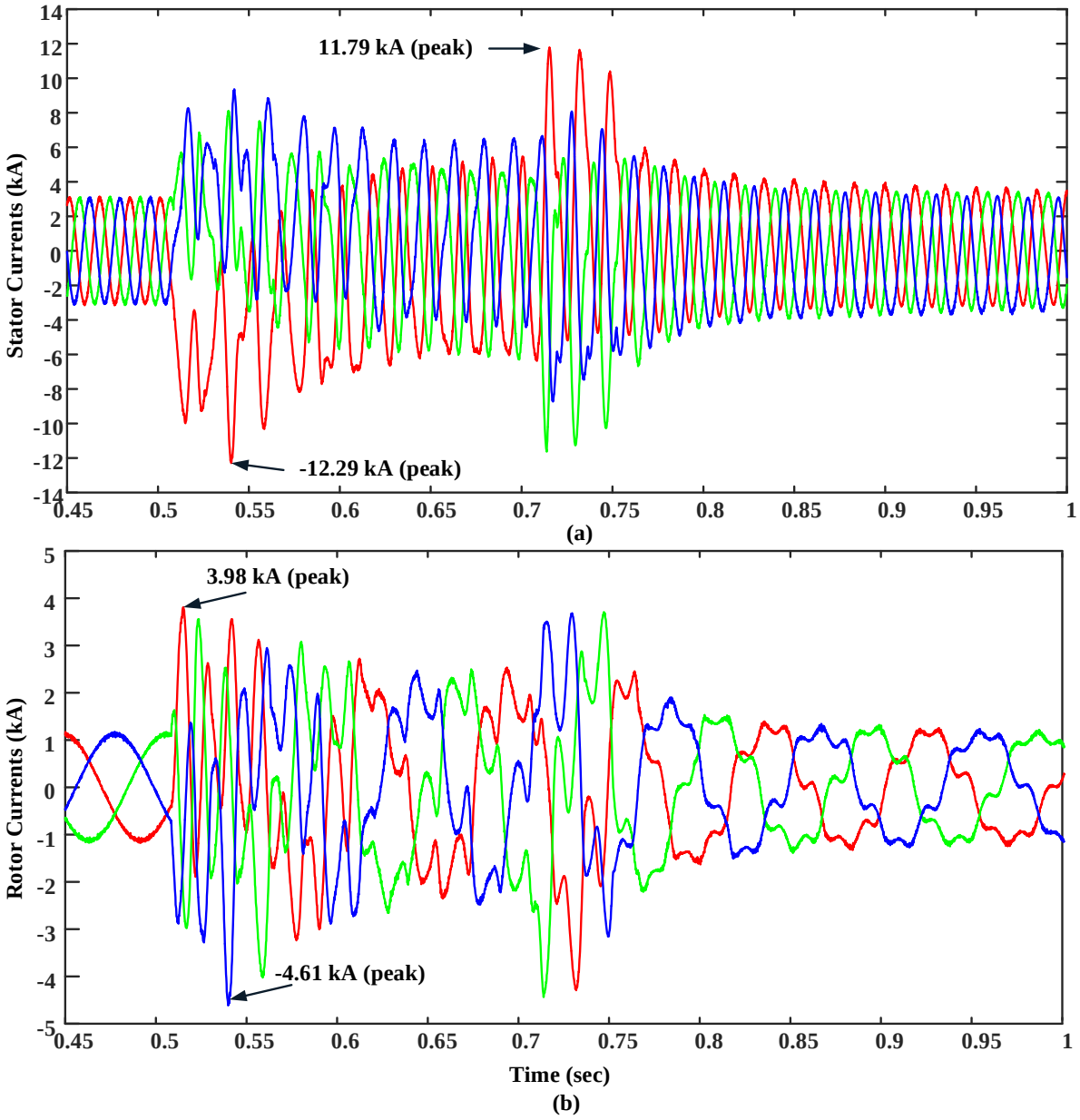

Figure 3.20: (a) Stator currents (b) Rotor currents with SDBR in rotor circuit

3.4.4 Series Dynamic Braking Resistor (SDBR) in Stator Circuit

A small size SBDR can be inserted in series with the stator circuit of the DFIG through the control of power electronic switches to balance the active power, which eventually improves the wind generator stability during a grid fault condition (Figure 3.21). Better re-

sponses of the terminal voltage and rotor speed of the DFIG can be achieved when the SDBR is connected at the stator during the grid fault instead of connecting in rotor [101].

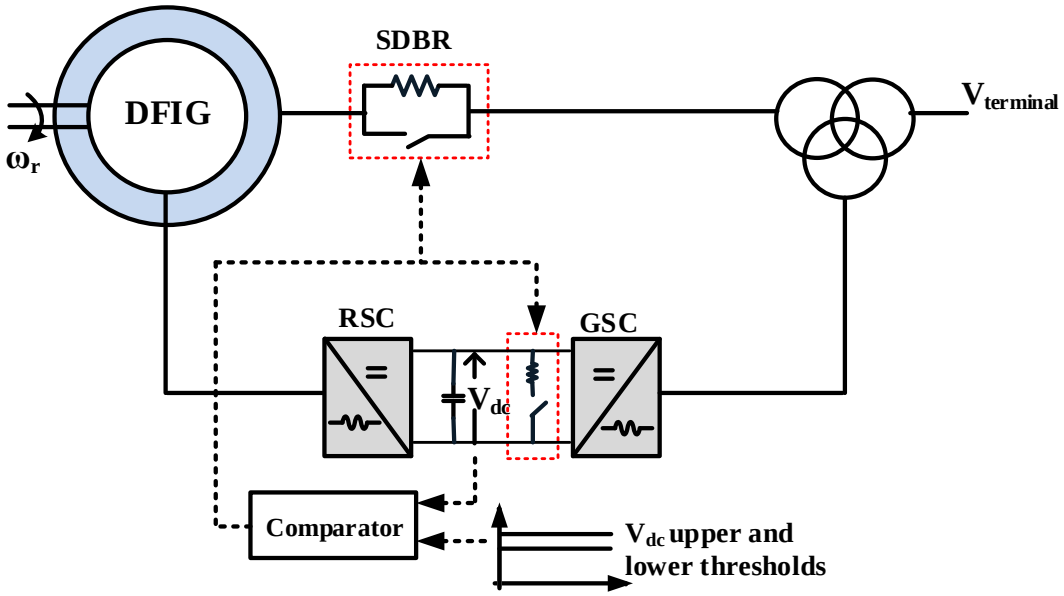

Figure 3.21: SDBR in Stator Circuit with DC-Link Voltage Protection Scheme

The SBDR can also balance the active power of the DFIG, and thus can also improve the DFIG wind generator stability during a fault [101]. The SDBR also increases the generator output and, therefore, reduces the speed increase during a voltage dip. This effect would improve the postfault recovery of the DFIG system and the entire wind farm, because the SDBR controls improves the rotor speed acceleration during a grid fault.

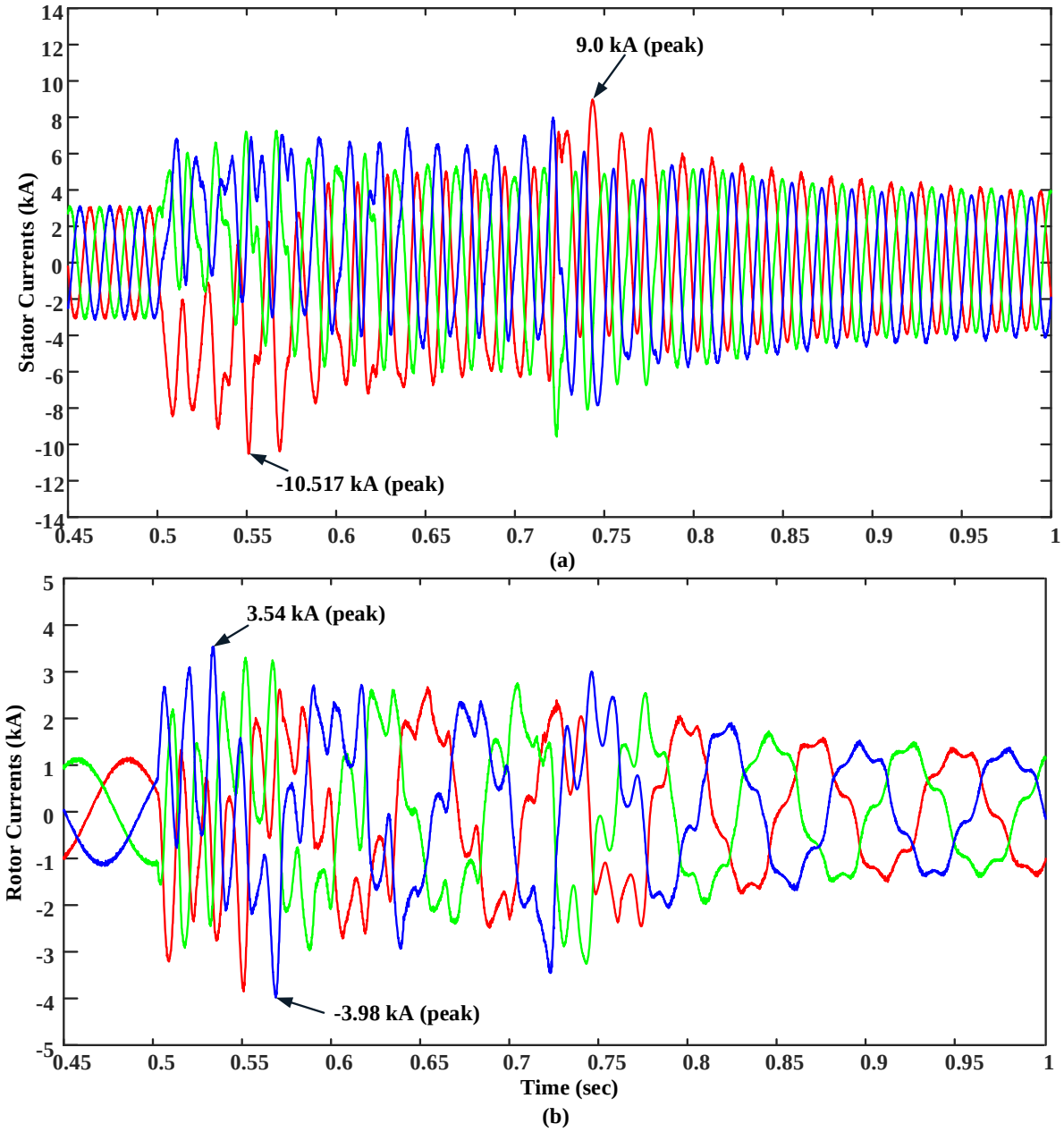

Figure 3.22: (a)Stator currents (b) Rotor currents with SDBR in stator circuit

3.5 Flux Decrement in Generator

During normal conditions, the flux linking the rotor is a constant but the flux linking the rotor will start decreasing as soon as the fault occurs. As a consequence, the internal voltage

is longer a constant and starts decreasing. Reference [30] discusses flux decrement effect in synchronous generators. Since there is no DC field supply in induction generators, neglecting the field DC supply E_{fd} in the synchronous generator equation gives an equation representing the flux decrement in induction generators. The following equation gives rate of change of voltage [30]

$$\frac{dE'_q}{dt} = -\frac{1}{T'_{d0}}(E'_q - (X_d - X'_d)I_d) \tag{3.42}$$

where, E'_q is the q-axis component of the voltage behind transient reactance, X'_d and T'_{d0} are open-circuit transient time constants. Figures 3.23, 3.24 and 3.25 shows 3 phase currents of a 3.4 MVA machine for a sustained 3 phase to ground fault.

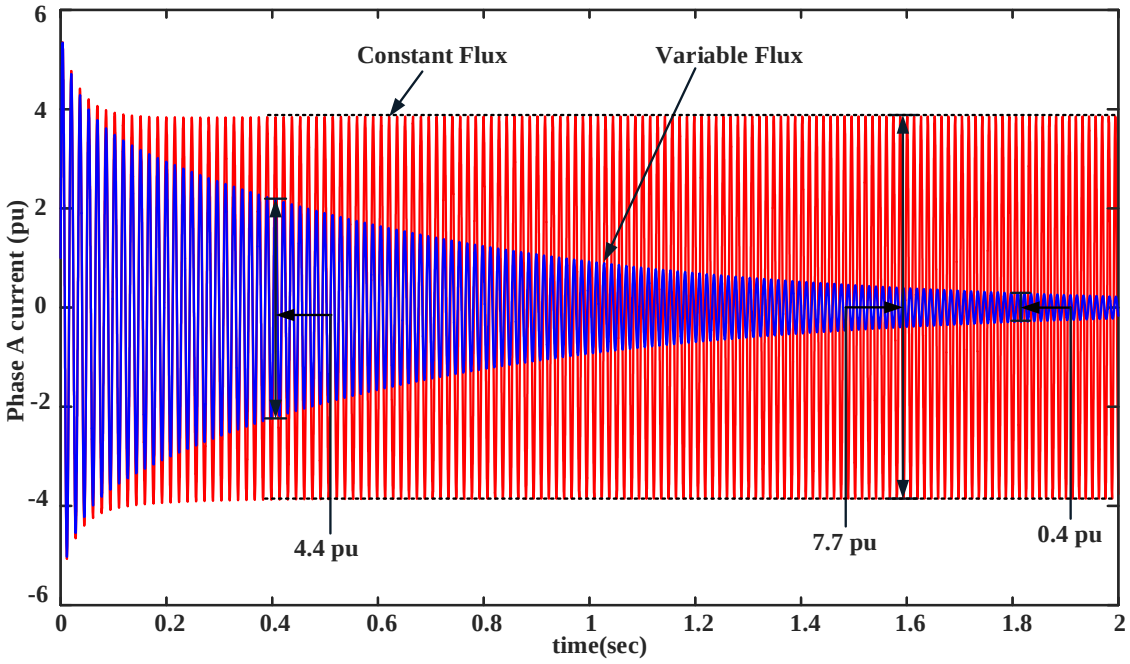

Figure 3.23: Comparison of A Phase current with constant and variable flux

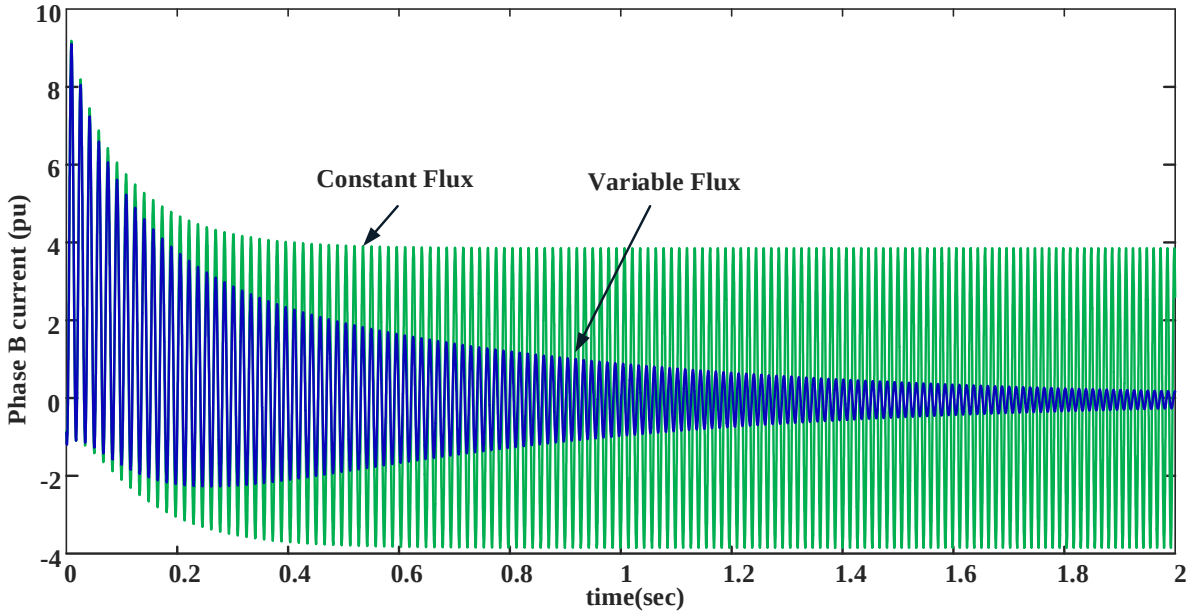

Figure 3.24: Comparison of B Phase current with constant and variable flux

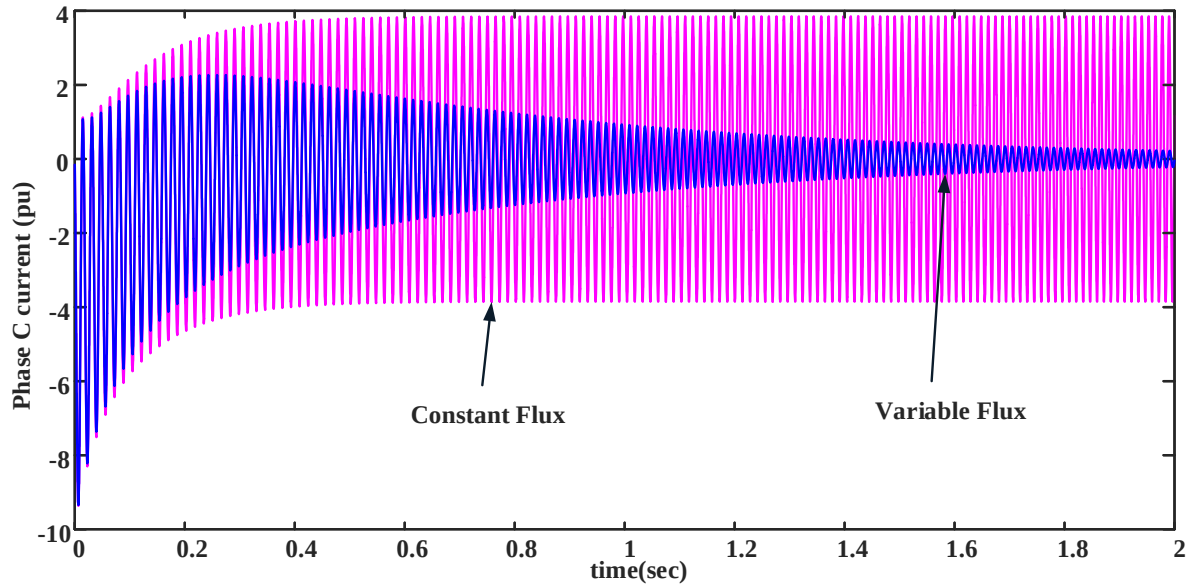

Figure 3.25: Comparison of C Phase current with constant and variable flux

When the flux is held constant, the fault current supplied remains constant after 0.4 sec. After 0.4 sec, the peak to peak fault current remains 7.7 pu with constant flux; whereas the

value is 4.4 pu at 0.4 sec and 0.6 pu at 1.8 sec with variable flux. It is clear that the fault current continues to decay and approaches zero while flux decrement is taken into account.

The flux decrement is implemented in all simulations included in this research work.

3.6 DFIG model validation results

Figure 3.26 shows the steady state real and reactive power of a DFIG system (figure 3.1) with rated wind speed of 14 m/sec. The input power from the turbine is 3 MW but the output power is not 3 MW due to internal losses. The steady state stator current is shown in figure 3.27.

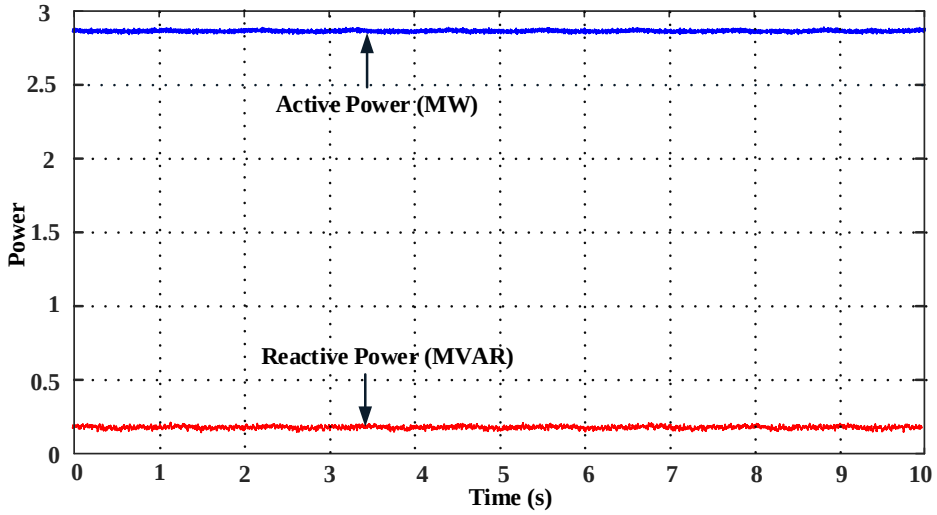

Figure 3.26: Steady state Real and Reactive Power

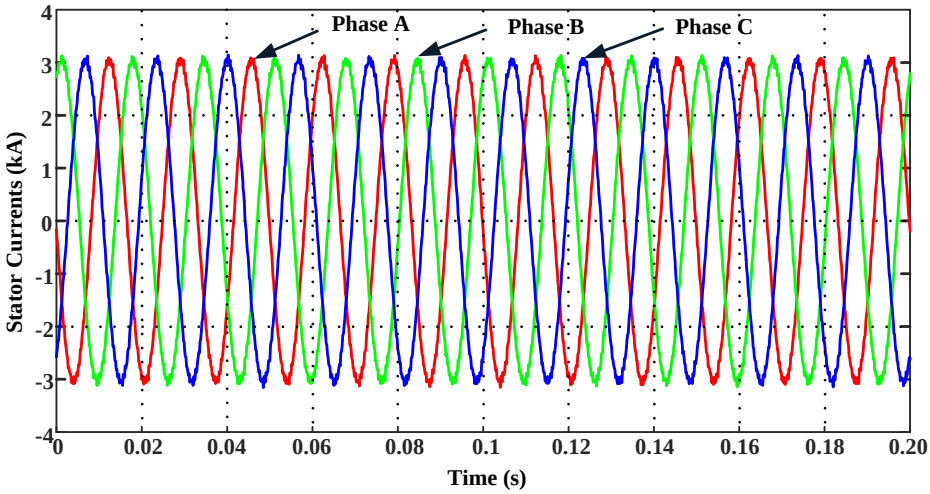

Figure 3.27: Steady state Stator currents

Figure 3.28 shows the response of a DFIG sytem's active power and pitch angle to a step change in wind speed from 12 m/sec to 16 m/sec. For wind speed less than 14 m/sec, the pitch angle is set to zero. For wind speeds greater than 14 m/ sec, the pitch control is activated.

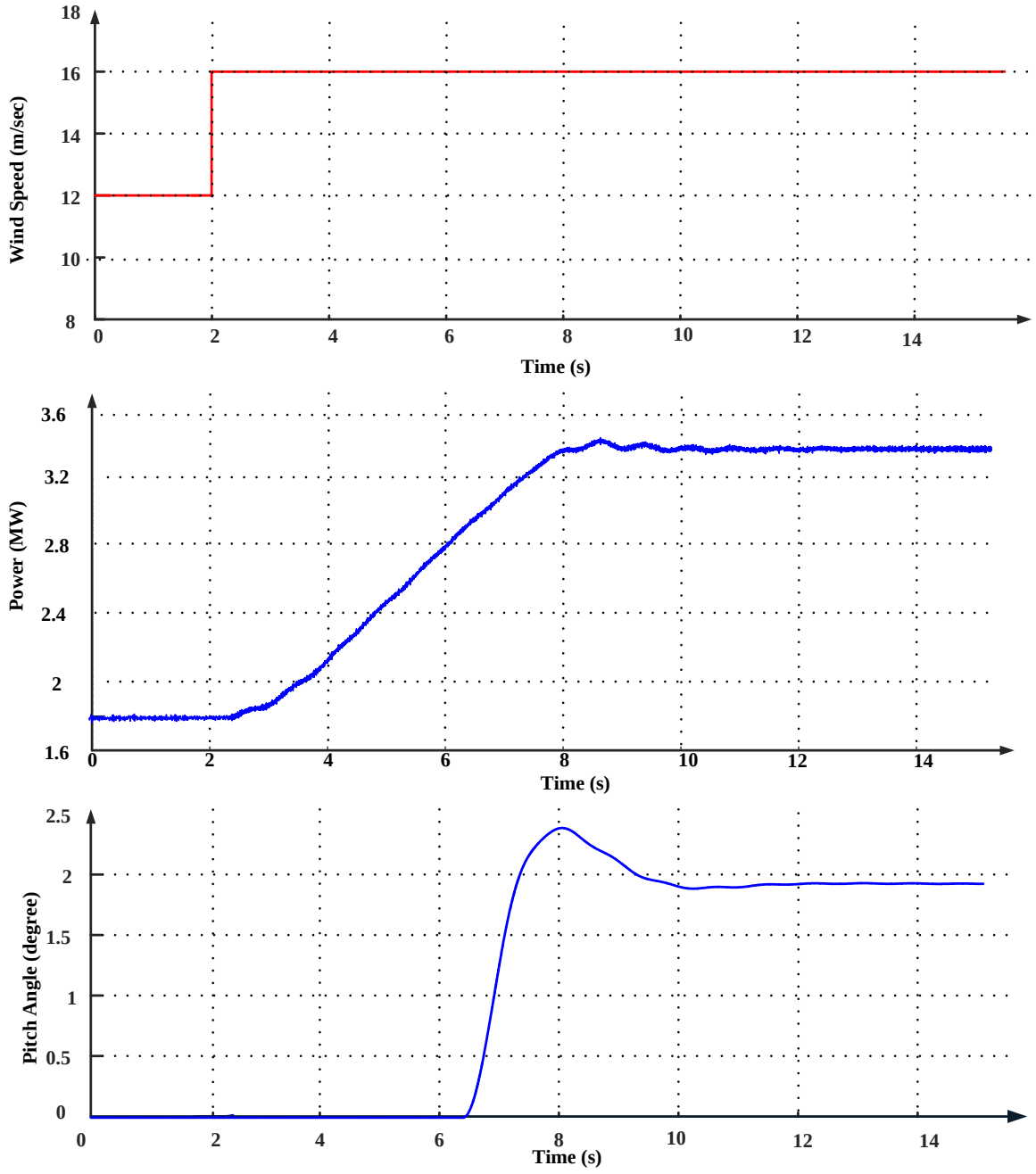

Figure 3.28: Response of Active Power and Pitch Angle to change in wind speed

Symmetrical fault application

The symmetrical (three phase to ground) fault is applied to the test system at the point of interconnection (POI) of the wind farm to the grid for 200 ms. POI is the node at which

metering for the wind farm is installed and is on the high voltage side of the main transformer at the substation.

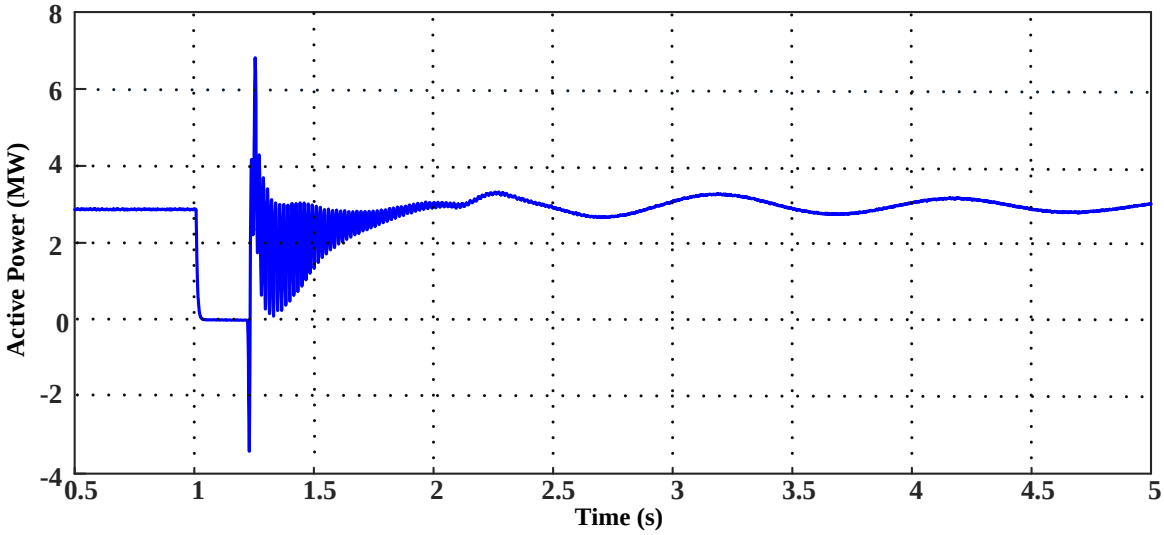

Figure 3.29: Active Power variation for symmetrical fault

Figure 3.29 shows the real power variation for a symmetrical fault. The fault is applied at 1 sec for 200ms. The real power supplied is zero during fault period and again tries to go back to original value with subsequent oscillations. The stator current is shown in figure 3.30.

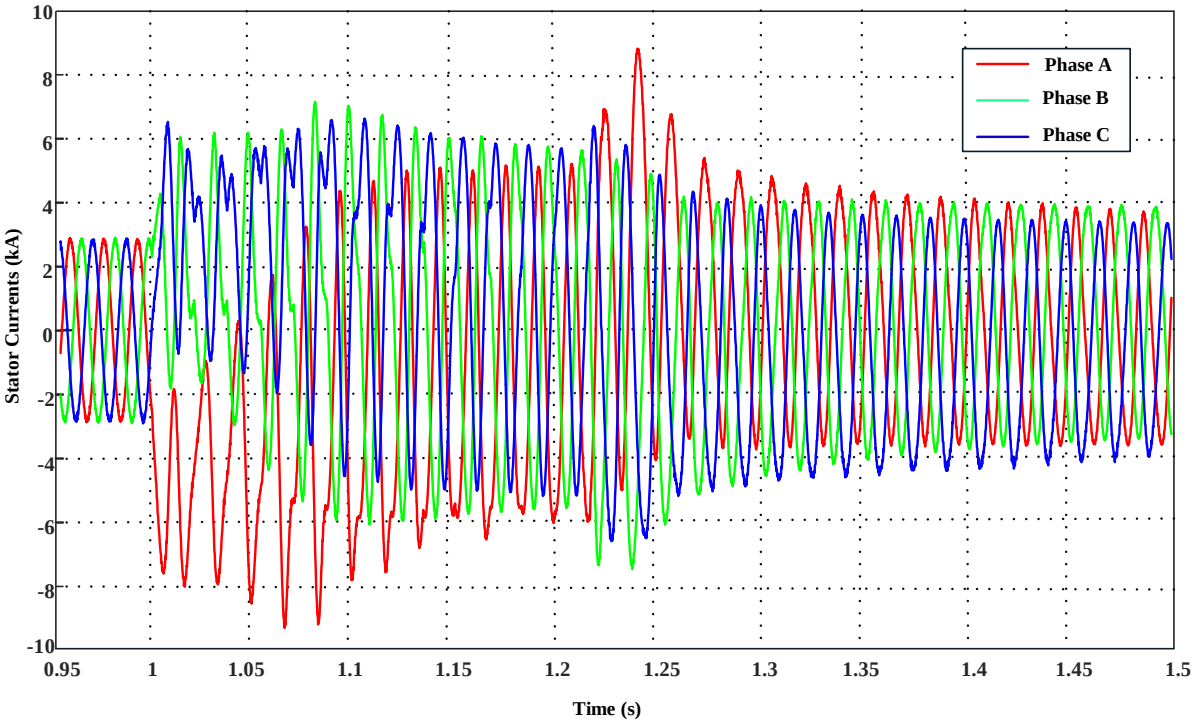

Figure 3.30: DFIG stator current variation for symmetrical fault

Unsymmetrical fault application

The unsymmetrical (single phase to ground) fault is applied to the test system at the point of interconnection (POI) of the wind farm to the grid for 200 ms. Unlike a symmetrical fault, the active power falls to zero for a fraction of the fault period as shown in Figure 3.31. Figure 3.32 shows the stator current behaviour for an unsymmetrical fault.

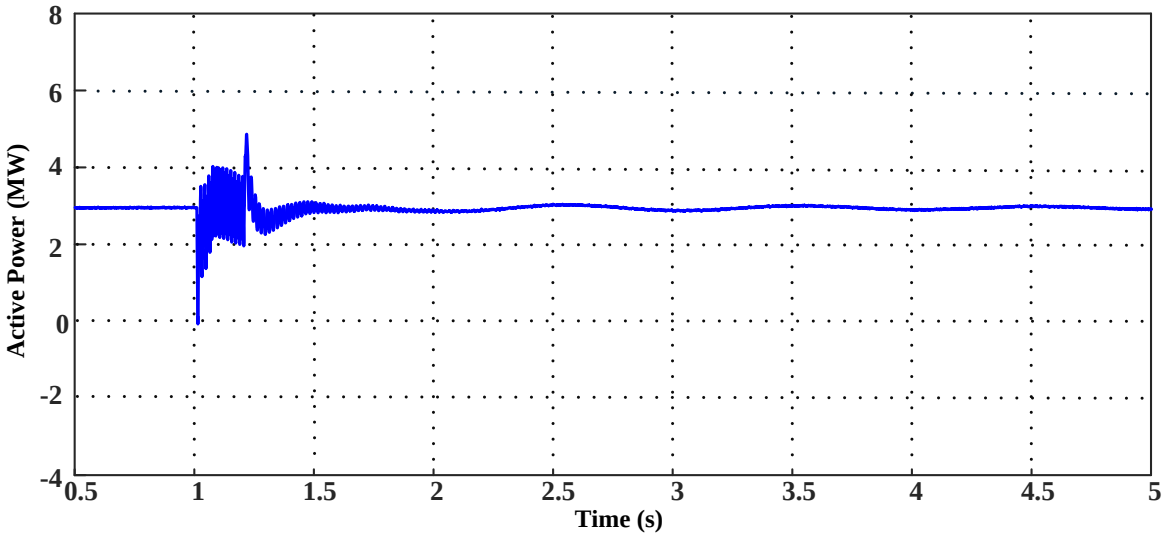

Figure 3.31: Active power variation for unsymmetrical fault

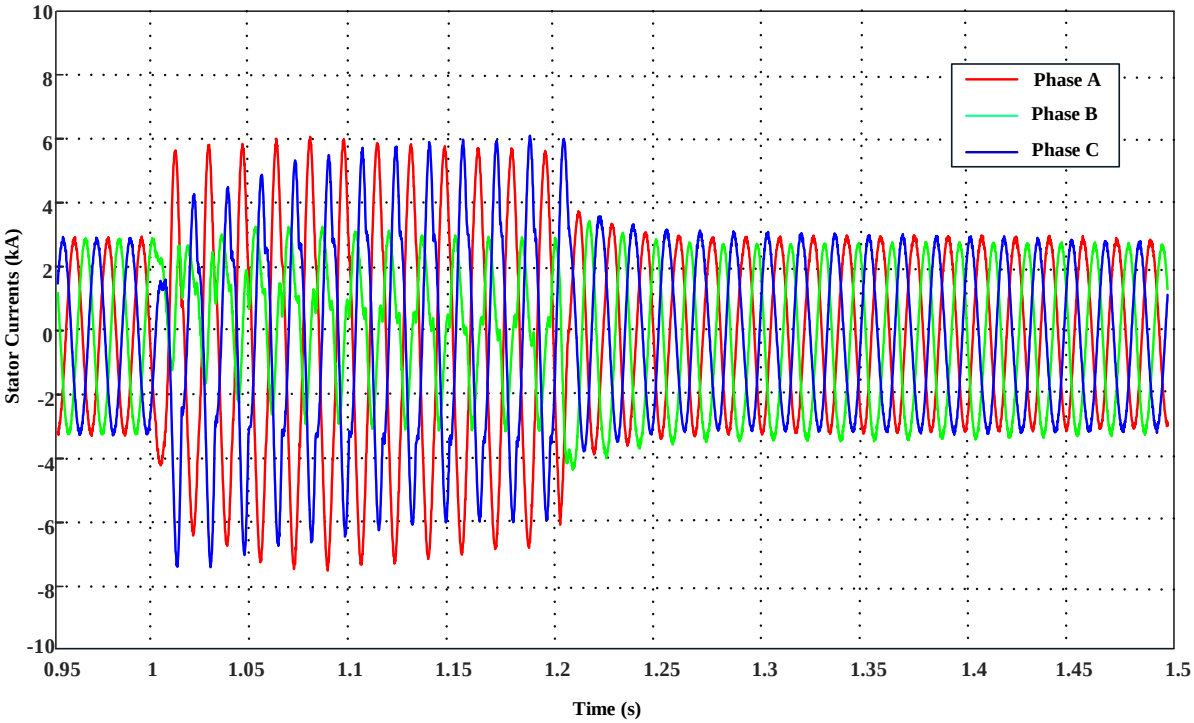

Figure 3.32: DFIG stator current variation for unsymmetrical fault

3.7 Summary

A detailed EMT model of a DFIG wind power plant was presented in this chapter. The wind power plant model included the mechanical drive train, pitch controller, generator, and rotor and grid side converter controller models. A three mass model was used for the mechanical drive train. The steady state and transient responses of the DFIG were also shown.

Different LVRT schemes were discussed and compared. When SDBR is placed in a rotor circuit, the instantaneous peak stator current is -12.29 kA and the instantaneous peak rotor current circuit is -4.61 kA. However, when the SDBR is placed in a stator circuit, the instantaneous peak stator current is -10.517 kA and the instantaneous peak rotor current circuit is -3.98 kA. Thus, SDBR in a stator circuit better controls both the stator and rotor currents. Because SDBR in a stator circuit dissipates active power, it reduces the mismatch between the mechanical input and active power output of the DFIG during a fault. Thus, it can also improve the DFIG wind generator stability during a fault.

This chapter also showed that the flux decrement in a generator is an important aspect to include in modelling. The results with constant flux as well as variable flux were presented, and current was shown to decay with variable flux. Thus, flux decrement effects must be incorporated for accurate modelling of the induction generator.

The next chapter describes the small signal analysis of a DFIG wind power plant transmitting power via a series compensated line. A detailed linearized model of the wind power plant is derived and an eigen value analysis is carried out to identify the participating states in sub-synchronous oscillations.

Chapter 4

Small Signal Analysis of DFIG Wind Power Plant

4.1 Introduction

In this chapter, small signal analysis is carried out for DFIG based wind farms connected to series compensated transmission lines. Small signal analysis aids in finding the participating states in sub-synchronous oscillations. A scenario is created using the model developed in RTDS, where sub-synchronous oscillations occur in a DFIG wind farm connected to a series compensated transmission line. The event is created by applying symmetrical and unsymmetrical faults at the point of interconnection. A frequency analysis of the fault current is done with the sub-synchronous component present.

A detailed linearized model of the same DFIG wind farm is developed for small signal analysis in MATLAB. A linearized model of the three mass model of the generator and turbine is utilized in the studies in order to determine whether sub-synchronous oscillations arise due to torsional interactions of the wind turbine and generator. Small signal analysis in this chapter includes eigenvalue analysis, participation factor analysis and sensitivity studies.

4.2 Sub-synchronous Oscillations in Wind Plants

Wind farms are located in wind-rich locations that are often far away from load centers. This wind farms from these locations have to be connected to load centers through long transmission. These lines are series compensated to improve their power transfer ca-

pability. Series capacitors introduce the risk of sub-synchronous resonance (SSR) [102] and sub-synchronous control interactions (SSCI) [10,103] in power systems. Sub-synchronous resonance is a condition where the series compensated electrical network exchanges energy with the generator turbine shaft system at sub-synchronous frequencies of the system [104–106].

Torsional Interaction:

The torsional interaction occurs when the natural mechanical torsional modes of oscillation of the generator turbine system and the electrical network resonant frequency coincide. This leads to a high level of energy exchange between the network and the generator turbine, resulting in sustained or fast growing oscillations that can eventually lead to damage to turbine shaft.

Induction Generator Effect:

The other cause for the occurrence of SSR is the induction generator effect. The induction generator effect occurs due to self-excitation, when the total resistance of the series resonant circuit (generator and series compensated transmission line) is negative at sub-synchronous frequencies creating negative damping. It makes the current and voltage oscillations to grow and eventually lead to excessive currents and voltages.

Sub-Synchronous Control Interactions:

SSCI is a phenomenon in which the wind turbine controllers have been observed to interact with the series compensated transmission line. Specifically, it is the control interaction between the power electronic control system and the series compensated transmission line. SSCI has no fixed frequency of concern, as the frequency of oscillations is based on the configuration of the controls and electrical system. The SSCI phenomenon is mainly observed in DFIG generators connected to series compensated transmission lines due to the controllers of the back-to-back converter being connected between the rotor of the generator and the grid.

Such an interaction phenomena for a DFIG wind farm has been studied in [10] which also identifies the control loops in the RSC that are responsible for the sub-synchronous

interactions. This indicates how the SSCI phenomena can be attributed to the interaction between the series compensated network and the power electronic converter of the DFIG generator. In order to study such a phenomena, the system shown in Figure 4.1 is modelled.

4.3 Test System Simulation and Analysis

Figure 4.1 shows the system developed in RTDS in which a DFIG wind farm is connected to a series compensated transmission line, where R_L and X_L represent the transmission line resistance and inductive reactance, respectively. X_C represents reactance of the series capacitor compensation. The series capacitor has a bypass switch that can be opened in order to include the series compensation in the line. The wind farm is represented by a single equivalent machine. The generator can be seen as a controllable impedance, the impedance of which depends upon settings of the controller.

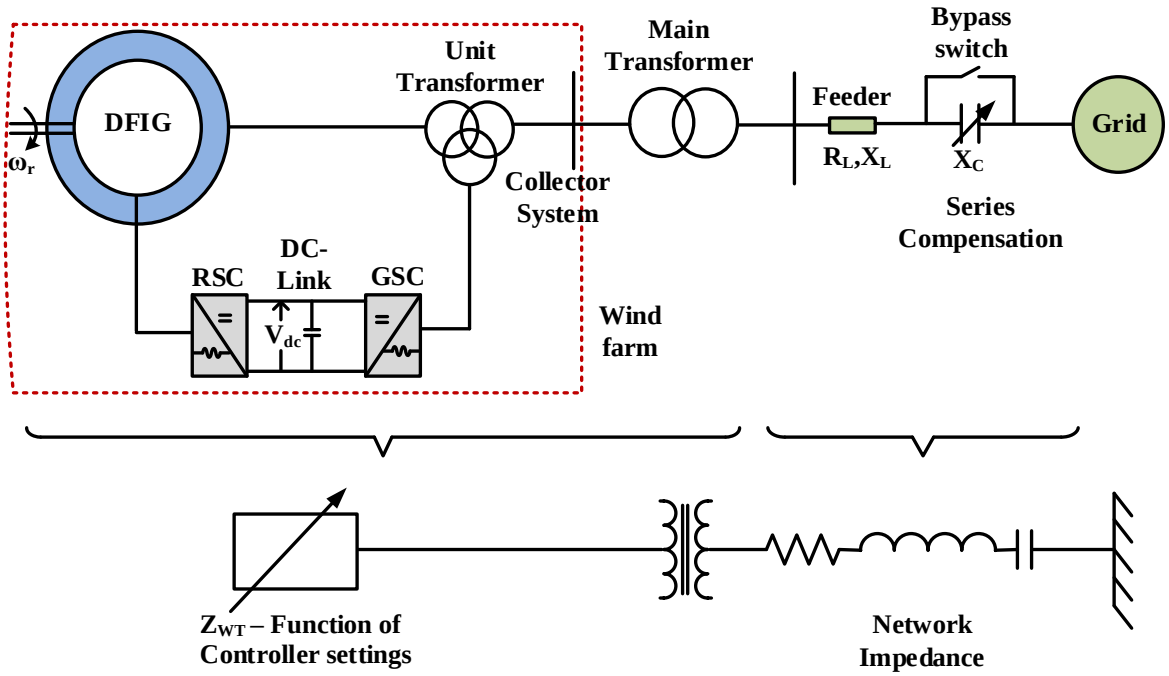

Figure 4.1: DFIG wind generator test system with series compensation

It is important that the fault contribution is found not only from a single generator

but from entire wind farm. A wind farm consists of several wind generator-transformer units that are connected to the main sub-station transformer through cables running from each unit. These cables form the collector circuit of the wind farm. This means that the fault calculations now must take into account the collector circuit impedances as well.

However, the fault contribution from a wind farm can be accurately calculated without taking the collector impedances into account and the equivalencing of a wind farm can be made simple yet accurate by ignoring all cable impedances [22, 85]. The difference in the total impedance of the wind farm with and without the cable was found to be less than 3 percent [85].

The research work in this thesis uses an aggregate model of the DFIG wind farm to study its short circuit behaviour. The collective behaviour of a group of wind turbines is represented by a lumped machine. This assumption is supported by several recent studies that suggest that wind farm aggregation provides a reasonable approximation for system interconnection studies [103]. The test system modeled consists of 150 generators, each of 3 MW capacity. It is assumed that all machines in the wind farm are working coherently and all see the same wind speed, which permits the generators to be lumped into one large equivalent machine. The parameters are given in Appendix A.3.

4.3.1 Application of Symmetrical Fault

Two different scenarios are studied with 50% and 70% series compensation of the transmission line. The series compensation is introduced on the transmission line by using the bypass switch of the series capacitor shown in figure 4.1. A 200 ms three phase fault is applied 7.0 s after the start of the simulation at the point of interconnection of the wind farm to the grid. The Phase A stator fault current measured is shown in Figure 4.2 with 50% compensation. A buildup of sub-synchronous oscillations can be observed in the waveforms of fault current.

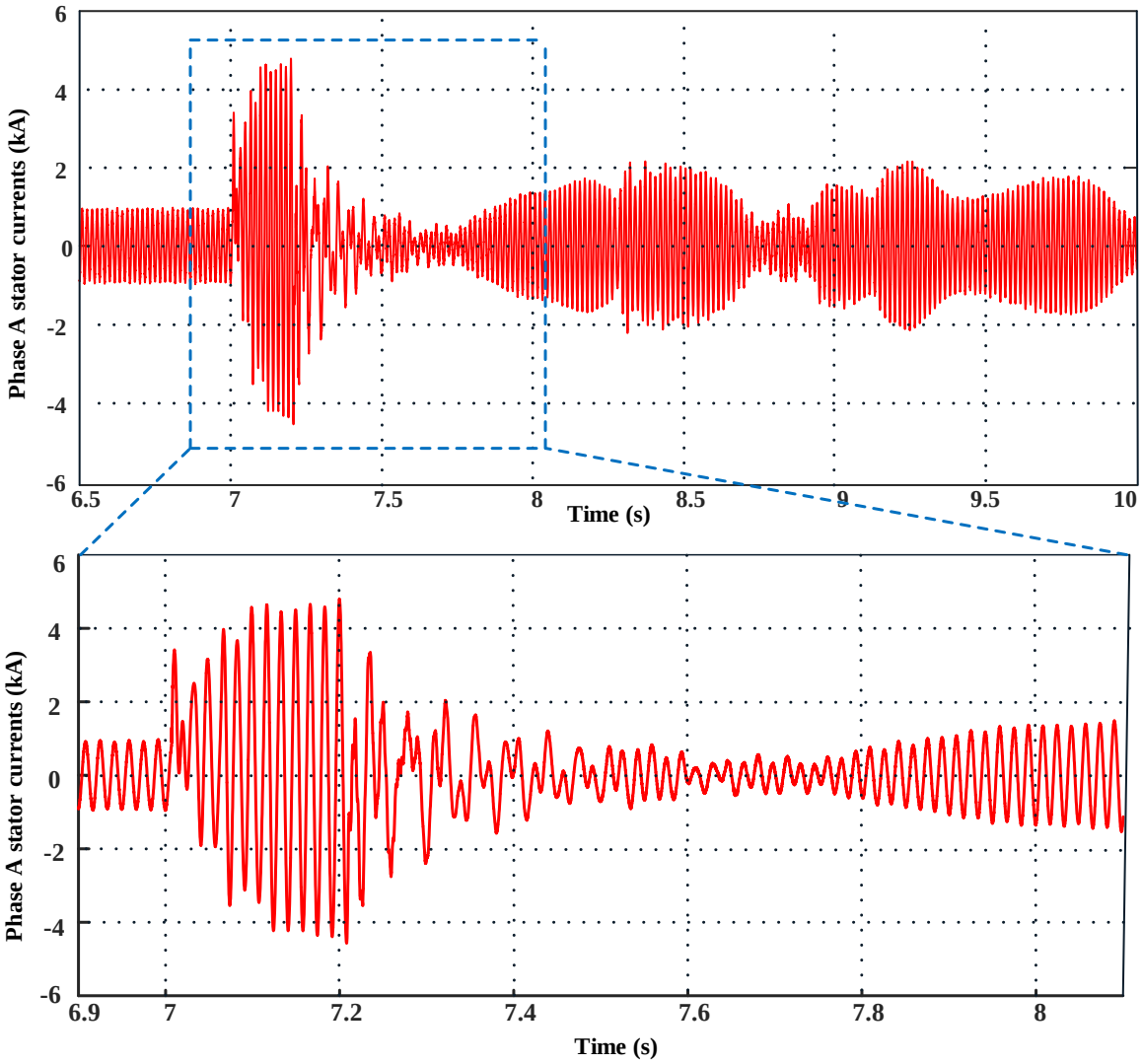

Figure 4.2: Type 3 wind farm symmetrical fault current with sub-synchronous frequency components (50% compensation)

Figure 4.3 compares the phase A stator currents obtained from a straightforward three-phase-fault and a three-phase-fault with the SSCI present. The magnitude of the fault current is significantly affected by the SSCI. This again confirms that models that are only able to represent the fundamental frequency components will be inaccurate for determining such complex fault behaviour.

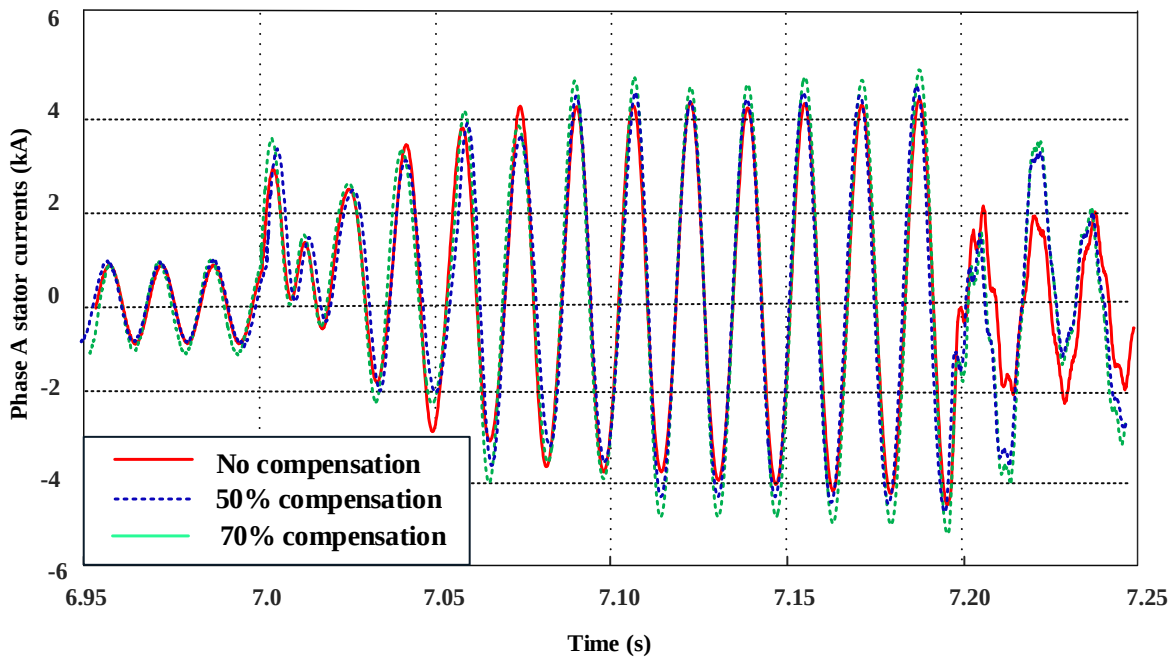

Figure 4.3: Comparison of stator fault current without and with compensation for a three phase fault

The stator current waveform is scanned using FFT to determine the relative magnitude of the sub-synchronous frequency component as compared to the fundamental frequency component. Figures 4.4 and 4.5 show the relative magnitudes of the harmonic components of the phase A stator fault current waveform (base frequency of 6 Hz is used for FFT) for 50% and 70 % compensation respectively. The dominant frequency components are the fundamental frequency component ($60Hz$) and the sub-harmonic frequency component : $\sim 36Hz$ in case of 50% compensation and $\sim 42Hz$ in case of 70 % compensation of transmission line.

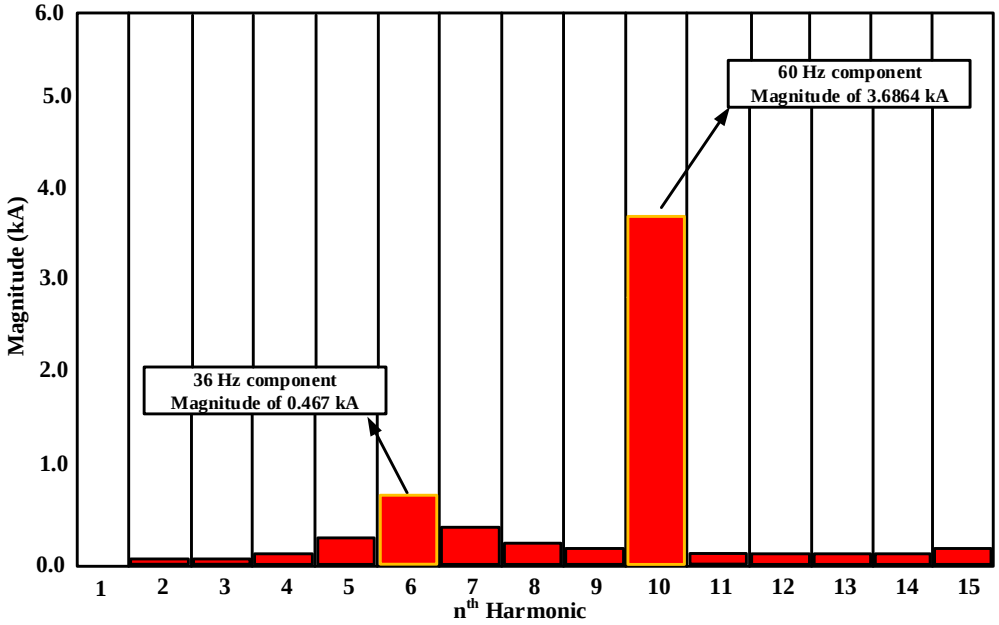

Figure 4.4: FFT analysis of phase A symmetrical fault current with 50% compensation

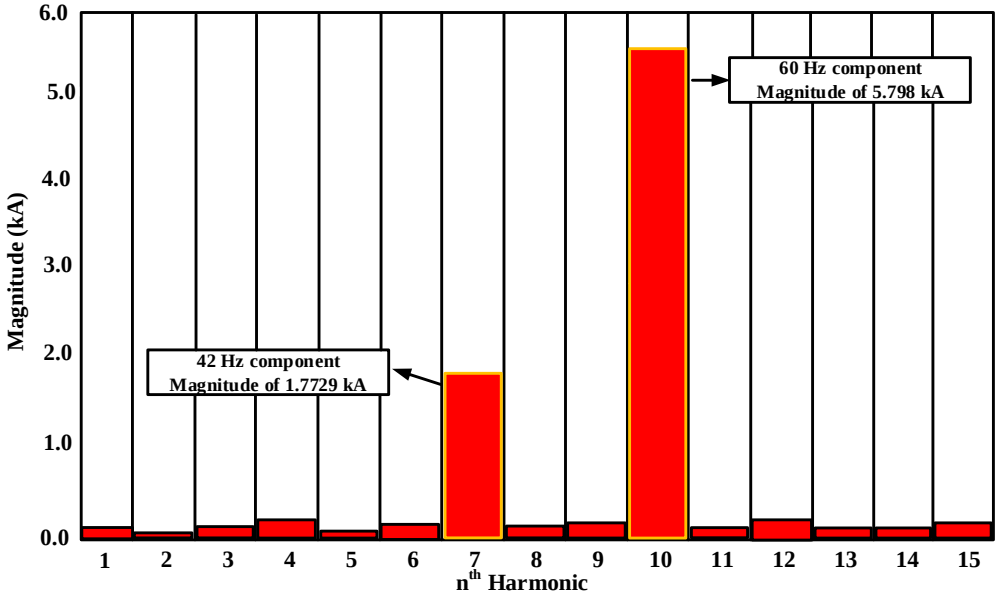

Figure 4.5: FFT analysis of phase A symmetrical fault current with 70% compensation

Following this, a Prony analysis of the waveform of the stator current is done. The

results of the Prony analysis in Figure 4.6 show that, apart from the fundamental frequency component, a sub-synchronous component of approximately 36.2 Hz is also present in the current waveform for 50% compensation. Tables 4.1 and 4.2 show the relative magnitudes of the most dominant frequency components in both scenario. These results correspond with the FFT analysis done before.

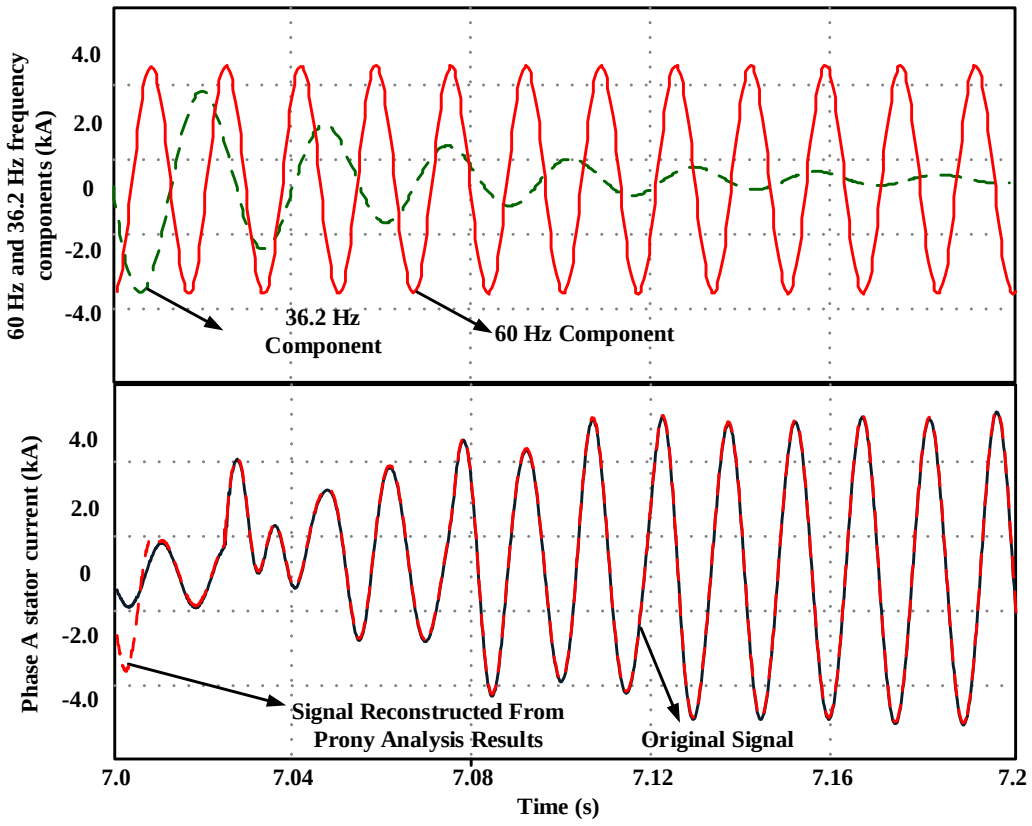

Figure 4.6: Prony analysis of phase A symmetrical fault current with 50% compensation

Table 4.1: Prony analysis of phase A symmetrical fault current with 50% compensation

Magnitude (kA)	**Phase (deg)**	**Frequency (Hz)**	**Damping (%)**
3.6864	11.692	60.0	-0.011
0.467	83.306	36.2 ($\sim 36Hz$)	19.25

Table 4.2: Prony analysis of phase A symmetrical fault current with 70% compensation

Magnitude (kA)	Phase (deg)	Frequency (Hz)	Damping (%)
5.798	74.917	60.0	-1.657
1.7729	29.332	41.977 ($\sim 42Hz$)	1.629

4.3.2 Application of Unsymmetrical Fault

Unsymmetrical fault (phase A to ground fault) behaviour was studied in a manner similar to symmetrical fault behaviour as discussed in the previous section. Following the insertion of the series compensation of 53.4 μF (50% compensation) and 37.9 μF (70% compensation), a 200 ms phase A to ground fault was applied and the fault current behaviour was analyzed. Figure 4.7 shows the comparison of phase A fault currents for a phase A to ground fault applied with and without the insertion of the series compensation. The figure shows that SSCI has a significant impact on the magnitude of the fault currents obtained.

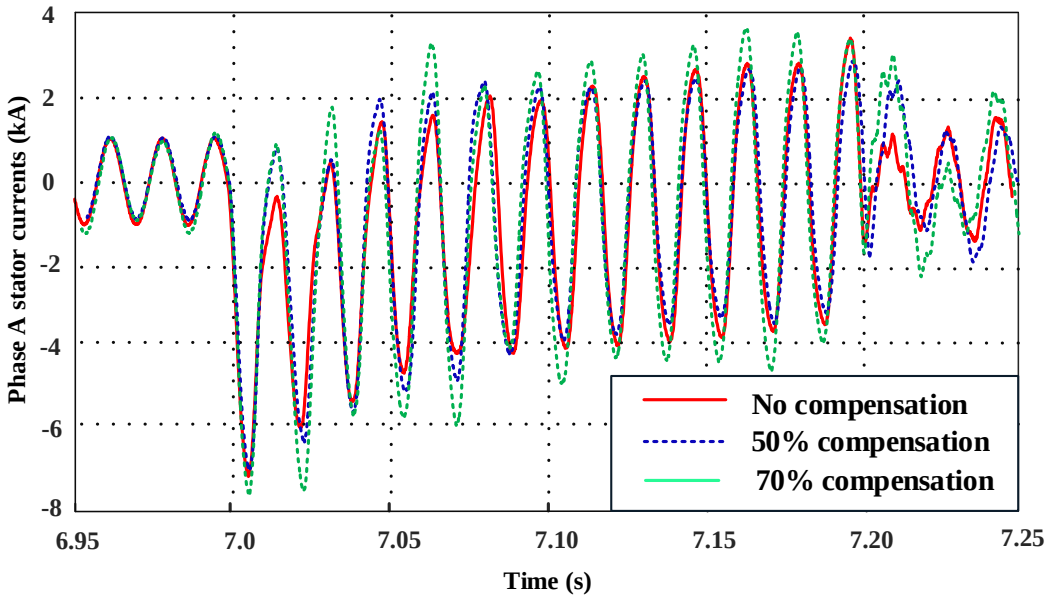

Figure 4.7: Comparison of phase A stator fault current without and with series compensation for a phase A to ground fault

For the unsymmetrical fault scenario, the fault current waveform was again analyzed with FFT and Prony analysis. The fault current's dominant frequency components were the fundamental frequency and the 36.2 Hz and 42 Hz sub-synchronous frequency components due to the occurrence of SSCI.

4.4 Frequency Scanning

In frequency scanning, the presence of a network resonance is identified by calculating the driving point impedance over the entire sub-synchronous frequency spectrum. This means determining the magnitude and phase angle of the driving point impedance. The magnitude and the phase angle values obtained from the frequency scan are plotted as a function of the scanning frequency. From this plot, the network resonant frequency at which sub-synchronous interactions could occur can be determined. This is the frequency at which there is a change in sign of the phase and a dip in the impedance magnitude. This corresponds to a series network resonance seen by the wind farm [48].

From the Prony analysis in the previous section, the most dominant frequency component observed following the fundamental frequency component was the sub-synchronous component of 36.2 Hz for a 50% compensation and 42 Hz for a 70% compensation. Figure 4.8 shows the results of the frequency scanning for three different percentages of series capacitor compensation. At each compensation level, the sub-synchronous component is found by determining the point where there is a dip in the impedance magnitude and a corresponding change of sign of the phase angle. For example, for 70% compensation, there is a dip in the impedance magnitude and a corresponding change of sign of the phase angle at 42 Hz. This re-establishes the insertion of the series compensation as the reason behind the occurrence of the sub-synchronous component in the current waveform.

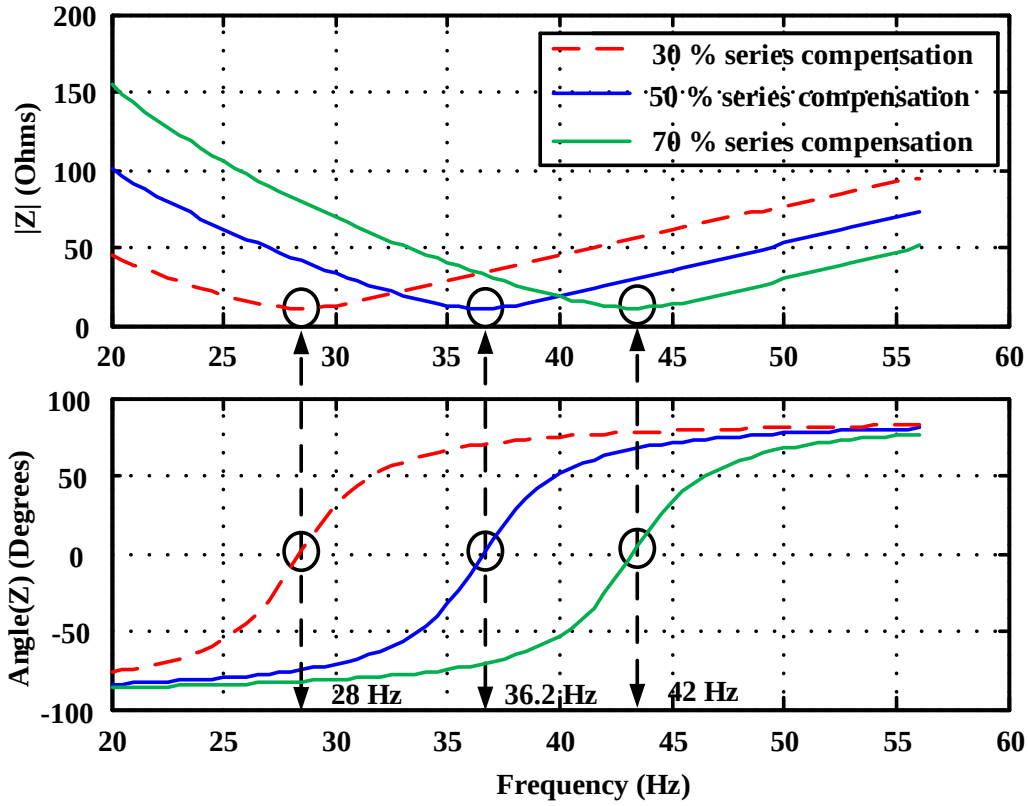

Figure 4.8: Frequency Scanning - magnitude and phase angle plot of network driving point impedance

4.5 Small Signal Analysis

Small signal stability is defined in the texts as the ability of the power system to maintain synchronism when subjected to small disturbances [102]. The disturbance is regarded as small if the equations describing the system response can be linearized for the purpose of analysis. The dynamic behaviour of a system may be expressed as a set of nonlinear differential equations as shown in Equation 4.1

$$\dot{x} = h(x, u) \tag{4.1}$$

$$y = g(x, u) \tag{4.2}$$

When linearizing a nonlinear system for small signal stability, the nonlinear equations are linearized around a specific operating point. The resulting set of linear differential equations describes the dynamic behaviour of the power system subject to a small disturbance around this operating point. In power systems, this specific operating point is the steady state operating point. For a small perturbation around the steady state point, the states and inputs will become,

$$x = x_0 + \Delta x \tag{4.3}$$

$$u = u_0 + \Delta u \tag{4.4}$$

Then, Equation 4.1 can be written as,

$$\dot{x_0} + \dot{\Delta x} = h(x_0 + \Delta x, u_0 + \Delta u) \tag{4.5}$$

$$y_0 + \Delta y = g(x_0 + \Delta x, u_0 + \Delta u) \tag{4.6}$$

Since the derivatives at steady state point are zero, the linearized equation can be written in the form,

$$\dot{\Delta x} = A\Delta x + B\Delta u \tag{4.7}$$

$$\Delta y = C\Delta x + D\Delta u \tag{4.8}$$

where, A, B, C and D are known as state or plant matrix, input or control matrix, output matrix and feed forward matrix, respectively.

4.5.1 Stability of Linearized Systems

4.5.1.1 Eigenvalue

The linearized state space model of a dynamic system is :

$$\dot{\Delta x} = A\Delta x + B\Delta u \tag{4.9}$$

The eigenvalues of the system matrix A are obtained by solving following equation:

$$det(A - \lambda I) = 0 \tag{4.10}$$

If the system has n state variables, equation 4.10 has n solutions $\lambda_1, \lambda_2, ..., \lambda_n$. These solutions are the eigenvalues of the system.
The stability criterion is [102]: if one of the eigenvalues have a negative real part – the system is stable; if at least one of the eigenvalues has a positive real part – the system is unstable; if the eigenvalues have real parts equal to zero, the system has an oscillatory response.

4.5.1.2 Modes

The state space model of the system with zero input is as:

$$\dot{\Delta x} = A\Delta x \tag{4.11}$$

The rate of change of change of each state variable is a linear combination of all the state variables. These cross couplings of the state variables can be eliminated by using the transformation given by,

$$\Delta x = \phi Z \tag{4.12}$$

where, ϕ is the right eigenvector matrix of system matrix A.
After the transformation, the state space model becomes

$$\dot{Z} = \wedge Z \tag{4.13}$$

$\wedge$ is a diagonal matrix with the eigenvalues as the diagonal elements. Therefore, the rate of change of i^{th} variable is given by,

$$\dot{z}_i = \lambda_i z_i \tag{4.14}$$

The transformation produces n independent variables. These variables are called the modes of the dynamical system. The modes describe the dynamic behaviour of the system. The time response of i^{th} mode is given by,

$$z_i(t) = z_i(0)e^{\lambda_i t} \tag{4.15}$$

The time dependent characteristics of a mode corresponding to an eigenvalue λ_i is given by $e^{\lambda_i t}$. Therefore, the modes and their stability is described by the eigenvalues as follows:

- A real eigenvalue corresponds to an aperiodic (non-oscillatory) mode. If eigenvalue is negative, the mode is a decaying mode and if it is positive, mode is unstable (aperiodic instability).

- A complex conjugate pair of eigenvalues corresponds to an oscillatory mode. If the eigenvalue pair is $\lambda = \sigma \pm j\omega$, the frequency of oscillation is given by,

$$f = \frac{\omega}{2\pi} \tag{4.16}$$

The damping ratio is given by,

$$\zeta = -\frac{\sigma}{\sqrt{\sigma^2 + \omega^2}} \tag{4.17}$$

The magnitude of the damping ratio determines the rate of decay of the amplitude of the oscillation. If the real part of the eigenvalues is negative (i.e. damping ratio is positive), the mode is stable.

4.5.1.3 Right Eigenvectors

The right eigenvector gives the mode shape, which shows the relative activity of the state variables when that mode is excited. The right eigenvector ϕ_i is given by,

$$A\phi_i = \lambda_i \phi_i \tag{4.18}$$

Assume, only i_{th} mode of the system is excited. Then, the state variables are given by,

$$\begin{bmatrix} \Delta x_1 \\ \Delta x_2 \\ \vdots \\ \Delta x_n \end{bmatrix} = \begin{bmatrix} \phi_{i1} \\ \phi_{i2} \\ \vdots \\ \phi_{in} \end{bmatrix} z_i \tag{4.19}$$

$\phi_{i1}, \phi_{i2}, \ldots, \phi_{in}$ are the elements of i_{th} right eigenvector ϕ_i.
The magnitudes of the elements of ϕ_i give the relative activities of the state variables in i_{th} mode, and the phase angles give the phase displacement of the state variables with reference to the mode.

4.5.1.4 Left Eigenvectors

The left eigenvector ψ_i is given by,

$$\psi_i A = \lambda_i \psi_i \tag{4.20}$$

Assume, only i_{th} mode of the system is excited. Then, the mode is given by,

$$z_i = \psi_{i1}\Delta x_1 + \psi_{i2}\Delta x_2 + \ldots + \psi_{in}\Delta x_n \tag{4.21}$$

$\psi_{i1}, \psi_{i2}, \ldots, \psi_{in}$ are the elements of i_{th} left eigenvector ψ_i.
The elements of ψ_i are the weights of the state variabie to the i_{th} mode.

4.5.1.5 Participation factor

The participation factors are generally indicative of the relative participations of the respective states in the corresponding modes. The participation factors are independent of the units and scaling. The participation factors are obtained from the muttiplications of the elements of the right eigenvector and the left eigenvector. The participation factor p_{ki} is given by,

$$p_{ki} = \phi_{ki}\psi_{ik} \tag{4.22}$$

where, ϕ_{ki} is the k^{th} element of i_{th} right eigenvector (a column vector), and ψ_{ik} is the k^{th} element of i_{th} left eigenvector (a row vector).
The participation factor represents the measure of participation of k_{th} state in shaping the time response of mode i. An important property of a participation factor is that it is a dimensionless quantity and sum of participation factors of a mode is unity.
The participation matrix of the system is

$$P = \begin{bmatrix} p_1 & p_2 & \ldots & p_n \end{bmatrix} z_i \tag{4.23}$$

where

$$p_i = \begin{bmatrix} p_{1i} \\ p_{2i} \\ \vdots \\ p_{ni} \end{bmatrix} \tag{4.24}$$

4.5.2 Wind Turbine Model

From Equation 3.7, the generator mechanical torque in maximum power tracking mode can be written as,

$$T_m = \frac{1}{2}\frac{\rho\pi R^2 C_p(\lambda,\beta)V_{wind}^3}{\omega_r} \tag{4.25}$$

Linearization of Equation 4.25 gives

$$\Delta T_m = \frac{3}{2}\frac{\rho\pi R^2 C_p(\lambda,\beta)V_{wind0}^2}{\omega_r 0}\Delta V_{wind} - \frac{1}{2}\frac{\rho\pi R^2 C_p(\lambda,\beta)V_{wind0}^3}{\omega_r 0^2}\Delta\omega_r \tag{4.26}$$

4.5.3 Mechanical Drive Train Model

The dynamic model of the three mass drive train model is represented by Equation 3.8. After linearizing Equation 3.8 and substituting value of T_m from Equation 4.25,

$$\Delta\dot{x}_{wt} = A_{wt}\Delta x_{wt} + B_{wt}\Delta u_{wt} \tag{4.27}$$

where,

$$\Delta x_{wt} = \left[\Delta\omega_b, \Delta\omega_h, \Delta\omega_r, \Delta\theta_{bh}, \Delta\theta_{hg}\right]^T$$

$$\Delta u_{wt} = \left[\Delta V_{wind}, \Delta T_e\right]^T$$

$$A_{wt} = \begin{bmatrix} 0 & 0 & -\frac{\rho\pi R^2 C_p V_{wind0}^3}{4H_b\omega_{r0}^2} & -\frac{K1}{2H_b} & 0 \\ 0 & 0 & 0 & \frac{K1}{2H_h} & -\frac{K2}{2H_h} \\ 0 & 0 & 0 & 0 & \frac{K2}{2H_g} \\ \omega_0 & -\omega_0 & 0 & 0 & 0 \\ 0 & \omega_0 & -\omega_0 & 0 & 0 \end{bmatrix}$$

$$B_{wt} = \begin{bmatrix} \frac{3\rho\pi R^2 C_p V_{wind0}^3}{4H_b\omega_{r0}^2} & -\frac{K1}{2H_b} \\ 0 & 0 \\ 0 & -\frac{1}{2H_g} \\ 0 & 0 \\ 0 & 0 \end{bmatrix}$$

4.5.4 Induction Generator Model

The non-linear stator and rotor equations in per unit can be written as,

$$\frac{1}{\omega_0}\frac{d\psi_{ds}}{dt} = -r_s I_{ds} + \psi_{qs} + V_{ds} \tag{4.28}$$

$$\frac{1}{\omega_0}\frac{d\psi_{qs}}{dt} = -r_s I_{qs} - \psi_{ds} + V_{qs} \tag{4.29}$$

$$\frac{1}{\omega_0}\frac{d\psi_{dr}}{dt} = -r_r I_{dr} + s\psi_{qr} + V_{dr} \tag{4.30}$$

$$\frac{1}{\omega_0}\frac{d\psi_{qr}}{dt} = -r_r I_{qr} - s\psi_{dr} + V_{qr} \tag{4.31}$$

where,

$$\psi_{ds} = L_{ss}I_{ds} + L_m I_{dr} \tag{4.32}$$

$$\psi_{qs} = L_{ss}I_{qs} + L_m I_{qr} \tag{4.33}$$

$$\psi_{dr} = L_m I_{ds} + L_{rr}I_{dr} \tag{4.34}$$

$$\psi_{qr} = L_m I_{qs} + L_{rr}I_{qr} \tag{4.35}$$

$$L_{ss} = (L_{ls} + L_m) \tag{4.36}$$

$$L_{rr} = (L_{lr} + L_m) \tag{4.37}$$

$$s = (\omega_e - \omega_r)/\omega_e \tag{4.38}$$

and w_0 is the base angular speed (rad/sec).

Above equations can be re-arranged as:

$$\frac{L_{ss}}{\omega_0}\frac{dI_{ds}}{dt} + \frac{L_m}{\omega_0}\frac{dI_{dr}}{dt} = -r_s I_{ds} + (L_{ss}I_{qs} + L_m I_{qr}) + V_{ds} \tag{4.39}$$

$$\frac{L_{ss}}{\omega_0}\frac{dI_{qs}}{dt} + \frac{L_m}{\omega_0}\frac{dI_{qr}}{dt} = -r_s I_{qs} - (L_{ss}I_{ds} + L_m I_{dr}) + V_{qs} \tag{4.40}$$

$$\frac{L_{rr}}{\omega_0}\frac{dI_{dr}}{dt} + \frac{L_m}{\omega_0}\frac{dI_{ds}}{dt} = -r_r I_{dr} + s(L_m I_{qs} + L_{rr}I_{qr}) + V_{dr} \tag{4.41}$$

$$\frac{L_{rr}}{\omega_0}\frac{dI_{qr}}{dt} + \frac{L_m}{\omega_0}\frac{dI_{qd}}{dt} = -r_r I_{qr} - s(L_m I_{ds} + L_{rr}I_{dr}) + V_{qr} \tag{4.42}$$

Linearizing the differential equations 4.39 - 4.42, the induction generator model in linear state space form can be written as:

$$\dot{\Delta x_g} = A_g \Delta x_g + B_g \Delta u_g \tag{4.43}$$

where,

$$\Delta x_g = \begin{bmatrix} \Delta I_{ds} & \Delta I_{qs} & \Delta I_{dr} & \Delta I_{qr} \end{bmatrix}^T$$

$$\Delta u_g = \begin{bmatrix} \Delta \omega_r & \Delta V_{ds} & \Delta V_{qs} & \Delta V_{dr} & \Delta V_{qr} \end{bmatrix}^T$$

4.5.5 Grid Side Converter (GSC)

The simplified control scheme of the grid-side conveter with PI controllers is shown in figure 4.9.

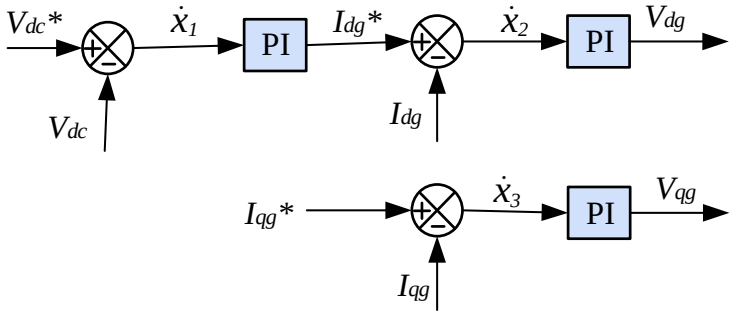

Figure 4.9: PI controllers for GSC

From figure 4.9, the following equations can be written:

$$\dot{x_1} = V_{dc} * - V_{dc} \tag{4.44}$$

$$\dot{x_2} = I_{dg} * - I_{dg} \tag{4.45}$$

$$\dot{x_3} = I_{qg} * - I_{qg} \tag{4.46}$$

$$I_{dg}* = K_{p,V_{dc}}.(V_{dc} * - V_{dc}) + K_{i,V_{dc}} x_1 \tag{4.47}$$

$$V_{dg} = K_{p,I_{dg}}(I_{dg} * - I_{dg}) + K_{i,I_{dg}} x_2 \tag{4.48}$$

$$V_{qg} = K_{p,I_{qg}}(I_{qg} * - I_{qg}) + K_{i,I_{qg}} x_3 \tag{4.49}$$

The state space model of the grid side converter controller can be obtained by linearizing equations 4.44 - 4.49 as:

$$\Delta\dot{x}_{gsc} = A_{gsc}\Delta x_{gsc} + B_{gsc}\Delta u_{gsc} \tag{4.50}$$

where,

$$\Delta x_{gsc} = \begin{bmatrix} \Delta x_1 & \Delta x_2 & \Delta x_3 \end{bmatrix}^T$$

$$\Delta u_{gsc} = \begin{bmatrix} \Delta V_{dc}* & \Delta V_{dc} & \Delta I_{dg} & \Delta I_{qg} & \Delta V_{dg} & \Delta V_{qg} \end{bmatrix}^T$$

4.5.6 Rotor Side Converter (RSC)

The rotor side conveter controller scheme is shown in figure 4.10. The direct axis controller controls the stator reactive power; whereas its quadrature axis controller controls

the rotor speed. The following differential and algebraic equations represent the rotor side converter controller.

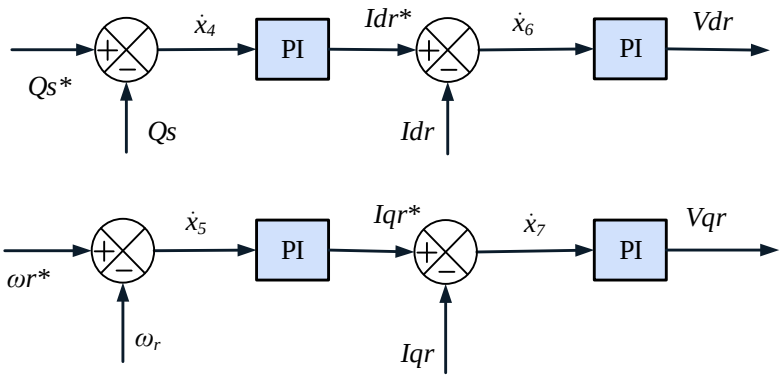

Figure 4.10: PI controllers for RSC

$$\dot{x_4} = Q_s * -Q_s \tag{4.51}$$

$$\dot{x_5} = \omega_r * -\omega_r \tag{4.52}$$

$$\dot{x_6} = I_{dr} * -I_{dr} \tag{4.53}$$

$$\dot{x_7} = I_{qr} * -I_{qr} \tag{4.54}$$

$$I_{dr}* = K_{p,Q_s}.(Q_s * -Q_s) + K_{i,Q_s}x_4 \tag{4.55}$$

$$I_{qr}* = K_{p,\omega_r}.(\omega_r * -\omega_r) + K_{i,\omega_r}x_5 \tag{4.56}$$

$$V_{dr} = K_{p,I_{dr}}.(I_{dr} * -I_{dr}) + K_{i,I_{dr}}x_6 \tag{4.57}$$

$$V_{qr} = K_{p,I_{qr}}.(I_{qr} * -I_{qr}) + K_{i,I_{qr}}x_7 \tag{4.58}$$

The linearization of equations 4.51 - 4.58 gives the state space model of the rotor side converter controller as:

$$\Delta\dot{x}_{rsc} = A_{rsc}\Delta x_{rsc} + B_{rsc}\Delta u_{rsc} \tag{4.59}$$

where,

$$\Delta x_{rsc} = \begin{bmatrix} \Delta x_4 & \Delta x_5 & \Delta x_6 & \Delta x_7 \end{bmatrix}^T$$
$$\Delta u_{gsc} = \begin{bmatrix} \Delta V_{wind} & \Delta Q_s* & \Delta \omega_r & \Delta I_{dr} & \Delta I_{qr} \end{bmatrix}^T$$

4.5.7 DC Link Capacitor Model

The DC link facilitates the power exchange between RSC and GSC. Assuming no loss in converters, following relation exist between DC link power(P_{dc}), GSC power(P_g) and RSC power(P_r).

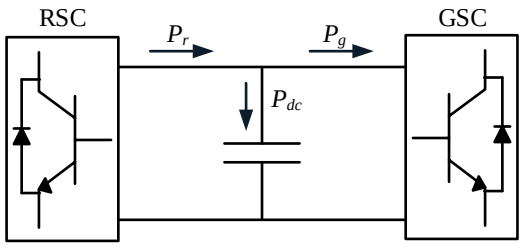

Figure 4.11: DC Link

$$P_{dc} = P_r - P_g \tag{4.60}$$

Further it can be written as,

$$v_{dc} C \frac{dv_{dc}}{dt} = (v_{qr} i_{qr} + v_{dr} i_{dr}) - (v_{qg} i_{qg} + v_{dg} i_{dg}) \tag{4.61}$$

Linearizing equation 4.61 gives the small signal model for the dc capacitor as,

$$\Delta \dot{x}_{dc} = 0.\Delta x_{dc} + B_{dc} \Delta u_{dc} \tag{4.62}$$

where,

$$\Delta x_{dc} = \begin{bmatrix} \Delta v_{dc} \end{bmatrix}$$
$$\Delta u_{gsc} = \begin{bmatrix} \Delta v_{dr} & \Delta v_{qr} & \Delta v_{dg} & \Delta v_{qg} & \Delta i_{dr} & \Delta i_{qr} & \Delta i_{dg} & \Delta i_{qg} \end{bmatrix}^T$$

4.5.8 Series Compensated Transmission Line

Figure 4.12 shows the series compensated transmission line.

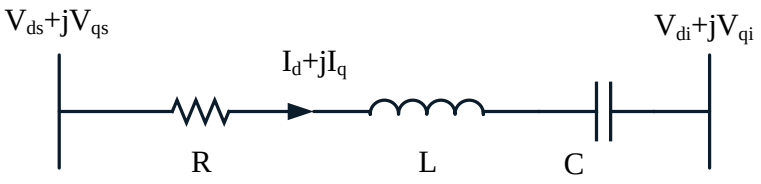

Figure 4.12: Series Compensated Line

The differential equations for series compensated transmission line is

$$L\frac{d}{dt}I_d = V_{ds} - RI_d + \omega_0 LI_q - V_{cd} - V_{di} \tag{4.63}$$

$$L\frac{d}{dt}I_q = V_{qs} - RI_q + \omega_0 LI_d - V_{cq} - V_{qi} \tag{4.64}$$

$$C\frac{dV_{cd}}{dt} = I_d + \omega_0 CV_{cq} \tag{4.65}$$

$$C\frac{dV_{cq}}{dt} = I_q - \omega_0 CV_{cd} \tag{4.66}$$

Linearilization of differential equations yields the state space model of the network as:

$$\Delta\dot{x}_N = A_N\Delta x_N + B_N\Delta u_N \tag{4.67}$$

where,

$$\Delta x_N = \begin{bmatrix}\Delta I_d & \Delta I_q & \Delta V_{cd} & \Delta V_{cq}\end{bmatrix}$$

$$\Delta u_N = \begin{bmatrix}\Delta V_{ds} & \Delta V_{qs} & \Delta V_{di} & \Delta V_{qi}\end{bmatrix}^T$$

4.5.9 Complete system

Combination of each components of wind power plant explained above gives the complete state space model of the wind power plant as [107]:

$$\Delta\dot{x}_{sys} = A_{sys}\Delta x_{sys} + B_{sys}\Delta u_{sys} \tag{4.68}$$

where,

$$\Delta x_{sys} = \begin{bmatrix} \Delta x_{wt} & \Delta x_g & \Delta x_{gsc} & \Delta x_{rsc} & \Delta x_{dc} & \Delta x_N \end{bmatrix}$$

$$\Delta u_{sys} = \begin{bmatrix} \Delta V_{wind} & \Delta V_{dc}* & \Delta Q_s* & \Delta V_{ds} & \Delta V_{qs} & \Delta V_{di} & \Delta V_{qi} \end{bmatrix}^T$$

4.5.10 Results

The test system used for this study is as shown in figure 4.1. The 450 MW DFIG wind power plant is connected to an infinite bus via a 345 kV line.

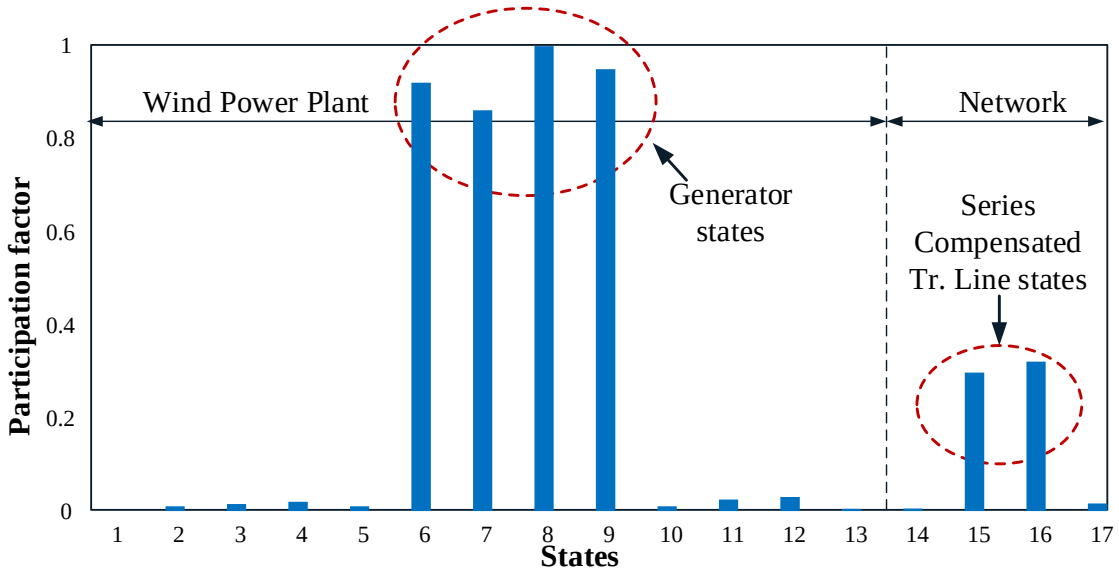

Figure 4.13: Participation factors of sub-synchronous mode with 50% compensation

Figure 4.13 shows the participation factors of sub-synchronous mode for the test system mentioned. The result presented is for 50 % compensation. The system states are grouped in such a way that states 1 to 5 represent the mechanical drive train, 6 to 9 represent the generator, 10 to 13 represent the rotor side converter controllers and rest represent the network. The dynamics of grid side converter is not considered as it does not have significant impact on the sub-synchronous mode [48]. Reference [47] also concludes that SSCI is most sensitive to controllers of the RSC.

It is clear from the figure 4.13 that the generator states and the network states participate in 36 Hz mode indicating a sub-synchronous interaction between the generator and the series compensated transmission line. There is no participation of the mechanical drive train states in this mode revealing that there is no torsional interaction present in this case. The participation of the controller states in the sub-synchronous mode is too small compared to the generator states and the states related to the series compensated transmission line.

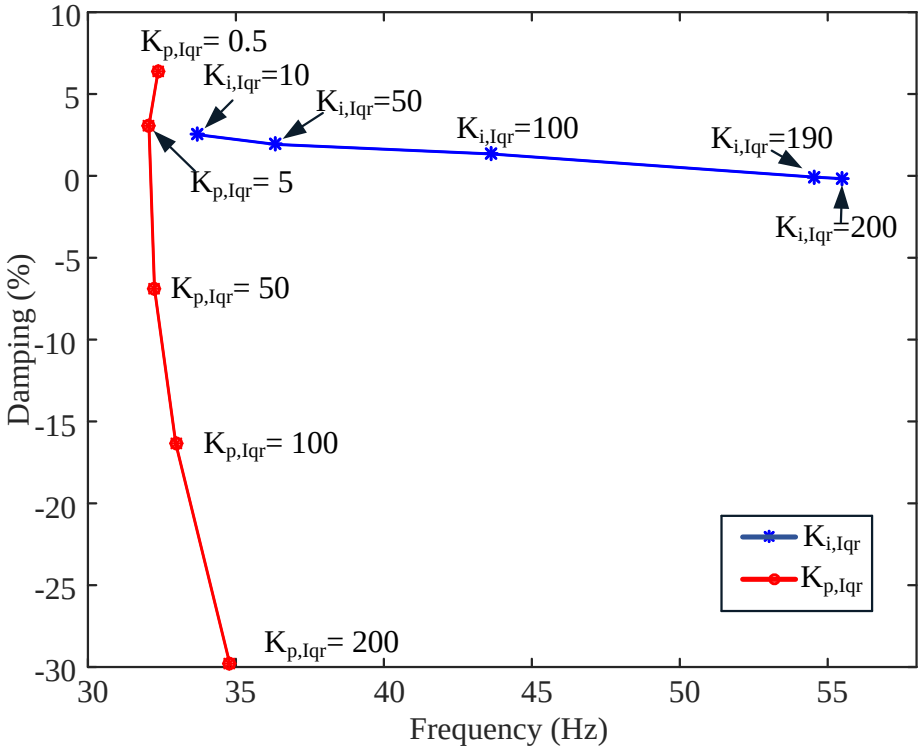

Figure 4.14: Sensitivity of damping to RSC q-axis controller

Figure 4.14 illustrates the sensitivity of damping ratio of the sub-synchronous mode to PI gains of RSC q-axis controller. The q-axis current proportional gain $K_{p,Iqr}$ is varied from 0.5 to 200 and the integral gain $K_{i,Iqr}$ is varied from 10 to 200. It is evident from the figure 4.14 that damping ratio is more sensitive to $K_{p,Iqr}$ than $K_{i,Iqr}$. As the proportional gain $K_{p,Iqr}$ increases, damping becomes poor.

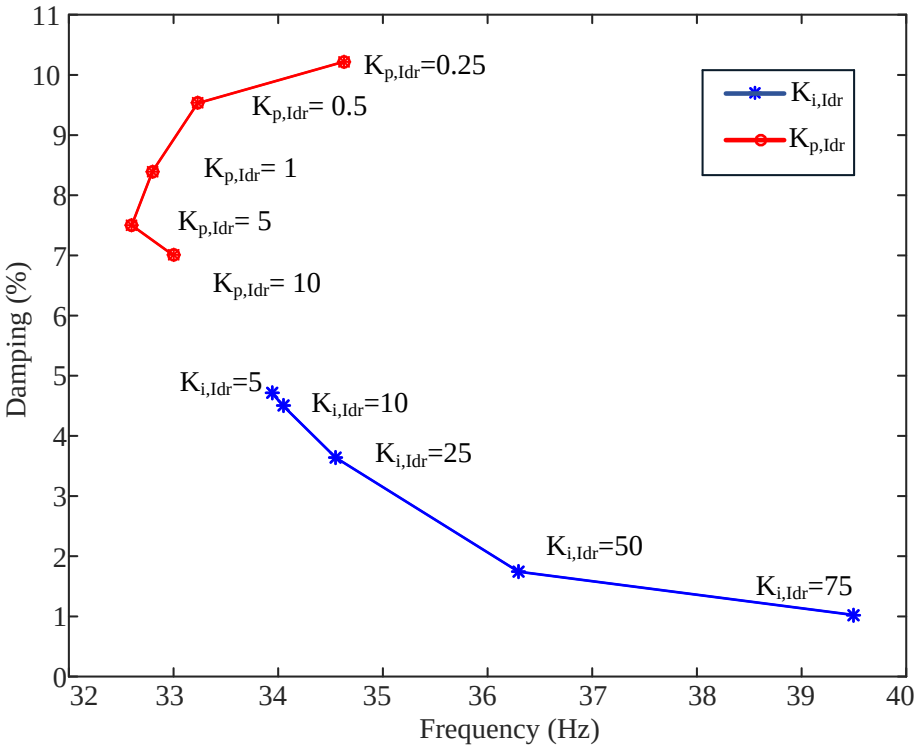

Figure 4.15: Sensitivity of damping to RSC d-axis controller

Figure 4.15 show the impact of d-axis current PI controller gains on the sub-synchronous mode frequency and damping. It also justifies that increasing the d-axis current gains $K_{p,Idr}$ and $K_{i,Idr}$ causes reduced damping. This indicates the rotor side converter controller has an adverse effect on the damping of sub-synchronous mode.

4.6 Summary

A comprehensive procedure to study sub-synchronous phenomena in power systems with DFIG wind power plant and series compensated transmission line was discussed in this chapter. modelling of wind power plant for small signal stability analysis was described in detail. Firstly, prony analysis of symmetrical and unsymmetrical fault currents for two different compensation level is carried out to find dominant frequency components. Following this, frequency scanning is performed to identify the presence of network resonances for

30%, 50% and 70% compensation level. Then a detailed eigenvalue analysis is performed to find out the cause of sub-synchronous oscillations. The proposed detailed analysis clearly identifies that RSC side state variables are the participating state variables. It is shown that the sub-synchronous interaction between DFIG wind power plant and a series compensated transmission line is due to an electrical interaction between the series capacitor and the wind generator component which is controllable through the rotor side converter controllers. The sensitivity of damping to PI controller gains of RSC is demonstrated. Among RSC controllers, the q axis proportional gain is more dominant.

The next chapter explains a fast and accurate dynamic phasor approach of modelling the DFIG wind farm. Selected frequency components are used in the analysis of the dynamic phasor model. An average value model of DFIG which is also discussed in the next chapter and the two models are compared with a detailed EMT simulation model.

Chapter 5

Dynamic Phasor Model and Average Value Model of DFIG

5.1 Introduction

Power utilities normally use either fundamental frequency representations or detailed EMT models in planning studies to model the short circuit behaviour of wind generators. The fundamental frequency type model provides a simplified method, but is incapable of incorporating some critical aspects of Type 3 DFIG behaviour, such as non- fundamental torsional interaction frequencies, making it inaccurate. EMT simulation is a widely accepted method for accurately modelling the behaviour of complex power systems and power electronic components. It is capable of modelling every component of the system in detail, including all of the associated frequency components. Even though EMT modelling is highly accurate and capable of detailed modelling, it is cumbersome when it comes to modelling a system of considerable size and complexity, such as a Type 3 wind farm consisting of hundreds of wind generators.

This chapter discusses the proposed dynamic phasor modelling approach for modelling Type 3 wind farms. The dynamic phasor modelling approach provides an accurate model that is neither based on fundamental frequency simplifications nor as cumbersome as a detailed EMT model. A middle ground between the fundamental frequency and EMT models is achieved using this proposed modelling method. This method is based on the generalized averaging scheme discussed in [62], in which the variables of the power system under study are represented as dynamic phasors or time varying Fourier coefficients. This method of

modelling, also known as dynamic phasor modelling, can be used to select only the required frequency components to accurately represent the desired fault behaviour of a Type 3 wind farm. The dynamic phasor models are as accurate as the detailed EMT models, but computationally more efficient [108]. Another fundamentally similar concept, referred to as shift frequency modelling in the literature, resembles the proposed dynamic phasor approach. The similarities between the shift frequency concept and the dynamic phasor approach as well the subtle differences found in the course of this research are also discussed in this chapter (Section 5.2.1).

This chapter also describes an average value model (AVM) of a Type 3 wind generator, which has appeared in the recent literature. In an AVM, the switches can be represented by equivalent current and voltage sources. An AVM is developed in this thesis for the back-to-back converters of the DFIG. It is shown that, with an AVM, the relationship between the modulation function and the system voltage/current can be easily represented.

Results using the proposed dynamic phasor model discussed in this thesis and the AVM are finally validated with a detailed EMT model.

5.2 Dynamic Phasor Approach

The Fourier series representation of a complex time domain periodic signal $x(\tau)$ with a period T is given by [109]

$$x(\tau) = \sum_{k=-\infty}^{\infty} X_k . e^{jk\omega\tau} \tag{5.1}$$

where $\omega = 2\pi/T$ and X_k is the k^{th} complex Fourier coefficient. When power system transients occur, the time domain signal is no longer purely periodic. In order to represent complex transient waveforms such as these, use of a modified form of the above Fourier series representation is required. This modified representation is known as dynamic phasors representation and is based on generalized averaging theory [62]. This model approximates the time domain waveform $x(\tau)$ as shown in Figure 5.1, in the interval $\tau\epsilon(t-T, t]$ by a

Fourier series representation as

$$x(\tau) = \sum_{-\infty}^{\infty} X_k(t).e^{jk\omega\tau}. \tag{5.2}$$

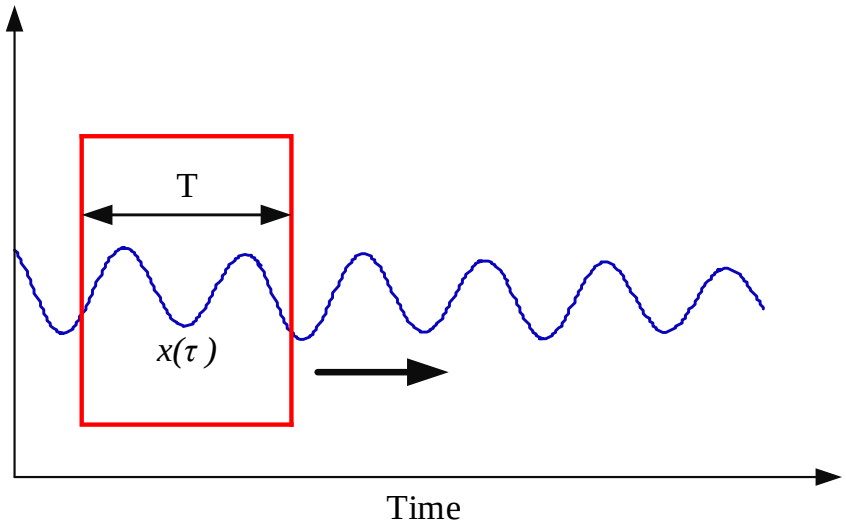

Figure 5.1: Window of time-period T sliding over time varying signal

In this representation, the Fourier coefficients X_k are time varying [69]. $\langle x\rangle_k(t)$ is the k^{th} time varying Fourier coefficient, which is defined as

$$X_k(t) = \frac{1}{T}\int_{t-T}^{t} x(\tau).e^{-jk\omega\tau}d\tau = \langle x\rangle_k(t). \tag{5.3}$$

This is represented as $\langle x\rangle_k$ in the upcoming sections for the sake of simplicity. The appropriate dynamic phasors (Fourier coefficients) to accurately represent the short circuit behaviour of the Type 3 wind generator must be determined. If K is the set of selected Fourier coefficients, the equation

$$x(t) \approx \sum_{k\epsilon K} X_k(t).e^{jk\omega\tau} \tag{5.4}$$

is the Fourier series approximation of the original signal.

5.2.1 Shift Frequency Concept

The electrical three phase quantities are naturally real valued signal [64]. The frequency spectrum of the real signal is shown in Figure 5.2. Adding the quadrature component as an imaginary part to the actual signal $x(t)$, the corresponding analytical signal $x_a(t)$ can be obtained using [64, 110]:

$$x_a(t) = x(t) + j\mathcal{H}[x(t)] \tag{5.5}$$

where $\mathcal{H}[x(t)]$ is the Hilbert transform of $x(t)$.

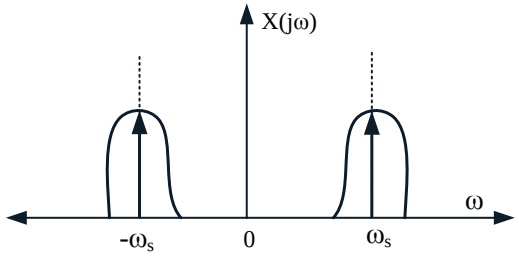

Figure 5.2: Frequency spectrum of real signal

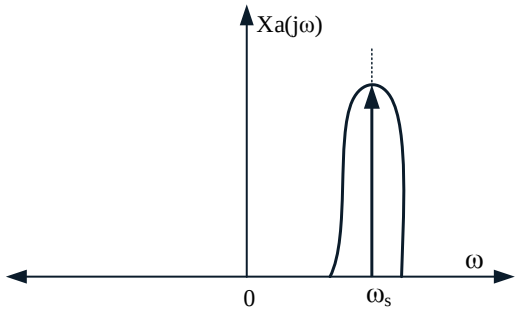

Figure 5.3: Frequency spectrum of analytical signal

The frequency shift of the analytical signal $x_a(t)$ could be done as follows [64, 110]:

$$x_{sh}(t) = x_a(t)e^{-j\omega_s t} \tag{5.6}$$

where $x_{sh}(t)$ is used to denote the shifted frequency.

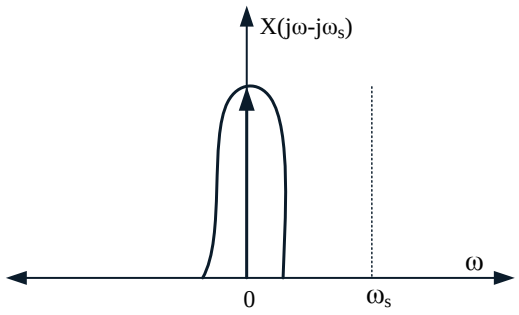

Figure 5.4: Frequency spectrum of shifted signal

The advantages and theoretical details of this approach for power system transients simulation were first studied in [63]. In [66], the three phase representation was relaxed and the concept was generalized to overcome the three phase limitation. The approach was then employed for combined simulation of electromagnetic and electromechanical transients. In [63] and [66], the authors refer to the baseband quantities as dynamic phasors.

If the major frequency content of the transients is concentrated only around the base system frequency, the use of the fundamental baseband representation of the system quantities would signficantly increase the simulation speed [69]. However, if the major transients are not concentrated around the fundamental frequency but instead around other sub-harominc or harmonic frequencies, this advantage is lost (which is the case for torsional interactions in a DFIG). When the frequency shift applied to the analytical signal is only $j\omega_s$, meaning $X_{sh}(j\omega) = X_a(j\omega - j\omega_s)$, the maximum frequency of the baseband signal with other harmonics will be higher than if the spectrum content is only condensed around the system frequency, as illustrated in Figure 5.5.

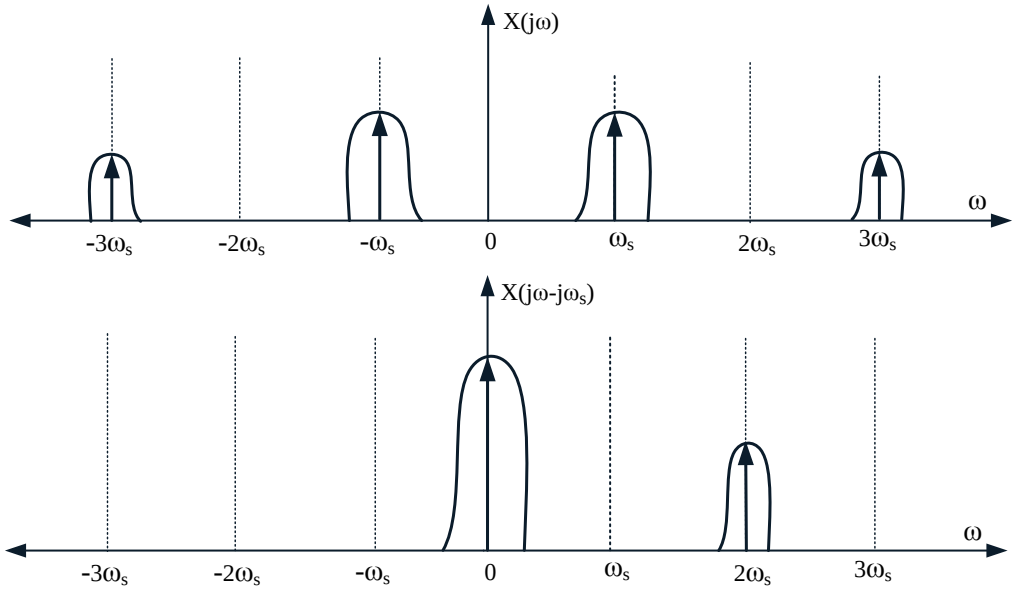

Figure 5.5: Frequency spectrum of baseband signal with higher harmonics

Transformation of Equation 5.1 into a frequency domain gives

$$X(j\omega) = \sum_{k=-\infty}^{\infty} X_k(j\omega - jk\omega_s) \tag{5.7}$$

From Equation 5.7, it can be seen that applying the dynamic phasor approach shifts all of the frequency components at $k\omega_s$ by $-k\omega_s$. This results in accumulation of all of the harmonics at zero frequency, as shown in Figure 5.6. This provides a significant benfit and allows for the use of larger simulation steps and therefore higher computational efficiency [79].

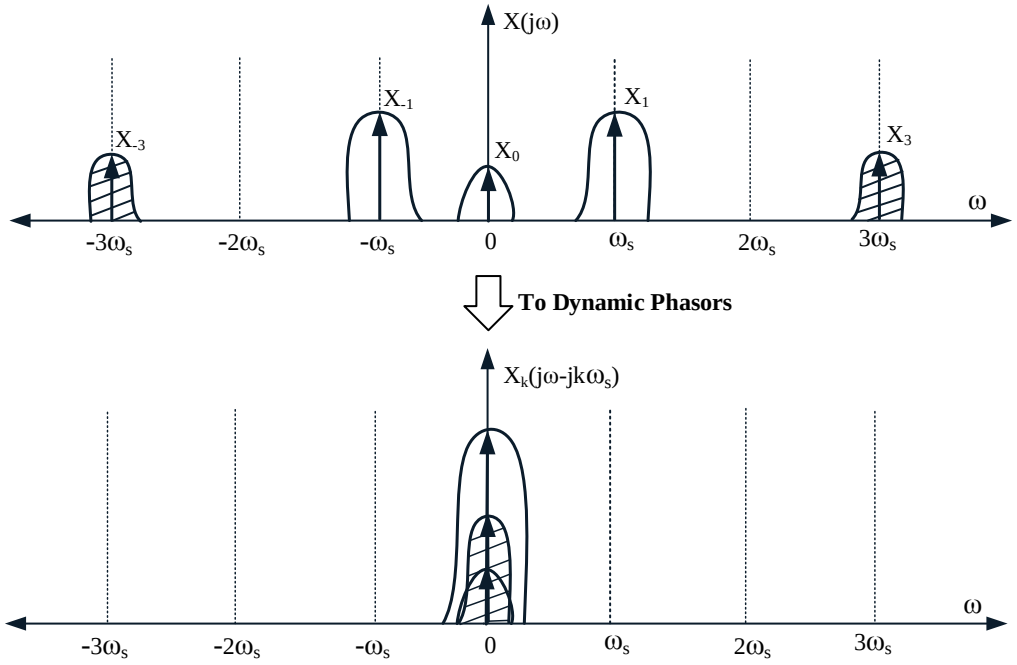

Figure 5.6: Frequency spectrum of Dynamic phasors

The above definition of dynamic phasor modelling can be extended for a three phase system with the equations

$$\begin{bmatrix} x_a \\ x_b \\ x_c \end{bmatrix} (\tau) = \sum_{-\infty}^{\infty} \begin{bmatrix} X_{a,k} \\ X_{b,k} \\ X_{c,k} \end{bmatrix} (t).e^{jk\omega\tau} \tag{5.8}$$

and

$$\begin{bmatrix} X_{a,k} \\ X_{b,k} \\ X_{c,k} \end{bmatrix} (t) = \frac{1}{T} \int_{t-T}^{t} \begin{bmatrix} x_a \\ x_b \\ x_c \end{bmatrix} (\tau).e^{-jk\omega\tau} d\tau = \begin{bmatrix} \langle x_a \rangle_k \\ \langle x_b \rangle_k \\ \langle x_c \rangle_k \end{bmatrix} (t). \tag{5.9}$$

The following properties of dynamic phasors are important in developing the model:

1. The relation between the derivative of $x(\tau)$ and the derivative of $X_k(t)$ is given by

$$\left\langle \frac{dx(t)}{dt} \right\rangle_k = \frac{dX_k(t)}{dt} + jk\omega X_k(t). \tag{5.10}$$

2. The product of two time-domain variables equals a discrete time convolution of the two dynamic phasor sets of variables given by

$$\langle xy \rangle_k = \sum_{l=-\infty}^{\infty} (X_{k-l} Y_l). \tag{5.11}$$

3. For a real valued signal x, the relationship between X_k and X_{-k} is given by

$$X_{-k} = X_k^* \tag{5.12}$$

Dynamic phasor in $dq0$ reference frame:

The $dq0$ reference frame is generally referred as a reference frame rotating with the synchronous speed. Mathematically, the $dq0$ or Park's transformation is given by the following equation [69]

$$\begin{bmatrix} x_d \\ x_q \\ x_0 \end{bmatrix} = \underbrace{\frac{2}{3} \begin{bmatrix} cos(\theta) & cos(\theta - \frac{2\pi}{3}) & cos(\theta + \frac{2\pi}{3}) \\ -sin(\theta) & -sin(\theta - \frac{2\pi}{3}) & -sin(\theta + \frac{2\pi}{3}) \\ \frac{1}{2} & \frac{1}{2} & \frac{1}{2} \end{bmatrix}}_{\text{Pt}} \cdot \begin{bmatrix} x_a \\ x_b \\ x_c \end{bmatrix} \tag{5.13}$$

where $\theta = \omega_s t$.

The inverse transformation matrix is defined as

$$\begin{bmatrix} x_a \\ x_b \\ x_c \end{bmatrix} = \underbrace{\begin{bmatrix} cos(\theta) & -sin(\theta) & 1 \\ cos(\theta - \frac{2\pi}{3}) & -sin(\theta - \frac{2\pi}{3}) & 1 \\ cos(\theta + \frac{2\pi}{3}) & -sin(\theta - \frac{2\pi}{3}) & 1 \end{bmatrix}}_{\text{Pi}} \cdot \begin{bmatrix} x_d \\ x_q \\ x_0 \end{bmatrix} \tag{5.14}$$

The derivatives of the time dependent transformation matrices Pt and Pi can be given as

$$\frac{dPt}{dt} = -\omega_s (J.Pt) \tag{5.15}$$

$$\frac{dPi}{dt} = \omega_s (Pi.J) \tag{5.16}$$

where

$$J = \begin{bmatrix} 0 & 1 & 0 \\ -1 & 0 & 0 \\ 0 & 0 & 0 \end{bmatrix} \tag{5.17}$$

In a dq0 reference frame rotating at synchronous speed, the positive sequence component will appear on the d and q axes as DC, i.e., with frequency 0 (k=0 for positive sequence components), and the negative sequence component will appear with a frequency of $2\omega_s$ (k=2 for negative sequence components). The zero sequence component will appear on the 0 axis with a frequency of ω_s (k=1 for zero sequence components). Hence, the designation $\langle x \rangle_0$ is used to represent the positive sequence, $\langle x \rangle_2$ the negative sequence, and $\langle x \rangle_1$ the zero sequence dynamic phasors, respectively. The transformer used in the test system is a Y-Δ transformer, and hence zero sequence dynamic phasors are ignored in the studies [111].

Dynamic phasor modelling based on the generalized averaging theory has significant potential and offers a number of advantages over conventional modelling methods. First, it makes the modelling computationally efficient compared to EMT modelling as only appropriate dynamic phasors are selected. Second, the selection of set K permits consideration of a wider bandwidth of frequencies, such as non-fundamental frequencies, making the method more accurate than traditional fundamental frequency approximations. References [53,68,73,75] describe the dynamic phasor modelling approach for accurately modelling complex power system components and its advantages. A dynamic phasor model of a Type 3 wind farm is developed in this thesis to accurately model its short circuit behaviour for balanced and unbalanced faults as well as when significant sub-synchronous frequencies are present in the system.

As the dynamic phasor model of the Type 3 wind farm system is capable of accurately modelling not only fault current behaviour such as balanced and unbalanced faults, but also sub-synchronous control interactions, it provides the necessary information to design both protection and control settings for wind farms. The model is also generic in nature, i.e., it does not require manufacturer proprietary information, such as control algorithms, which are difficult to obtain. The model developed in this research work will serve as a powerful tool for a power utility engineer to design relay settings as well as control settings for damping SSCI oscillations for a Type 3 wind farm connected to a series compensated transmission line.

5.3 Dynamic Phasor Modelling of DFIG

modelling the various components of the Type 3 wind generator test system was described in chapter 3 in terms of $dq0$ time domain differential equations. The parameters of the test system are given in Appendix A.3. By substituting the differential equations for different components of the test system in Equation 5.10 above, the dynamic phasor model equations are obtained and described in this section.

The selection of the set (K) of dynamic phasors for each of these components is based on the required short circuit behaviour to be studied, namely a symmetrical or unsymmetrical fault with or without the influence of sub-synchronous interactions. As explained previously, the dynamic phasor modelling technique proposed in this research work is capable of modelling sub-synchronous frequency components to accurately represent SSCI phenomena. In section 4.3.1, the frequency of the sub-synchronous component for SSCI occurrence in the Type 3 wind farm test system in which the wind farm was connected to a 50 % compensated transmission line was determined to be 36.2 Hz, which is approximately 0.6 times the system fundamental frequency of 60 Hz. Hence, such a sub-synchronous frequency component would appear on the d and q axes at a frequency approximately 24 HZ (60 Hz-36 Hz) which is $0.4\omega_s$. This frequency component is denoted by K=0.4 [70, 71].

Another scenario was also studied for 70 % compensation level of transmission line. The frequency of sub-synchronous component was determined to be 42 Hz, which is approximately 0.7 times the system fundamental frequency of 60 Hz. Hence, such a sub-synchronous frequency component would appear on the d and q axes at a frequency approximately 18 Hz (60 Hz-42 Hz) which is $0.3\omega_s$. This frequency component is denoted by K=0.3. The sub-synchronous frequency dynamic phasor will be represented by $\langle x \rangle_{0.3}$. Further, based on the degree of compensation, the frequency of this sub-synchronous component would change as described in Section 4.4.

Accordingly, the correct value of K can be selected to represent the appropriate sub-synchronous component accurately. Table 5.1 gives the appropriate choice of dynamic phasors to represent the different fault scenarios discussed in Section 5.3.1.

Table 5.1: Selection of appropriate dynamic phasors

Fault Condition	**Dynamic phasors**
Symmetrical Fault	$\langle x_{dq} \rangle_0$
Unsymmetrical Fault	$\langle x_{dq} \rangle_0$, $\langle x_{dq} \rangle_2$
Symmetrical Fault with SSCI (50% compensation)	$\langle x_{dq} \rangle_0$, $\langle x_{dq} \rangle_{0.4}$
Unsymmetrical Fault with SSCI (50% compensation)	$\langle x_{dq} \rangle_0$, $\langle x_{dq} \rangle_2$, $\langle x_{dq} \rangle_{0.4}$
Symmetrical Fault with SSCI (70% compensation)	$\langle x_{dq} \rangle_0$, $\langle x_{dq} \rangle_{0.3}$
Unsymmetrical Fault with SSCI (70% compensation)	$\langle x_{dq} \rangle_0$, $\langle x_{dq} \rangle_2$, $\langle x_{dq} \rangle_{0.3}$

Mechanical Drive Train:

The dq dynamic phasor model for the drive train, consisting of the blades, hub and generator is represented by three mass model and is obtained by substituting equations 3.8 - 3.12 in 5.10. It is given by

$$\frac{d\langle \omega_b \rangle_k}{dt} = \frac{\langle T_m \rangle_k - K_1 \langle \theta_{bh} \rangle_k}{2H_b} - jk\omega_s \langle \omega_b \rangle_k \tag{5.18}$$

$$\frac{d\langle \omega_h \rangle_k}{dt} = \frac{K_1 \langle \theta_{bh} \rangle_k - K_2 \langle \theta_{hg} \rangle_k}{2H_h} - jk\omega_s \langle \omega_h \rangle_k \tag{5.19}$$

$$\frac{d\langle \omega_r \rangle_k}{dt} = \frac{K_2 \langle \theta_{hg} \rangle_k - \langle T_e \rangle_k}{2H_g} - jk\omega_s \langle \omega_r \rangle_k \tag{5.20}$$

$$\frac{d\langle \theta_{bh} \rangle_k}{dt} = \omega_s . (\langle \omega_b \rangle_k - \langle \omega_h \rangle_k) - jk\omega_s \langle \theta_{bh} \rangle_k \tag{5.21}$$

$$\frac{d\langle \theta_{hg} \rangle_k}{dt} = \omega_s . (\langle \omega_h \rangle_k - \langle \omega_r \rangle_k) - jk\omega_s \langle \theta_{hg} \rangle_k \tag{5.22}$$

where the electrical torque is

$$\langle T_e \rangle_k = \langle \psi_{qr} . i_{dr} \rangle_k - \langle \psi_{dr} . i_{qr} \rangle_k . \tag{5.23}$$

and the mechanical torque is

$$\langle T_m \rangle_k = \frac{1}{2} \frac{\rho \pi R^2 C_p(\lambda, \beta) V_{wind}^3}{\langle \omega_r \rangle_k} \tag{5.24}$$

The dynamic phasors for ω_r and T_e are chosen based on the type of fault, as shown in Table 5.1. For the mechanical torque T_m, only the positive sequence dynamic phasors are chosen.

Stator Voltages:

The dynamic phasor model for the stator voltage is as

$$\frac{d\langle \psi_{ds} \rangle_k}{dt} = \langle V_{ds} \rangle_k - r_s \langle I_{ds} \rangle_k + \langle \psi_{qs} \rangle_k - jk\omega_s \langle \psi_{ds} \rangle_k \tag{5.25}$$

$$\frac{d\langle \psi_{qs} \rangle_k}{dt} = \langle V_{qs} \rangle_k - r_s \langle I_{qs} \rangle_k - \langle \psi_{ds} \rangle_k - jk\omega_s \langle \psi_{qs} \rangle_k \tag{5.26}$$

where,

$$\langle \psi_{ds} \rangle_k = L_{ss} \langle I_{ds} \rangle_k + L_m \langle I_{dr} \rangle_k \tag{5.27}$$

$$\langle \psi_{qs} \rangle_k = L_{ss} \langle I_{qs} \rangle_k + L_m \langle I_{qr} \rangle_k \tag{5.28}$$

The appropriate choice of the dynamic phasors for the stator flux linkages ψ_{dqs}, currents i_{qds}, i_{dqr} and voltages V_{dqs} are based on Table 5.1.

Rotor Voltages:

The dynamic phasor model the rotor voltage is similarly obtained as

$$\frac{d\langle \psi_{dr} \rangle_k}{dt} = \langle V_{dr} \rangle_k - r_r \langle I_{ds} \rangle_k + s\langle \psi_{qr} \rangle_k - jk\omega_s \langle \psi_{dr} \rangle_k \tag{5.29}$$

$$\frac{d\langle \psi_{qr} \rangle_k}{dt} = \langle V_{qr} \rangle_k - r_r \langle I_{qr} \rangle_k - s\langle \psi_{dr} \rangle_k - jk\omega_s \langle \psi_{qr} \rangle_k \tag{5.30}$$

where,

$$\langle \psi_{dr} \rangle_k = L_m \langle I_{ds} \rangle_k + L_{rr} \langle I_{dr} \rangle_k \tag{5.31}$$

$$\langle \psi_{qr} \rangle_k = L_m \langle I_{qs} \rangle_k + L_{rr} \langle I_{qr} \rangle_k \tag{5.32}$$

The appropriate choice of the dynamic phasors for the rotor flux linkages ψ_{dqr}, currents i_{dqs}, i_{dqr} and voltages V_{dqr} are based on Table 5.1. The dynamic phasor dq equation of the

slip, obtained by substituting equation 4.38 in 5.10, is given as

$$\langle s \rangle_k = \frac{\omega_s - \langle \omega_r \rangle_k}{\omega_s} \tag{5.33}$$

where k is selected as shown in Table 5.1.

Flux Decrement:

The flux linking the rotor is a constant during normal conditions, but the flux linking the rotor starts decaying as soon as the fault occurs. As a consequence, the internal voltage is no more a constant and starts decreasing. Reference [30] discusses flux decrement effect in synchronous generator. Omitting the field DC supply E_{fd} in synchnous generator equation gives equation representing flux decrement in induction generator. The following equation gives rate of change of voltage

$$\langle \frac{dE'_q}{dt} \rangle k = -\frac{1}{T'_{d0}} (\langle E'_q \rangle k - (X_d - X'_d) \langle I_d \rangle k) \tag{5.34}$$

DC Link Capacitor:

The dynamic phasor model of the DC link capacitor is obtained by substituting Equation 4.61 in 5.10 is

$$\frac{1}{\omega_s} C \frac{d\langle V_{dc} \rangle_k}{dt} = \frac{\langle v_{qr} i_{qr} \rangle_k + \langle v_{dr} i_{dr} \rangle_k - \langle v_{qg} i_{qg} \rangle_k - \langle v_{dg} i_{dg} \rangle_k}{\langle V_{dc} \rangle_k} - jk \langle V_{dc} \rangle_k. \tag{5.35}$$

The set of appropriate dynamic phasors is selected based on Table 5.1.

The dynamic phasor model equations for the PI controllers in the GSC are obtained from Equations 4.44 to 4.49 and in the RSC are obtained from Equations 4.51 to 4.58 by using the properties of the dynamic phasors as shown below.

Grid Side Controller:

$$\frac{d\langle x_1 \rangle_k}{dt} = (\langle {V_{dc}}^* \rangle_k - \langle V_{dc} \rangle_k) - jk\omega_s \langle x_1 \rangle_k \tag{5.36}$$

$$\frac{d\langle x_2 \rangle_k}{dt} = (\langle i^*_{dg} \rangle_k - \langle i_{dg} \rangle_k) - jk\omega_s \langle x_2 \rangle_k \tag{5.37}$$

$$\frac{d\langle x_3\rangle_k}{dt} = (\langle i^*_{qg}\rangle_k - \langle i_{qg}\rangle_k) - jk\omega_s\langle x_3\rangle_k \tag{5.38}$$

$$\langle I^*_{dg}\rangle_k = K_{p,V_{dc}}.(\langle V^*_{dc}\rangle_k - \langle V_{dc}\rangle_k) + K_{i,V_{dc}}\langle x_1\rangle_k \tag{5.39}$$

$$\langle V_{dg}\rangle_k = K_{p,I_{dg}}.(\langle I^*_{dg}\rangle_k - \langle I_{dg}\rangle_k) + K_{i,I_{dg}}\langle x_2\rangle_k \tag{5.40}$$

$$\langle V_{qg}\rangle_k = K_{p,I_{qg}}.(\langle I^*_{qg}\rangle_k - \langle I_{qg}\rangle_k) + K_{i,I_{qg}}\langle x_3\rangle_k \tag{5.41}$$

Rotor Side Controller:

$$\frac{d\langle x_4\rangle_k}{dt} = (\langle Q^*_s\rangle_k - \langle Q_s\rangle_k) - jk\omega_s\langle x_4\rangle_k \tag{5.42}$$

$$\frac{d\langle x_5\rangle_k}{dt} = (\langle \omega^*_r\rangle_k - \langle \omega_r\rangle_k) - jk\omega_s\langle x_5\rangle_k \tag{5.43}$$

$$\frac{d\langle x_6\rangle_k}{dt} = (\langle I^*_{dr}\rangle_k - \langle I_{dr}\rangle_k) - jk\omega_s\langle x_6\rangle_k \tag{5.44}$$

$$\frac{d\langle x_7\rangle_k}{dt} = (\langle I^*_{qr}\rangle_k - \langle I_{qr}\rangle_k) - jk\omega_s\langle x_7\rangle_k \tag{5.45}$$

$$\langle I^*_{dr}\rangle_k = K_{p,Q_s}.(\langle Q^*_s\rangle_k - \langle Q_s\rangle_k) + K_{i,Q_s}\langle x_4\rangle_k \tag{5.46}$$

$$\langle I^*_{qr}\rangle_k = K_{p,\omega_r}.(\langle \omega^*_r\rangle_k - \langle \omega_r\rangle_k) + K_{i,\omega_r}\langle x_5\rangle_k \tag{5.47}$$

$$\langle V_{dr}\rangle_k = K_{p,I_{dr}}.(\langle I^*_{dr}\rangle_k - \langle I_{dr}\rangle_k) + K_{i,I_{dr}}\langle x_6\rangle_k \tag{5.48}$$

$$\langle V_{qr}\rangle_k = K_{p,I_{qr}}.(\langle I^*_{qr}\rangle_k - \langle I_{qr}\rangle_k) + K_{i,I_{qr}}\langle x_7\rangle_k \tag{5.49}$$

The appropriate choice of the set K of dynamic phasors (refer to Table 5.1) for modelling the controllers in the RSC and GSC is very important for accurate representation of the

specific fault behaviour under study. This is important, especially for the model to accurately represent the SSCI behaviour, as the controllers play an important role in the occurrence of this phenomena.

Series Compensated Transmission Line :

Apart from the controllers and converters, the series compensated transmission line must also be accurately represented using the appropriate dynamic phasors to accurately obtain the SSCI behaviour of a Type 3 wind farm. This is due to the fact that SSCI behaviour is primarily dependent on the RSC and GSC controller settings and the series compensation in the transmission line. The dynamic phasor model equations, as shown below, are obtained from Equations 4.63 to 4.66 using the properties of dynamic phasors that have been defined previously.

$$L\frac{\langle dI_d\rangle_k}{dt} = \langle v_{ds}\rangle_k - R\langle I_d\rangle_k + \omega_s L\langle I_q\rangle_k - \langle v_{cd}\rangle_k - v_{di} \tag{5.50}$$

$$L\frac{\langle dI_q\rangle_k}{dt} = \langle v_{qs}\rangle_k - R\langle I_q\rangle_k - \omega_s L\langle I_d\rangle_k - \langle v_{cq}\rangle_k - v_{qi} \tag{5.51}$$

$$C\frac{\langle dV_{cd}\rangle_k}{dt} = \langle I_d\rangle_k + \omega_s C\langle v_{cq}\rangle_k \tag{5.52}$$

$$C\frac{\langle dV_{cq}\rangle_k}{dt} = \langle I_q\rangle_k + \omega_s C\langle v_{cd}\rangle_k \tag{5.53}$$

5.3.1 Fault behaviour without Series Compensated Transmission Line

5.3.1.1 Symmetrical Fault behaviour

For the test system comprised of an aggregate model of 150 DFIGs, the fault behaviour for a symmetrical three phase fault of 200 ms applied at 7.0 s at the point of interconnection with the grid obtained from the detailed EMT model is shown in Figure 5.7. For this scenario the series compensation was not applied in the transmission line.

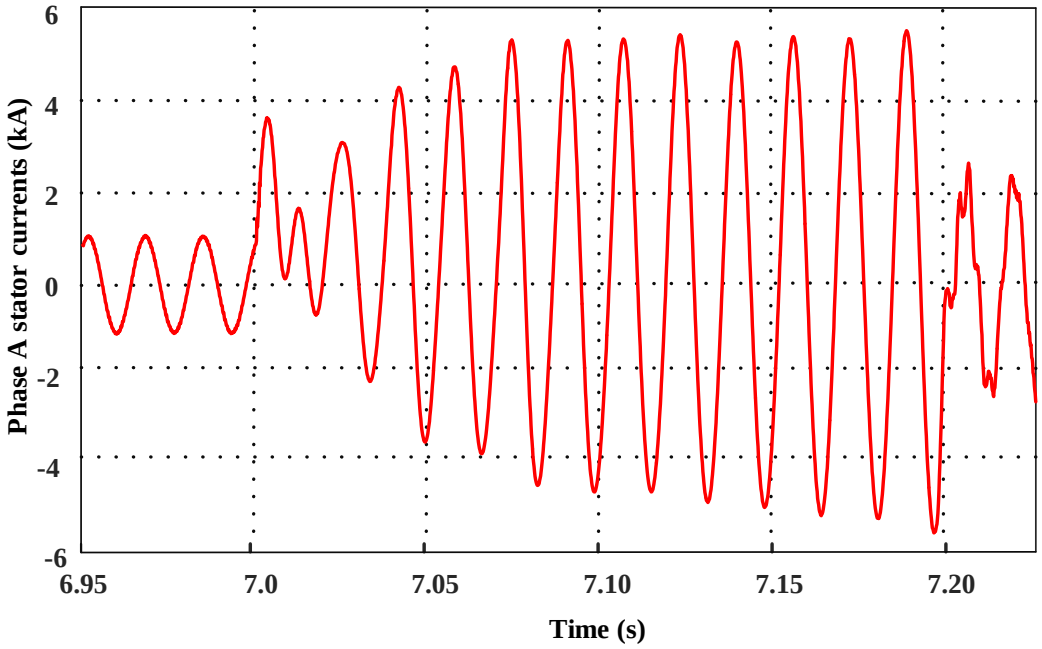

Figure 5.7: Fault current for Type 3 wind farm symmetrical fault application - EMT model

The above fault current for the symmetrical fault scenario mainly consists of the 60 Hz fundamental frequency component as demonstrated in the previous chapters. The test system was modeled with the proposed dynamic phasor model discussed in Section 5.3. The appropriate dynamic phasors must be chosen for accurate modelling. The variation of the positive sequence dynamic phasor is shown in Figure 5.8 below. The positive sequence component of the current is the most dominant frequency component for the symmetrical

fault condition.

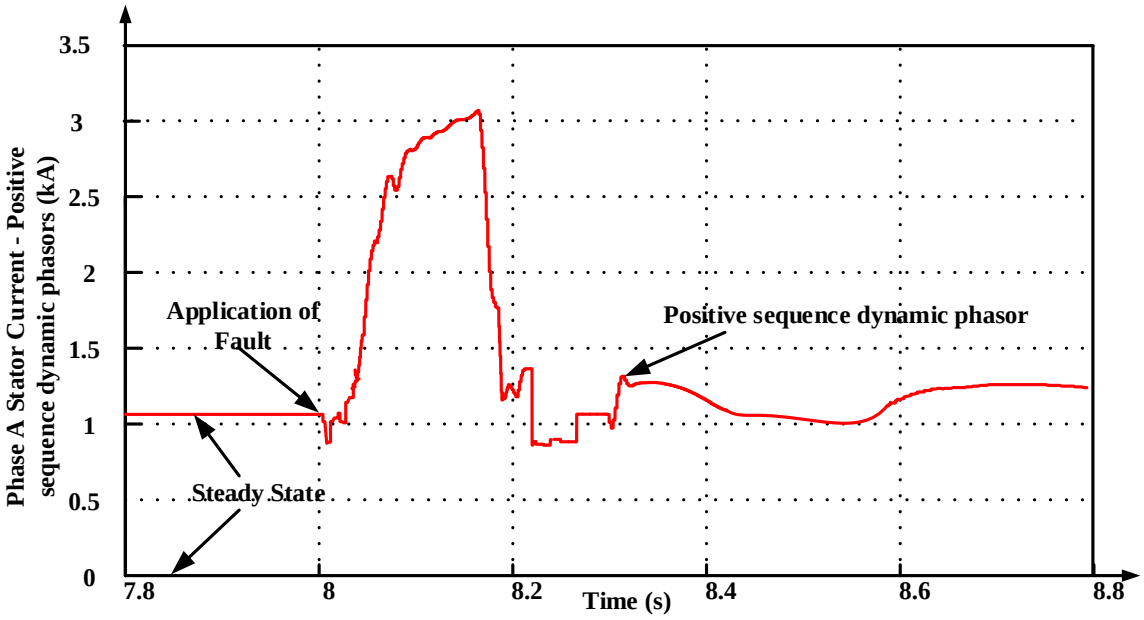

Figure 5.8: Relative magnitude of positive and negative sequence dynamic phasors for a symmetrical fault

The appropriate choice of the required dynamic phasors (Fourier coefficients) to accurately represent the symmetrical short circuit behaviour would be the 60 Hz fundamental frequency coefficients (positive sequence dynamic phasor). Negative sequence dynamic phasors are not included as this is a symmetrical fault. The selection of appropriate dynamic phasors was discussed previously in Table 5.1.

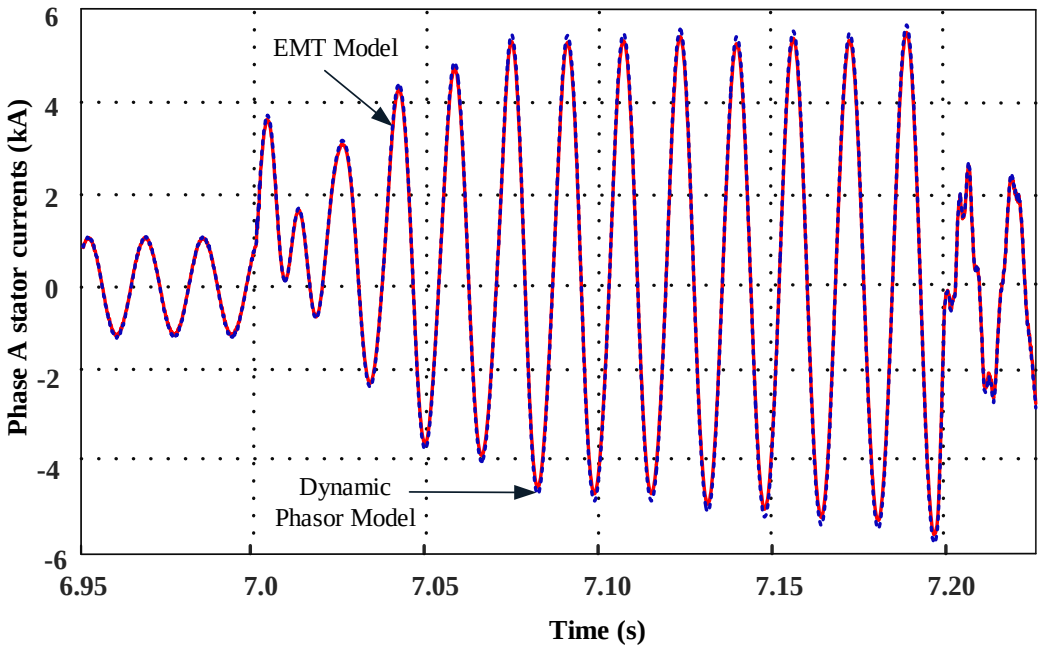

Figure 5.9: Comparison of EMT and dynamic phasor modelling for symmetrical fault

The fault current output (phase A stator current) for the symmetrical three phase fault is shown in Figure 5.9, which compares the EMT and dynamic phasor model results. The fault current waveforms show that the positive sequence dynamic phasor is capable of accurately representing the symmetrical fault behaviour of the Type 3 wind generator. However, the upcoming sections show that just using the positive sequence (fundamental frequency) dynamic phasor is not sufficient to obtain accurate short circuit behaviour.

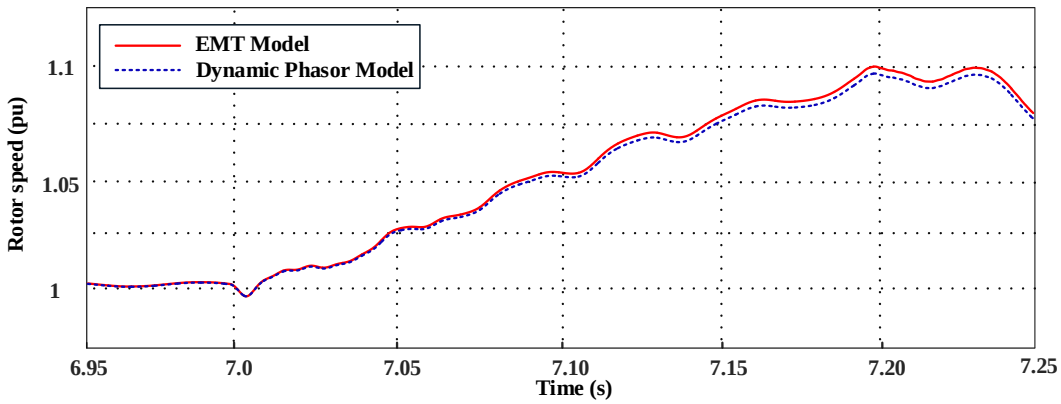

Figure 5.10: Rotor speed for symmetrical fault

Figure 5.10 shows response of rotor speed to symmetrical fault. The responses of detailed EMT model and dynamic phasor model is very close. From figure 5.10 it is clear that there is a speed drop immediately after the fault occurs, caused by transient torques developed by the interaction of currents and fluxes.

5.3.1.2 Unsymmetrical Fault behaviour

For the same test system under study, a 200 ms unsymmetrical phase A to ground fault was applied and the response of the wind farm in terms of the phase A fault current is shown in Figure 5.11 below.

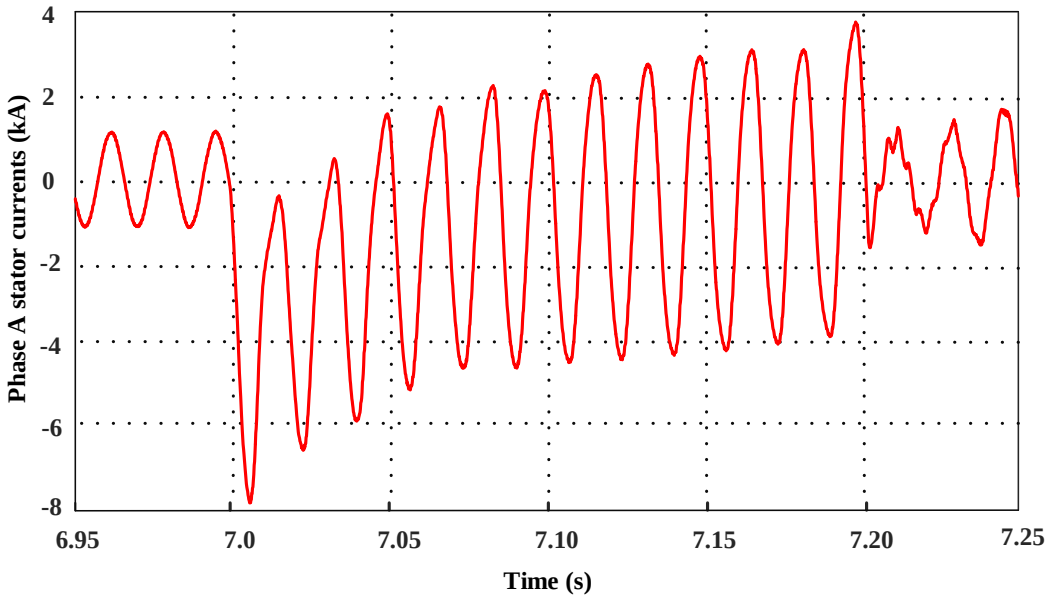

Figure 5.11: Fault current for Type 3 wind farm unsymmetrical fault application - EMT model

The unsymmetrical fault current contains both positive and negative sequence components. Hence, both the positive and negative sequence dynamic phasors were chosen in order to accurately model the unsymmetrical fault behaviour. Figure 5.12 below shows the relative magnitudes of the positive and negative sequence dynamic phasors.

The accuracy of the dynamic phasor model was assessed by comparison with the EMT model results. In order to represent the unsymmetrical fault behaviour, the appropriate choice of Fourier coefficients would be the positive sequence coefficient and the negative sequence coefficient. Now, considering both of these components, the phase A stator fault current obtained from the dynamic phasor model is compared with the EMT simulation results as shown in Figure 5.13. The rotor speed response to an unsymmetrical fault is shown in figure 5.14. A high degree of accuracy was achieved with the dynamic phasor representation for unsymmetrical fault behaviour of the Type 3 wind farm.

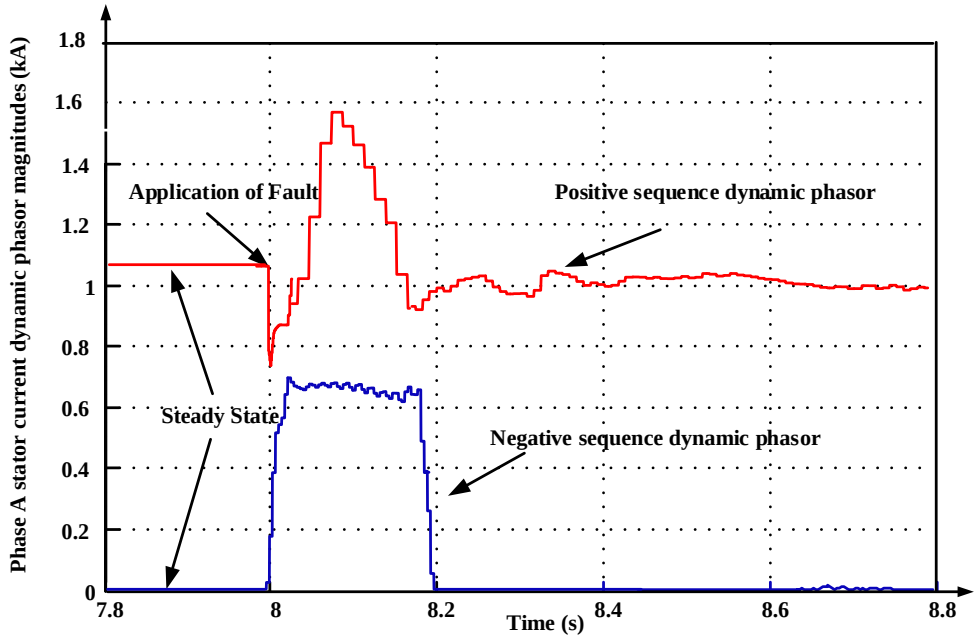

Figure 5.12: Relative magnitude of positive and negative sequence dynamic phasors for an unsymmetrical fault

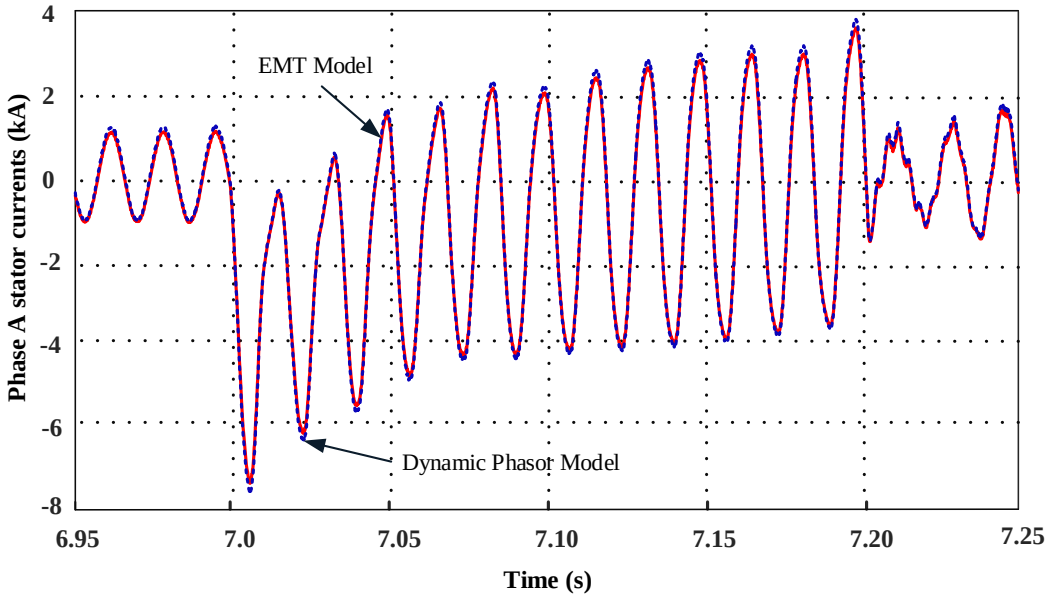

Figure 5.13: Comparison of EMT and dynamic phasor modelling for Type 3 wind farm unsymmetrical fault application

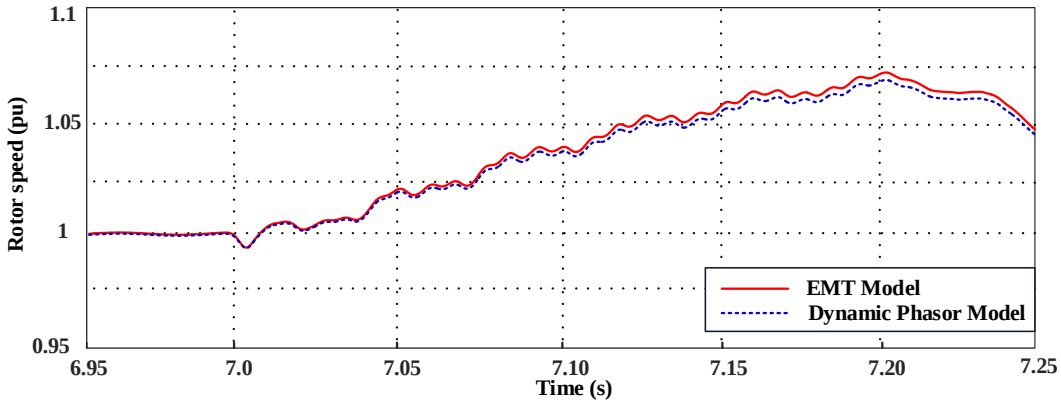

Figure 5.14: Rotor speed for unsymmetrical fault

5.3.2 Fault behaviour with a Series Compensated Transmission Line

Chapter 4 discussed the scenario of a Type 3 wind farm connected to a series compensated transmission line. The interaction between the series compensated line and the Type 3 wind generator with the converters led to SSCI and the presence of sub-synchronous frequencies in the fault current waveform. In order to test the accuracy of the proposed dynamic phasor model to represent such a fault behaviour, the correct choice of the appropriate dynamic phasors (Fourier coefficients) is critical.

5.3.2.1 Symmetrical Fault behaviour

The fault current behaviour of the Type 3 wind farm with the series compensated line for a 200 ms 3 phase fault is shown below in Figure 5.15. In Section 4.3, FFT analysis and prony analysis of the fault current waveform were used to show that, apart from the fundamental frequency component, a sub-synchronous frequency component with an approximate frequency of 36.2 Hz for 50 % compensation and 41.977 Hz for 70 % compensation were also present. This value was verified by the frequency scanning technique in Section 4.4.

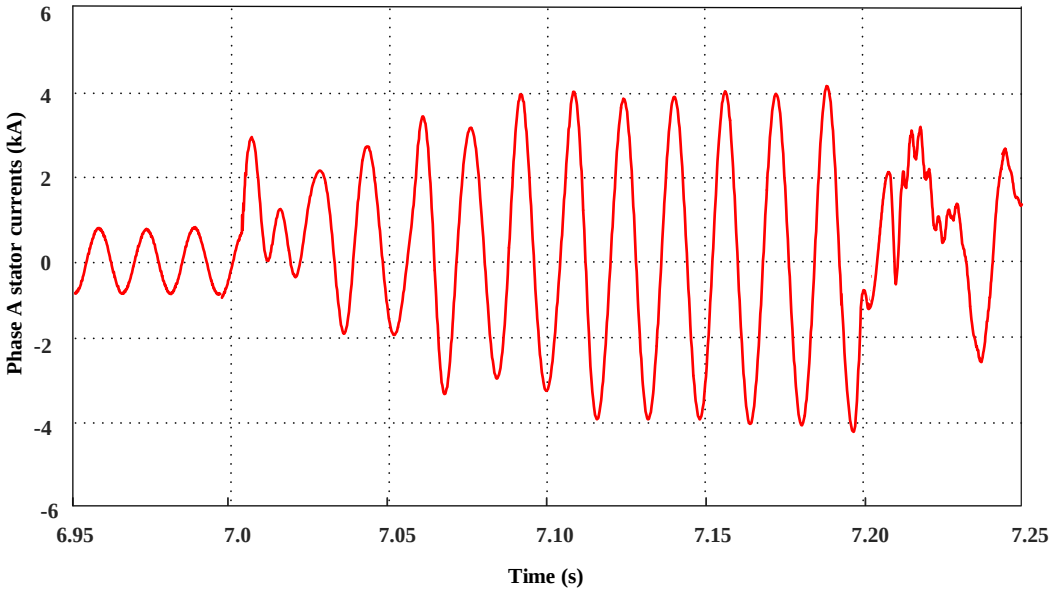

Figure 5.15: Type 3 wind farm phase A fault current for symmetrical fault with 50% compensation - EMT model

For accurate representation of this type of a fault, as shown in Table 5.1, the positive sequence and sub-synchronous component dynamic phasors are to be chosen. The negative sequence dynamic phasor is not included as this is a symmetrical fault. Figure 5.16 shows the relative magnitude of the positive sequence component dynamic phasors for a 200 ms three phase fault for a Type 3 wind farm with a 50% series compensated transmission line.

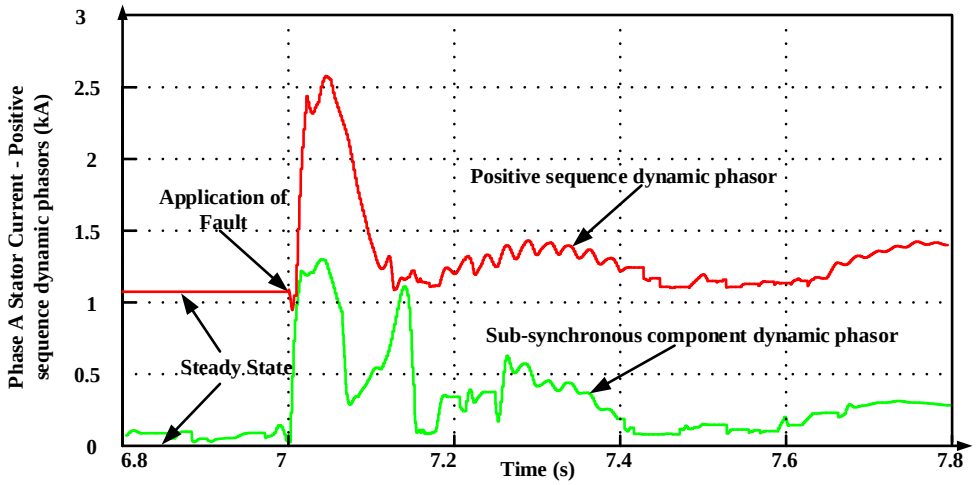

Figure 5.16: Relative magnitude of positive and sub-synchronous component dynamic phasors for a symmetrical fault in a 50% compensated Type 3 wind farm

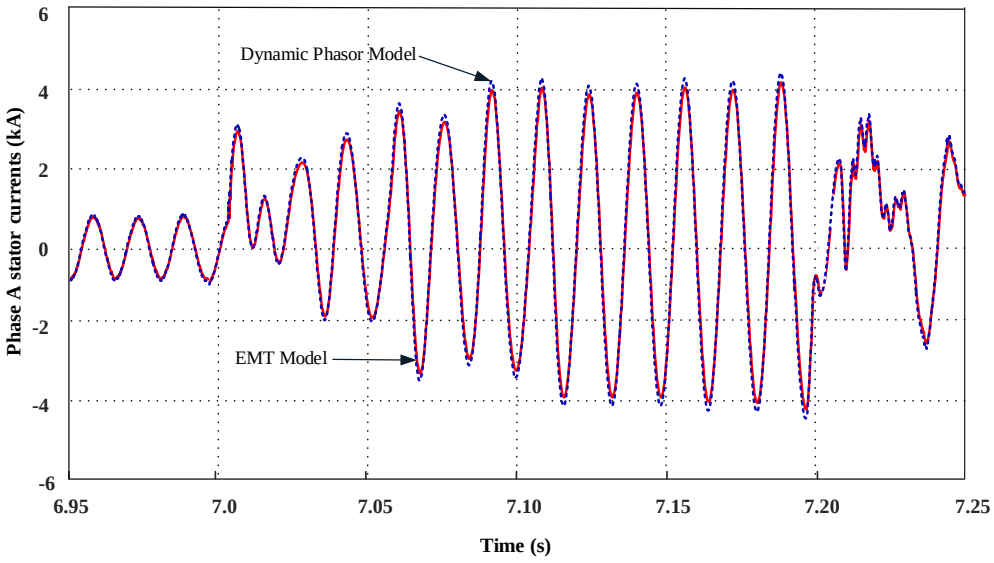

Figure 5.17: Comparison of EMT and dynamic phasor modelling for 50% compensated Type 3 wind farm symmetrical fault application

Figure 5.17 shows the comparison of the phase A fault current obtained from the EMT and the dynamic phasor modelling considering both the fundamental and sub-synchronous

frequency Fourier coefficients.

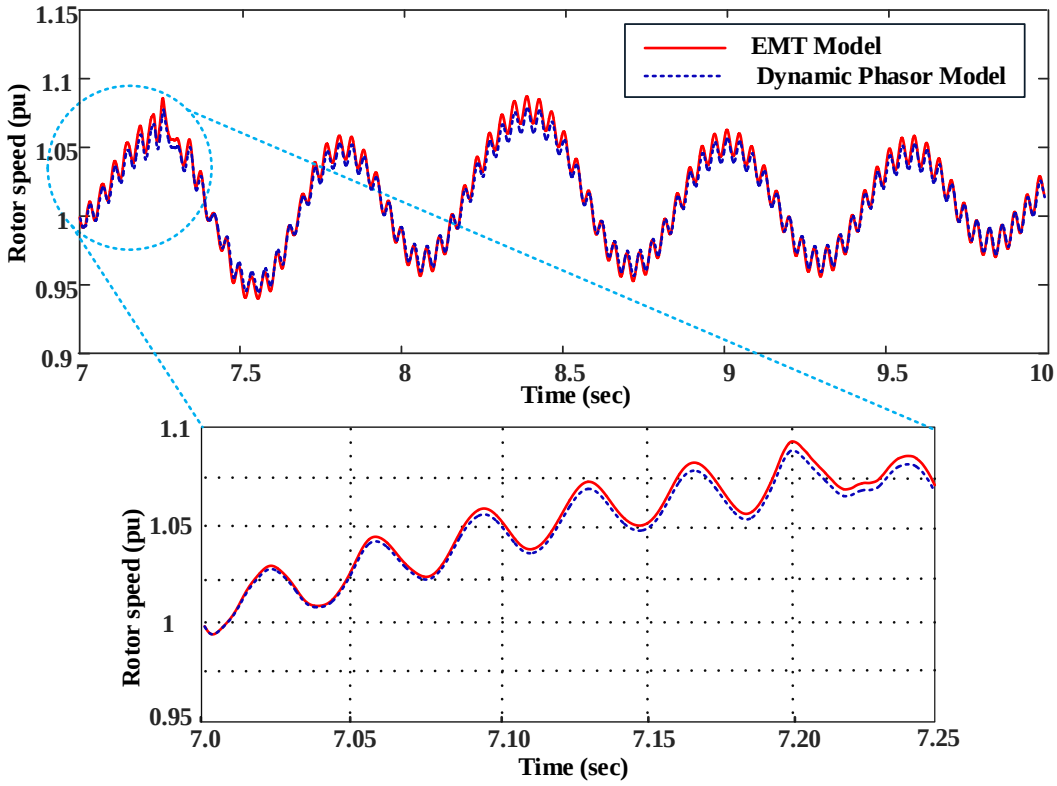

Figure 5.18: Rotor speed for 50% compensation under symmetrical fault

Figure 5.18 compares rotor speed response of EMT model and dynamic phasor model to symmetrical fault.

The rotor response shows that it has some low frequency (0-1 Hz) oscillations. Since 6 Hz is used as base frequency while developing dynamic phasors, these low frequency oscillations are taken care by (0-6)Hz frequency bandwidth.

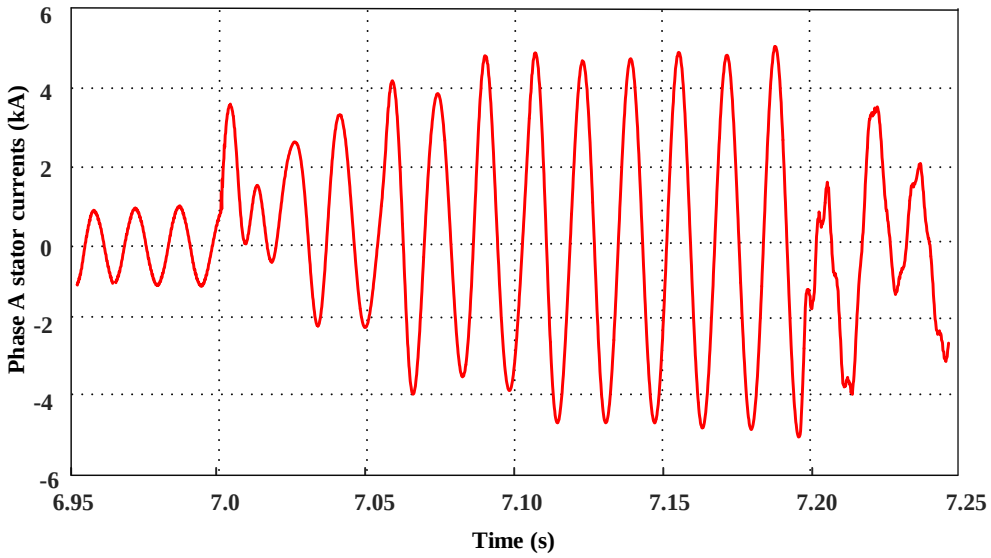

Figure 5.19: Type 3 wind farm phase A fault current for symmetrical fault with 70 % series compensation - EMT model

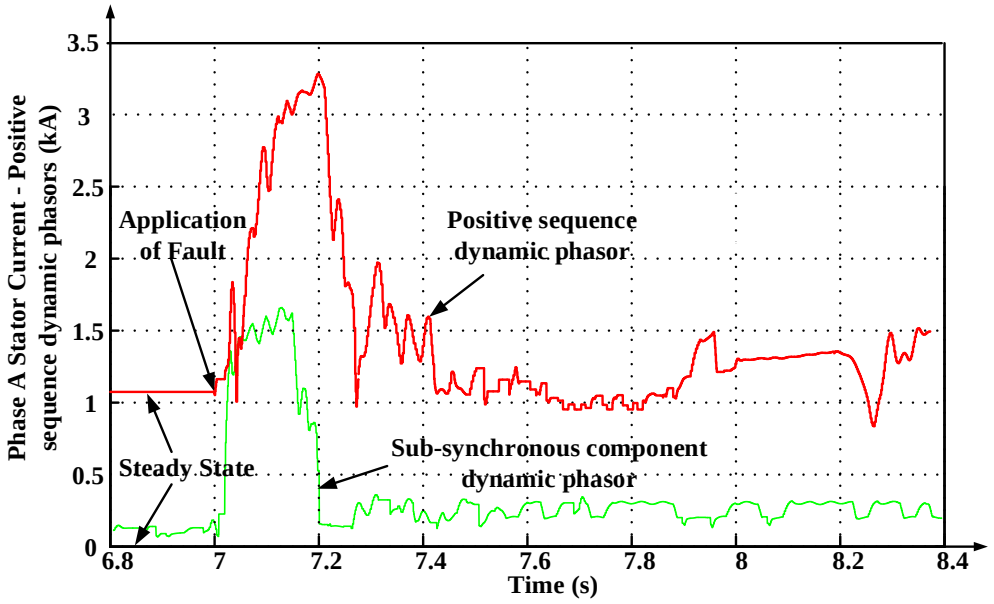

Figure 5.20: Relative magnitude of positive and sub-synchronous component dynamic phasors for a symmetrical fault in 70% compensated Type 3 wind farm

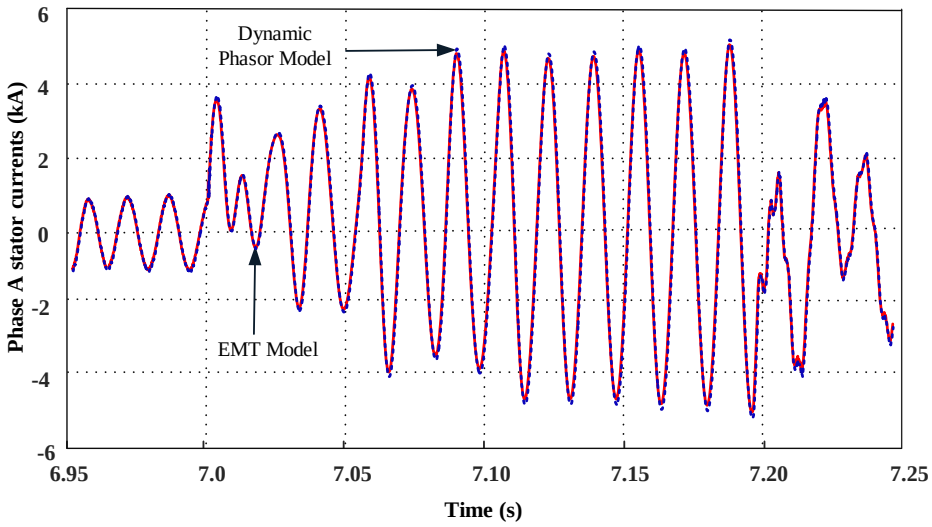

Figure 5.21: Comparison of EMT and dynamic phasor modelling for 70 % compensated Type 3 wind farm symmetrical fault application

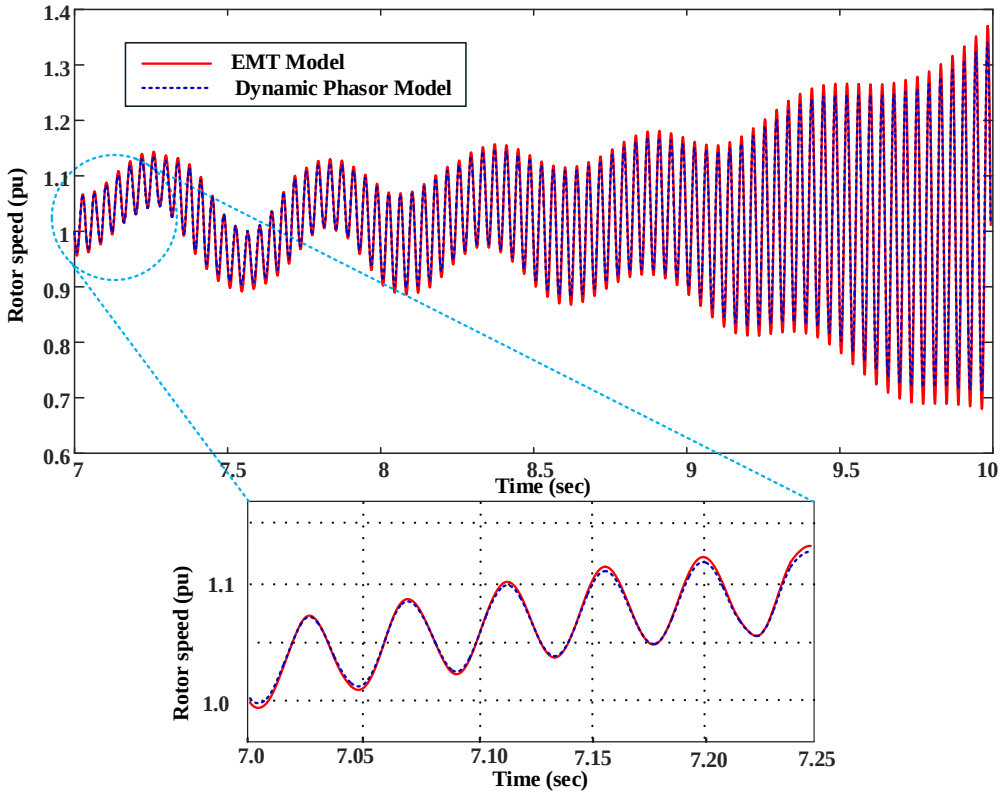

Figure 5.22: Rotor speed for 70% compensation under symmetrical fault

Figure 5.19, 5.20, 5.21 and 5.22 show result for 70 % compensation. The accuracy of the dynamic phasor model is high, even for scenarios with sub-synchronous oscillations.

5.3.2.2 Unsymmetrical Fault behaviour

The dynamic phasor model is also tested for accuracy for representing the unsymmetrical fault behaviour of a series compensated Type 3 wind farm. The phase A fault current obtained from the detailed EMT model for 50% compensation is shown in Figure 5.23 below.

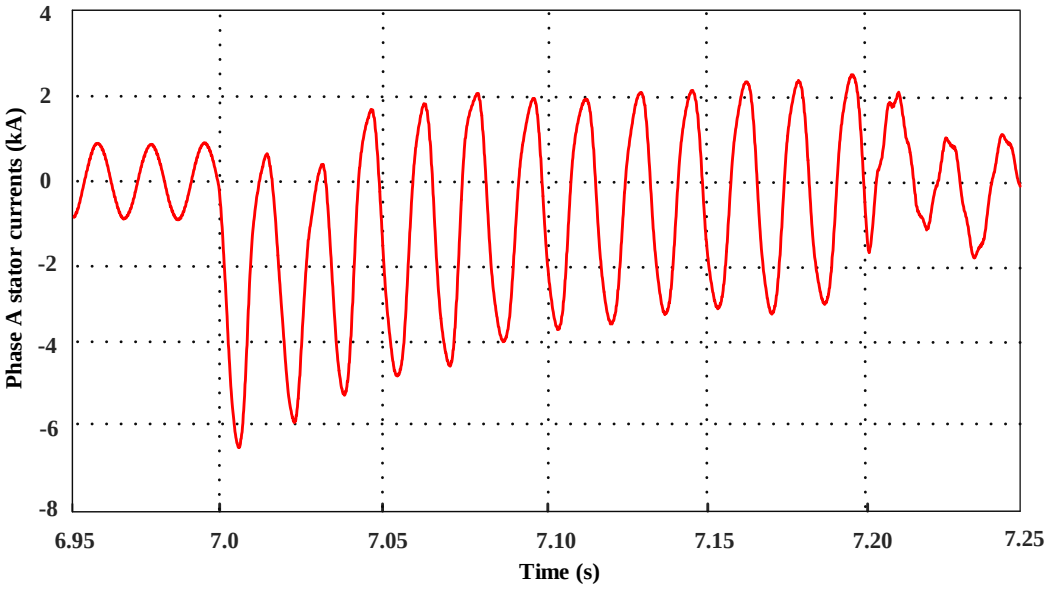

Figure 5.23: Type 3 wind farm phase A fault current for unsymmetrical fault with 50 % series compensation - EMT model

The dynamic phasor model for the Type 3 wind farm is developed by choosing the appropriate Fourier coefficients, which are the positive sequence, negative sequence and sub-synchronous component dynamic phasors as explained in Table 5.1. Figure 5.24 below shows the relative magnitudes of the dynamic phasors. Using this selection of dynamic phasors, the model was developed. Figure 5.25 shows dynamic phasor response which is in line with EMT model response.

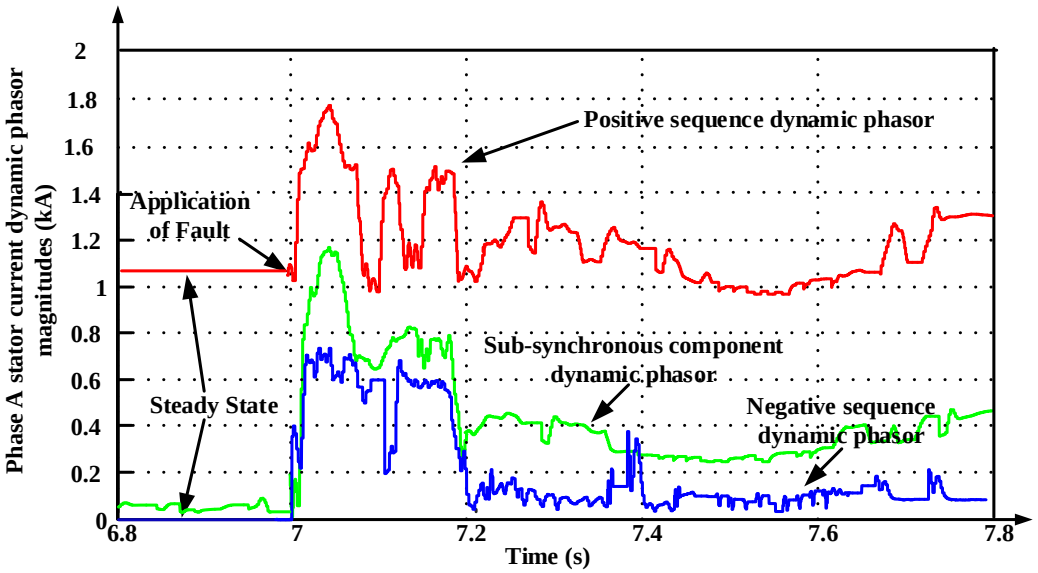

Figure 5.24: Relative magnitude of positive sequence, negative sequence and sub-synchronous component dynamic phasors for an unsymmetrical fault in a 50% compensated Type 3 wind farm

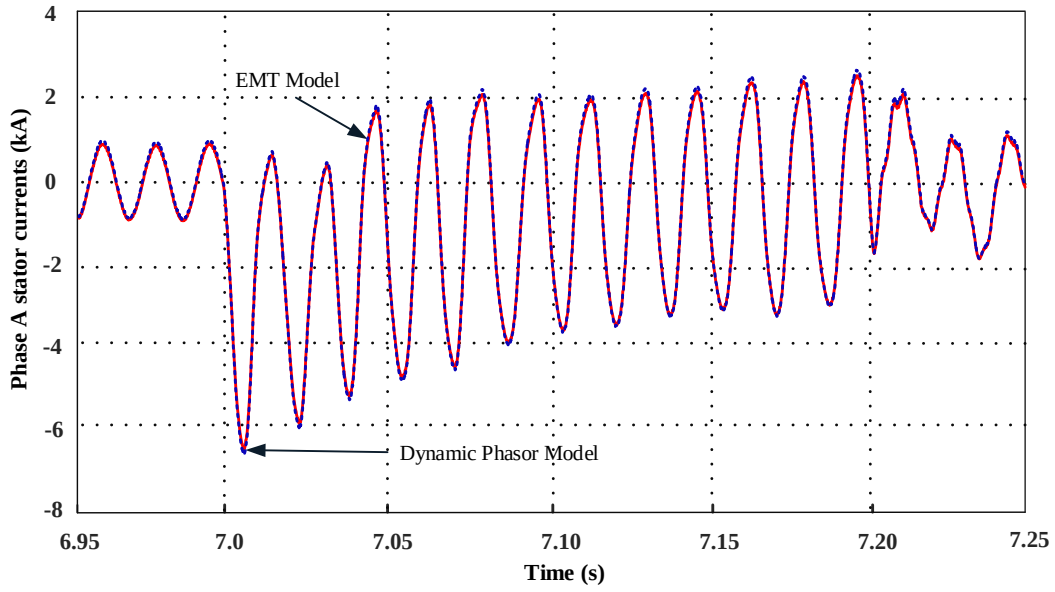

Figure 5.25: Comparison of EMT and dynamic phasor modelling for 50 % compensated Type 3 wind farm unsymmetrical fault application

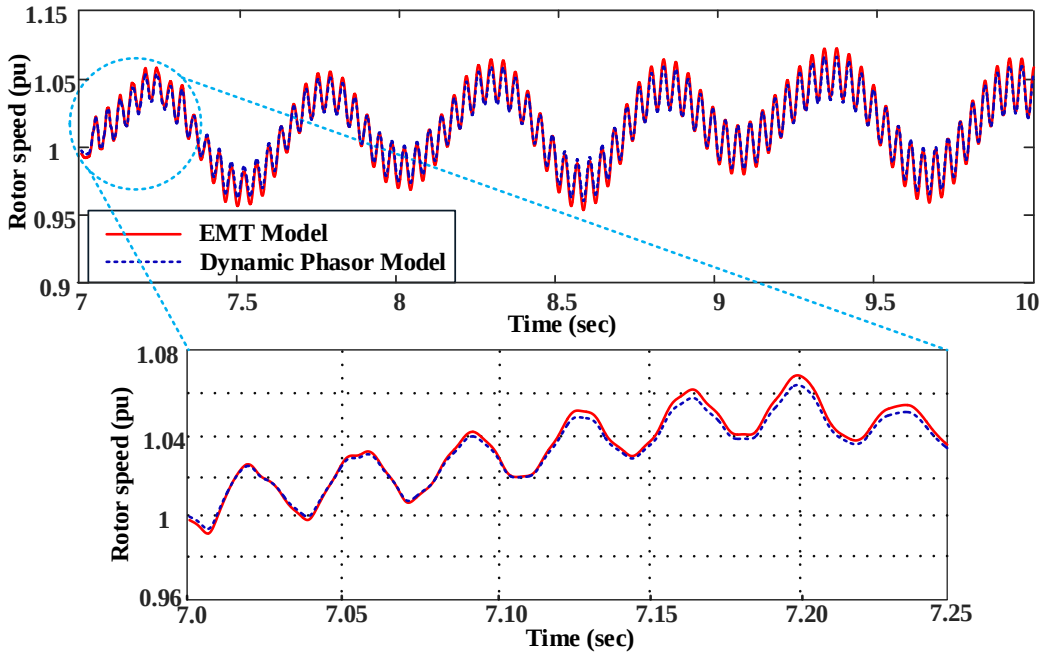

Figure 5.26: Rotor speed for 50% compensation under unsymmetrical fault

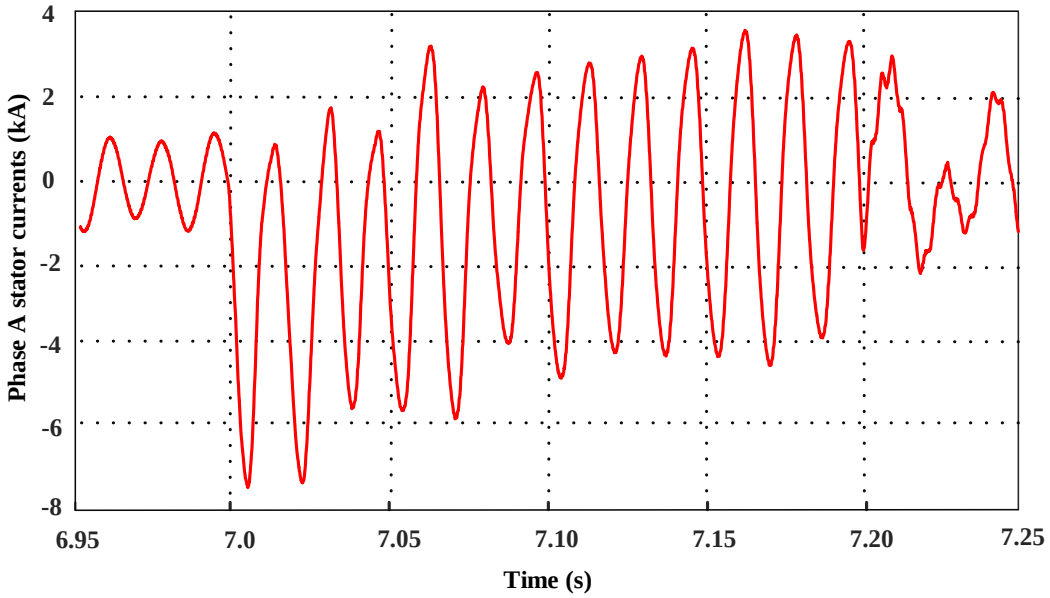

Figure 5.27: Type 3 wind farm phase A fault current for unsymmetrical fault with 70 % series compensation - EMT model

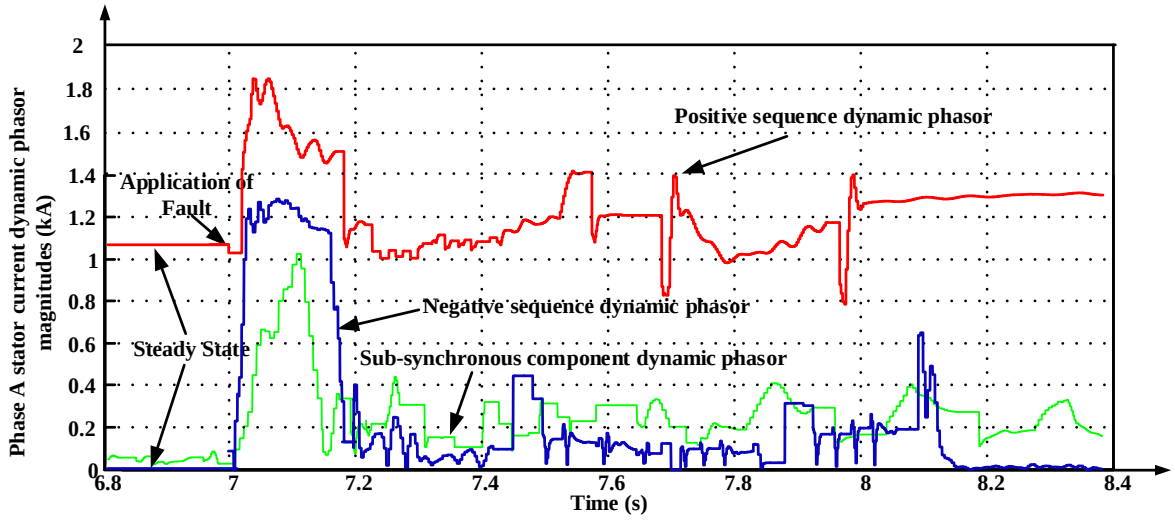

Figure 5.28: Relative magnitude of positive sequence, negative sequence and sub-synchronous component dynamic phasors for an unsymmetrical fault in a 70 % compensated Type 3 wind farm

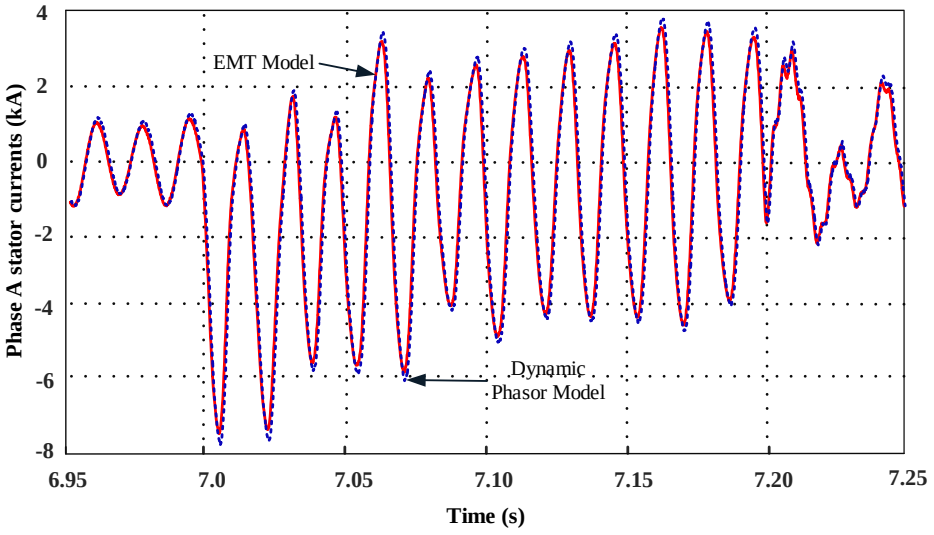

Figure 5.29: Comparison of EMT and dynamic phasor modelling for 70 % compensated Type 3 wind farm unsymmetrical fault application

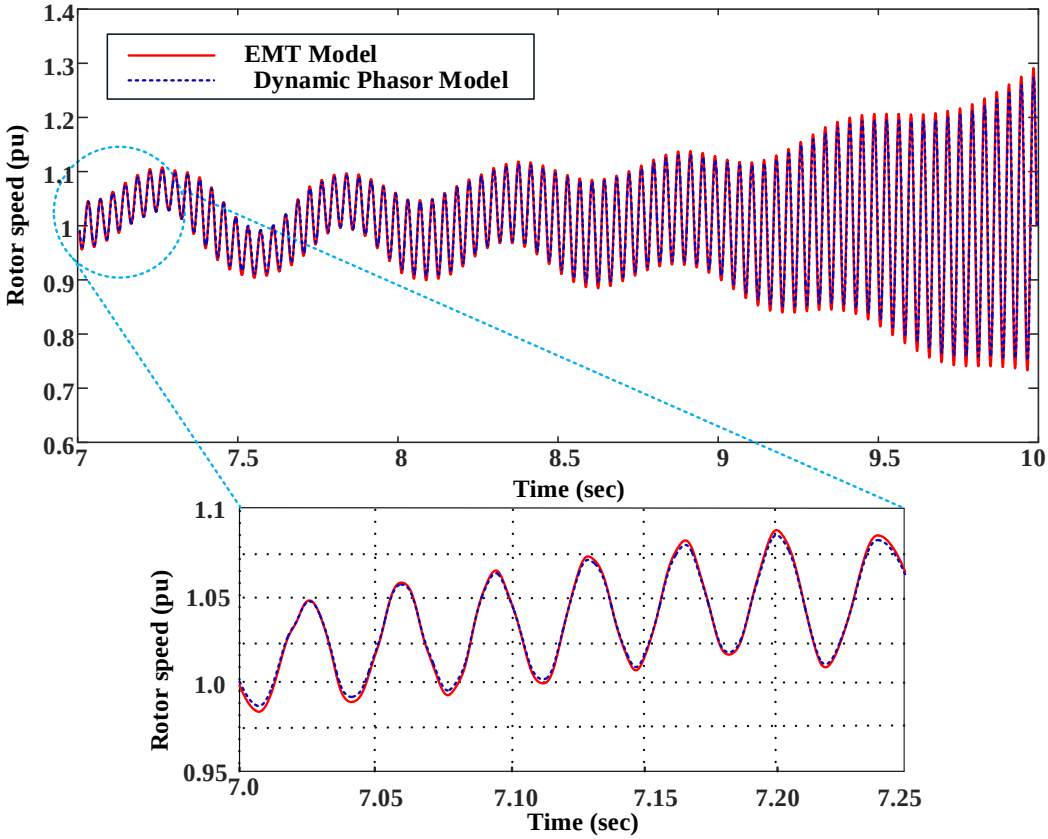

Figure 5.30: Rotor speed for 70% compensation under unsymmetrical fault

Figures 5.27, 5.28, 5.29 and 5.30 shows results for 70 % compensation scenario. It shows the high level of accuracy achieved with the developed model as compared to EMT simulation results.

5.4 Average Value Model

This section describes the average-value modelling of the voltage source converters used in DFIG wind power plant. The detailed model simulation of power electronic switches is time consuming due to change of the system topology in every switching instant. The approach that is used to overcome this issue is to obtain a time invariant circuit topology by averaging the power electronic switchings, which is called as average value modelling

technique in the literature. The average value model represents the switches by equivalent current and voltage sources. In average value models, some details of the power electronic converter such as higher harmonic contents are eliminated. However, these details are not significantly useful in many cases, and can therefore be ignored.

5.4.1 Average Value modelling of DFIG

As mentioned in Chapter 3, SPWM technique is used to generate firing pulses for the back-to-back converter used in DFIG. In the SPWM technique, a switching pulse is generated from comparison of a high frequency triangular waveform with a sinusoidal reference signal. The SPWM scheme and the dynamic average-value outputs are illustrated in figure 5.31. The frequency of the sinusoidal reference signal should be relatively small compared to the triangular waveform frequency. Within a short time period, the sinusoidal waveform can be approximated with a constant value, as illustrated in figure 5.31.

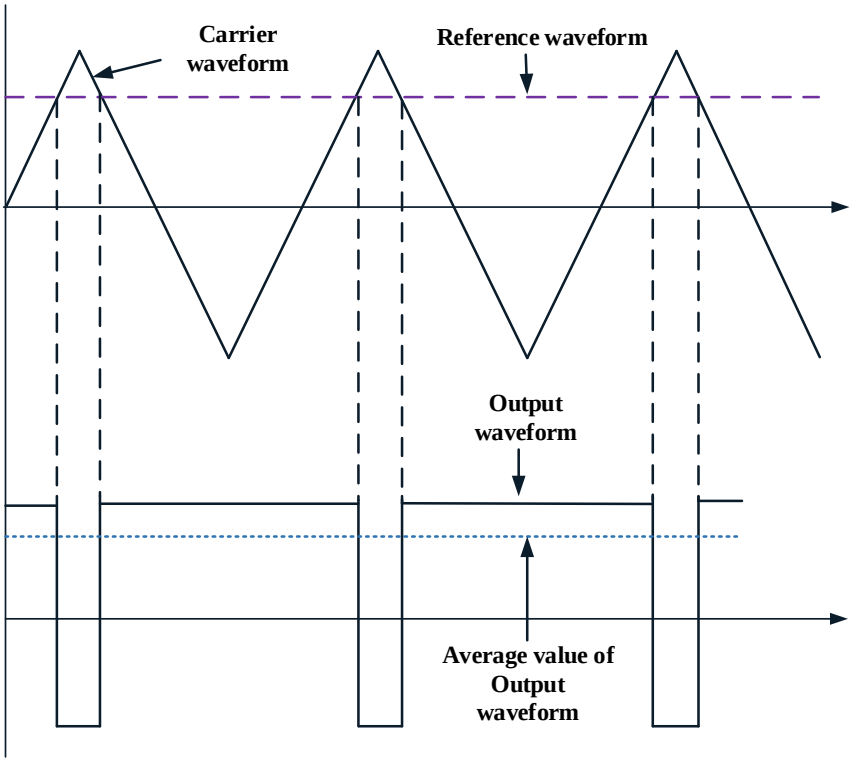

Figure 5.31: PWM scheme and Average value output

The average value of variable $x(\tau)$ over a switching cycle of T is [112, 113]

$$\bar{x}(t) = \frac{1}{T}\int_0^T x(\tau)d\tau \tag{5.54}$$

where $\bar{x}(t)$ is the averaged voltage (or current) waveform of the conveter as discussed in [112]. Using equation 5.54, the AC voltage of a converter can be written as [112, 113]

$$\bar{v}_a(t) = \bar{m}_a(t)\frac{V_{dc}}{2} \tag{5.55}$$

where $\bar{v}_a(t)$ and $\bar{m}_{abc}(t)$ are the averaged values phase a output voltage and modulation index respectively.

For phases b and c,

$$\bar{v}_b(t) = \bar{m}_b(t)\frac{V_{dc}}{2} \tag{5.56}$$

$$\bar{v}_c(t) = \bar{m}_c(t)\frac{V_{dc}}{2} \tag{5.57}$$

The modulation indices of the three phases are determined in a way the output phase voltages generate symmetrical three phase voltage. The relationship between the modulation indices of phases a, b, and c is as follows:

$$\bar{m}_a(t) = m.cos(\theta) \tag{5.58}$$

$$\bar{m}_b(t) = m.cos(\theta - \frac{2\pi}{3}) \tag{5.59}$$

$$\bar{m}_c(t) = m.cos(\theta + \frac{2\pi}{3}) \tag{5.60}$$

In dq frame, Equations 5.55-5.57 can be written as,

$$\bar{v}_d(t) = \bar{m}_d(t)\frac{V_{dc}}{2} \tag{5.61}$$

$$\bar{v}_q(t) = \bar{m}_q(t)\frac{V_{dc}}{2} \tag{5.62}$$

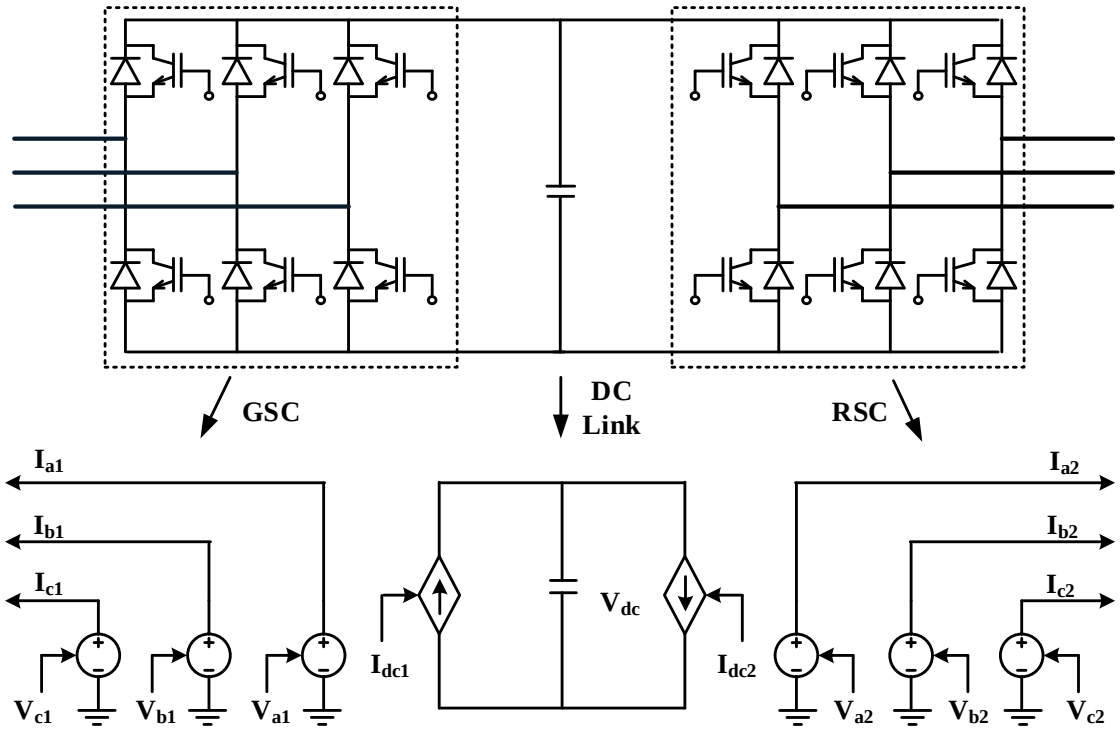

Figure 5.32: Average value model for back to back converters

If the converter is lossless, the DC side power and AC side power are equal [112]. Then, DC side current can be calculated as,

$$P_{dc}(t) = P_{ac}(t) \tag{5.63}$$

$$V_{dc}(t)I_{dc}(t) = v_a(t)i_a(t) + v_b(t)i_b(t) + v_c(t)i_c(t) \tag{5.64}$$

$$I_{dc}(t) = \frac{v_a(t)i_a(t) + v_b(t)i_b(t) + v_c(t)i_c(t)}{V_{dc}(t)} \tag{5.65}$$

Furthermore, in dq frame,

$$I_{dc}(t) = \frac{\frac{3}{2}\left[v_d(t)i_d(t) + v_q(t)i_q(t)\right]}{V_{dc}(t)} \tag{5.66}$$

5.4.2 Simulation Results

Figures 5.33 and 5.34 show a comparison of the transient response of the DFIG wind generator stator current with the Average value model (AVM), the detailed EMT Model and the proposed Dynamic Phasor model to a 6 cycle symmetrical and unsymmetrical fault at the DFIG terminal. Figures 5.33 and 5.34 show that the responses of the AVM and the proposed dynamic phasor model are very close with the EMT model in steady state condition.

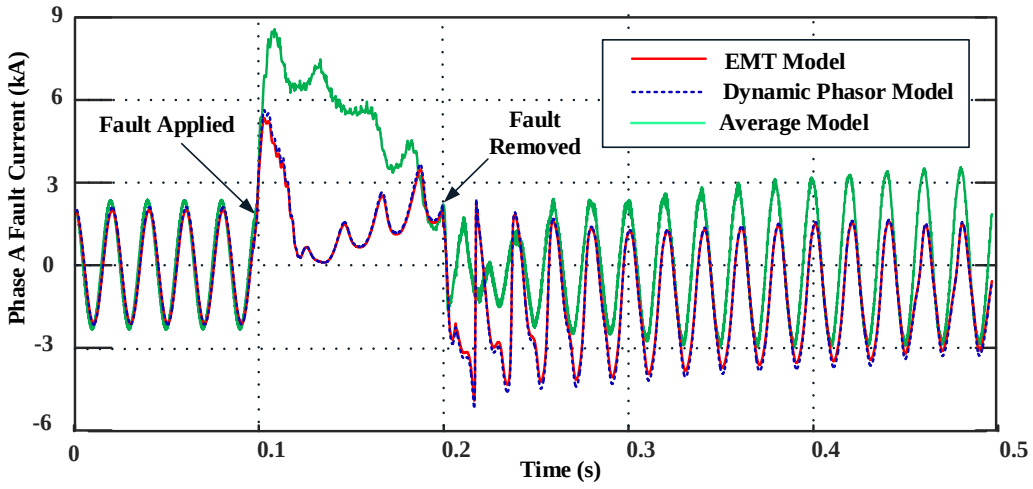

Figure 5.33: Phase A stator current for symmetrical fault

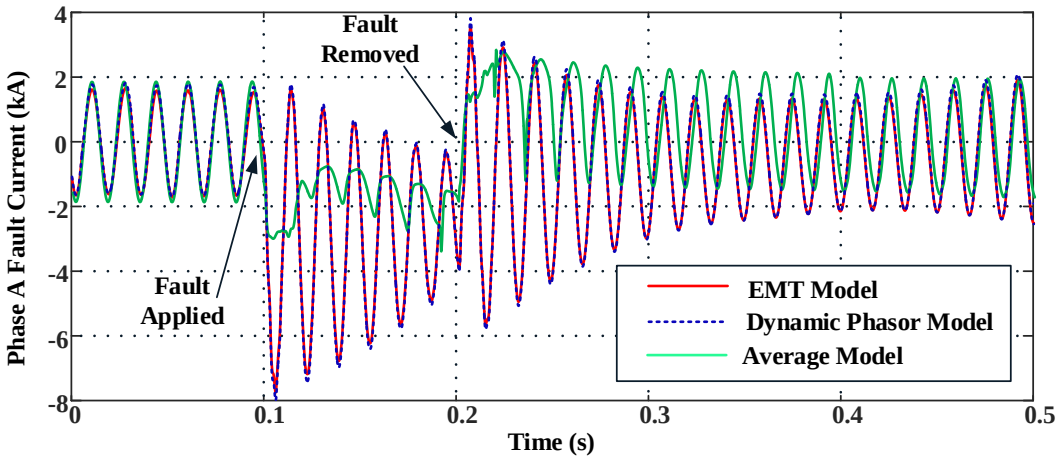

Figure 5.34: Phase A stator current for unsymmetrical fault

The response of EMT model and the dynamic phasor model are still similar during fault period but there is a mismatch between response of AVM and the EMT model for fault period. The deviations in the transient response of the AVM from the EMT model are due to the simplifications that are used in the AVM which does not represent the IGBT switches and the high switching frequency dynamics of the VSC. Figure 5.35 shows the rotor speed response for a symmetrical fault condition. The AVM rotor speed plot response is not accurate compared with the dynamic phasor model and EMT rotor speed plots.

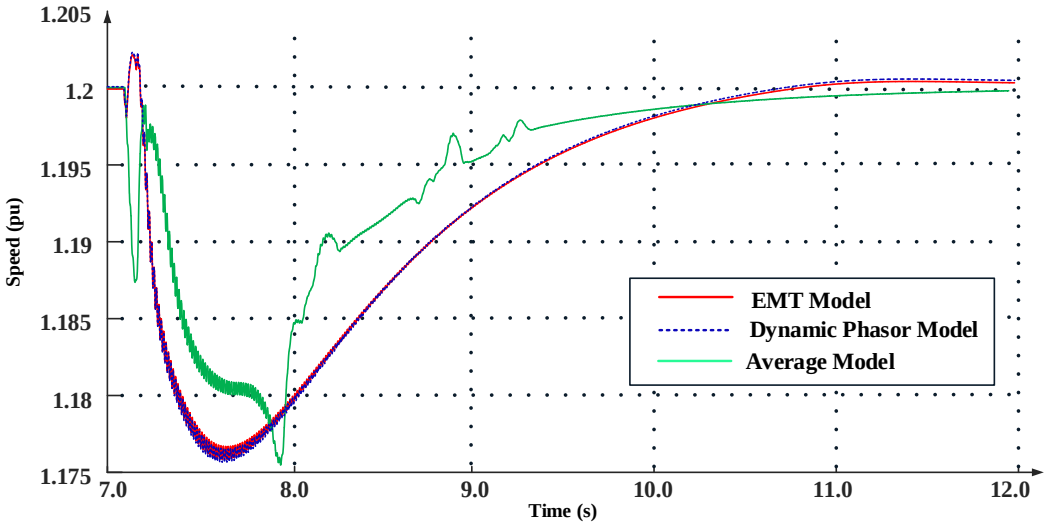

Figure 5.35: Rotor speed for symmetrical fault

5.5 Summary

This chapter discussed the dynamic phasor modelling of power system variables as time-varying Fourier coefficients. Using this modelling approach allows selective inclusion of only the appropriate dynamic phasors based on the fault behaviour to be represented, making it computationally efficient. The dynamic phasor modelling was further researched in detail and the differences from other alternative terminology "shift-frequency" approaches used in the literature were also discussed. In the shift frequency approach, the frequency spectrum of all signals is shifted by frequency ω_s so that the system frequency spectrum lies around 0 Hz. Therefore, the simulation speed is significantly faster than EMT simulations, that utilize small time step differential equations. When other harmonics are taken into consideration in a shift frequency modelling, the simulation speed would be not as different from detailed EMT simulations.

With the proposed dynamic phasor modelling approach, however,all frequency components are shifted to 0 Hz. Therefore, larger simulation timesteps can be used and the simulation speed will be faster while still maintaining high accuracy (as EMT). The dynamic

phasor model of the DFIG wind farm was tested for two different compensation levels: 50 and 70%. The results for rotor speed showed that low frequency (0-1 Hz) components were also present. Because 6 Hz was used as base frequency while developing the dynamic phasors, these low frequency oscillations were taken care of by the 0-6 Hz frequency bandwidth in the dynamic phasor model.

An average value model of the DFIG wind generator was also developed and the results compared with the proposed dynamic phasor model. This work showed that the dynamic phasor model is fast and accurate even during complex control interactions and LVRT periods.

Chapter 6

Summary, Conclusions, Contributions and Future Work

6.1 Summary

Chapter 1 discussed the background with the present scenario of wind power integration and its foreseeable growth for future energy needs. Wind generators have evolved from conventional Type 1 squirrel cage induction generators and Type 2 wound rotor induction generators to complex power electronic converter based Type 3 doubly fed induction generator based and Type 4 full converter based wind generators. Type 3 is currently the most commonly used type, comprising approximately 66% of all wind generators.

Chapter 2 discussed the various types of wind turbine generators and the different modelling techniques used to represent their short circuit behaviour. Type 1 and Type 2 wind generators can be accurately represented using a voltage behind transient reactance model. A fundamental frequency based model can accurately model their symmetrical fault behaviour. However, such simplified modelling techniques are not accurate enough to represent the fault behaviour of Type 3 wind generators due to their inherent assumptions. Even though the voltage dependent current source model is accurate, it is a black box approach and not a standalone model as it depends on other modelling techniques for the fault current values. The WECC Type 3 generic WTG model is also presented. This model uses only a two mass model, which is inadequate for capturing the electromechanical oscillatory behaviour.

The detailed modelling of wind farm components was carried out in Chapter 3. The equations representing multimass, induction machine, rotor side converter, grid side converter,

and electrical networks were presented. It also covered control schemes for RSC and GSC. The effect of flux decrement was also investigated in this chapter. Various LVRT topologies were discussed and compared.

modelling of DFIG wind farms connected to series compensated transmission lines for small signal analysis was discussed in detail in Chapter 4. The proposed detailed analysis clearly identifid the participating state variables of the sub-synchronous oscillation mode. The root cause of SSCI was also identified.

Chapter 5 discussed the shift frequency approach, the proposed dynamic phasor approach and the average value modelling approach. In the shift frequency approach, the real signal was shifted by ω_s. This approach was found to be efficient if only the base system frequency (60 Hz) is considered. When subharmonics or higher harmonics were included, however, this approach was not as efficient. The proposed dynamic phasor modelling technique was found to accurately represent sub-harmonic SSCI effects in a DFIG wind farm, and at the same time, not be as cumbersome to build as a detailed EMT model. The main idea behind the dynamic phasors approach was to represent the system quantities by their time varying Fourier coefficients. This model could selectively model only those frequency components required for the fault behaviour under study, making it efficient. The model was shown to be capable of accurately representing both symmetrical and unsymmetrical fault behaviour as well as sub-synchronous interactions with a high degree of accuracy by comparing its results against benchmark detailed EMT models for two different compensation levels: 50 and 70%. In the AVM, the power electronics switches were replaced by equivalent voltage and current sources. The transient response of the AVM was compared with that of the detailed EMT model. It was clear from the studies that the AVM is not accurate for short circuit studies.

6.2 Conclusions

The new research included real-time simulation modelling, including multi-mass behaviour, flux decrement effects on the faulted current, and low voltage ride through behaviours using SDBR in rotor and stator circuits. The root cause of sub-synchronous frequencies in Type

3 wind generators was analyzed using small signal analysis and sub-synchronous oscillations were shown to be due to control interactions between the rotor side controller of the induction generator and the series capacitor in the transmission line. Dynamic phasor modelling was further researched in detail in the thesis and the differences from other alternative "shift-frequency" approaches in popular use in the literature were also discussed. An average value model of the Type 3 wind generator was developed and the results compared with the dynamic phasor model; this showed that the dynamic phasor model is fast and accurate even during complex control interactions, such as LVRT periods.

6.3 Contributions of the Thesis

This thesis advanced the Type 3 generic type modelling of DFIG wind generators previously carried out at the Real-Time Simulations Laboratory at the University of Saskatchewan in 2013. The following are the main contributions of this thesis :

- *Detailed modelling of a Type 3 wind generator in RTDS/RSCAD (including use of multi-mass model and consideration of flux decrement effects on fault current behvaior):* A Type 3 wind power generation system, which is widely used in the industry, was modeled in RTDS/RSCAD. The multimass turbine equations, induction machine equations, and converter equations were developed in a d-q reference frame. A decoupled method was used for the rotor and grid side converters to independently control the real and reactive power . Flux decrement effects in the rotor were also included in the model developed. The rotor d-q current controlled the stator side active and reactive power while the grid side converter d-q current controlled the rotor side complex power.

- *Comparison of different topologies for LVRT:* This research work investigated different topologies for LVRT: conventional crowbar, DC-link voltage protection scheme, SDBR in rotor circuit, and SDBR in stator circuit. The research work showed that use of SDBR on the stator side along with a DC link voltage protection scheme provided better control and operation of the wind farm.

- *A comprehensive analysis of sub-synchronous interactions in a Type 3 wind farm:* This thesis discussed and theoretically analyzed the sub-synchronous control interactions in a Type 3 wind farm. The root cause of the sub- synchronous interaction in a power systems with Type 3 wind power plants and series compensated transmission lines was analyzed using small-signal analysis. The findings were in agreement with those reported by University of Manitoba researchers. It was shown that the sub-synchronous interactions in wind farm systems were caused by interactions between the wind power plant generator electrical system and the series capacitor.

- *Developing a Type 3 wind farm model taking into account both fundamental and non-fundamental frequency behaviour:* Detailed EMT models are capable of accurately representing a Type 3 wind farm's short circuit behaviour but are cumbersome and computationally demanding. In this thesis, a dynamic phasor modelling technique, based on a generalized averaging method and which has the ability to represent both fundamental and non-fundamental frequency behaviour, was proposed and implemented. This modelling approach allows the user to selectively add frequency components other than the fundamental frequency representation, namely the sub-synchronous frequency components. The sub-synchronous interaction scenario was modeled by considering two different series compensation levels in the transmission line connected to the Type 3 wind farm test system. This method was tested for symmetrical fault, unsymmetrical fault, and sub-synchronous interaction scenarios of Type 3 wind farms. The dynamic phasor modelling was further researched in detail in this thesis and the differences from other alternative "shift-frequency" approaches in popular use in the literature were discussed. An average value model of the Type 3 wind farm was developed and the results compared with the dynamic phasor model; this showed that the dynamic phasor model is fast and accurate even during complex control interactions, such as LVRT periods.

6.4 Future Work

- The dynamic phasor model was developed in a real time simulation environment. A separate MATLAB code for the dynamic phasor model can be developed for DFIG wind farms. Such an analysis will firmly quantify the computational benefits of simulating with a dynamic phasor model.

- The proposed dynamic phasor model needs validation with real fault data records obtained from utilities. This will provide a realistic validation of the proposed dynamic phasor modelling approach in addition to the EMT modelling approach carried out in this thesis.

- In this research, an aggregate model of the wind farm was used for fault studies. Only faults occurring outside the wind farms were considered; scenarios of faults inside the wind farm, i.e., faults occurring on the feeders connecting the individual wind generators to the substation, were not studied. The impedance of individual cables connecting the wind generator to the substation were also not considered. The short circuit behaviour of individual generators for faults occurring inside the wind farm and considering internal cable impedance must be studied.

- A Type 3 wind power plant was the main focus of this thesis. However, there is a possibility that other types of wind generators could be introduced to wind farms when new generation is added. The new technologies being introduced are Type 4 wind power plants, in which the wind turbine and the generator are decoupled from the external AC system by the converter in front of the unit so turbine generator interaction with the rest of the power system is unlikely. However, there could be converter controller interactions happening within the wind farm. This could be an interesting topic for future research.

References

[1] "Renewables 2016 Global Status Report," Renewable Energy Policy Network for the 21st Century (REN21), Tech. Rep., 2016.

[2] "Global Wind Report - Annual Market Update 2012," Global Wind Energy Council, Brussels, Tech. Rep., 2012.

[3] *Latest wind farm approval could trigger a renewable energy surge.* http://www.abc.net.au/news/2016-08-15/more-wind-farms-on-the-way-for-queensland/7736056.

[4] *Canada Wind Energy Association.* http://www.canwea.ca/.

[5] "Renewable Energy Essentials: Wind," International Energy Agency, Tech. Rep., 2008.

[6] M. Bejaoui, B. Marinescu, I. Slama-Belkhodja, and E. Monmasson, "Control of doubly-fed induction generator for wind energy in network context," *IET Renewable Power Generation*, vol. 8, no. 2, pp. 109–118, 2014.

[7] T. Ackermann, *Wind power in power systems, Second Edition.* John Wiley & Sons, 2012.

[8] E. Muljadi, N. Samaan, V. Gevorgian, Jun Li, and S. Pasupulati, "Short circuit current contribution for different wind turbine generator types," in *Power and Energy Society General Meeting, IEEE*, Minneapolis, Minnesota, USA, 2010, pp. 1–8.

[9] E. Gursoy and R. A. Walling, "Representation of variable speed wind turbine generators for short circuit analysis," in *Electrical Power and Energy Conference (EPEC), IEEE*, Winnepeg, Manitoba, Canada, Oct 2011, pp. 444–449.

[10] G. D. Irwin, A. K. Jindal, and A. L. Isaacs, "Sub-synchronous control interactions between Type 3 wind turbines and series compensated AC transmission systems," in *Power and Energy Society General Meeting, IEEE*, Detroit, Michigan, USA, 2011, pp. 1–6.

[11] C. Karawita and U. Annakkage, "A hybrid network model for small signal stability analysis of power systems," in *Power and Energy Society General Meeting, IEEE*, Minneapolis, Minnesota, USA, July 2010, pp. 25–29.

[12] A. Luna, F. K. A. Lima, D. Santos, P. Rodriguez, E. H. Watanabe, and S. Arnaltes, "Simplified Modeling of a DFIG for Transient Studies in Wind Power Applications," *IEEE Transactions on Industrial Electronics*, vol. 58, pp. 9–20, 2011.

[13] M. Kayikci and J. V. Milanovic, "Assessing Transient Response of DFIG-Based Wind Plants - The Influence of Model Simplifications and Parameters," *IEEE Transactions on Power Systems*, vol. 23, pp. 545–554, May 2008.

[14] E. Muljadi, N. Samaan, V. Gevorgian, Jun Li, and S. Pasupulati, "Different Factors Affecting Short Circuit Behavior of a Wind Power Plant," *IEEE Transactions on Industry Applications*, vol. 49, no. 1, pp. 284–292, 2013.

[15] W. P. Wagner, "Short circuit contribution of large induction motors," *Proceedings of the Institution of Electrical Engineers*, vol. 116, no. 6, pp. 985–990, 1969.

[16] S. S. Kalsi, B. Adkins, and D. D. Stephen, "Calculation of system fault currents due to induction motors," *Proceedings of the Institution of Electrical Engineers*, vol. 118, no. 1, pp. 201–215, 1971.

[17] J. Morren and S. W. H. de Haan, "Short Circuit Current of Wind Turbines With Doubly Fed Induction Generator," *IEEE Transactions on Energy Conversion*, vol. 22, pp. 174–180, 2007.

[18] E. Muljadi and V. Gevorgian, "Short circuit modeling of a wind power plant," in *Power and Energy Society General Meeting, IEEE*, Detroit, Michigan, USA, 2011.

[19] P. Karaliolios, A. Ishchenko, E. Coster, J. Myrzik, and W. Kling, "Overview of short circuit contribution of various distributed generators on the distribution network," in *43rd International Universities Power Engineering Conference*, 2008, pp. 1–6.

[20] D. F. Howard, J. Restrepo, T. Smith, M. Starke, J. Dang, and R. G. Harley, "Calculation of Fault Current Contribution of Type 1 Wind Turbine Generators," in *Power and Energy Society General Meeting, IEEE*, Detroit, Michigan, USA, 2011, pp. 1–7.

[21] T. Ackermann, Ed., *Wind Power in Power Systems*. John Wiley & Sons, Ltd, 2005.

[22] S. Brahma, M. Chaudhary, and S. Ranade, "Some findings about equivalencing windfarms with Type 1 and Type 2 induction generators," in *North American Power Symposium*, Boston, Massachusetts, USA, 2011, pp. 1–6.

[23] M. Chaudhary, S. M. Brahma, and S. J. Ranade, "Short circuit analysis of Type II induction generator and wind farm," in *IEEE PES Transmission and Distribution Conference and Exposition*, Montevideo, Uruguay, 2012, pp. 1–5.

[24] C. Abbey, J. Morneau, J. Mahseredjian, and G. Joos, "Modeling requirements for transient stability studies for wind parks," in *Power Engineering Society General Meeting, IEEE*, Montreal, Quebec, Canada, 2006, p. 6.

[25] J. G. Slootweg and W. L. Kling, "Aggregated modelling of wind parks in power system dynamics simulations," in *Power Tech Conference Proceedings, IEEE*, vol. 3, Bologna, Italy, 2003, p. 6.

[26] Markus Poller and S. Achilles, "Aggregated Wind Park Models for Analyzing Power System Dynamics," in *4th Int. Workshop Large-Scale Integration of Wind Power and Transmission Networks for Offshore Wind Farms*, Billund, Denmark, Oct 2003.

[27] H. Liu and Z. Chen, "Aggregated modelling for wind farms for power system transient stability studies," in *2012 Asia-Pacific Power and Energy Engineering Conference*, March 2012, pp. 1–6.

[28] D. E. Kim and M. A. El-Sharkawi, "Dynamic equivalent model of wind power plant using an aggregation technique," *IEEE Transactions on Energy Conversion*, vol. 30, no. 4, pp. 1639–1649, 2015.

[29] L. Fan, R. Kavasseri, Z. L. Miao, and C. Zhu, "Modeling of DFIG Based Wind Farms for SSR Analysis," *IEEE Transactions on Power Delivery*, vol. 25, no. 4, pp. 2073–2082, 2010.

[30] R. Ramanujam, *Power System Dynamics: Analysis and Simulation*. PHI Learning Pvt. Ltd., 2009.

[31] F. Iov, A. D. Hansen, P. E. Sørensen, and N. A. Cutululis, "Mapping of grid faults and grid codes," Risø National Laboratory, Tech. Rep., 2007.

[32] M. Mohseni and S. M. Islam, "Transient control of dfig-based wind power plants in compliance with the australian grid code," *IEEE Transactions on Power Electronics*, vol. 27, no. 6, pp. 2813–2824, June 2012.

[33] M. Tsili and S. Papathanassiou, "A review of grid code technical requirements for wind farms," *IET Renewable Power Generation*, vol. 3, no. 3, pp. 308–332, 2009.

[34] J. Morren and S. de Haan, "Ridethrough of wind turbines with doubly-fed induction generator during a voltage dip," *IEEE Transactions on Energy Conversion*, vol. 20, pp. 435–441, 2005.

[35] A. Safaei, S. Hosseinian, H. A. Abyaneh, N. Fallah-Amini, and H. Hashemi-Dezaki, "Investigation of sfcl impacts on crowbar protection of dfig based wind turbine," in *Electrical Power Distribution Networks Conference (EPDC), 2015 20th Conference on*. IEEE, 2015, pp. 280–286.

[36] J. Yang, J. E. Fletcher, and J. OReilly, "A series-dynamic-resistor-based converter protection scheme for doubly-fed induction generator during various fault conditions," *IEEE Transactions on Energy Conversion*, vol. 25, no. 2, pp. 422–432, 2010.

[37] P. Huang, M. S. El Moursi, W. Xiao, and J. L. Kirtley, "Subsynchronous resonance mitigation for series-compensated dfig-based wind farm by using two-degree-of-freedom control strategy," *IEEE Transactions on Power Systems*, vol. 30, no. 3, pp. 1442–1454, 2015.

[38] P. Pourbeik, R. Koessler, D. Dickmander, and W. Wong, "Integration of large wind farms into utility grids (part 2-performance issues)," in *Power Engineering Society General Meeting, 2003, IEEE*, vol. 3. IEEE, 2003.

[39] C. Wagner, "Self-excitation of induction motors with series capacitors," *Electrical Engineering*, vol. 60, no. 12, pp. 1241–1247, 1941.

[40] A. E. Leon and J. A. Solsona, "Sub-synchronous interaction damping control for dfig wind turbines," *IEEE Transactions on Power Systems*, vol. 30, no. 1, pp. 419–428, 2015.

[41] J. Adams, V. A. Pappu, and A. Dixit, "Ercot experience screening for sub-synchronous control interaction in the vicinity of series capacitor banks," in *2012 IEEE Power and Energy Society General Meeting*. IEEE, 2012, pp. 1–5.

[42] H. A. Mohammadpour and E. Santi, "SSR damping controller design and optimal placement in rotor-side and grid-side converters of series-compensated dfig-based wind farm," *IEEE Transactions on Sustainable Energy*, vol. 6, no. 2, pp. 388–399, 2015.

[43] H. A. Mohammadpour, A. Ghaderi, and E. Santi, "Analysis of sub-synchronous resonance in doubly-fed induction generator-based wind farms interfaced with gate–controlled series capacitor," *IET Generation, Transmission & Distribution*, vol. 8, no. 12, pp. 1998–2011, 2014.

[44] H. A. Mohammadpour and E. Santi, "Sub-synchronous resonance analysis in DFIG-based wind farms: Definitions and problem identificationpart I," in *2014 IEEE Energy Conversion Congress and Exposition (ECCE)*. IEEE, 2014, pp. 812–819.

[45] H. A. Mohammadpour and E. Santi, "Sub-synchronous resonance analysis in DFIG-based wind farms: Mitigation methodsTCSC, GCSC, and DFIG controllerspart II,"

in *2014 IEEE Energy Conversion Congress and Exposition (ECCE)*. IEEE, 2014, pp. 1550–1557.

[46] C. Karawita and U. D. Annakkage, "Multi-infeed hvdc interaction studies using small-signal stability assessment," *IEEE Transactions on Power Delivery*, vol. 24, no. 2, pp. 910–918, 2009.

[47] H. A. Mohammadpour and E. Santi, "Analysis of subsynchronous control interactions in DFIG-based wind farms: ERCOT case study," in *2015 IEEE Energy Conversion Congress and Exposition (ECCE)*. IEEE, 2015, pp. 500–505.

[48] D. H. R. Suriyaarachchi, U. D. Annakkage, C. Karawita, and D. A. Jacobson, "A Procedure to Study Sub-Synchronous Interactions in Wind Integrated Power Systems," *IEEE Transactions on Power Systems*, vol. 28, no. 1, pp. 377–384, Feb 2013.

[49] N. Johansson, L. Angquist, and H. P. Nee, "A Comparison of Different Frequency Scanning Methods for Study of Subsynchronous Resonance," *IEEE Transactions on Power Systems*, vol. 26, no. 1, pp. 356–363, 2011.

[50] M. Sahni, D. Muthumuni, B. Badrzadeh, A. Gole, and A. Kulkarni, "Advanced screening techniques for sub-synchronous interaction in wind farms," in *Transmission and Distribution Conference and Exposition (T D), 2012 IEEE PES*, Orlando, Florida, USA, 2012, pp. 1–9.

[51] B. Badrzadeh, M. Sahni, D. Muthumuni, Y. Zhou, and A. Gole, "Sub-synchronous interaction in wind power plants part I: Study tools and techniques," in *Power and Energy Society General Meeting, IEEE*, San Diego, CA, USA, 2012, pp. 1–9.

[52] Mohsen Ghafouri, Ulas Karaagac, Houshang Karimi, and Jean Mahseredjian, "Sub-synchronous resonance dapming in DFIG-based wind farms using optimal control," in *IEEE*, 2016.

[53] D. H. R. Suriyaarachchi, U. D. Annakkage, C. Karawita, D. Kell, R. Mendis, and R. Chopra, "Application of an SVC to damp sub-synchronous interaction between

wind farms and series compensated transmission lines," in *Power and Energy Society General Meeting, IEEE*, San Diego, CA, USA, 2012, pp. 1–6.

[54] M. S. El Moursi, B. Bak Jensen, and M. H. Abdel Rahman, "Novel STATCOM Controller for Mitigating SSR and Damping Power System Oscillations in a Series Compensated Wind Park," *Power Electronics, IEEE Transactions on*, vol. 25, no. 2, pp. 429–441, 2010.

[55] R. K. Varma, S. Auddy, and Y. Semsedini, "Mitigation of Subsynchronous Resonance in a Series-Compensated Wind Farm Using FACTS Controllers," *IEEE Transactions on Power Delivery*, vol. 23, no. 3, pp. 1645–1654, 2008.

[56] A. Ellis, Y. Kazachkov, E. Muljadi, P. Pourbeik, and J. Sanchez-Gasca, "Description and technical specifications for generic wtg modelsa status report," in *2011 IEEE/PES Power Systems Conference and Exposition*, 2011.

[57] J. J. Sanchez-Gasca, "Generic wind turbine generator models for wecc-a second status report," in *2015 IEEE Power & Energy Society General Meeting.* IEEE, 2015, pp. 1–5.

[58] P. Pourbeik, A. Ellis, J. Sanchez-Gasca, Y. Kazachkov, E. Muljadi, J. Senthil, and D. Davies, "Generic stability models for type 3 & 4 wind turbine generators for wecc," in *Power and Energy Society General Meeting (PES), 2013 IEEE*, 2013, pp. 1–5.

[59] J. Peralta, H. Saad, S. Dennetière, and J. Mahseredjian, "Dynamic performance of average-value models for multi-terminal vsc-hvdc systems," in *2012 IEEE Power and Energy Society General Meeting.* IEEE, 2012, pp. 1–8.

[60] R. Jain, B. K. Johnson, and H. L. Hess, "Performance of line protection and supervisory elements for doubly fed wind turbines," in *2015 IEEE Power & Energy Society General Meeting.* IEEE, 2015, pp. 1–5.

[61] P. C. Krause and C. H. Thomas, "Simulation of Symmetrical Induction Machinery," *IEEE Transactions on Power Apparatus and Systems*, vol. 84, pp. 1038 – 1053, Nov 1965.

[62] S. R. Sanders, J. M. Noworolski, X. Z. Liu, and G. C. Verghese, "Generalized averaging method for power conversion circuits," *IEEE Transactions on Power Electronics*, vol. 6, pp. 251–259, 1991.

[63] V. Venkatasubramanian, "Tools for dynamic analysis of the general large power system using time-varying phasors," *International Journal of Electrical Power & Energy Systems*, vol. 16, no. 6, pp. 365–376, 1994.

[64] F. Gao and K. Strunz, "Frequency-adaptive power system modeling for multiscale simulation of transients," *IEEE Transactions on Power Systems*, vol. 24, no. 2, pp. 561–571, 2009.

[65] Aleksandar M. Stankovic, Bernard C. Lesieutre, and T. Aydin, "Applications of Generalized Averaging to Synchronous and Induction Machines," in *28th North American Power Symposium, M.I.T*, Nov 1996.

[66] S. Henschel, "Analysis of electromagnetic and electromechanical power system transients with dynamic phasors," Ph.D. dissertation, University of British Colombia, 1999.

[67] L. Piyasinghe, Z. Miao, and L. Fan, "Dynamic phase based model of Type 1 wind generator for unbalanced operation," in *Power Electronics and Machines in Wind Applications, IEEE*, Denver, USA, 2012, pp. 1–5.

[68] T. Demiray, F. Milano, and G. Andersson, "Dynamic Phasor Modeling of the Doubly-fed Induction Generator under Unbalanced Conditions," in *Power Tech, IEEE*, Lausanne, Switzerland, 2007, pp. 1049–1054.

[69] Turhan Hilmi Demiray, "Simulation of Power System Dynamics using Dynamic Phasor Models," Ph.D. dissertation, Swiss Federal Institute of Technology, Zurich, 2008.

[70] S. Chandrasekar, "Short circuit modeling of wind turbine generators," Master's thesis, University of Saskatchewan, 2013.

[71] S. Chandrasekar and R. Gokaraju, "Dynamic phasor modeling of Type 3 DFIG wind generators (including SSCI phenomenon) for short-circuit calculations," *IEEE Transactions on Power Delivery*, vol. 30, no. 2, pp. 887–897, 2015.

[72] S. R. Deore, P. B. Darji, and A. M. Kulkarni, "Dynamic phasor modeling of modular multi-level converters," in *2012 IEEE 7th International Conference on Industrial and Information Systems (ICIIS)*. IEEE, 2012, pp. 1–6.

[73] P. Mattavelli, G. C. Verghese, and A. Stankovic, "Phasor dynamics of thyristor-controlled series capacitor systems," *IEEE Transactions on Power Systems*, vol. 12, no. 3, pp. 1259–1267, 1997.

[74] M. A. Hannan and K. W. Chan, "Modern power systems transients studies using dynamic phasor models," in *Power System Technology, 2004. PowerCon 2004. 2004 International Conference on*, vol. 2, Nov 2004, pp. 1469–1473 Vol.2.

[75] P. C. Stefanov and A. M. Stankovic, "Modeling of UPFC operation under unbalanced conditions with dynamic phasors," *IEEE Transactions on Power Systems*, vol. 17, no. 2, pp. 395–403, 2002.

[76] M. A. Hannan, A. Mohamed, and A. Hussain, "Modeling and power quality analysis of STATCOM using phasor dynamics," in *IEEE International Conference on Sustainable Energy Technologies*, Kathmandu, Nepal, 2008, pp. 1013–1018.

[77] M. Daryabak, "Modeling Line-Commutated Converter HVDC Transmission Systems Using Dynamic Phasors," Ph.D. dissertation, University of Manitoba, 2016.

[78] Z. Miao, L. Piyasinghe, J. Khazaei, and L. Fan, "Dynamic phasor-based modeling of unbalanced radial distribution systems," *IEEE Transactions on Power Systems*, vol. 30, no. 6, pp. 3102–3109, 2015.

[79] T. Yang, S. Bozhko, J. M. Le-Peuvedic, G. Asher, and C. I. Hill, "Dynamic phasor modeling of multi-generator variable frequency electrical power systems," *IEEE Transactions on Power Systems*, vol. 31, no. 1, pp. 563–571, Jan 2016.

[80] R. A. Walling and M. L. Reichard, "Short circuit behavior of wind turbine generators," in *Protective Relay Engineers, 2009 62nd Annual Conference for*, March 2009, pp. 492–502.

[81] M. Chaudhary, S. M. Brahma, and S. J. Ranade, "Interpreting the short circuit behavior of type 4 wind turbine generator," in *2014 IEEE PES T D Conference and Exposition*, April 2014, pp. 1–5.

[82] N. Z. BinWu, Yongqiang Lang and Samir Kouro, *Power Conversion and Control of Wind Energy Systems*. John Wiley & Sons, Inc., 2011.

[83] A. D. Hansen and L. H. Hansen, "Wind turbine concept market penetration over 10 years (1995–2004)," *Wind energy*, vol. 10, no. 1, pp. 81–97, 2007.

[84] *Advanced Analysis of Electric Machines and Drive Systems, EE444*, University of Saskatchewan.

[85] Joint Working Group on Fault Current Contributions from Wind Plants, "Fault Current Contributions from Wind Plants - Draft 7.1," IEEE Power Systems Relaying Committee, Tech. Rep., 2012.

[86] R. Walling, R. Harley, D. Miller, and G. Henneberg, "Fault current contributions from wind plants," in *Protective Relay Engineers, 2015 68th Annual Conference for, College Station, TX, USA*, 2015, pp. 137–227.

[87] W. Price *et al.*, "Simplified wind turbine generator aerodynamic models for transient stability studies," in *2006 IEEE PES Power Systems Conference and Exposition*. IEEE, 2006, pp. 986–992.

[88] P. Pourbeik, "Proposed changes to the wecc wt3 generic model for type 3 wind turbine generators," EPRI, Tech. Rep., 2014.

[89] J. Mahseredjian, V. Dinavahi, and J. A. Martinez, "Simulation tools for electromagnetic transients in power systems: Overview and challenges," *IEEE Transactions on Power Delivery*, vol. 3, no. 24, pp. 1657–1669, 2009.

[90] T. M. J. Giesbrecht, "Small Time-step ($<2\mu$sec) VSC model for the real time digital simulator." Electrimacs, 2005.

[91] *RTDS User Manual*.

[92] H. W. Dommel, "Digital computer solution of electromagnetic transients in single and multiphase," *Networks IEEE*, vol. 88, no. 4, pp. 388–399, 1969.

[93] O. Anaya Lara, N. Jenkins, J. Ekanayake, P. Cartwright, and M. Hughes, *Wind energy generation: modelling and control*. John Wiley & Sons, 2011.

[94] "Matlab r2016a documentation." The MathWorks Inc., Tech. Rep.

[95] H. Li and Z. Chen, "Transient stability analysis of wind turbines with induction generators considering blades and shaft flexibility," in *Industrial Electronics Society, 2007. IECON 2007. 33rd Annual Conference of the IEEE*, Nov 2007, pp. 1604–1609.

[96] R. Pena, J. C. Clare, and G. M. Asher, "Doubly fed induction generator using back-to-back pwm converters and its application to variable-speed wind-energy generation," *IEE Proceedings - Electric Power Applications*, vol. 143, no. 3, pp. 231–241, May 1996.

[97] "Generation and load interconnection standard," AESO, Tech. Rep., 2006.

[98] V. Akhmatov, "Analysis of dynamic behavior of electric power systems with large amount of wind power," Ph.D. dissertation, Technical University of Denmark, 2003.

[99] O. Anaya-Lara, Z. Liu, G. Quinonez-Varela, and J. R. McDonald, "Optimal dfig crowbar resistor design under different controllers during grid faults," in *Electric Utility Deregulation and Restructuring and Power Technologies, 2008. DRPT 2008. Third International Conference on*. IEEE, 2008, pp. 2580–2585.

[100] K. Okedu, S. Muyeen, R. Takahashi, and J. Tamura, "Comparative study between two protection schemes for dfig-based wind generator," in *Electrical Machines and Systems (ICEMS), 2010 International Conference on*. IEEE, 2010, pp. 62–67.

[101] K. E. Okedu, S. Muyeen, R. Takahashi, and J. Tamura, "Wind farms fault ride through using dfig with new protection scheme," *IEEE Transactions on Sustainable Energy*, vol. 3, no. 2, pp. 242–254, 2012.

[102] P. Kundur, *Power System Stability and Control*. New York: McGraw-Hill, 1994.

[103] Lingling Fan, R. Kavasseri, Zhixin Lee Miao, and Chanxia Zhu, "Modeling of DFIG Based Wind Farms for SSR Analysis," *IEEE Transactions on Power Delivery*, vol. 25, pp. 2073–2082, 2010.

[104] K. Padiyar, *Analysis of Subsynchronous Resonance in Power Systems*. Springer Science & Business Media, 1999, vol. 471.

[105] P. Anderson, B. Agrawal, and J. Van Ness, "Subsynchronous resonance in power systems," 1990.

[106] I. S. working group *et al.*, "First benchmark model for computer simulation of subsynchronous resonance," *IEEE transactions on power apparatus and systems*, vol. 96, no. 5, pp. 1565–1572, 1977.

[107] M. Parniani and M. Iravani, "Computer analysis of small-signal stability of power systems including network dynamics," *IEE Proceedings-Generation, Transmission and Distribution*, vol. 142, no. 6, pp. 613–617, 1995.

[108] T. Demiray, G. Andersson, and L. Busarello, "Evaluation study for the simulation of power system transients using dynamic phasor models," in *Transmission and Distribution Conference and Exposition: Latin America*, 2008, pp. 13–15.

[109] A. Yazdani and R. Iravani, "A generalized state-space averaged model of the three-level NPC converter for systematic DC-voltage-balancer and current-controller design," *IEEE Transactions on Power Delivery*, vol. 20, no. 2, pp. 1105–1114, 2005.

[110] J. R. Martí, H. W. Dommel, B. D. Bonatto, and A. F. Barrete, "Shifted frequency analysis (sfa) concepts for emtp modelling and simulation of power system dynamics," in *Power Systems Computation Conference (PSCC), 2014*. IEEE, 2014, pp. 1–8.

[111] Y. Zhou, P. Bauer, J. A. Ferreira, and J. Pierik, "Operation of grid-connected dfig under unbalanced grid voltage condition," *IEEE Transactions on Energy Conversion*, vol. 24, no. 1, pp. 240–246, 2009.

[112] A. Yazdani and R. Iravani, *Voltage-Sourced Converters in Power Systems: Modeling, Control, and Applications*. John Wiley & Sons, 2010.

[113] E. Tara, S. Filizadeh, J. Jatskevich, E. Dirks, A. Davoudi, M. Saeedifard, K. Strunz, and V. Sood, "Dynamic average-value modeling of hybrid-electric vehicular power systems," *IEEE Transactions on Power Delivery*, vol. 27, no. 1, pp. 430–438, 2012.

Appendix A

System data

A.1 Type 1 Wind Generator Test System Parameters

Table A.1: Type 1 wind generator test system data

Generator data	$1.717\,MVA$, $1.545\,MW$, $0.575\,kV$, $60\,Hz$, $Poles = 6$, $H = 4.55\,s$, $R_{stator} = 0.00727\,p.u$, $R_{rotor} = 0.00514\,p.u$, $L_m = 2.9922 p.u$, $L_{stator} = 0.1766 p.u$, $L_{rotor} = 0.1610 p.u$
Transmission line data	$R_{Line} = 0.002\,\Omega$, $L_{line} = 2.36e-5\,H$
Transformer data	$2\,MVA$, $60\,Hz$, $Y-\Delta$, $0.575/34.5\,kV$, $X_t = 0.05\,pu$

A.2 Type 2 Wind Generator Test System Parameters

Table A.2: Type 2 wind generator test system data

Generator data	$2.283 MVA$, $0.6 kV$, $60 Hz$, $H = 4.7 s$, $R_{stator} = 0.017 p.u$, $R_{rotor} = 0.0215\,p.u$, $L_m = 16.497\,p.u$, $L_{stator} = 0.340\,p.u$, $L_{rotor} = 0.3577\,p.u$
Transmission line data	$R_{Line} = 0.002\,\Omega$, $L_{line} = 2.36e-5\,H$
Transformer data	$2.5\,MVA$, $60\,Hz$, $Y-\Delta$, $0.6/34.5\,kV$, $X_t = 0.05\,pu$

A.3 Type 3 Wind Generator Test System Parameters

Table A.3: Type 3 wind generator test system data

Generator data	$3.4\,MVA$, $0.69\,kV$, $60\,Hz$, $R_{stator} = 0.0054\,p.u$, $R_{rotor} = 0.00607\,p.u$, $L_m = 4.362\,p.u$, $L_{stator} = 0.102\,p.u$, $L_{rotor} = 0.11\,p.u$
Back to Back converter	$R_{IGBT-ON} = 0.0001\,\Omega$, $R_{IGBT-OFF} = 5000\,\Omega$.
Rotor side controller	$K_{p,Q_s} = 1.0$, $K_{i,Q_s} = 1.0\,s$, $K_{p,\omega_r} = 1.0$, $K_{i,\omega_r} = 1.0\,s$, $K_{p,I_{dr}} = 1.0$, $K_{i,I_{dr}} = 2.0\,s$, $K_{p,I_{qr}} = 1.0$, $K_{i,I_{qr}} = 2.0\,s$
Grid side controller	$K_{p,V_{dc}} = 1.0$, $K_{i,V_{dc}} = 0.02\,s$, $K_{p,I_{qg}} = 0.1$, $K_{i,I_{qg}} = 0.1\,s$, $K_{p,I_{dg}} = 1.0$, $K_{i,I_{dg}} = 0.02\,s$
Transmission line data	$240\,kms$, $R_{Line} = 0.3107e-7\,p.u/m$, $X_{Line} = 0.3479e-6\,p.u/m$, $B_{Line} = 5.1885e-6\,p.u/m$
Unit Transformer	$3.4\,MVA$, $60\,Hz$, $Y-Y-Y$, $33/0.69/0.69\,kV$, $X_{1-2} = 0.0888\,p.u$, $X_{1-3} = 0.1663\,p.u$, $X_{2-3} = 0.0875\,p.u$
Interface Transformer	$3.4\,MVA$, $60\,Hz$, $\Delta-Y$, $33/345\,kV$, $X = 0.06\,p.u$
Main Transformer	$500\,MVA$, $60\,Hz$, $\Delta-Y$, $33/345\,kV$, $X = 0.06\,p.u$

A.4 Mechanical Drive Train parameters

Table A.4: Mechanical Drive Train parameters

Parameter	Value
Blade inertia (H_b)	$4.0\,sec$
Hub inertia (H_h)	$0.30\,sec$
Generator inertia (H_g)	$0.42\,sec$

Appendix B

B.1 Relationship between $\alpha\beta$ and dq reference frames

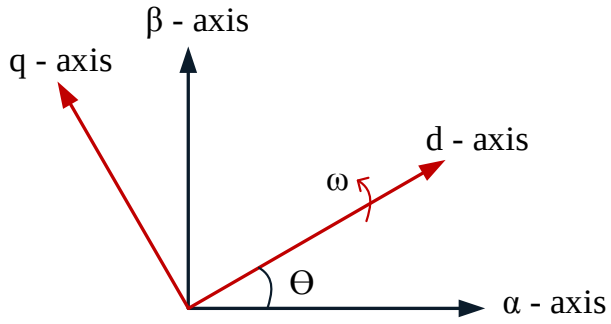

Figure B.1: $\alpha\beta$ to dq transformation

The transformation from $\alpha\beta$ to dq reference frame is as:

$$\begin{bmatrix} U_d \\ U_q \end{bmatrix} = \begin{bmatrix} cos(\theta) & sin(\theta) \\ -sin(\theta) & cos(\theta) \end{bmatrix} \begin{bmatrix} U_\alpha \\ U_\beta \end{bmatrix} \tag{B.1}$$

And the inverse transformation is

$$\begin{bmatrix} U_\alpha \\ U_\beta \end{bmatrix} = \begin{bmatrix} cos(\theta) & -sin(\theta) \\ sin(\theta) & cos(\theta) \end{bmatrix} \begin{bmatrix} U_d \\ U_q \end{bmatrix} \tag{B.2}$$

B.2 Relationship between two reference frames in dq domain

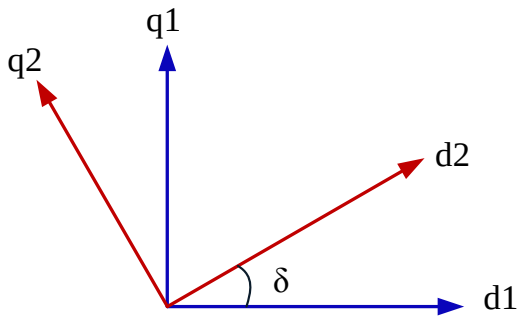

Figure B.2: Two reference frames in dq domain

Projection of a vector expressed in one reference frame $d1q1$ into other reference frame $d2q2$ is obtained via

$$\begin{bmatrix} U_{d2} \\ U_{q2} \end{bmatrix} = \begin{bmatrix} cos(\delta) & sin(\delta) \\ -sin(\delta) & cos(\delta) \end{bmatrix} \begin{bmatrix} U_{d1} \\ U_{q1} \end{bmatrix} \tag{B.3}$$

And the inverse transformation is

$$\begin{bmatrix} U_{d1} \\ U_{q1} \end{bmatrix} = \begin{bmatrix} cos(\delta) & -sin(\delta) \\ sin(\delta) & cos(\delta) \end{bmatrix} \begin{bmatrix} U_{d2} \\ U_{q2} \end{bmatrix} \tag{B.4}$$

Appendix C

Interconnections of Sub-systems for Small Signal Analysis

After linearizing the dynamic equations of all sub-systems, the complete system state space model is developed by interfacing all of the sub-systems as shown in figure C.1.

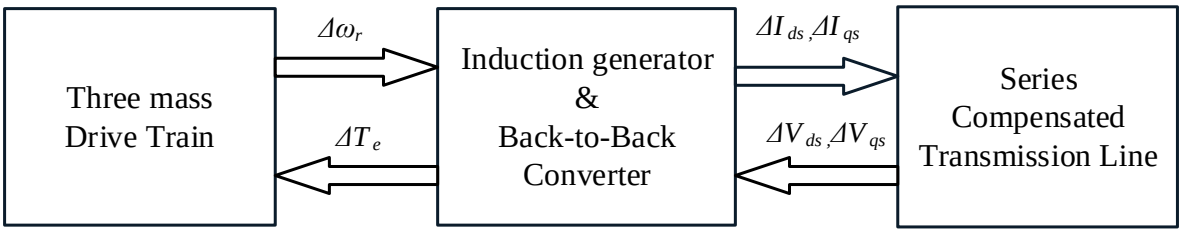

Figure C.1: Sub-systems Interconnections

Interconnection of Multi-mass Drive Train and Generator

The linearized equation for drive train is

$$\Delta\dot{x}_{wt} = A_{wt}\Delta x_{wt} + B_{wt}\Delta u_{wt} \tag{C.1}$$

where,

$$\Delta x_{wt} = \Big[\Delta\omega_b, \Delta\omega_h, \Delta\omega_r, \Delta\theta_{bh}, \Delta\theta_{hg}\Big]^T$$
$$\Delta u_{wt} = \Big[\Delta V_{wind}, \Delta T_e\Big]^T$$

It can be rewritten as,

$$\Delta\dot{x}_{wt} = A_{wt}\Delta x_{wt} + B_{wt1}\Delta V_{wind} + B_{wt2}\Delta T_e \tag{C.2}$$

Also

$$\begin{bmatrix}\Delta T_e\end{bmatrix} = \begin{bmatrix}C_{gt}\end{bmatrix}\begin{bmatrix}\Delta x_g\end{bmatrix}$$

Now, Equation C.2 can be rearranged as,

$$\Delta\dot{x}_{wt} = A_{wt}\Delta x_{wt} + B_{wt2}C_{gt}\Delta x_g + B_{wt1}\Delta V_{wind} \tag{C.3}$$

The induction machine model in linear state space form is

$$\Delta\dot{x}_g = A_g\Delta x_g + B_g\Delta u_g \tag{C.4}$$

where,

$$\Delta x_g = \begin{bmatrix}\Delta I_{ds} & \Delta I_{qs} & \Delta I_{dr} & \Delta I_{qr}\end{bmatrix}^T$$
$$\Delta u_g = \begin{bmatrix}\Delta\omega_r & \Delta V_{ds} & \Delta V_{qs} & \Delta V_{dr} & \Delta V_{qr}\end{bmatrix}^T$$

Equation C.4 can be rewritten as

$$\Delta\dot{x}_g = A_g\Delta x_g + B_{g1}\Delta\omega_r + B_{g2}\Delta u_{g2}$$

or,

$$\Delta\dot{x}_g = B_{g1}\Delta\omega_r + A_g\Delta x_g + B_{g2}\Delta u_{g2}$$

or,

$$\Delta\dot{x}_g = B_{g1}\begin{bmatrix}0 & 0 & 1 & 0 & 0\end{bmatrix}\Delta x_{wt} + A_g\Delta x_g + B_{g2}\Delta u_{g2}$$

or,

$$\Delta\dot{x}_g = B_{g1}C_{tg}\Delta x_{wt} + A_g\Delta x_g + B_{g2}\Delta u_{g2} \tag{C.5}$$

Combining equations C.3 and C.5,

$$\begin{bmatrix}\Delta\dot{x}_{wt}\\ \Delta\dot{x}_g\end{bmatrix} = \begin{bmatrix}A_{wt} & B_{wt2}C_{gt}\\ B_{g1}C_{tg} & A_g\end{bmatrix}\begin{bmatrix}\Delta x_{wt}\\ \Delta x_g\end{bmatrix} + \begin{bmatrix}B_{wt1} & 0\\ 0 & B_{g2}\end{bmatrix}\begin{bmatrix}\Delta V_{wind}\\ \Delta u_{g2}\end{bmatrix} \tag{C.6}$$

In the same fashion, each sub-systems are interconnected to form complete state space model of the wind power plant as :

$$\Delta\dot{x}_{sys} = A_{sys}\Delta x_{sys} + B_{sys}\Delta u_{sys} \tag{C.7}$$

where,

$$\Delta x_{sys} = \begin{bmatrix} \Delta x_{wt} & \Delta x_g & \Delta x_{gsc} & \Delta x_{rsc} & \Delta x_{dc} & \Delta x_N \end{bmatrix}^T$$
$$\Delta u_{sys} = \begin{bmatrix} \Delta V_{wind} & \Delta V_{dc}* & \Delta Q_s* & \Delta V_{ds} & \Delta V_{qs} & \Delta V_{di} & \Delta V_{qi} \end{bmatrix}^T$$

Appendix D

Dommel's Algorithm

H. Dommels algorithm is a digital computer solution for transient phenomena [92]. The digital computer cannot give a continuous signal for transient phenomena; instead it sends out signal solution at discrete point at an interval Δt. To eliminate or reduce the limit, H. Dommel uses trapezoidal rule to obtain an equivalent for inductance and capacitance. In Dommels algorithm inductor and capacitor are represented by a parallel combination of a resistance and a current source depending on previous state. The interval between two states is Δt, the integration time step.

The solution for transients is a step-by-step process with a time interval t .That means the time is divided into t= Δt 2 Δt 3Δt... . When solving the state v(t), the state v(t-Δt) should have been known.

Inductance

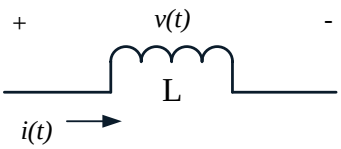

Figure D.1: Inductance

$$v(t) = L * \frac{di(t)}{dt} \tag{D.1}$$

$$i(t) = \frac{1}{L}\int v(t)dt \tag{D.2}$$

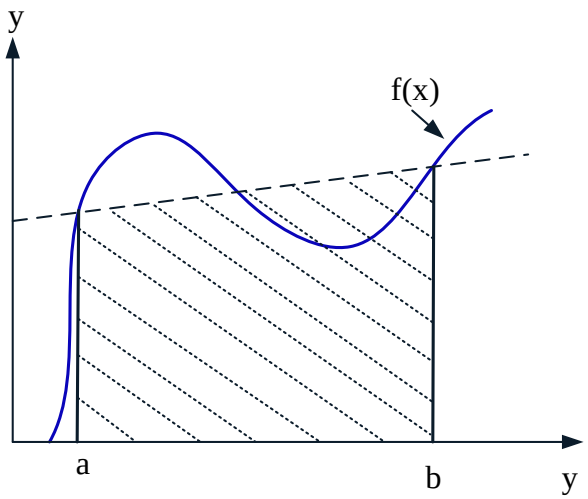

Figure D.2: Trapezoidal rule of Integration

Applying trapezoidal rule of integration (Figure D.2)

$$\begin{aligned}\int_a^b f(x)dx &= \text{Area of the trapezoid} \\ &= \frac{1}{2}(\text{Sum of parallel sided})(\text{height}) \\ &= (b-a)\frac{f(a)+f(b)}{2}\end{aligned} \tag{D.3}$$

$$\int_{t-\Delta t}^{t} i(t)dt = \frac{1}{L}\int_{t-\Delta t}^{t} v(t)dt \tag{D.4}$$

$$i(t) - i(t-\Delta t) = \frac{1}{L}\frac{\Delta t}{2}[v(t) - v(t-\Delta t)]$$

$$i(t) = \frac{\Delta t}{2L}v(t) + I_h(t-\Delta t) \tag{D.5}$$

where

$$I_h = i(t-\Delta t) + \frac{\Delta t}{2L}v(t-\Delta t)$$

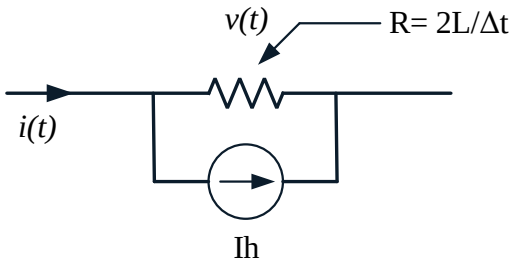

Figure D.3: Equivalent circuit for inductor

Here I_h is considered as an equivalent History Term Current since it can be determined by only quantities from previous state. Figure D.3 is the equivalent circuit for inductance.

Capacitance

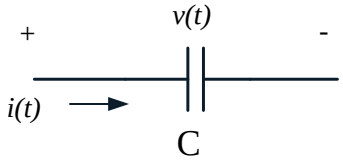

Figure D.4: Capacitance

$$i(t) = C * \frac{dv(t)}{dt} \tag{D.6}$$

$$v(t) = \frac{1}{C} \int i(t)dt \tag{D.7}$$

Applying trapezoidal rule of integration, we get

$$i(t) = \frac{2C}{\Delta t} v(t) + I_h(t - \Delta t) \tag{D.8}$$

where

$$I_h = -i(t - \Delta t) + \frac{2C}{\Delta t} v(t - \Delta t)$$

Similarly, I_h is also considered as an equivalent History Term. Figure D.5 is the equivalent circuit for capacitance.

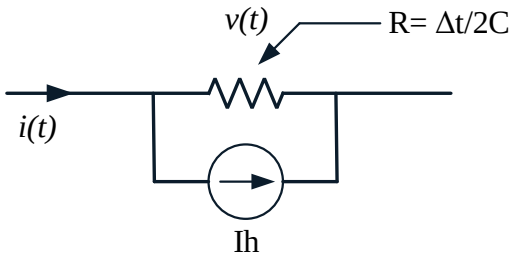

Figure D.5: Equivalent circuit for capacitance

Implementation

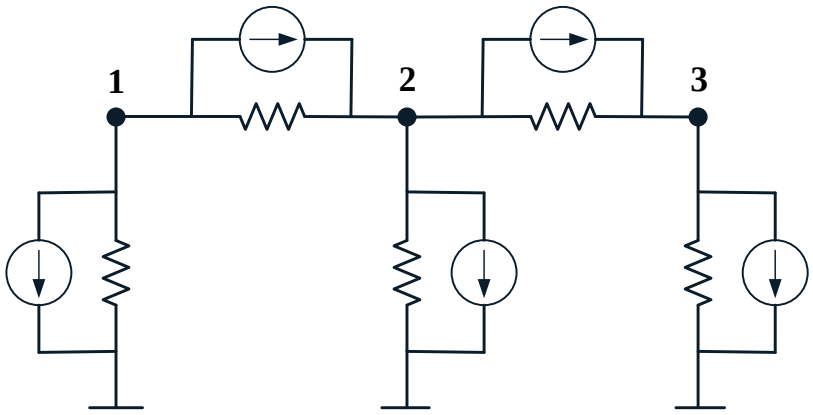

Figure D.6: Equivalent circuit for all power systems

All power systems consist of current source, voltage source, transmission lines, and load, and all these components can be substituted by the equivalent circuit only using a parallel combination of R and I_h which were discussed above.

To solve this circuit, nodal equations are utilized.

$$\begin{bmatrix} V_1 \\ V_2 \\ V_3 \end{bmatrix} = \begin{bmatrix} G11 & G12 & G13 \\ G21 & G22 & G23 \\ G31 & G32 & G33 \end{bmatrix}^{-1} \begin{bmatrix} I_1 \\ I_2 \\ I_3 \end{bmatrix} \tag{D.9}$$

where $\begin{bmatrix} G11 & G12 & G13 \\ G21 & G22 & G23 \\ G31 & G32 & G33 \end{bmatrix}$ is the conductance matrix.

Solution steps:

1. Calculate I_{1h}, I_{2h}, I_{3h} first using the data of pre-state or initial state.
2. Calculate V_1, V_2, V_3 using the nodal equation and the I_{1h}, I_{2h}, I_{3h} acquired in (1).
3. Consider I and V computed in (1) and (2) as the history state quantities for next state and calculate equivalent History Term Current I_h prepare for next state.
4. Repeat from (1) until the end of t.